Identification of Hadronic τ Decays and Observation Potential of CP-violating effects in SUSY at ATLAS

Dissertation
zur Erlangung des Doktorgrades
des Department Physik
der Universität Hamburg

vorgelegt von
Diplom-Physiker Björn Gosdzik
geboren in Bad Pyrmont

Hamburg
Januar 2011

Gutachter der Dissertation:	Dr. Philip Bechtle Prof. Dr. Peter Schleper
Gutachter der Disputation:	Dr. Philip Bechtle Prof. Dr. Gudrid Moortgat-Pick
Datum der Disputation:	24. Februar 2011
Vorsitzende des Prüfungsausschusses:	Prof. Dr. Caren Hagner
Vorsitzender des Promotionsausschusses:	Prof. Dr. Joachim Bartels
Leiterin des Departments Physik:	Prof. Dr. Daniela Pfannkuche
Dekan der MIN-Fakultät :	Prof. Dr. Heinrich Graener

Die Neugier steht immer an erster Stelle eines Problems, das gelöst werden will.

Galileo Galilei

Abstract

In November 2009 the ATLAS experiment started operation at the Large Hadron Collider (LHC) at CERN. The detector is optimized to search for the Higgs Boson and new physics at the TeV scale. Until the end of the data-taking period with proton-proton collisions on November 3rd, 2010, the ATLAS detector recorded an integrated luminosity of 45.0 pb^{-1} at a center-of-mass energy of $\sqrt{s}$=7 TeV.

In many signals of the Standard Model and new physics (e.g. SUSY and Higgs) τ-leptons play an important role. A cut-based approach for the identification of hadronically decaying τ-leptons is being used, particularly for the first data-taking period. Using Monte Carlo Data, the development of a cut-based identification method for hadronically decaying τ-lepton with the ATLAS detector at the Large Hadron Collider (LHC) with a center-of-mass energy of $\sqrt{s} = 14$ TeV is presented. The separation of signal and the large QCD jet background is a challenge to the identification of hadronically decaying τ-lepton. The identification is separated into two methods: the calorimeter-based method uses exclusive calorimeter information, while the calorimeter+track-based method combines calorimeter and tracking information. The cut optimization is separately accomplished for τ candidates with one charged decay product (1-prong) and τ candidates with three charged decay products (3-prong). Additionally the optimization is split into bins of the visible transverse energy of the τ candidate ($E_{\mathrm{T}}^{\mathrm{vis}}$). First of all the optimization is presented and afterwords the performance of the cut-based identification method is discussed. The reconstruction efficiency for τ-leptons is determined by comparing first data corresponding to an integrated luminosity of 244 nb^{-1} and Monte Carlo simulation. The effect of systematic uncertainties is investigated.

The CP violation predicted by the Standard Model is not sufficient to explain the matter – anti-matter asymmetry in the universe of the order of $\mathcal{O}(10^{-10})$. Hence new sources of CP violation are required. One possible approach is CP violation in the supersymmetric extension of the Standard Model. The CP violation can be evoked in models with so-called "minimal supergravity" (mSUGRA) by introducing a complex phase. In such models the lightest supersymmetric particle (LSP) is the neutralino one. The triple product of the final state in cascade decay chains with two- or three-body decays is sensitive for CP-violating effects. For this purpose the mass and momentum of all decay products must be known. The potential to observe CP violation in $\tilde{t}$ cascade decay chains with the ATLAS detector is investigated, with the CP violation added to the trilinear coupling ϕ_A. The momentum reconstruction of the neutralino one as well as the determination of the triple product asymmetry are presented.

Zusammenfassung

Im November 2009 hat das ATLAS Experiment am Large Hadron Collider (LHC) am CERN seinen Betrieb aufgenommen. Der Detektor ist dabei auf die Suche nach dem Higgs Boson und der Suche nach neuer Physik an der TeV Skala optimiert. Bis zum Ende der Datennahme Periode mit proton-proton Kollisionen am 03. November 2010 hat der ATLAS Detektor eine integrierte Luminosität von 45.0 pb^{-1} bei einer Schwerpunktsenergie von $\sqrt{s}$ =7 TeV aufgezeichnet.

In vielen Signalen des Standarmodells und neuer Physik (z.B. SUSY und Higgs) stellen τ Leptonen eine wichtige Signatur dar. Insbesondere für die ersten Datennahmen sollen schnittbasierende Ansätze bei der Identifikation von hadronisch zerfallenden τ Leptonen zur Anwendung kommen. Unter der Verwendung von Monte Carlo Daten wird die Entwicklung einer schnittbasierten Methode zur Identifikation von hadronisch zerfallenden τ-Lepton mit dem ATLAS Detektor bei der vorgesehenen Schwerpunktsenergie von $\sqrt{s}$ = 14 TeV vorgestellt. Die Herausforderung bei der Identifikation von hadronisch zerfallenden τ-Leptonen ist die Trennung von Signal und umfangreichen QCD Jet Untergrund. Die Identifikation ist aufgeteilt in zwei Methoden: die Kalorimeter-basierte Methode verwendet ausschließlich Kalorimeter Informationen, während die Kalorimeter+Track-basierte Methode Kalorimeter und Tracking Informationen kombiniert. Die Optimierung der Schnitte wird dabei getrennt für τ Kandidaten mit einem geladenen Zerfallsprodukt (1-prong) und τ Kandidaten mit drei geladenen Zerfallsprodukten (3-prong) durchgeführt. Zusätzlich wird die Optimierung in Bins der sichtbaren transversalen Energie der τ Kandidaten ($E_{\text{T}}^{\text{vis}}$) unterteilt. Es wird zuerst die Optimierung vorgestellt und anschließend die Leistung der schnittbasierten Identifikationsmethode diskutiert. Die Effizienz der τ Rekonstruktion wird anhand des Vergleiches von ersten Daten mit einer integrierten Luminosität von 244 nb^{-1} und Monte Carlo Simulation durchgeführt. Dabei wird der Effekt von systematischen Unsicherheiten untersucht.

Die durch das Standard Modell vorhergesagte CP Verletzung ist nicht ausreichend um die Materie-Antimaterie Asymmetrie im Universum in der Größenordnung von $\mathcal{O}(10^{-10})$ zu erklären. Daher sind weitere Quellen für CP Verletzung notwendig. Eine Möglichkeit ist die CP Verletzung in der supersymmetrischen Erweiterungen des Standard Modells. In Modelle mit so genannter “minimal supergravity” (mSUGRA) kann die CP Verletzung durch Einführung einer komplexen Phase hervorgerufen werden. In diesem Modell ist das leichteste supersymmetrische Teilchen (LSP) das Neutralino eins. Bei Kaskaden Zerfällsketten mit zwei- oder dreikörper Zerfällen ist das Triple Produkt der Entzustände sensitiv auf CP-verletzende Effekte. Dazu werden die Massen und Impulse aller am Zerfall beteiligten Teilchen benötigt. Es wird die Möglichkeit untersucht, CP Verletzung in $\tilde{t}$ Kaskaden Zerfallsketten mit dem ATLAS Detektor festzustellen, bei der die CP Verletzung der trilinearen Kopplung ϕ_A beigegeben wird. Dabei wird die Impulsrekonstruktion des Neutralino eins sowie die Bestimmung der Asymmetrie der Triple Produkte vorgestellt.

Contents

1. Introduction

A brief historic overview

Since antiquity people try to understand nature, such as the behavior of stars and planets. In the first half of the 6th century BC the Greek philosopher Thales ($\Theta\alpha\lambda\tilde{\eta}\varsigma$) attempt to explain natural phenomena without reference to mythology and is therefore regarded as the founder of philosophy and science. First writings covering physics were prepared by Aristotle ($A\rho\iota\sigma\tau o\tau\acute{\epsilon}\lambda\eta\varsigma$), who was a student of Plato ($\Pi\lambda\acute{\alpha}\tau\omega\nu$). The first idea of the existence of fundamental particles, was described by Leucippus ($\Lambda\epsilon\acute{\upsilon}\kappa\iota\pi\pi o\varsigma$) and his student Democritus ($\Delta\eta\mu\acute{o}\kappa\rho\iota\tau o\varsigma$) in the first half of 5th century BC. They developed a model in which the world is composed of empty space and matter of smallest indivisible elements, called atoms. Henceforward disputes moved from pure cosmological questions to more abstract subjects such as the origin and composition of matter.

The vision that the Earth is located in the center of the universe while all celestial bodies are moving on spheres around it (geocentric model) was founded by Ptolemy ($\Pi\tau o\lambda\epsilon\mu\alpha\tilde{\imath}o\varsigma$) and was accepted for more than 1500 years. Primary in the late 16th century it was replaced by Nicolaus Copernicus, Galileo Galilei and Johannes Kepler by the heliocentric model. This age marks the beginning of a new are of physicists with the most famous being Isaac Newton. In his famous scientific book *PhilosophiæNaturalis Principia Mathematic* [1] he described universal gravitation and the three laws of motion. This work builds the fundament for classical mechanics. The area of modern physics started with the work of Albert Einstein. He thought that Newtonian mechanics is not enough to describe the laws of classical mechanics and the laws of the electromagnetic field. His works about the special theory of relativity [2] and general relativity [3] describe the interaction of matter (and fields) with space and time and extended the Newtonian mechanics. Einstein also contributed to problems of quantum theory, which provides a mathematical description of particles and finally results in the description of particles within the Standard Model.

The Standard Model of elementary particle physics is the theory of fundamental particle physics. Developed in the middle of the 20th century it is very successful in describing the interactions of particles and it was finalized in the mid 1970s with the experimental confirmation of the quarks. The Standard Model contains 2 kinds of fundamental particle: fermions, such as electrons, neutrinos, and quarks forming matter and anti-matter, while gauge bosons mediate the electromagnetic, weak, and strong interactions between matter particles. The symmetry group of the Standard Model is a gauge group, a local symmetry group in which the Lagrangian is invariant under local transformation.

Although the Standard Model is very successful, it is not complete and contains several fundamental problems. Unbroken gauge theories can only describe massless particles. In contrast the Z and W gauge bosons have mass. Hence the gauge symmetry must be spontaneously broken. This mechanism is described by the Higgs mechanism and comes together with the not yet discovered Higgs boson. Furthermore the Standard Model does not consider general relativity, such as gravitation and dark energy, it does not contain dark matter which is observed in cosmological experiments, it does not account for neutrino oscillation, and the hierarchy problem is not solved. The amount of CP violation observed in the Standard Model is not sufficient to explain the matter – anti-matter asymmetry in the universe. The CP symmetry is a combination of the charged conjugate symmetry and parity symmetry. If particles are

interchanged with their anti-particles (C symmetry) and left and right were flipped the laws of physics are the same. In other words the C symmetry transforms a particle in its anti-particle and the P symmetry creates a mirror of the physical system. The strong and electromagnetic interaction are invariant under CP transformation while they are violated under certain types of weak interactions. If CP was preserved matter and anti-matter were produced in equal parts after the Big Bang and they would have canceled each other (annihilation) resulting in an universe made of radiation instead of matter. Since the universe is made of matter, CP must be violated.

The result is a likewise subject Leucippus and Democritus were considered about: what is (dark) matter, what is the origin of the matter – anti-matter asymmetry, how does matter (and anti-matter) obtain their masses, why do coupling constants have the values that were measured, and are there exact three generations?

With the start of the Large Hadron Collider (LHC) in November 2009 a new area of modern physics has started and it is expected to get a clue for new physics. With a center-of-mass energy of up to $\sqrt{s} = 14$ TeV the LHC makes a step forward in search for the not yet discovered Higgs boson. The Higgs mechanism is an extension to the Standard Model that explains the mechanism how particles obtain their masses. At the terascale new physics phenomena should pop up. Supersymmetric extensions of the Standard Model (SUSY) provide many solutions such as candidates for dark matter or new source of CP violation, or models with additional space dimensions (extra dimensions) that predicts the formation of micro black holes at the TeV scale.

About this thesis

One of the main physics goals of the ATLAS experiment at the LHC at CERN is the search for new physics. With its never before gained center-of-mass energy the LHC is able to produce new particles such as supersymmetric partners of the Standard Model particles as predicted by supersymmetric models. At the LHC the so-called sparticels can be produced with masses of several TeV, if they exist. With the ATLAS detector the properties of these particles can be measured such as mass, couplings, and lifetime. A comprehensive selection of SUSY models opens new approaches such as CP-violating effects in the framework of minimal supergravity (mSUGRA). Well-known Standard Model particles become sensitive to new phenomena since they appear in the final state of cascade decay chains.

This thesis covers two topics. The first one is the identification of hadronically decaying τ-leptons at the ATLAS detector with a cut-based method. τ-leptons are electron like leptons of the third generation and were discovered in 1975. With spin 1/2 and the same charge as the electron the τ-lepton interacts electromagnetic and weakly, but with 1.78 GeV it is almost 3500 times heavier than the electron. For the decay of gauge bosons, Higgs bosons or SUSY cascade decays, the τ-lepton carries important information on the polarization of the decaying resonances and on the spin correlation in case of pair production. In various SUSY scenarios the τ-lepton becomes the dominant decay mode at large $\tan\beta$[1] in SUSY cascade decays and can be used to determine the mass of the lightest supersymmetric particle (LSP) that serves as a good candidate for dark matter. Hence the identification and measurement of the invariant mass of two τ-leptons with high precision is essential.

With a lifetime of 2.9×10^{-13} s the τ-lepton can only be identified by its decay products. With almost 64 % of the time, the hadronic decay is the dominate decay mode for τ-leptons. At hadron colliders this decay is subject of a large background composed mainly of QCD jets. The separation of the τ signal in this QCD environment is a challenge on the identification algorithm.

The second topic covers the possibility to observe CP-violating effects in the supersymmetric exten-

[1] Ratio of Higgs the vacuum expectation values

sion of the Standard Model at the LHC. Since the CP-violating sources in the Standard Model are not sufficient to explain the matter – anti-matter asymmetry in the universe, new source of CP violation must be explored. In the scenario used for the study the CP violation occurs in the complex phase of the trilinear coupling of stop cascade decays, which goes into the mixing matrix of the stop masses. Triple products of the momenta of the final state particles are sensitive to CP-violating effects. If the asymmetry in the triple product can be measured at the LHC, CP-violating effects in the stop sector can be observed. The study was performed with 500 fb^{-1} to define the areas of the mSUGRA parameter space.

After the introduction, the theoretical framework is described in the second chapter of this thesis. The Standard Model with focus on quantum chromodynamics is introduced, followed by supersymmetry with a detailed description of CP violation in the minimal supersymmetric model. In chapter three the Large Hadron Collider and the ATLAS experiment, including a general view of the detector and the trigger are described. Chapter four gives an overview of the data taking periods from November 2009 until November 2010, Monte Carlo event generator and detector simulation. Finally the alternative detector simulation framework DELPHES is described including validation and improvement of the electron and muon reconstruction and identification.

In the fifth chapter the phenomenology and topology, as well as the reconstruction of hadronically decaying τ-leptons in ATLAS are described. The chapter is completed by the performance of the ATLAS detector for τ-lepton identification with first 7 TeV data. Chapter six presents the development of the cut-based identification of hadronic τ decays. Two methods are described: the calorimeter-based identification method uses only calorimeter information, while the calorimeter+track-based identification method combines calorimeter and tracking information. Finally the performance of the cut-based identification method is discussed.

In chapter seven the observation potential of CP-violating effects in SUSY with the ATLAS detector is presented. The chapter starts with a general introduction of the formalism and continues with a description of the momentum reconstruction of the stop cascade decay $\tilde{t} \rightarrow t + \tilde{\chi}_2^0 \rightarrow t + \tilde{\ell}^{\pm} + \ell_N^{\mp} \rightarrow t + \tilde{\chi}_1^0 + \ell_N^{\mp} + \ell_F^{\pm}$. Finally the results to observe the triple product asymmetry for an integrated luminosity of 500 fb^{-1} with the ATLAS detector are discussed.

2. The Standard Model and its Supersymmetric Extension

The Standard Model and gravity is one of the most successful theories in the history of natural science. The era of particle physics started in 1897 with the discovery of the electron by J. J. Thomson [4], and became crucial in 1964, when M. Gell-Mann postulated the quarks [5]. The Standard Model itself was established with the detection of the W- and Z-Boson with the UA1 and UA2 detectors at the Super Proton Synchrotron (SPS) at CERN in 1983 and the observation of the top quark, the heaviest of the six quarks in 1995 by the CDF and D0 experiments at Fermilab [6, 7]. Its latest discovery was the tau neutrino in 2000 [8]. Nevertheless many questions are unanswered:

- The mechanism how particles obtain their mass is not understood. One possible solution is the Higgs mechanism [9, 10].
- The different strength of the couplings, i.e. the large difference of the weak scale and Planck scale is summarized in the hierarchy problem.
- The observed CP-violation alone can not explain the asymmetry of matter and anti-matter in the universe [11, 12].
- Only 4 % of the universe consists of matter but 25 % are so-called dark matter. While its gravitation can be measured by astronomical experiments its origin is unknown [13].
- The mechanism behind neutrino masses.

This chapter describes the theory of the Standard Model in Section 2.1 and a detailed description of the QCD at hadron colliders is given in Section 2.2. The supersymmetric extension of the Standard Model, which provides approaches to answer many open questions such as new sources of CP violation is described in Section 2.3.

2.1. The Standard Model

2.1.1. General framework

The Standard Model describes all known particles and their interactions except of gravity. In its simplest version it has 19 free parameters from which 17 are known with varying errors. These parameters are the three coupling constants of the gauge group $\mathrm{SU}_C(3)\times\mathrm{SU}_L(2)\times\mathrm{U}_Y(1)$, three lepton and six quark masses, the mass of the Z boson which sets the scale of the weak interactions and the four parameters describing the rotation from the weak to the mass eigenstates of the quarks. One of the two remaining parameters is the CP-violating parameter for strong interaction which must be very small. The last parameter is associated with the mechanism which is responsible for the breaking of the $\mathrm{SU}_L(2) \times \mathrm{U}_Y(1)$. This could be the mass of a neutral scalar boson H^0.

The Standard Model is based on relativistic quantum field theory (QFT) [14] and follows the laws of the special relativity but not the general relativity such as gravitation. QFT's describes the behavior of particles with the Lagrangian formalism using the Lagrangian density $\mathcal{L}$. It formulates the theory of fundamental interactions, the Standard Model of the strong and the electroweak interactions. The special thing of QFT is "second quantization". While quantum mechanics describes successful a non-relativistic single particle system, a new framework is needed to create and destroy particles. In QFT all particles are described relativistically by quantum fields where the classical field variable becomes a quantum operator. This is similar to quantizing a theory that is already quantized, thus it leads to "second quantization".

Fermions

Fermions are particles with half-integral spin, which are statistically described by Fermi-Dirac statistics [15, 16]. The quintessence of this statistics is that no two particles can occupy the same state. That is connected to the Pauli exclusion principle [17] that indicates that no two particles can have the same quantum numbers. In contrast bosons are statistically described by the Bose-Einstein statistics and have integral spin. Unlike to fermions they are not subject to the Pauli exclusion principle, i.e. an unlimited number of particles can occupy the same state.

The Standard Model introduces 12 fundamental particles with spin 1/2, 6 leptons and 6 quarks. Leptons can be subdivided in charged particles and uncharged particles. Quarks again can be subdivided into up-type quarks with $\frac{2}{3}$ charge and down-type quarks with $\frac{1}{3}$ charge. While leptons participate only to electroweak interactions, quarks participate also to the strong interaction.

Fermions are separated into three generations. Each generation consist of a charged lepton and a neutrino associated to the lepton, and a up- and down-type quark. From the first generation to the third generation the masses increases from a few eV for the electron-neutrino up to a few hundred GeV for the top quark. The mechanism of mass is unknown and the masses cannot be determined from the Standard Model but have to be measured from experiments. Tab. 2.1 summarizes charge and mass of all three fermion generations.

In the Standard Model fermions are described by spinors and are represented by Majorana fields. These fields contain left-handed and right-handed parts, except for neutrinos which are assumed to exist as left-handed particles only.

Table 2.1.: Mass and charge of fermions in the Standard Model. All Quark masses are given in the $\overline{\text{MS}}$ [18] schema except for the top mass which can be measured directly.

	Quarks			**Leptons**		
Generation		mass [MeV]	charge [e]		mass [MeV]	charge
First	up (u)	1.5 – 3.3	$\frac{2}{3}$	electron	0.511	-1
	down (d)	3.5 – 6.0	$-\frac{1}{3}$	ν_e	$< 2{\cdot}10^{-6}$	0
Second	charm (c)	1.27	$\frac{2}{3}$	muon	105.658	-1
	strange (s)	104	$-\frac{1}{3}$	ν_μ	< 0.19	0
Third	top (t)	171200	$\frac{2}{3}$	tauon	1776.84	-1
	bottom (b)	4200	$-\frac{1}{3}$	ν_τ	< 18.2	0

Interactions

The strong, weak, and electromagnetic interactions can be expressed by the symmetry group of the Standard Model which is $SU_C(3) \times SU_L(2) \times U_Y(1)$. Gauge bosons are associated to each generator of the algebra of the group:

- **Strong interaction SU_c(3):** The eight spin-one particles associated with the factor $SU_C(3)$ are called gluons and they are thought to be massless. The subscript "C" is meant to indicate "color". Any particle transforming under the strong interaction and which couples to gluons carries color.
- **Electroweak interaction SU_L(2) and U_Y(1):** Three spin-one gauge-bosons are associated to the group $SU_L(2)$ and one is associated to the group $U_Y(1)$. The subscript "L" stands for left-handed and denotes that only left-handed fermions transforms under the weak interaction. The subscript "Y" stands for the quantum number associated to the group, the *weak hypercharge* Y. The four spin-one bosons associated to $SU_L(2) \times U_Y(1)$ are related to physical bosons. The weak interaction is mediated by three massive bosons, two charged $W^{\pm}$and one neutral Z^0, the electromagnetic interaction is mediated by the photon.

Table 2.2.: $SU_L(2)$ doublets and $U_Y(1)$ singlets with electroweak quantum numbers and electromagnetic charge.

			T_3	Y	Q
$\begin{pmatrix}\nu_e\\ e\end{pmatrix}_L$	$\begin{pmatrix}\nu_\mu\\ \mu\end{pmatrix}_L$	$\begin{pmatrix}\nu_\tau\\ \tau\end{pmatrix}_L$	$\begin{pmatrix}1/2\\ -1/2\end{pmatrix}$	$\begin{pmatrix}-1\\ -1\end{pmatrix}$	$\begin{pmatrix}0\\ -1\end{pmatrix}$
$\begin{pmatrix}u\\ d\end{pmatrix}_L$	$\begin{pmatrix}c\\ s\end{pmatrix}_L$	$\begin{pmatrix}t\\ b\end{pmatrix}_L$	$\begin{pmatrix}+1/2\\ -1/2\end{pmatrix}$	$\begin{pmatrix}1/3\\ 1/3\end{pmatrix}$	$\begin{pmatrix}+2/3\\ -1/3\end{pmatrix}$
e_R	μ_R	τ_R	0	-2	-1
u_R	c_R	t_R	0	+4/3	+2/3
d'_R	s'_R	b'_R	0	-2/3	-1/3

The fermion multiplets and their quantum numbers are summarized in Tab. 2.2. The left-handed states of leptons and quarks are doublets under $SU_L(2)$, while the right-handed states are singlets. The electric charge is given by

$$Q = T_3 + \frac{Y}{2}, \tag{2.1}$$

with the weak isospin T_3 and the weak hypercharge Y.

The W^+ and W^- can be expressed as a real and imaginary part of a complex, charged field:

$$W^{\pm}_{\mu} = \frac{1}{\sqrt{2}} \left(W^1_{\mu} \mp i W^2_{\mu}\right) \tag{2.2}$$

The remaining vector fields are W^3_{μ} and B_{μ} and the mass eigenstates of the photon and Z^0 are a combination of W^3_{μ} and B_{μ}:

$$\begin{pmatrix}Z^0_{\mu}\\ A_{\mu}\end{pmatrix} = \begin{pmatrix}\cos\theta_W & -\sin\theta_W\\ \sin\theta_W & \cos\theta_W\end{pmatrix} \begin{pmatrix}W^3_{\mu}\\ B_{\mu}\end{pmatrix} \tag{2.3}$$

with A_μ representing the massless photon and the weak-mixing angle or Weinberg angle θ_W. The electric charge is connected to the mixing angle via the coupling constant of the weak interaction g_1 and g_2:

$$Q = g_1 \cos\theta_W = g_2 \sin\theta_W \tag{2.4}$$

The value of the mixing angle is $\theta_W \approx 0.231$.

All other fields couple to the Higgs field and get mass terms. The mass and mixing of the quarks arise from the Yukawa interactions with the Higgs condensate

$$\mathcal{L}_Y = -Y^d_{ij}\overline{Q^I_{Li}}\phi d^I_{Rj} - Y^u_{ij}\overline{Q^I_{Li}}\epsilon\phi^* u^I_{Rj} + h.c. \tag{2.5}$$

where $Y^{u,d}$ are 3×3 complex matrices, ϕ is the Higgs field, i, j are generation labels, and ϵ is the 2×2 antisymmetric tensor. Q^I_L are left-handed quark doublets, and d^I_R and u^I_R are right-handed down- and up-type quark singlets. Equation (2.5) yields mass terms for the quarks when the Higgs field acquires a vacuum expectation value (VEV).

The Standard Model is described in more detail in [19–24].

2.1.2. The Higgs mechanism

Breaking of the electroweak symmetry $\mathrm{SU}_L(2) \times \mathrm{U}_Y(1) \rightarrow \mathrm{U}_{em}(1)$ and the origin of mass of all known particles is one of the most fundamental problems of the Standard Model. The Higgs mechanism provides a framework to mediate mass to the gauge bosons [9,10] via charged and neutral Goldstone bosons which end up as the longitudinal components of the gauge bosons and give mass to the $W^\pm$ and Z^0 bosons.

The Higgs mechanism introduces a weakly-coupled spin-zero particle to the Standard Model with a potential that is minimized at a non-zero field value. The mechanism postulates a self-interacting complex doublet of scalar fields, called the Higgs field:

$$\phi = \begin{pmatrix} \phi^+ \\ \phi^0 \end{pmatrix} \tag{2.6}$$

The Lagrangian of this field is

$$\mathcal{L}_H = (D_\mu \phi)^\dagger (D^\mu \phi) - V(\phi) \tag{2.7}$$

with the Higgs potential

$$V(\phi) = -\mu^2 \phi^\dagger \phi + \frac{\lambda}{4}\left(\phi^\dagger \phi\right)^2 \tag{2.8}$$

where μ^2 and λ are constants of the potential. In the ground state, the vacuum, the potential has a minimum. The minimum does not occur for $\phi = 0$ and $\mu^2,\ \lambda > 0$. The neutral component of the scalar doublet acquires a symmetry-breaking vacuum expectation value of

$$< \phi >= \frac{1}{\sqrt{2}}\begin{pmatrix} n \\ v \end{pmatrix} \text{ with } v = \frac{2\mu}{\sqrt{\lambda}}. \tag{2.9}$$

The Lagrangian is symmetric under the gauge transformation of the $\mathrm{SU}_L(2) \times \mathrm{U}_Y(1)$ group but the vacuum configuration $< \phi >$ is not symmetric: the symmetry is spontaneously broken. If the potential (2.8) is expanded around the vacuum, the Higgs doublet field can be written as

$$\phi = \frac{1}{\sqrt{2}}\begin{pmatrix} 0 \\ v + H(x) \end{pmatrix} \tag{2.10}$$

and the potential can be written as

$$V = \mu^2 H^2 + \frac{\mu^2}{v} H^3 + \frac{\mu^2}{4v^2} h^4 = \frac{M_H^2}{2} H^2 + \frac{M_H^2}{2v} H^3 + \frac{M_H^2}{8v^2} H^4. \tag{2.11}$$

Three Goldstone bosons are generated and the remaining component of the complex doublet becomes the Higgs boson, a scalar particle that has not been discovered yet. The Higgs field couples to fermions via the Yukawa interactions and gives mass to them. In general all particles couple to the Higgs boson H with the strength m/v where m is the mass of any particle. Since $m \ll v$ for all known particles H must couple weakly to all of them. In the SM the mass of the Higgs boson is given by

$$m_H = \sqrt{\lambda/2}v \tag{2.12}$$

with λ as the Higgs self-coupling parameter. The four LEP experiments ALEPH, DELPHI, L3, and OPAL established a lower band for the Higgs boson mass of 114.4 GeV at 95 % C.L. [25], while the Tevatron excluded a region for the Higgs mass of $m_H = 158 - 175$ GeV at 95 % C.L. [26]. Electroweak fits performed by the Gfitter project [27] predict a mass of the Higgs boson with the *standard fit* of $m_H = 95.7^{+30.6}_{-24.2}$ GeV with the $2\,\sigma$ interval of [44, 76] GeV. The *complete fit* including all direct searches predicts a mass of $m_H = 120.6^{+17.9}_{-5.2}$ GeV with the $2\,\sigma$ interval of [6.2, 34.7] GeV. The $\Delta\chi^2$ profile versus the Higgs mass of the *standard fit* is shown in Fig. 2.1a and for the *complete fit* in Fig. 2.1b.

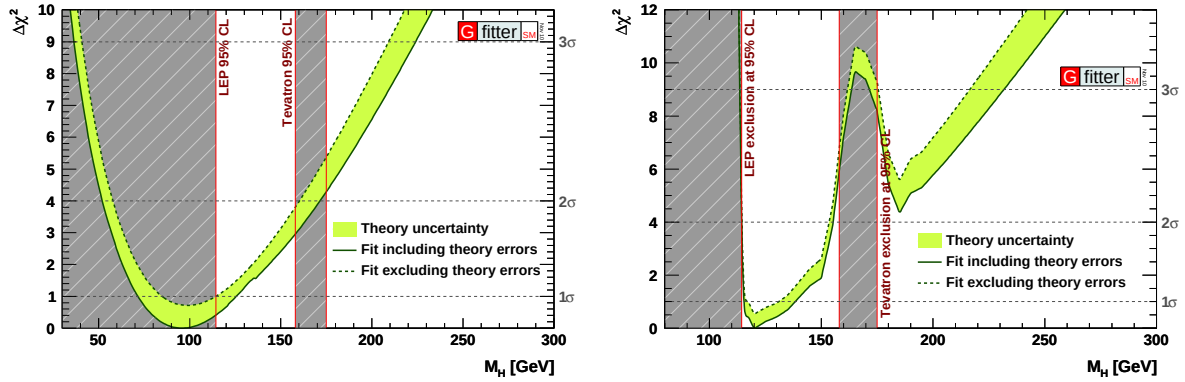

(a) (b)

Figure 2.1.: $\Delta\chi^2$ as a function of M_H for the standard fit (a) and complete fit (b). The solid (dashed) lines give the result when including (ignoring) theoretical errors. The minimum χ^2 of the fit including theoretical errors is used for both curves to obtain the offset-corrected χ^2 [27].

2.1.3. Renormalisability

An important issue of QFT for the description of physical phenomena is that all observables should remain finite at all energies and at all orders of coupling constant. That means physical observables like charge and mass are expressed as perturbative series in powers of the coupling constant α_S in the case of QCD. The calculation can be performed by Taylor expanding the Lagrangian. Every term can be represented by Feynman diagrams which can contain internal loops. The calculation to finite order diverges, because integrals over all possible momenta of the virtual particles of the internal loops are

not finite, unless the momentum integral is cut off at an arbitrary energy scale μ. As an example the contribution of higher order can be parametrized depending on the energy scale Q^2 as

$$R_n = \sum_n a_n \left(\ln \frac{Q^2}{\mu^2} \right)^n , \tag{2.13}$$

which grows to infinity if calculated in finite order and $Q^2 \to \infty$.

In the Standard Model all interactions with divergences in finite order calculation can be corrected by a counter term. This is called renormalization and includes the cutoff of loop diagrams at μ, the replacement of the true coupling constant by an effective coupling, and the multiplication of the external fermion and boson wave function with a new normalization factor. Hence renormalization leads to a different perturbative description of observables.

2.1.4. Problems of the Standard Model

Although the Standard Model is the probably most successful theory in natural science and describes the fundamental particles and their interactions with very good agreement to the theoretical predictions, it contains some unsolved problems. That motivates the extension of the model and the construction of more powerful collider like the LHC or a future international linear collider (ILC). This section gives a short overview on the problems that arise either from cosmological measurements, intrinsic problems, or theoretical nature.

- In the Standard Model the electromagnetic and weak interactions are unified to the electroweak interaction. If the unification with the strong interaction appears at the Planck scale ($E_{\text{GUT}} \sim 10^{16}$ GeV, GUT: Grand Unified Theory [28]) new particles with a mass of the order of E_{GUT} should appear. These particles should already appear at low energies as loop corrections to the Higgs boson. The problem, that the mass of the Higgs boson is 30 order of magnitudes smaller than the Planck scale is known as the **hierarchy problem** [29–32]. In supersymmetric theories [33–35], the running couplings converge in one point at the GUT scale.

- Cosmological observations show, that only 4 % of the content of the universe is made of matter that is described by the Standard Model. About 76 % is made of dark energy which is responsible for the acceleration of the universe. The remaing 20 % is made of **dark matter** [36] which is responsible for the gravitational effects seen in astrophysical observations. Due to its small mass the neutrino from the SM is excluded as the exclusive source for dark matter. If the lightest particle in supersymmetric extensions (LSP) is stable it serves as a good candidate for dark matter.

- In the Standard Model the only source for CP violation is the complex phase of the Cabibbo-Kobayashi-Maskawa matrix (CKM) [11, 12]. But this source is not sufficient to explain the cosmologically observation of the **matter – anti-matter asymmetry** in the universe [37–39]. A possible solution are complex phases in supersymmetric extensions. This mechanism is explained in Section 2.3.4 and Chapter 7.

- The **gravitational force** is weak enough to be neglected in particle physics at the electroweak scale. But at energies at the Planck scale gravity becomes as strong as the Standard Model forces. Hence the SM is not the final description of nature. Again supersymmetry is a good candidate for an elegant solution. If supersymmetry is treated as a local gauge symmetry, it becomes a theory of gravity, since a supersymmetric transformation includes a space-time transformation. This is exploited in supergravity theories.

2.2. Quantum Chromodynamics

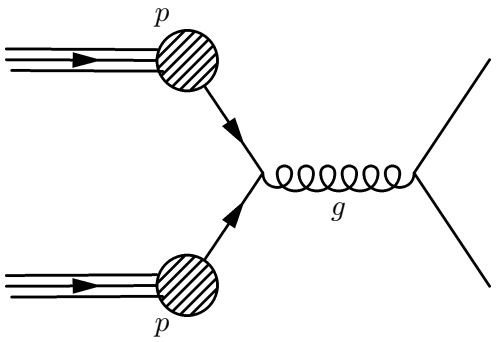

Figure 2.2.: Parton interaction in a proton-proton collision at the LHC

The Quantum Chromodynamics (QCD) is the gauge theory of quarks and gluons [40] and describes the strong interaction. Since the LHC is a hadron-hadron collider a good understanding of QCD at high momentum scales is essential.

The fermions of the symmetry group $SU_C(3)$ are quarks with three different flavors, called color (red, green, and blue). They are described by a triplet of spinor which Caria's a color index:

$$\psi_a = \begin{pmatrix} \psi_1 \\ \psi_2 \\ \psi_3 \end{pmatrix}, \tag{2.14}$$

and the quark part of the QCD Lagrangian can be written as

$$\mathcal{L}_q = \bar{\psi}_a \left(i\gamma^\mu \partial_\mu \delta_{ab} - g_s \gamma^\mu t^C_{ab} \mathcal{A}^C_\mu - m \right) \psi_b, \tag{2.15}$$

with γ^μ as Dirac matrices, $\mathcal{A}^C_\mu$ as gluon fields, a Lorentz index μ, and a color index C running from 1...8. This color group has eight generators:

$$t^C = \frac{1}{2}\lambda^C, \qquad C = 1...8, \tag{2.16}$$

which are expressed in terms of eight 3×3 Gell-Mann matrices λ^A. The second part of the Lagrangian comes from the gluons:

$$\mathcal{L}_G = -\frac{1}{4} F^A_{\mu\nu} F^{A\mu\nu}, \tag{2.17}$$

with the field tensor of the gluons $F^A_{\mu\nu}$. The strength of the field can be written as

$$F^A_{\mu\nu} = \partial_\mu \mathcal{A}^A_\nu - \partial_\nu \mathcal{A}^A_\nu - g_s f_{ABC} \mathcal{A}^B_\mu \mathcal{A}^C_\nu, \tag{2.18}$$

where f_{ABC} are the structure constants of $SU_C(3)$. The strong coupling constant g_s can be expressed in terms of the finestructure constant of the strong interaction:

$$\alpha_s = \frac{g_s^2}{4\pi}. \tag{2.19}$$

The coupling constant of the Quantum Electrodynamics (QED) it is a running constant. At the LHC it values ranges from $\alpha_s = 0.08$ at a scale of 5 TeV to $\alpha_s \sim 1$ at a scale of 0.5 GeV.

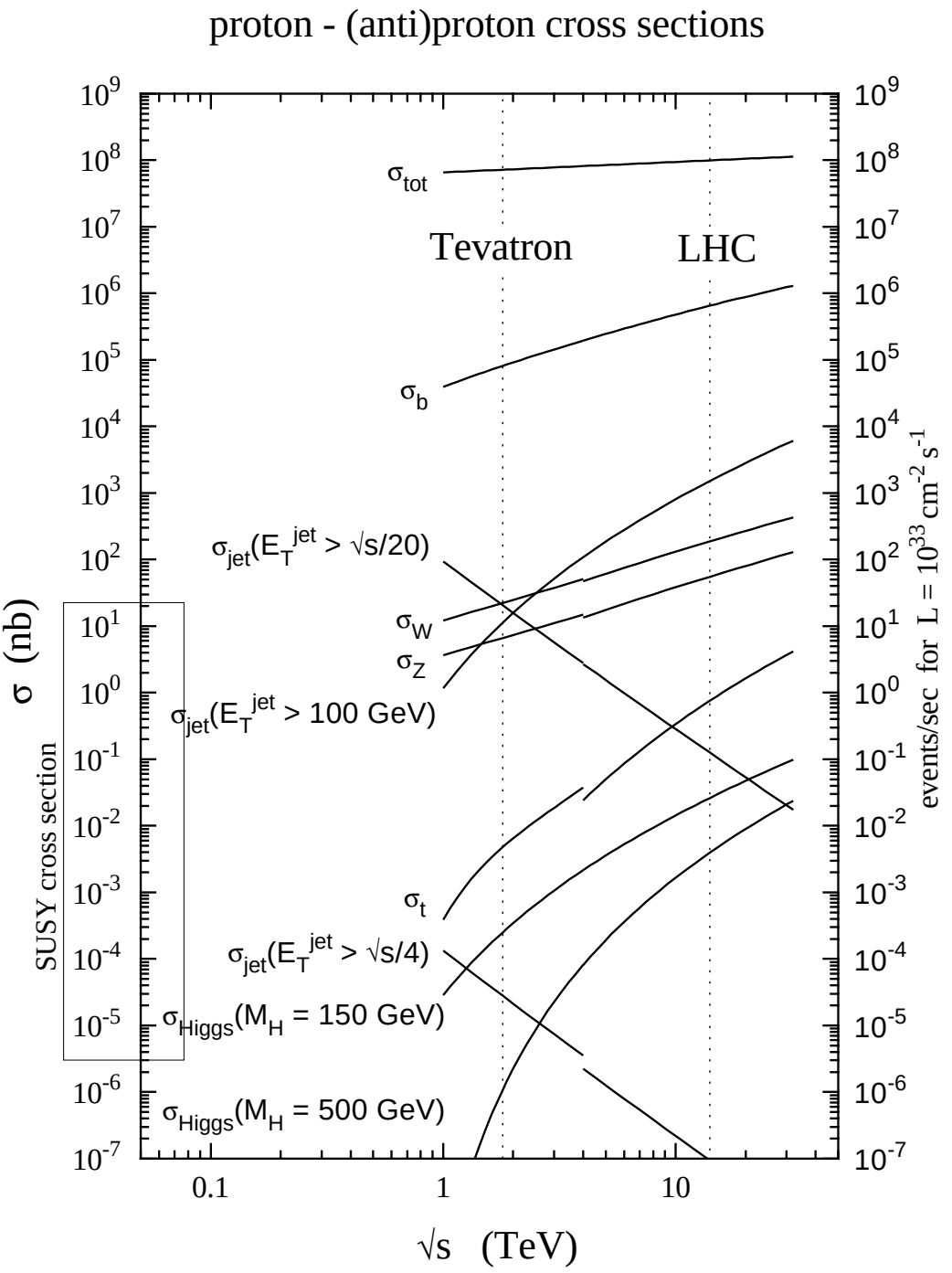

Figure 2.3.: Cross sections for hard scattering against the center-of-mass energy $\sqrt{s}$. The line for the LHC represents the cross section at a center-of-mass energy at $\sqrt{s} = 14$ TeV [41].

For proton-proton collisions the understanding of initial-state hadrons is essential. The Feynman diagram of a parton interaction in a proton-proton collision at the LHC is shown in Fig. 2.2, while the cross sections for selected processes at the Tevatron with a center-of-mass energy of $\sqrt{s} = 1.96\,\text{TeV}$ and the LHC at $\sqrt{s} = 14\,\text{TeV}$ is shown in Fig. 2.3.

In the simplest description protons consist of two up-quarks and one down-quarks, the so-called valence quarks. A more detailed description adds further quarks, so-called sea quarks, and gluons to the content of the proton. Valence quarks and sea quarks are the partons of the proton. The momentum of the proton is carried by all partons. The momentum distribution of quarks and gluons within the proton is described by the *parton distribution functions* (PDFs). A good knowledge of the PDFs is crucial for physics analyses at the LHC.

The momentum distribution can be determined experimentally with Deep Inelastic Scattering (DIS) and fitting the data from different experiments. This has been done at the electron-proton collider HERA. The kinematic of DIS processes is described with two main variables, the parton momentum x as fraction of the total proton momentum and the momentum transfer Q^2 from the electron to the interacting parton. An example for a PDF shows Fig. 2.4. It combines the results from H1 and ZEUS for the valence quarks (xu_v and xd_v), the gluons (xg) and the sea quarks (xS) at a momentum transfer of $Q^2 = 10\,\text{GeV}^2$. The kinematic region for x and Q^2 at HERA, fixed target experiments and the LHC is shown in Fig. 2.5.

In case of hadron-hadron collisions at high energy each hadron must be described in terms of PDFs. There are several techniques to make QCD predictions at the LHC.

Fixed-order predictions involve the first couple of terms in the QCD perturbative expansion for a given cross section. One example is the process $pp \to Z$. At Leading Order (LO) the $pp \to Z$ cross section involves a single underlying hard partonic process, namely $q\bar{q} \to Z$ which is purely electroweak. At Next Leading Order (NLO), contributions from gluon-quark scattering appears. LO cross section requires the calculation of $\mathcal{O}(\alpha_s)$ while the NLO cross sections additionally requires all $\mathcal{O}\left(\alpha_s^2\right)$ contributions.

Monte Carlo parton-shower programs rely on the soft and collinear approximation. They describe common events, including the hadron-level detail that is essential for the correct simulation of detector effects on event reconstruction and they have equal event weights like real data. A more detailed description on Monte Carlo (MC) programs is given in Chapter 4.

2.2.1. Fragmentation and Hadronization

To understand the detector response the process of final state partons has to be understood. The emission of secondary gluons or quarks is called final-state radiations or fragmentation and can be described perturbatively. The rate of the fragmentation is of the order $\alpha\log^2(q^2/\Lambda^2_{QCD})$ with Λ_{QCD} as the QCD scale. Hard, large angle radiations are rare, while soft and collinear radiations are common. Typically there are several final-state radiations which can also radiate. Hence the partons become several partons, most of them moving in almost the same direction as the original parton, building a collection of hadrons. This process is called hadronization. The transition from partons to hadrons involves strong interaction at energy scale at or below Λ_{QCD}. Finally primary hadrons decay into stable particles.

In all phases the QCD plays an important role. The fragmentation process of the primary quark – anti-quark pair into a set of high energy partons and the hadronization of these partons is described in this section. It is not obvious that fragmentation and hadronization can be treated separately and it requires that the mathematical description of both parts of the event evolution can be factorized. Although it is not proved, the separate descriptions of fragmentation and hadronization reproduces experimental results very well.

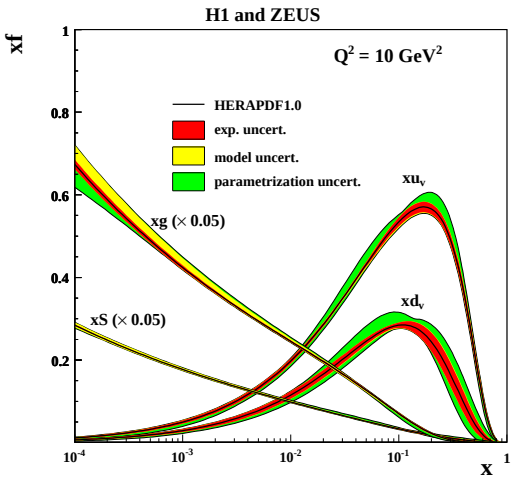

Figure 2.4.: Parton distribution functions from HERAPDF1.0, xuv, xdv, xS, xg, at $Q^2 = 10\,\text{GeV}^2$ [42].

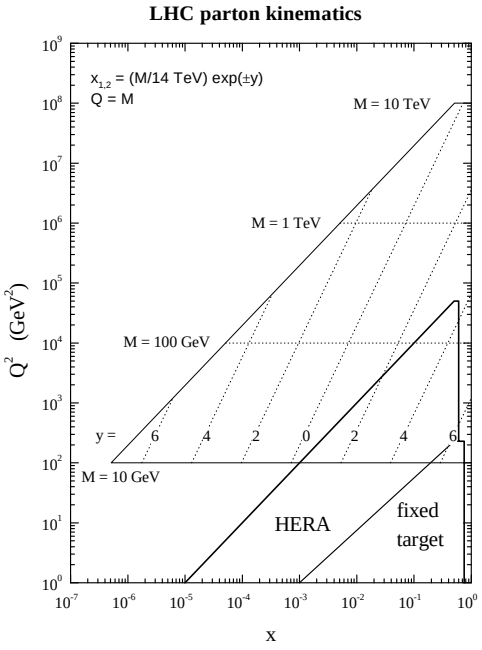

Figure 2.5.: Kinematic region of Q^2 and x probed in the production of an object of mass M and rapidity y at the LHC for $\sqrt{s} = 14\,\text{TeV}$ [43].

Fragmentation

Over the past 30 years QCD has been extensively studied in e^+e^- annihilation to hadrons. The advantage of this process is that only the final state involves QCD and huge quantities of data have been collected.

As already mention the emission of gluons of high energy can be calculated perturbatively. The lowest order (LO) cross section for $e^+e^- \to q\bar{q}g$ for quarks with negligible mass ($m_q \ll Q = \sqrt{s}$) is [44]

$$\frac{d\sigma}{dx_1 dx_2} = \sigma_0 \frac{2\alpha_s}{3\pi} \frac{x_1^2 + x_2^2}{(1-x_1)(1-x_2)}, \tag{2.20}$$

where x_1 and x_2 are the scaled momenta $x_i = p_i / \frac{1}{2}Q$, and σ_0 is the $e^+e^- \to q\bar{q}$ cross section. For $x_i \to 1$ ($i = 1,2$) or gluons of vanishing energy this formula diverges.

Once a gluon has been emitted it can emit further gluons, and so forth. Most of the emissions will either be in almost the same direction as the original quark (due to collinear divergence) and/or soft. But this pictures gives only a description of events in terms of gluons and quarks, although real events consist of hadrons.

Physically a three parton final state with $x_i \approx 1$ for at least one of the quarks, is meaningless since this corresponds to a gluon being collinear with one of the quarks. A two-parton final state describes the final state better where the gluon is associated with the hadronization process of its nearby quark.

In Monte Carlo generators QCD matrix elements are used to describe the fragmentation of quarks (see also Chapter 4). The three-parton matrix element has been calculated up to two-loops [45], and first order matrix elements are available for final states with 5 partons [46].

A more successful description of hadronic events offers the parton shower approach. It is based on a rearrangement of the usual perturbation expansion (see Eq. (2.13)) to

$$\sum_n a_n \left(\alpha_s \ln \frac{Q^2}{\Lambda^2_{\mathrm{QCD}}} \right)^n + \alpha_s \sum_n b_n \left(\alpha_s \ln \frac{Q^2}{\Lambda^2_{\mathrm{QCD}}} \right)^n + ... \tag{2.21}$$

In MC generators, parton shower models bases on the probability that a given parton branches during a given decrease of the energy scale Q^2. By summing the splitting function for all possible final states and interaction over the Q^2 range this probability can be calculated. The iterative evolution of the shower model is stopped as soon as all partons have been tracked down to an energy Q_0 of the order of 1 GeV, that is still sufficiently larger than Λ_{QCD}. The Monte Carlo generators proceed with non-perturbative hadronization of the shower partons.

Parton shower models are very successful in describing secondary partons which are soft and almost collinear to the primary partons, but their results for high energy partons with large transverse momentum (that leads to three or more jets) is not satisfying. Therefore the rates and properties of events with more than 2 high energy partons are matched to matrix element calculations for these configurations.

Hadronization

As describe in the section before perturbation theory breaks down when the strong coupling constant $\alpha_s(Q^2)$ exceeds unity at an energy scale around Λ_{QCD}. At this energy scale the transition of partons into hadrons takes place. This transition is called hadronization. Different classes of phenomenological models exist. They differ in the way how gluons created during fragmentation are treated, how different partons interact during the hadronization, and in the number, type, and momentum distribution of the created hadrons. Primary partons are confined to hadrons by creating $q\bar{q}$ pairs and forming mesons by combining with the additional (anti-)quark. The production of baryons is a complicated process and a common problem for all three models. Currently two scenarios exist. The first scenario creates diquark – anti-diquark pairs with the same method as quark – anti-quark pairs are created for the hadronization procedure [47]. This can be combined with additional quarks to form hadrons. The second scenario performs a step-by-step baryon production and is called popcorn model [48]. In this scenario $q\bar{q}$ pairs with color not matching to their neighboring quarks. In this color field additional $q\bar{q}$ pairs can emerge before mesons are formed.

The three hadronization models are:

- **Independent hadronization** A simple approach to describe the creation of jets of hadrons from a primary or secondary parton, created during the fragmentation [49]. This model has mostly been removed from Monte Carlo generators, because it has several intrinsic problems. Since it is hard to find an applicable termination of the iteration, the energy left after creation of a hadron might be insufficient to form another hadron. Hence the remaining isolated hadron is discarded. I.e. that energy, longitudinal momentum, charge, color, and flavor are not conserved. Furthermore jet correlations, as observed in data, are by construction not included in this scheme and the suppression of the creation of heavy $q\bar{q}$ pairs (charm, bottom) has to be put in manually.

- **Cluster hadronization** The problems of the independent hadronization model, like non-conservation of energy, momentum, etc. can be avoided if the partons are combined to massive,

colorless clusters which hadronize. This can be motivated by the preconfinement property of perturbative parton showers [50, 51]. Partons created in a perturbative shower tend to form color-neutral sets of partons with similar momentum and small spatial separation. These sets have finite invariant masses of the order of the energy scale where the shower evaluation was terminated.

Clusters are constructed from a quark, an anti-quark, and an arbitrary number of gluons. Usually gluons are split into $q\bar{q}$ pairs before the cluster is built and the cluster consists of quarks only. The clusters decay to two hadrons, each, where one flavor of each hadron is determined from the intrinsic cluster (anti-)flavor, and the respective other flavor is created by addition of a $q\bar{q}$ pair. Baryons are produced by the creation of diquark pairs instead of a quark pair.

The suppression of heavier flavors and diquarks is achieved automatically by the restricted phase space for such cluster decays. That means very massive clusters (mass $> \mathcal{O}(1\,\mathrm{GeV}/c^2)$ for light quarks) can decay only to one hadron and one sub-cluster.

- **String hadronization** The first string model was proposed by Artru and Mennessier in 1974 [52]. It describes hadronization via color flux tubes or strings, that are spanned between two quarks. It seems more natural to handle gluons with strings than with the cluster or independent scheme. Perturbative gluons are integrated in the strings that connect two nearby quarks and appear as a kink in the string.

  The force between two color sources with large distance is independent of the distance due to the self-interaction of gluons. If the transverse extension of the string is constant over its full length and much smaller than the longitudinal extension, the energy density, or string tension κ is constant along the string. One can estimate a diameter of $\mathcal{O}(1\,\mathrm{fm})$ and a tension of $\kappa \approx 1\,\mathrm{GeV/fm}$. As the quarks fly apart, the string is stretched. With increasing the distance d between the quark and anti-quark (or the length of the string) the energy stored in the string increases with $E(d) \propto \kappa d$. If a virtual $q\bar{q}$ pair fluctuates out of the vacuum somewhere at the string with the same color as the endpoint quarks, the color field is compensated and the string breaks into two pieces. This procedure recurs until the remaining energy of the string segments is below a threshold that is needed to transform another virtual $q\bar{q}$ pair into a real one. The probability to create a $q\bar{q}$ pair on the string per unit length and per unit time is a constant since the string is assumed to be uniform along its length.

  The most well-known string hadronization model was invented by the Lund group [53] and is used by the JETSET [54] and PYTHIA [55, 56] Monte Carlo event generators. This model does not use a necessarily constant $q\bar{q}$ pair creation probability but breaks strings exactly where necessary to ensure the production of on-shell hadrons. String breaks are causally disconnected, hence they can be treated in any possible order. The hadronization starts at the outer ends of the string, and is continued towards the inside until the invariant mass of the remaining strings drops below a threshold. Finally the remaining string is split into two hadrons.

  Since the creation of $q\bar{q}$ pairs takes the quark mass into account, $q\bar{q}$ pairs are created locally, i.e. at one space point. To transfer a virtual $q\bar{q}$ pair into mass-shell particles, energy has to be taken from the string. It is assumed that both quarks of the $q\bar{q}$ pair have a transverse momentum of the same size, but opposite directions. With a mass m_q, and a transverse momentum p_T with respect to the string, the minimum required energy is $E_\mathrm{min} = 2\sqrt{m_q^2 + p_\mathrm{T}^2} = 2m_\mathrm{T}$. Since baryon production requires two quarks and two anti-quarks it is less likely than meson production.

  After the quark flavor for a hadron have been chosen, the Lund model selects the remaining quantum numbers in the next step (e.g. spin, orbital angular momentum) for the hadron. Finally the

longitudinal momentum is determined with a fragmentation function.

Jets

Jets are essential for collider physics, since theory and experimental results are often presented in terms of jet cross sections. They are input to almost all physics analyzes, like new physics (since new particles may decay to quarks and/or gluons, forming jets), the Higgs searches, top physics, Monte Carlo validation, or PDF fits.

The definition of jets involves different considerations:

- Which particles are grouped into a jet? Different jet algorithms follow a set of rules. They are controlled via different parameters, like R which determines the angular reach of the jet algorithm.
- The manner how the momenta of particles inside the jet are combined? This is known as the "recombination scheme". The most common way is to add the 4-vectors of the particles, that gives massive jets.

For the definition of a jet there are two main classes in common use: cone algorithms, which take a top-down approach, and sequential recombination algorithm, based on a bottom-up approach.

Many types of cone algorithm are available, but the all rely on the idea that soft and collinear branching does not modify the basic direction of energy flow. Since ATLAS uses a recombination algorithm, the default anti-k_t algorithm is described. Detailed description of the different jet algorithm is given in [57].

Sequential-recombination jet algorithms use a bottom-up approach to construct a jet, since they invert the sequence of splittings of the parton shower. The anti-k_t algorithm defines a distance for every pair of particles

$$d_{ij} = \frac{1}{\max(p_{ti}^2, p_{tj}^2)} \frac{\Delta R_{ij}^2}{R^2}, \tag{2.22}$$

where R is the radius of a cone around the seed. The beam distance for every particle is defined as

$$d_{i,B} = \frac{1}{p_{ti}^2}. \tag{2.23}$$

The algorithm proceeds by searching for the smallest of d_{ij} and d_{ib}. If d_{ij} is the smallest, the two particles i and j are recombined into a single new particle. If d_{ib} is the smallest, the particle i is removed from the list of particles and called a jet. This process is repeated until no particles are left.

Objects that are close in angle prefer to cluster early, but that clustering tends to occur with a hard particle. I.e. jets are "growing" in concentric circles out from a hard core until they reach a radius R.

The anti-k_t algorithm is collinear (and infrared) safe, that means that it is safe to use with fixed-order QCD predictions and it has been implemented in the FASTJET jet-finding code [58].

The anti-k_t algorithm does not provide information on the substructure of the jet. If a jet contains two hard cores, the algorithm first reconstruct those hard cores and merge the resulting two subjects.

2.3. Supersymmetry

In Section 2.1.4 it was already mentioned that the Standard Model has many open questions. Among other thinks it has to be extended to describe physics at higher energies and to form a framework to the Planck mass $m_P = (G_N)^{-1/2} \simeq 1.2 \times 10^{19}$ GeV, where quantum gravity effects become important. It is obvious that new physics exist in the 17 orders of magnitude in energy between the present physics

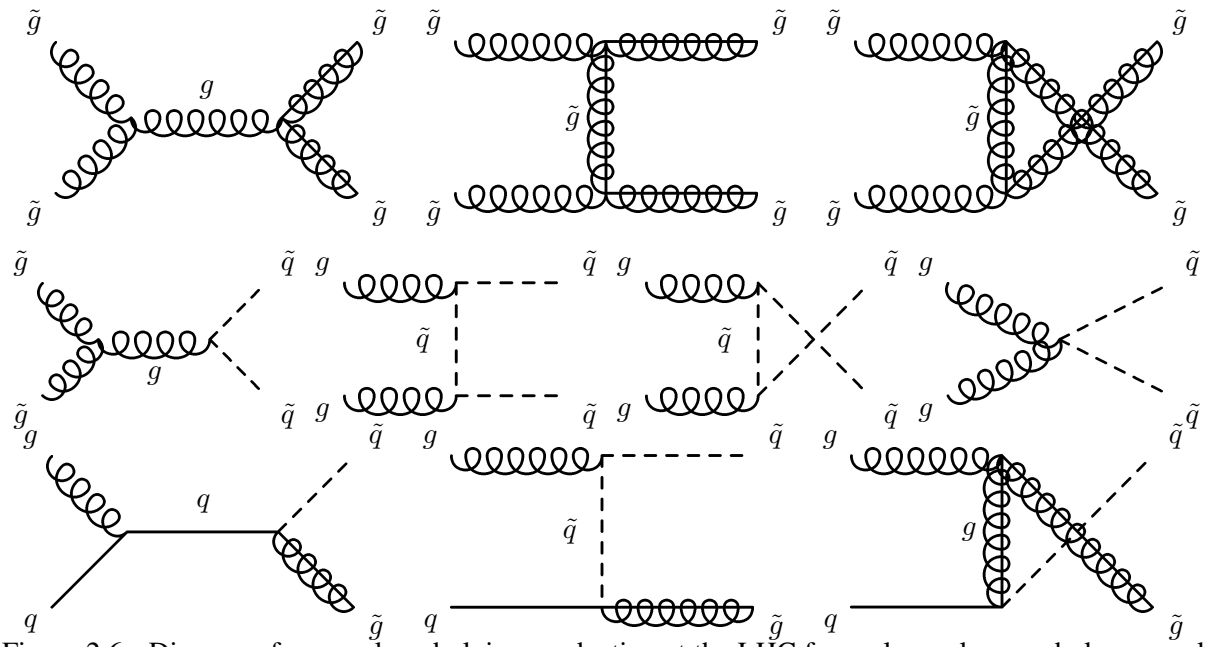

Figure 2.6.: Diagrams for squark and gluino production at the LHC from gluon-gluon and gluon-quark fusion.

near electroweak scale, m_W, and the Planck scale. The huge ratio of m_P/m_W is know a the "hierarchy problem" [29–32].

Supersymmetry also provides smart solutions for cosmological questions. The cancellation of fermionic and bosonic divergences resolves the problem of the light Higgs mass. New particles are implied by the extension and if R-parity is conserved the lightest supersymmetric particle (LSP) is stable and serves as a good candidate for dark matter. Finally SUSY predicts very precisley $\sin^2\theta_W$ [59].

According to the theorem of Coleman and Mandula [60], the continuous symmetries of QFT are restricted. They consist of space-time symmetry (Poincare group) internal symmetry, and supersymmetry. The basic idea of supersymmetry (SUSY) is to impose a new extension of the Poincare space-time symmetry to relate excitations of different spins. Therefore it predicts that every particle has a superpartner. For instance if the electron has a partner with the same mass but spin 0 the symmetry would be perfect. Since no superpartners have been observed yet, SUSY must be spontaneously broken.

Supersymmetry includes several models which can be classified according to the mechanism by which supersymmetry breaking is mediated, i.e. coupled to the SM sector. The hidden sector models can be divided into three groups:

- **Gravity mediation:** The mediation is through Planck scale suppressed couplings to scalar fields that get VEVs due to SUSY breaking in the hidden sector. Examples for such models are "dilation-dominated" and G_2 models, "anomaly mediation", minimal supergravity (mSUGRA), gravitino LSP models and "no-scale" models.

- **Gauge mediation:** In this model SUSY is broken by some new dynamics in a hidden sector, and communicated to some heavy "messenger" fields that also carry charges under the SM gauge group. This gauge mediated supersymmetry breaking is also called GMSB.

- **Bulk mediation:** This model combines SUSY with some extra-dimensional framework. The

messengers of SUSY breaking to the SM sector are via fields that propagate in the full "bulk" space that includes the extra dimensions. Examples include gaugino mediation and radion mediation.

2.3.1. Introduction

Assuming one loop contributions to the Higgs boson mass, the Lagrangian is given by

$$\mathcal{L} \sim -\mathrm{g_F}\bar{\psi}\psi h - \mathrm{g_S^2}h^2\phi^2 \tag{2.24}$$

with the Higgs field h, massive scalars ϕ, fermions ψ, and the fermion (scalar) loop corrections $\mathrm{g_F}$ ($\mathrm{g_S}$). For the one-loop contribution to m_{H}^2 one can write:

$$m_{\mathrm{H}}^2 \sim m_{\mathrm{H0}}^2 + \frac{\mathrm{g_F^2}}{4\pi^2}\left(\Lambda^2 + m_{\mathrm{F}}^2\right) - \frac{\mathrm{g_S^2}}{4\pi^2}\left(\Lambda^2 + m_{\mathrm{S}}^2\right). \tag{2.25}$$

If $\mathrm{g_S} = \mathrm{g_F}$ the terms with Λ^2 cancel and if the fermion and scalar masses are not too different, the one-loop contribution can be written as

$$m_{\mathrm{H}}^2 \sim m_{\mathrm{H0}}^2 + \frac{\mathrm{g_F^2}}{4\pi^2}\left(m_{\mathrm{F}}^2 - m_{\mathrm{S}}^2\right). \tag{2.26}$$

If the mass difference is larger than about a TeV, the cancellation is unnatural and must be a result of a symmetry, the supersymmetry.

In supersymmetry new particles are combined into a superfield, which contains fields differing by one-half spin. It connects particles with different spin but the same quantum numbers. Since no supersymmetric particles have been observed yet SUSY particles must have different masses and supersymmetry must be broken. There are two types of superfields (or supermultiplets)[1]:

1. **Chiral Superfields:** These fields consist of a complex scalar field, S, and a 2-component Majorana fermion field, ψ.

2. **Massless Vector Superfields:** These fields consist of a massless gauge field with the field strength $F_{\mu\nu}^{\mathrm{A}}$ and a 2-component Majorana fermion field, λ_{A}, referred to as *gaugino*. The index A is the gauge index.

To accomplish a supersymmetric transformation from a bosonic state into a fermionic state, and vice versa, an operator Q is needed that generates such transformation. This operator must be an anticommuting spinor:

$$Q|Boson\rangle = |Fermion\rangle, \qquad Q|Fermion\rangle = |Boson\rangle. \tag{2.27}$$

Since spinors are intrinsically complex objects, the hermitian conjugate of Q, $Q^\dagger$ is also a symmetry operator. Q and $Q^\dagger$ carry spin angular momentum 1/2, because they are fermionic operators, so it's clear that supersymmetry must be a space-time symmetry. For theories with chiral fermions (like the Standard Model), the generators Q and $Q^\dagger$ must satisfy an algebra of anticommutation and commutation relation with the schematic form

$$\{Q, Q^\dagger\} = P^\mu, \tag{2.28}$$

$$\{Q, Q\} = \{Q^\dagger, Q^\dagger\} = 0, \tag{2.29}$$

$$[P^\mu, Q] = [P^\mu, Q^\dagger] = 0, \tag{2.30}$$

[1]The superfield also contain "auxiliary fields", which are fields with no kinetic energy terms in the Lagrangian

where P^μ is the four-momentum generator of space-time translations. This algebra is assumed by the Coleman-Mandula theorem [60]. In a supersymmetric extension of the Standard Model, each of the know fundamental particles is in either a chiral supermultiplet or a vector supermultiplet, and must have a superpartner with a spin differing by 1/2. All SM fermions are members of chiral multiplets since their left-handed parts transform directly under the gauge group than their right-handed parts. To give their spin-0 superpartners a name, a prepending "s" for scalar is added to their name. Thus fermions become *sfermions* and quarks and fermions are called *squarks* and *sfermions*, respectively. They have the corresponding symbol but with a tilde ($\tilde{}$).

Since the Higgs scalar boson has spin-0 it is also part of a chiral supermultiplet. But it needs two chiral supermultiplets to cancel a gauge anomaly the electroweak gauge symmetry would suffer and therefore inconsistent as a quantum theory. The constraint for this cancellation of the gauge anomaly includes

$$Tr(Y^3) = Tr(T_{3\mathrm{L}}^2 Y) = 0 \tag{2.31}$$

with T_3 as the third component of the weak isospin and Y the weak hypercharge, respectively. The spin-1/2 superpartners of the Higgs are called *higgsinos*. The chiral supermultiplets of the Minimal Supersymmetric Standard Model (MSSM) are summarized in Tab. 2.3.

The vector bosons of the Standard Model resides in gauge supermultiplets and their fermionic superpartners are called *gauginos*. The superpartner of the gluon is the *gluino*. The electroweak gauge symmetry has four spin-1 gauge bosons, $W^\pm$, W^0, and B^0. Their spin-1/2 superpartners are $\tilde{W}^\pm$, $\tilde{W}^0$, and $\tilde{B}^0$ and are called *winos* and *bino*. The eigenstates of the W^0 and B^0 mix to the mass eigenstates Z^0 and γ. The corresponding gaugino mixtures are called zino ($\tilde{Z}^0$) and photino ($\tilde{\gamma}$). The gauge supermultiplets of the MSSM are summarized in Tab. 2.4.

The three-level Feynman diagrams for the production of squarks and gluions via gluon-gluon and quark-gluon fusion at the LHC is shown in Fig. 2.6. If the corresponding masses lie in the reach of the LHC the cross section for the gluino and squark production is much larger than for electroweak gaugino production.

Table 2.3.: Chiral supermultiplets in the Minimal Supersymmetric Standard Model.

Names		spin 0	spin 1/2	$\mathrm{SU}_C(3) \times \mathrm{SU}_L(2) \times \mathrm{U}_Y(1)$
squarks, quarks	Q	$\begin{pmatrix}\tilde{u}_\mathrm{L} & \tilde{d}_\mathrm{L}\end{pmatrix}$	$\begin{pmatrix}u_\mathrm{L} & d_\mathrm{L}\end{pmatrix}$	$(3, 2, \frac{1}{6})$
($\times$ 3 families)	$\bar{u}$	$\tilde{u}_\mathrm{R}^*$	$u_\mathrm{R}^\dagger$	$(\bar{3}, 1, -\frac{2}{3})$
	$\bar{d}$	$\tilde{d}_\mathrm{R}^*$	$d_\mathrm{R}^\dagger$	$(\bar{3}, 1, \frac{1}{3})$
sleptons, leptons	L	$\begin{pmatrix}\tilde{\nu} & \tilde{e}_\mathrm{L}\end{pmatrix}$	$\begin{pmatrix}\nu & e_\mathrm{L}\end{pmatrix}$	$(1, 2, \frac{1}{2})$
($\times$ 3 families)	$\bar{e}$	$\tilde{e}_\mathrm{R}^*$	$e_\mathrm{R}^\dagger$	$(1, 1, 1)$
Higgs, higgsinos	H_u	$\begin{pmatrix}H_\mathrm{u}^+ & H_\mathrm{u}^0\end{pmatrix}$	$\begin{pmatrix}\tilde{H}_\mathrm{u}^+ & \tilde{H}_\mathrm{u}^0\end{pmatrix}$	$(1, 2, +\frac{1}{2})$
	H_u	$\begin{pmatrix}H_\mathrm{d}^0 & H_\mathrm{d}^-\end{pmatrix}$	$\begin{pmatrix}\tilde{H}_\mathrm{d}^0 & \tilde{H}_\mathrm{d}^-\end{pmatrix}$	$(1, 2, -\frac{1}{2})$

2.3.2. The MSSM

The Minimal Supersymmetric Standard Model (MSSM) respects the same $\mathrm{SU}_C(3) \times \mathrm{SU}_L(2) \times \mathrm{U}_Y(1)$ gauge symmetry as the SM and the particle content of the MSSM was already discussed in the previous section and is summarized in Tab. 2.3 and Tab. 2.4.

Table 2.4.: Gauge supermultiplets in the Minimal Supersymmetric Standard Model.

Names	spin 1/2	spin 1	$SU_C(3) \times SU_L(2) \times U_Y(1)$
gluino, gluon	$\tilde{g}$	g	(8, 1, 0)
winos, W bosons	$\tilde{W}^{\pm}\ \tilde{W}^0$	$W^{\pm}\ W^0$	(1, 3, 0)
bino, B boson	$\tilde{B}^0$	B^0	(1, 1, 0)

The Lagrangian of the MSSM introduces many new parameters. Overall there are 105 parameters, among 21 masses, 43 CP violating phases and mixing angles that cannot be rotated away by redefining the phases and flavor basis for the quark and lepton supermultiplets, that have no counterpart in the SM. The only freedom in constructing the supersymmetric Lagrangian is contained in a function called *superpotential*:

$$W_{\text{MSSM}} = \bar{u}\mathrm{y_u}QH_u - \bar{d}\mathrm{y_d}QH_d - \bar{e}\mathrm{y_e}LH_d + \mu H_u H_d. \tag{2.32}$$

The number of parameters can be reduced by requiring underlying physics such as Grand Unified Theory (GUT) which is called the "constrained MSSM" (CMSSM). Two of the most popular and simplest models are the "gauge-mediated" scenario (GMSB) which is described by 6 new parameters and "minimal supergravity" (mSUGRA) which is described by 5 parameters:

- A common scalar mass, m_0^2
- A common gaugino mass, $m_{1/2}$
- A common trilinear coupling, A_0
- Sign of a Higgs mass parameter, sign(μ)
- The ratio of the two Higgs vacuum expectation values, $\tan\beta = \frac{v_u}{v_d}$

R-parity

In the SM the baryon number B and lepton number L is conserved. This conservation is not assumed but it is a consequence of the fact that there are no possible renormalizable Lagrangian terms that violate B and L, furthermore they are violated by non-perturbative electroweak effects [61]. Therefore a new symmetry has to be add to the MSSM which eliminates B and L violating terms in the renormalizable superpotential and under which the MSSM is invariant [62]. This new symmetry is called "R-parity" or "matter parity". For each particle it is defined as

$$P_{\text{R}} = (-1)^{3(\text{B-L})+2\text{s}}, \tag{2.33}$$

where s is the spin of the particle. All Standard Model particles and the Higgs boson have odd R-parity (P_{R} = -1), while all supersymmetric particles (sparticles) have even R-parity (P_{R} = +1). If R-parity is exactly conserved this has three important phenomenological consequences:

- The lightest supersymmetric particle must be stable. If the LSP is electrically neutral, it interacts only weakly with matter and is therefore a good candidate for non-baryonic dark matter.
- Each sparticle other than the LSP must eventually decay into a state that contains an odd number of LSPs (usually one).
- In collider experiments, sparticles can only be produced as a pair.

2.3.3. SUSY breaking

As discussed in the sections before in the supersymmetric extension of the Standard Model all particles have a superpartner, called sparticle, with the same quantum numbers and the same mass but a spin differing by 1/2. Since no sparticles have been observed in current experiments their mass has to be larger and SUSY must be broken. This can be done in unknown way (mSUGRA, GMSB, etc.) or just by parametrizing. This breaking can be obtained by introducing explicit "soft" mass terms to the MSSM Lagrangian:

$$\mathcal{L}_{\text{soft}} = -(\frac{1}{2}M_a\lambda^a\lambda^a + \frac{1}{6}a^{ijk}\phi_i\phi_j\phi_k + \frac{1}{2}b^{ij}\phi_i\phi_j + t^i\phi_i) + c.c. - (m^2)^i_j\phi^{j*}\phi_i. \tag{2.34}$$

M_a is the gaugino mass for each gauge group, $(m^2)^i_j$ and b^{ij} are scalar squared-mass terms, a^{ijk} is (scalar)^3 coupling and t^i is a "tadpole" coupling. The soft terms in $\mathcal{L}_{\text{soft}}$ give mass to all of the scalars and gauginos. The full Lagrangian of the MSSM can be found in [34] and [63].

There are several models breaking supersymmetry spontaneously. One is the O'Raifeartaig (F-term) supersymmetry breaking [64], where the breaking is due to a non-zero F-term[2] VEV:

$$\langle 0|F_i|0\rangle \neq 0. \tag{2.35}$$

The simplest model has three chiral supermultiplets with

$$W = -k\Phi_1 + m\Phi_2\Phi_3 + \frac{y}{2}\Phi_1\Phi_3^2, \tag{2.36}$$

k, m and y are parameter of this model and can be chosen to be real and positive. From (2.36) the scalar potential is

$$V = |F_1|^2 + |F_2|^2 + |F_3|^2, \tag{2.37}$$

$$F_1 = k - \frac{y}{2}\phi_3^{*2}, \quad F_2 = -m\phi_3^*, \quad F_3 = -m\phi_2^* - y\phi_1^*\phi_3^*. \tag{2.38}$$

Supersymmetry must be broken, since $F_1 = 0$ and $F_2 = 0$ are not consistent. Assuming that $m^2 > yk$, the absolute minimum of the potential is at $\phi_2 = \phi_3 = 0$, with ϕ_1 undetermined. That means at the minimum $F_1 = k$ and $V = k^2$.

2.3.4. CP violation in the MSSM

With the six quark flavors, the weak current is described by unitary transformations among the three quark doublets. The mixing between these three doublets is described by the Cabibbo-Kobayashi-Maskawa matrix (CKM) [11, 12], which is the 3×3 unitary matrix

$$V_{\text{CKM}} = \begin{pmatrix} V_{ud} & V_{us} & V_{ub} \\ V_{cd} & V_{cs} & V_{cb} \\ V_{td} & V_{ts} & V_{tb} \end{pmatrix} \tag{2.39}$$

Since the charged-current interactions involve only left-handed components it violates both C and P. In the lepton sector CP violation can not occur except the model would be extended by a neutrino mass matrix. In fact small neutrino masses are observed [65].

[2]For Lagrangians for chiral superfield the effective potential is given by $V = F_i^\dagger F_i$. where F_i is an auxiliary field

The source of CP violation in the Standard Model is not sufficient to explain the baryon asymmetry of the universe of

$$\eta = \frac{n_B - n_{\bar{B}}}{n_\gamma} = (6.14 \pm 0.25) \times 10^{-10}, \tag{2.40}$$

with n_B, $n_{\bar{B}}$ and n_γ the number of densities of baryons, anti-baryons and photons, respectively. The ingredients for baryogenesis are baryon number violation, C and CP violation, and departure from equilibrium. They are present in the SM but not with sufficient strength. Hence a new source of CP violation is required [38, 39, 66].

In extensions of the SM, CP violation can be either explicit or spontaneous. In the MSSM the explicit CP violation occurs via phases in the Lagrangian, which can not be rotated away by redefinitions of the field. Spontaneous CP violation occurs if an extra Higgs field with a complex vacuum expectation value is present. This can lead to a vanishing θ term as well as to a complex CKM matrix. Spontaneous CP violation is not possible in the MSSM since the Higgs potential conserves CP.

The MSSM contains 105 free parameters [67] and a large number of these parameters may have non-zero CP-violating phases [68]. Those phases that can be rotated away by a redefinition of the fields are unphysical.

In general, the gaugino mass parameters M_i ($i = 1, 2, 3$), the higgsino mass parameter μ, and the trilinear couplings A_f are chosen to be complex:

$$M_i = |M_i| e^{i\phi_i}, \qquad \mu = |\mu| e^{i\phi_\mu}, \qquad A_f = |A_f| e^{i\phi_f}, \tag{2.41}$$

but not all of these phases are physical. The physical combinations are Arg($M_i \mu$) and Arg($A_f \mu$). They can

- affect sparticle masses and couplings through their mixing
- induce CP mixing in the Higgs sector through radiative corrections
- influence CP-even observables like cross sections and branching ratios
- lead to interesting CP-odd asymmetries at colliders.

Although certain combinations of the phases are constrained by the experimental upper bounds of electric dipole moments (EDMs) they can significantly influence the collider phenomenology of Higgs and SUSY particles and also the properties of neutralino dark matter.

Higgs-sector CP mixing

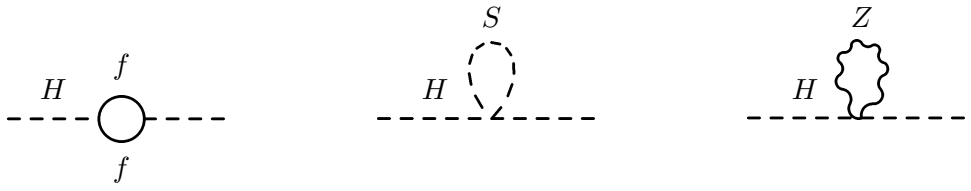

Figure 2.7.: Loop correction to the Higgs Boson from a fermion, a heavy complex scalar, and a boson.

In the MSSM the neutral Higgs sector consists of two CP-even states, h^0 and H^0, and one CP-odd state, A^0. Complex parameters, such as (2.41), have a dramatic effect by inducing a mixing between the

three neutral states through loop corrections [69–71]. The resulting mass eigenstates H_1, H_2, and H_3 are no longer eigenstates of CP. The largest effect comes from stop loops. Figure 2.7 shows Feynman diagrams of loop corrections to m_H^2.

Now it is possible to develop a significant CP-odd component for the lightest Higgs boson, H_1 such that its coupling to a pair of vector bosons becomes vanishing small. At LEP this weakens the bound on the lightest Higgs boson mass. The LEP exclusions for the CPX scenario with maximal phases is shown in Fig. 2.8. The top mass is taken to be $m_t = 174.3$ GeV. The CPX scenario [72] is the default benchmark scenario for studying CP-violating Higgs-mixing phenomena. It is defined as

$$\begin{aligned} M_{\tilde{Q}_3} = M_{\tilde{U}_3} = M_{\tilde{D}_3} = M_{\tilde{L}_3} = M_{\tilde{E}_3} = M_{\text{SUSY}}, \\ |\mu| = 4M_{\text{SUSY}}, \qquad |A_{t,b,\tau}| = 2M_{\text{SUSY}}, \qquad |M_3| = 1 \text{ TeV} \end{aligned} \tag{2.42}$$

The free parameter of this model are $\tan\beta$, the charged Higgs boson pole mass $M_{H^\pm}$, the common SUSY scale M_{SUSY}, and the CP phases. The discovery potential for Higgs bosons at ATLAS in the CPX scenario with $\phi_{t,b,3} = \pi/2$ is shown in Fig. 2.9. At small $\tan\beta$ and small Higgs masses an uncovered region remains.

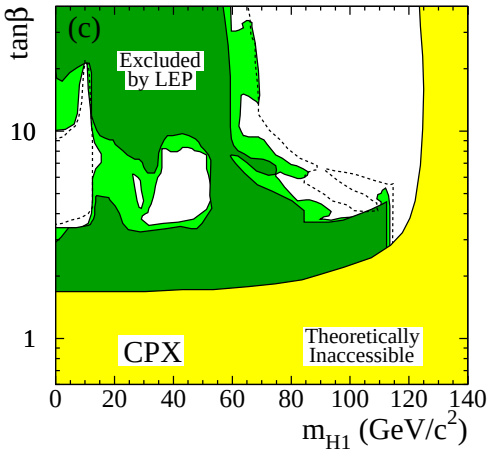

Figure 2.8.: Exclusions in the $(m_{H_1}, \tan\beta)$ projection, in the case of the CP-violating CPX scenario. Exclusions are at 95 % CL (light-green) and 99.7 % CL (dark-green) [73].

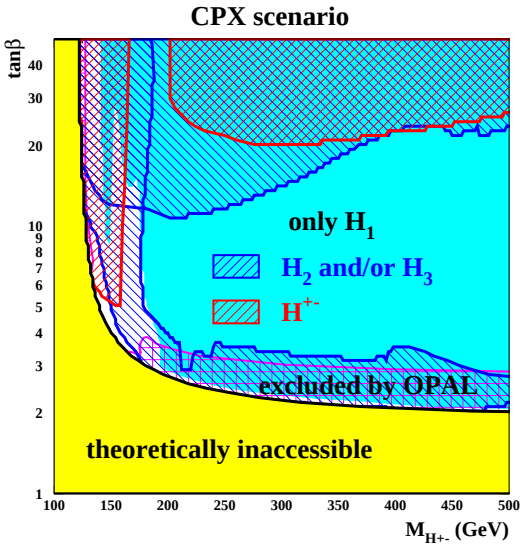

Figure 2.9.: ATLAS discovery potential for Higgs boson in the CPX scenario with 300 fb^{-1} [74].

Gauginos and sfermions

Since the CP-violating phases from (2.41) directly enter the neutralino, chargino, and sfermion mass matrices, they have an important impact on the masses and couplings of these particles. There are two different ways to measure the effects of phases.

On the one hand, there are CP-even observables, like sparticle masses, cross sections, and branching ratios. To allow parameter determination, these observables need to be measured very precisely. Furthermore the beam polarization is essential, hence this way is of particularly interest for the ILC.

On the other hand, there are CP-odd (or T-odd) observables, e.g. rate asymmetries or triple product asymmetries, which are a direct signal of CP violation. The measurement of CP-odd effects is essential, to prove that CP is violated and to determine the model parameters, including phases.

At the LHC the triple product correlations can be investigated with many different processes. The decay of $\tilde{t}$'s has been studied both in three-body [75] and two-body [76] cascade decays. For the study described in Chapter 7 the following $\tilde{t}$ production process:

$$pp \to \tilde{t}_1 \tilde{t}_1^*, \tag{2.43}$$

with the following two-body decays was considered:

$$\tilde{t}_1 \to \tilde{\chi}_2^0 t, \qquad \tilde{\chi}_2^0 \to \tilde{\ell} \ell_{\mathrm{N}}, \qquad \tilde{\ell} \to \tilde{\chi}_1^0 \ell_{\mathrm{F}}, \qquad t \to b + W, \tag{2.44}$$

where ℓ_{N} and ℓ_{F} denote the near and far leptons respectively. The CP-odd observables can be built from triple products of final state of reconstructable particles, e.g. $\vec{p}_{\ell_{\mathrm{N}}} \cdot (\vec{p}_t \times \vec{p}_W)$. If the charge of the decaying $\tilde{t}_1$ is known, particle and anti-particle can be distinguished. Hence the process with the charge-conjugated process can be combined to make unambiguous observation of CP-violation via T-odd observables. Therefore it is important to classify all terms of the corresponding amplitude squared with respect to their T-odd and T-even character. The squared amplitude $|T|^2$ of the above process can be expressed in the form

$$\begin{aligned} |T|^2 = 4|\Delta(\tilde{t}_1)|^2 |\Delta(\tilde{\chi}_2^0)|^2 |\Delta(\tilde{\ell})|^2 |\Delta(t)|^2 P(\tilde{t}_1 \tilde{t}_1^*) \Big\{ & P(\tilde{\chi}_2^0 t) D(\tilde{\chi}_2^0) D(\tilde{\ell}) D(t) \\ & + \sum_{a=1}^{3} \Sigma_P^a(\tilde{\chi}_2^0) \Sigma_D^a(\tilde{\chi}_2^0) D(\tilde{\ell}) D(t) + \sum_{b=1}^{3} \Sigma_P^b(t) \Sigma_D^b(t) D(\tilde{\chi}_2^0) D(\tilde{\ell}) \\ & + \sum_{a,b=1}^{3} \Sigma_P^{ab}(\tilde{\chi}_2^0 t) \Sigma_D^a(\tilde{\chi}_2^0) \Sigma_D^b(t)\ D(\tilde{\ell}) \Big\}, \end{aligned} \tag{2.45}$$

where a, b = 1,2,3 refers to the polarization states of the neutralino $\tilde{\chi}_i^0$ and the top quark t. Furthermore

- $\Delta(\tilde{t}_1)$, $\Delta(\tilde{\chi}_2^0)$, $\Delta(\tilde{\ell})$, and $\Delta(t)$ are the pseudo-propagators of the intermediate particles.
- $P(\tilde{t}_1 \tilde{t}_1^*)$, $P(\tilde{\chi}_2^0 t)$, $D(\tilde{\chi}_2^0)$, $D(\tilde{\ell})$, and $D(t)$ are the terms in the production and decay that are independent of the spin of the decaying neutralino and top.
- $\Sigma_P^a(\tilde{\chi}_2^0)$, $\Sigma_D^a(\tilde{\chi}_2^0)$, $\Sigma_P^b(t)$, $\Sigma_D^b(t)$, and $\Sigma_P^{ab}(\tilde{\chi}_2^0)$ are the spin-dependent terms giving the correlations between production and decay of the $\tilde{\chi}_2^0$ and t.
- The slepton $\tilde{\ell}$ produces no spin correlation term in the amplitude since it is a scalar.

The spin-independent terms do not cause any T-odd terms. The spin-dependent terms often can be divided into T-even and T-odd terms, depending on the process. For the above process, a sequence of 2-body decay, $\Sigma_P^{ab}(\tilde{\chi}_2^0 t) = \Sigma_{P,even}^{ab}(\tilde{\chi}_2^0 t) + \Sigma_{P,odd}^{ab}(\tilde{\chi}_2^0 t)$, all other spin-dependent terms only lead to T-even terms[3]. Therefore, the T-odd term in the amplitude is $\sum_{a,b=1}^{3} \Sigma_P^{ab}(\tilde{\chi}_2^0 t) \Sigma_D^a(\tilde{\chi}_2^0) \Sigma_D^b(t) D(\tilde{\ell})$.

[3] In 3-body decays spin-dependent terms from both the production $\Sigma_P^{ab}(\tilde{\chi}_2^0 t)$ as well as from the 3-body decay $\Sigma_D^a(\tilde{\chi}_2^0)$ lead to CP-odd contributions

In the MSSM, both the $\tilde{t}$ and $\tilde{\chi}^0$ are mixtures of eigenstates. The $\tilde{t}$ sector is defined by the mass matrix $\mathcal{M}_{\tilde{t}}$ in the basis of gauge eigenstates $(\tilde{t}_L, \tilde{t}_R)$. The 2×2 mass matrix is given as

$$\mathcal{M}^2_{\tilde{t}} = \begin{pmatrix} m_t^2 + m_{LL}^2 & m_{LR}^* m_t \\ m_{LR} m_t & m_t^2 + m_{RR}^2 \end{pmatrix}, \tag{2.46}$$

where

$$m_{LL}^2 = M_{\tilde{Q}}^2 + m_Z^2 \cos 2\beta (\frac{1}{2} - \frac{2}{3} \sin^2 \theta_W), \tag{2.47}$$

$$m_{RR}^2 = M_{\tilde{U}}^2 + \frac{2}{3} m_Z^2 \cos 2\beta \sin^2 \theta_W, \tag{2.48}$$

$$m_{LR} = A_t - \mu^* \cot \beta, \tag{2.49}$$

with $\tan\beta = v_2/v1$ the ratio of the vacuum expectation values of the two neutral Higgs fields, $M_{\tilde{Q}}$ and $M_{\tilde{U}}$ the soft scalar masses, and the supersymmetric higgsino mass parameter μ. From these parameters μ and A_t can take complex values which yield to CP violation in the $\tilde{t}$ sector

$$A_t = |A_t| e^{i\phi_t}, \qquad \mu = |\mu| e^{i\phi_\mu}, \qquad (0 \leq \phi_t, \phi_\mu < 2\pi). \tag{2.50}$$

The four neutralinos $\tilde{\chi}_i^0$ (i = 1,2,3,4) are mixture of the neutral U(1) and SU(2) gauginos, $\tilde{B}$ and $\tilde{W}^3$, and the higgsinos, $\tilde{H}_1^0$ and $\tilde{H}_2^0$. The mass matrix is given as

$$\mathcal{M}_N = \begin{pmatrix} M_1 & 0 & -m_Z \cos\beta \sin W & m_Z \sin\beta \sin W \\ 0 & M_2 & m_Z \cos\beta \cos W & -m_Z \sin\beta \cos W \\ -m_Z \cos\beta \sin W & m_Z \cos\beta \cos W & 0 & -\mu \\ m_Z \cos\beta \sin W & -m_Z \sin\beta \cos W & -\mu & 0 \end{pmatrix}, \tag{2.51}$$

with M_1 and M_2 as the gaugino masses. The CP violation enters at the M_1 parameter:

$$M_1 = |M_1| e^{i\phi_1}, \qquad (0 \leq \phi_1 < 2\pi). \tag{2.52}$$

Any complex phases contained in both mixing matrices will yield CP-violating effects and can be seen in observables that exploit the covariant product. The Lorentz invariant covariant product can be expanded in terms of the explicit energy and momentum components

$$\begin{aligned} \epsilon_{\mu\nu\rho\sigma} p^\nu_{\tilde{\chi}_2^0} p^\mu_{\ell_N} p^\rho_W p^\sigma_t =& E_{\tilde{\chi}_2^0} \vec{p}_{\ell_N} \cdot (\vec{p}_W \times \vec{p}_t) + E_W \vec{p}_t \cdot (\vec{p}_{\tilde{\chi}_2^0} \times \vec{p}_{\ell_N}) \\ & - E_{\ell_N} \vec{p}_W \cdot (\vec{p}_t \times \vec{p}_{\tilde{\chi}_2^0}) - E_t \vec{p}_{\tilde{\chi}_2^0} \cdot (\vec{p}_{\ell_N} \times \vec{p}_W). \end{aligned} \tag{2.53}$$

Since the top and the W boson can be measured from the final state momenta, the first term in (2.53) shows the CP sensitive triple product, that can be measured. This triple product is not Lorentz invariant, hence it can vary in both magnitude and sign in different reference frames. For the rest frame of the $\tilde{\chi}_2^0$ the covariant product is

$$\epsilon_{\mu\nu\rho\sigma} p^\nu_{\tilde{\chi}_2^0} p^\mu_{\ell_N} p^\rho_W p^\sigma_t \rightarrow m_{\tilde{\chi}_2^0} \vec{p}_{\ell_N} \cdot (\vec{p}_W \times \vec{p}_t), \tag{2.54}$$

since all other terms of the covariant product vanish with $\vec{p}_{\tilde{\chi}_2^0} \rightarrow 0$.

For the study of Chapter 7 two triple products are very useful and can be used as T-odd observables:

$$\mathcal{T}_{\ell_N} = \vec{p}_{\ell_N} \cdot (\vec{p}_W \times \vec{p}_t), \tag{2.55}$$

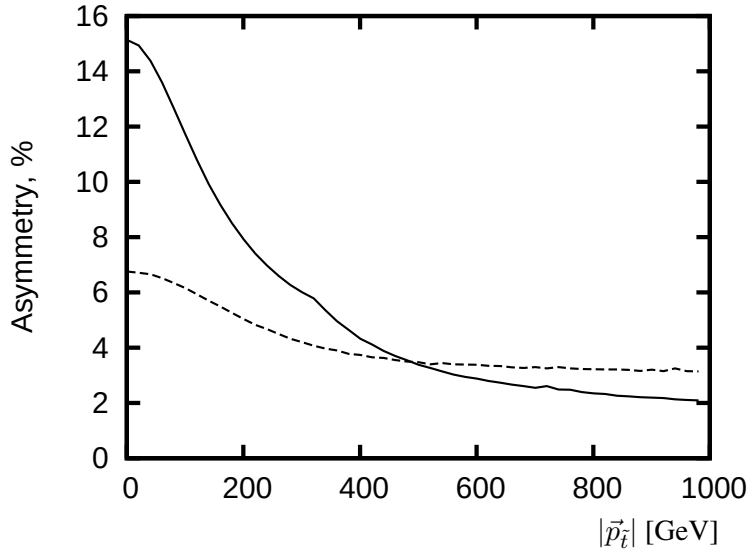

Figure 2.10.: Asymmetry $\mathcal{A}_T$ from Eq. (2.57) for the triple products $\mathcal{T}_{\ell_N}$ (solid) and $\mathcal{T}_{\ell\ell}$ (dotted) as function of the stop momentum in the laboratory frame [77].

$$\mathcal{T}_{\ell\ell} = \vec{p}_b \cdot (\vec{p}_{\ell^+} \times \vec{p}_{\ell^-}), \tag{2.56}$$

where ℓ^+ and ℓ^- are the two leptons produced in the $\tilde{\chi}_2^0$ cascade decay. The identification of the near and far lepton is not required for (2.56).

The T-odd asymmetry is defined as

$$\mathcal{A}_T = \frac{N_{\mathcal{T}_+} - N_{\mathcal{T}_-}}{N_{\mathcal{T}_+} + N_{\mathcal{T}_-}} = \frac{\int \text{sign}\{\mathcal{T}_f\}|T|^2 d\text{lips}}{\int |T|^2 d\text{lips}}, \tag{2.57}$$

where $f = \ell_N$ or $\ell\ell$, $d$lips denotes Lorentz invariant phase space and $N_{\mathcal{T}_+}$ ($N_{\mathcal{T}_-}$) are the numbers of events for which $\mathcal{T}$ is positive (negative). The denominator in Eq. (2.57), $\int |T|^2 d\text{lips}$, is proportional to the cross section of the combined production and decay processes. The T-odd asymmetry for both triple products is shown in Fig. 2.10.

Conclusion

The Standard Model is the most successful theory of particle physics but it leaves many open questions. The idea of a supersymmetric extension of the Standard Model provides an elegant solution to many of theoretical and experimental problems. If the lightest SUSY particle is stable, it serves as a good candidate for dark matter and CP-violating effects in SUSY can help to explain the baryon asymmetry in the universe. Supersymmetry also achieves unification of the forces and solves the hierarchy problem.

In the MSSM explicit CP violation can occur via phases in the Lagrangian. CP-violating effects can appear either in the Higgs-sector or the gaugino and sfermion sector. The CP violation enters the mixing matrices of masses via complex phases. A direct signal of CP violation can be observed via CP-odd (or T-odd) observables, like rate asymmetries of asymmetries of the triple product of the final state.

3. The LHC and the ATLAS Experiment

To access the TeV-scale for particle physics the Large Hadron Collider (LHC) with a center of mass energy of 14 TeV was built. At four interaction points three experiments had been installed to investigate the final state particles of the proton-proton collisions and one experiment for physics with heavy ion collisions (lead (Pb) or gold (Au)) at 5.5 TeV per nucleon pair.

ATLAS[1] [78] and CMS[2] are multipurpose detectors, built for the search of many kind of new physics (Higgs Boson, supersymmetry, extra dimensions, etc.) and important Standard Model (like the top). LHCb[3] is a specialized detector for B-physics and ALICE[4] a dedicated detector for heavy ion collisions. The LHC is described in Section 3.1 and the ATLAS detector in Section 3.2.

3.1. The Large Hadron Collider at CERN

The LHC [79] is a superconducting particle accelerator, which was built in the former Large Electron Positron (LEP) tunnel 50 – 100 m below the surface at CERN[5]. The two-ring accelerator has a circumference of 26.7 km and will bring protons as well as heavy-ions (Pb or Au) to head-on collisions. Figure 3.1 shows the tunnel and the underground infrastructure of the LHC.

The LHC is supplied with protons and Pb (or Au) by the injection chain linac, PS and SPS. The injection energy is 450 GeV per proton. First collisions with this injection energy took place from November 23th 2009 to December 18th 2009. From March 30th 2010 up to the end of 2011 the LHC will run with half of its final center of mass energy of 7 TeV (3.5 TeV per proton). From November 2010 until the end of the first period in December 2010 the LHC run with heavy ion collisions. After a longer shutdown of one year the LHC will reach its nominal center of mass energy of 14 TeV.

The LHC circulates two proton beams, one clockwise and one anti-clockwise, and brings them to collision at the four interaction points (IP) of the experiments. Design parameters are 2808 bunches per beam with a bunch spacing of 25 ns. Each bunch is 7.55 cm long and filled with $1.15 \cdot 10^{11}$ protons. At collision energy the stored energy per beam is 362 MJ.

The number of events is given by:

$$N_{event} = \mathcal{L}\sigma_{event}, \tag{3.1}$$

where σ_{event} is the cross-section for the event under study and $\mathcal{L}$ the machine luminosity. This luminosity depends only on machine parameters and is given by:

$$\mathcal{L} = \frac{N_b^2 n_b f_{rev} \gamma_r}{4\pi\epsilon_n \beta^*} F, \tag{3.2}$$

where N_b is the number of particles per bunch, n_b the number of bunches per beam, f_{rev} the revolution frequency, γ_r[6] the relativistic gamma factor, ϵ_n the normalized transverse beam emittance, β^* the beta

[1] **A T**oroidal **L**HC **A**pparatu**S**
[2] **C**ompact **M**uon **S**olenoid
[3] **L**arge **H**adron **C**ollidor **b**eauty
[4] **A L**arge **I**on **C**ollidor **E**xperiment
[5] **C**onseil **E**uropeeen pour la **R**echerche **N**ucleaire
[6] $\gamma_r = \frac{1}{\sqrt{1-\beta_r^2}}$

function at the collision point and F the geometric luminosity reduction factor due to the crossing angle at the IP:

$$F = 1/\sqrt{1 + (\frac{\theta_c \sigma_z}{2\sigma^*})}, \tag{3.3}$$

where θ_c is the full crossing angle at the IP, σ_z the RMS bunch length and σ^* the transverse RMS beam size at the IP. For ATLAS as one of the two high luminosity experiments the nominal luminosity will be $\mathcal{L} = 10^{34}\text{cm}^{-2}\text{s}^{-1}$. The transverse emittance is defined through the invariance of the area enclosed by the single particle phase space. The normalized transverse emittance is defined as

$$\epsilon_n = \epsilon \gamma_r \beta_r, \tag{3.4}$$

with $\beta_r = \frac{v}{c}$ as the relativistic beta factor where v is the velocity of the particle and c the speed of light in vacuum. The beta function β^* is also known as the amplitude function. Together with the emittance it defines the amplitude of a betatron oscillation performed by particles within a magnet field:

$$E = \sqrt{\epsilon \beta^*}. \tag{3.5}$$

The high luminosity excludes the use of anti-proton beams as they are used at the Tevatron and one common vacuum and magnet system for both beams. Therefore the LHC is designed as a proton-proton collider with two separated magnetic fields and vacuum chambers in the main arcs and with common sections only at the insertion regions of the four experiments.

Such a high luminosity is needed since many of the interesting signals have a very low cross section compared to the background. The cross section for the production of a Higgs boson with a mass of m_H= 150 GeV and m_H= 500 GeV at a center-of-mass energy of $\sqrt{s}$ = 14 TeV and an integrated luminosity of $\mathcal{L} = 10^{33}\text{cm}^{-2}\text{s}^{-1}$ is shown in Fig. 2.3.

To keep the protons on a circulating track a magnetic field of 8.33 T is necessary. The magnetic system contains of 1232 superconducting dipole magnets, each 14.3 m long with a bending radius of 2804 m and operated at a temperature of 1.9 K. Furthermore quadrupole magnets are installed to focus the beam.

The machine performance of the LHC is limited by seven main effects:

- **Beam-Beam limit:** The maximum particle density per bunch is limited by the beam-beam interaction that each particle experiences when the bunches of both beams collide at the interaction point. This beam-beam interaction can be measured by the linear tune shift which is given by

  $$\xi = \frac{N_{\text{bunch}} r_p}{4\pi\epsilon_n}, \tag{3.6}$$

  where $r_p = e^2/(4\pi\epsilon_0 m_p c^2)$ is the classical proton radius. The tune is the number particle trajectory oscillations during one revolution in the storage ring. The oscillation occurs in both directions, transverse and longitudinal.

- **Mechanical aperture:** The geometrical aperture of the LHC is given by the dimensions of the beam screen. The height of the beam screen is approximately 2×17.3 mm and the total width is 2×22 mm. In terms of the RMS beam size a minimum aperture of 10σ is required. Assuming tolerances for the machine imperfections and the magnet alignment and geometry a peak nominal beam size of 1.2 mm is implied. Combined with a β-function of 180 m in the LHC arcs this implies a maximum acceptable transverse beam emittance of ϵ_n = 3.75 μm. Together with the beam-beam limit the limit of the maximum bunch intensity in the LHC is $N_{bunch}(\text{nominal}) = 1.15 \cdot 10^{11}$.

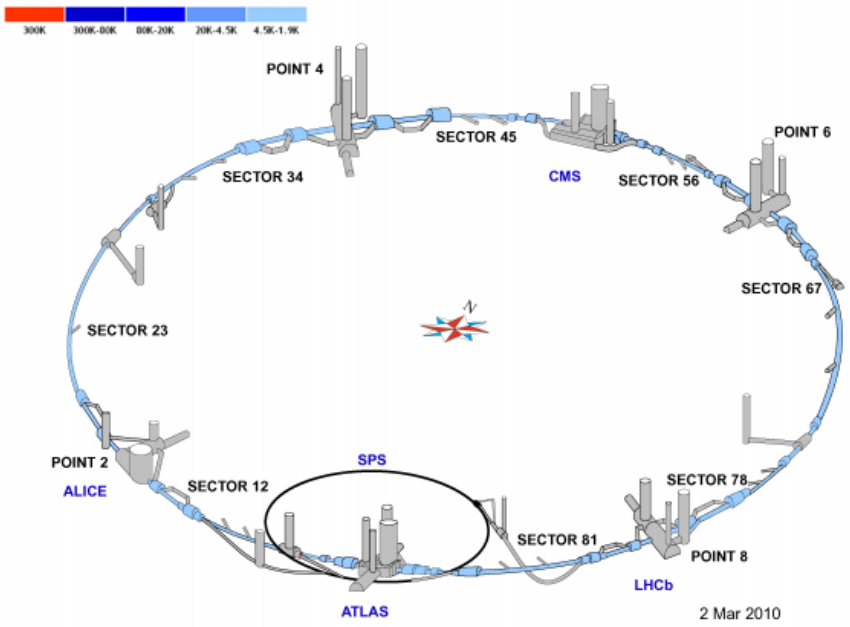

Figure 3.1.: The LHC tunnel and underground infrastructure [79].

- **Maximum dipole field and Magnet quench limit:** The maximum γ_r is limited by the dipole field in the storage ring. A field of nominal 8.33 T corresponds to a beam energy of 7 TeV. The actual field attainable in the storage ring depends on the head load and temperature margins inside the cryo-magnets and therefore on the beam losses in the machine during operation.

- **Energy stored in beams and magnetic fields:** A total beam current of 0.584 A corresponds to a stored energy of approximately 362 MJ. The LHC magnet system itself contains a stored electromagnetic energy of approximately 600 MJ, yielding a stored energy of more than 1 GJ. At the end of each run or in case of a malfunction or an emergency this energy must be absorbed safely. Therefore the beam dumping system and the magnet system provide additional limits for the maximum attainable beam energies and intensities.

- **Heat load:** There are two effects of head load. The first is synchrotron radiation. Although it is small in hadron storage rings compared to electron colliders it still can impose practical limits to the maximum gainable beam intensity if the radiation must be absorbed. The second effect is the head deposition from luminosity induced losses in the IR and impedance issue which must be absorbed by the LHC cryogenics system.

- **Field quality and dynamic aperture:** To ensure a loss-free operation of the machine a high field quality is required since field quality errors corrupt the particle stability in the storage ring. The decay of persistent currents and their 'snap back' at the beginning of ramping is a characterizing feature of superconducting magnets. Therefore small beam losses require a tight control of the magnet field errors during the production of the magnets and the machine operation. If fixed limits for the beam losses due to the quench levels of the superconducting magnets are assumed, the

accuracy of the field quality correction during operation limits the maximum gainable machine performance.

- **Collective beam instabilities:** Charged particles in each beam interact with each other via electromagnetic fields and the conducting boundaries of the vacuum system. This can result in collective beam instabilities. These collective effects are a function of the vacuum system geometry and its surface properties and are usually proportional to the beam currents. Therefore they can limit the maximum gainable beam intensities in the LHC.

The lifetime of the luminosity is not constant in the LHC during a physics run but decays due to degradation of intensity and emittances of the circulating beams.

The collisions themselves are the main reason for the luminosity decay. Because of this effect the initial decay time of bunch intensity is given by

$$\tau_{\mathrm{nuclear}} = \frac{N_{\mathrm{tot},0}}{\mathcal{L}\sigma_{\mathrm{tot}}k}, \tag{3.7}$$

with $N_{\mathrm{tot},0}$ as the initial beam intensity, $\mathcal{L}$ the initial luminosity, σ_{tot} the total cross section of $\sigma_{tot} = 10^{-25}\mathrm{cm}^2$ at 7 TeV and k the number of interaction points. With a nominal luminosity of $\mathcal{L} = 10^{34}\mathrm{cm}^{-2}\mathrm{s}^{-1}$ and two high luminosity experiments (ATLAS and CMS) the initial decay time is 44.85 h.

The decay of the beam intensity and luminosity is given by

$$N_{tot}(t) = \frac{N_{tot,0}}{1 + t/\tau_{nuclear}}, \tag{3.8}$$

$$\mathcal{L}(t) = \frac{\mathcal{L}_0}{(1 + t/\tau_{\mathrm{nuclear}})^2}, \tag{3.9}$$

and the time required to reach 1/e of the initial luminosity is given by

$$t_{\mathrm{1/e}} = (\sqrt{e} - 1)\tau, \tag{3.10}$$

This gives a luminosity decay time of $\tau_{nuclear,\mathrm{1/e}xs}$ = 29 h.

There are also other contributions to the beam losses like toucheck scattering and particle losses due to a slow emittance blow up coming from particle scattering on residual gas, the nonlinear force of the beam-beam interaction, RF noise and IBS scattering. The synchrotron ration damping in the LHC can partially compensate the blow up due to decreasing the bunch dimensions at top energy. Finally the net luminosity lifetime is given by

$$\frac{1}{\tau_{\mathcal{L}}} = \frac{1}{\tau_{IBS}} + \frac{2}{\tau_{rest-gas}} + \frac{1}{\tau_{nuclear,\mathrm{1/e}}}, \tag{3.11}$$

with a transverse IBS growth time of τ_{IBS} = 80 h and a vacuum beam lifetime of $\tau_{rest-gas}$ = 100 h one can obtain a luminosity lifetime of $\tau_{\mathcal{L}}$ = 14.9 h.

For more information on particle accelerator physics see [80, 81].

3.2. The ATLAS Detector

The ATLAS Detector [78] is a multipurpose detector which is installed at the LHC. It is located in a huge cavern at point 1 around 90 m below the surface and is almost as large as the cavern.

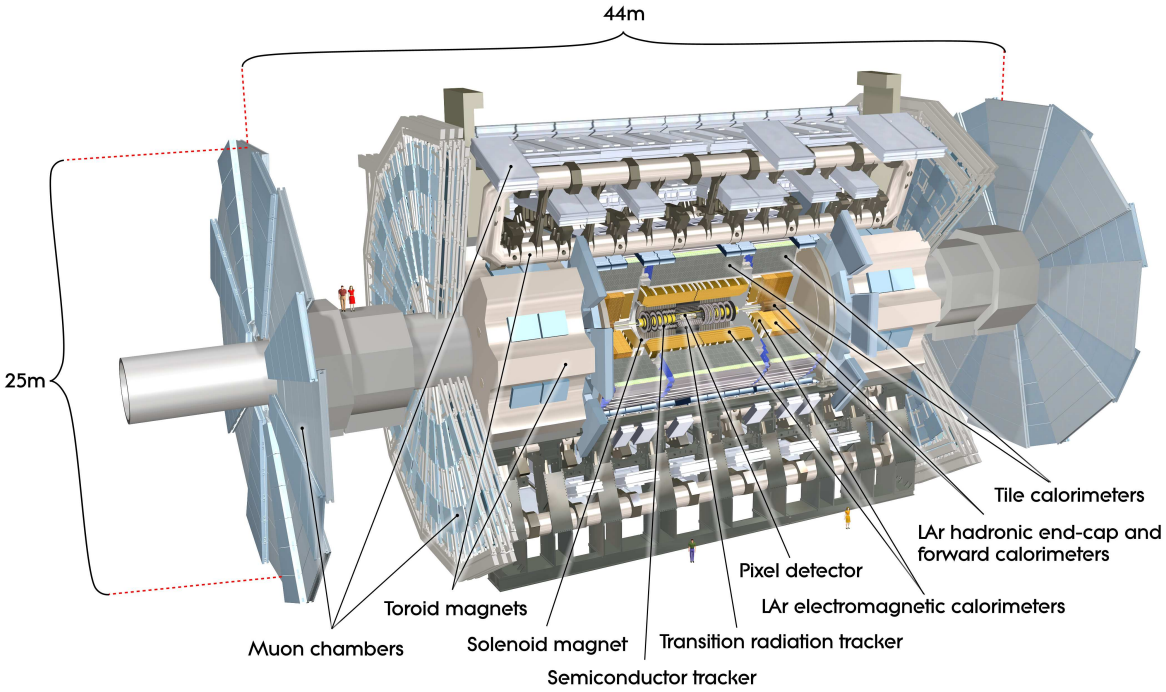

Figure 3.2.: Cut-away view of the ATLAS detector. The detector is 44 m long, 25 m high and the overall weight is approximately 7000 tonnes [78].

Since the coordinate system and nomenclature to describe the ATLAS detector and particles emerging from p-p collisions are used frequently in this thesis they need to be described first. As the origin of the coordinate system the interaction point is defined. The beam direction defines the z-axis while the x-y plane is transverse to the beam direction. The positive x-axis is pointing from the interaction point to the center of the LHC ring and the positive y-axis is pointing upwards. The A-side of the detector is defined as the side with positive z-axis and C-side as the side with negative z-axis. As usual the azimuthal angle ϕ is measured around the beam axis, and the polar angle θ is the angle from the beam axis. Instead of the polar angle the pseudo-rapidity defined as $\eta = -\ln\tan(\theta/2)$ is used (in case of heavy objects such as jets, the rapidity $y = 1/2\ln[(E+p_z)/(E-p_z)]$ is used instead). The transverse momentum p_T, the transverse energy E_T and missing transverse energy E_T^{miss} are defined in the x-y plane. Finally the distance ΔR in the pseudo-rapidity-azimuthal angle space is defined as $\Delta R = \sqrt{\Delta\eta^2 + \Delta\phi^2}$.

The LHC will provide a rich physics potential. Therefore a large set of processes have been defined to cover most of the new phenomena and to define the requirements for the ATLAS detector. This list contains high precision tests of QCD, electroweak interactions, and flavor physics which are enabled due to the high luminosity and increased cross-sections. The top quark will be produced with a rate of a few tens of Hz.

Another important topic is the search for the Standard Model Higgs boson. To define the performance of important subsystems this process has been used as benchmark. Due to the large QCD background the predominant decay mode of the Higgs into hadrons would be difficult to detect and at low masses ($m_H < 2m_Z$), where the natural width is only a few MeV, the observed width would be defined by the instrumental resolution.

To study new heavy gauge bosons Z' and W' with masses up to ~ 6 TeV high-resolution lepton mea-

surements and charge identification are needed in the p_{T}-range of a few TeV. For very high-p_{T} jet measurements quark compositeness were used as benchmark process.

In case of the decay of supersymmetric particles, such as squarks and gluinos, the experiment would measure a significant missing transverse energy, $E_{\mathrm{T}}^{\mathrm{miss}}$, in the final state which is expected for a lightest stable supersymmetric particle (LSP), and a number of leptons and jets. A large number of hard isolated photons is expected if the LSP decays into a photon and a gravitino.

In terms of these physics goals a set of general requirements for LHC detectors can be defined [82].

- The detectors require fast, radiation-hard electronics and sensor elements to deal with the experimental conditions at the LHC. To handle the particle flux and reduce the influence of overlapping events (pile-up) a high granularity is needed.
- Large pseudo-rapidity acceptance with almost full azimuthal angle coverage.
- Good charged-particle momentum resolution and reconstruction efficiency is required for the Inner Detector. For offline tagging of τ-leptons and b-jets, the vertex detector close to the interaction point needs to observe secondary vertices.
- For electron and photon identification a very good electromagnetic (EM) calorimeter is needed, together with a full-coverage hadronic calorimeter for accurate jet and missing transverse energy measurements.
- Good muon identification and momentum resolution over a wide range of momenta are fundamental requirements.
- To archive an acceptable trigger rate for interesting physics processes highly efficient triggering on low transverse-momentum objects with good background rejection is required.

An overall layout of the ATLAS detector is shown in Fig. 3.2. The detector is forward-backward symmetric with respect to the interaction point. It has two magnet configurations, a thin superconducting solenoid surrounding the Inner Detector, and three large superconducting toroids (one Barrel and two end-caps) around the calorimeters. The magnet system is described in Section 3.2.3.

The Inner Detector is inserted in a 2 T solenoid field. It contains different subsystems to achieve pattern recognition, momentum and vertex measurements and electron identification. The Inner Detector and its subsystems are described in detail in Section 3.2.2.

The liquid-argon (LAr) electromagnetic sampling calorimeter has a high granularity and therefore an excellent energy and position resolution. It covers the pseudo-rapidity range $|\eta| < 3.2$. The hadronic barrel calorimeter in the range $|\eta| < 1.7$ is provided by a scintillator-tile calorimeter. In the end-caps with range $|\eta| > 1.5$ LAr technique is also used. Finally the LAr forward calorimeter extends the pseudo-rapidity coverage to $|\eta| < 4.9$. All calorimeters are described in Section 3.2.4.

The muon spectrometer surrounds the calorimeter and is described in Section 3.2.5. To minimize multiple-scattering and to provide excellent muon momentum resolution the air-core toroid system generates strong bending power in a large volume within a light and open structure.

With an event data recording limit of 200 Hz and a proton-proton interaction rate of 1 GHz at design luminosity of $\mathcal{L} = 10^{34}\mathrm{cm}^{-2}\mathrm{s}^{-1}$ an overall rejection factor of 5×10^6 against minimum-bias processes is required. To achieve the final data taking rate of 200 Hz a trigger with three levels is used. The Level 1 (L1) Trigger and the High Level Trigger (HLT) with the Level 2 (L2) Trigger and the Event Filter (EF). The Trigger and the Data Acquisition are described in Section 3.2.6.

Table 3.1 lists some of the important performance goals and some measured performance values of the ATLAS detector. The number of channels for each sub-detector and the operational fraction during

Table 3.1.: Performance goals and measured performance pf the ATLAS detector [78].

Detector component	Required resolution	Measured resolution
Tracking	$\sigma_{p_T}/p_T = 0.05\,\% p_T \oplus 1\,\%$	$\sigma_{p_T}/p_T = (4.83 \pm 0.16) \times 10^{-4}\text{GeV}^{-1} \times p_T$ [83]
EM Calorimeter	$\sigma_E/E = 10\,\%/\sqrt{E} \oplus 0.7\,\%$	$\sigma_E/E \sim 1\,\%/\sqrt{E} \oplus 0.7\,\%$ [84]
Had Calorimeter Barrel and end-cap Forward	 $\sigma_E/E = 50\,\%/\sqrt{E} \oplus 3\,\%$ $\sigma_E/E = 100\,\%/\sqrt{E} \oplus 10\,\%$	 $\sigma_E/E = 50\,\%$ at 20 – 30 GeV
Muon Spectrometer	$\sigma_{p_T}/p_T = 10\,\%$ at p_T = 1 TeV	$\sigma_{p_T}/p_T = 4 - 5\,\%$ [86] at $p_T > 10$ GeV

Table 3.2.: Number of channels and approximate operational fraction of the sub-detectors.

Sub-detector	**Number of channels**	**Approximate Operational Fraction**
Pixel	80 M	97.3 %
SCT	6.3 M	99.2 %
TRT	350 k	97.1 %
LAr EM Calorimeter	170 k	97.9 %
Tile Calorimeter	9800	96.8 %
Hadronic end-cap LAr Calorimeter	5600	99.9 %
Forward LAr Calorimeter	3500	100 %
LVL1 Calo Trigger	7160	99.9 %
LVL1 Muon RPC Trigger	370 k	99.5 %
LVL1 Muon TGC Trigger	320 k	100.0 %
MDT Muon Drift Tubes	350 k	99.5 %
CSC Cathode Strip Chambers	31 k	98.5 %
RPC Barrel Muon Chambers	370 k	97.0 %
TGC end-cap Muon Chambers	320 k	98.4 %

the data taking period 2010 is shown in Tab. 3.2. For each sub-detector at least 97 % of the channels are operational.

3.2.1. Installation

The construction of the ATLAS components was distributed over many institutes around the world. These components then had to be brought to CERN where in most cases the final assembly and testing were done on the surface. The underground installation was accomplished in six phases:

- **Phase 1:** Infrastructure in the main cavern, feet and rails. In May 2003 the main cavern was hand over to ATLAS. The general infrastructure like the metallic structure around the cavern walls, temporary electricity and lightning and the overhead traveling cranes were installed first. Finally the 18 stainless steel support feet were lowered one by one and the main rails were installed. The feet provide the mechanical support for most of the ATLAS subsystems amounting to about 6000 t.

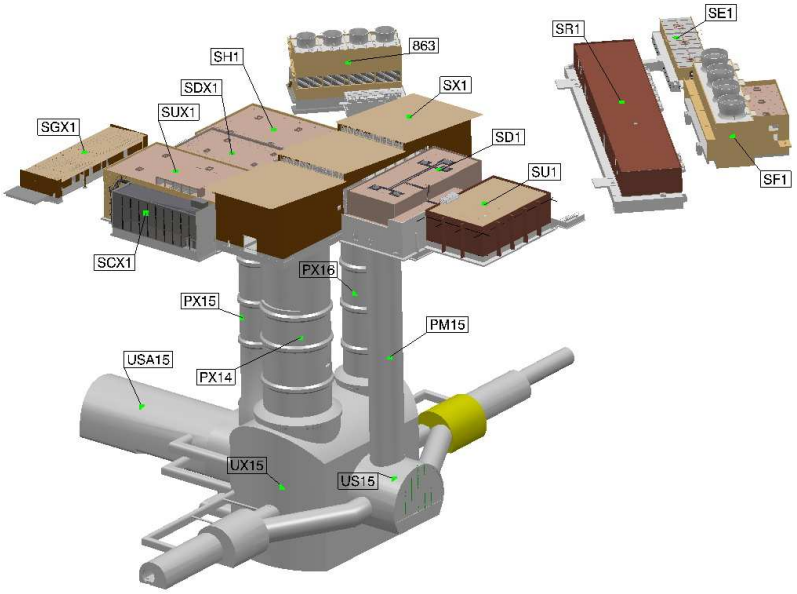

Figure 3.3.: Surface buildings and ATLAS cavern at point 1 [78].

- **Phase 2:** Barrel calorimetry and barrel toroid. Each barrel toroid coil with a weight of 100 t and a total length of 25 m was lifted down by the surface crane on side A. In the cavern they were picked up by the two 65 t underground traveling cranes and put into their final position. In parallel the first 100 muon barrel chambers were installed in between the struts/girders and the ATLAS feet. The lower part of the tile calorimeter was lowered in March 2004. 32 of 64 individual tile calorimeter modules were then assembled together. In October 2004 the LAr barrel calorimeter cryostat was then lowered into this half-cradle. The tile module assembly was then continued until the full barrel calorimeter was completed in October 2005.

- **Phase 3:** end-cap calorimeters and muon barrel chambers. In January 2006 the first end-cap calorimeter was assembled on side C. It was then moved inside the barrel toroid in February 2006. The first of the 656 barrel muon chambers was installed on side A in February 2006. The installation of the second end-cap calorimeter on side A was completed in May 2006 but it was not moved into its final position. The magnetic field of the solenoid was switched on and measured in June 2006.

- **Phase 4:** Muon big wheels, Inner Detector and completion of muon barrel. The installation of the first end-cap muon middle station (often referred to as big wheel) started in April 2006 and was completed in September 2006. Afterwards it was moved against the barrel magnet in November 2006 after installing the services. The second of four big wheels was completed in March 2007 and the end-cap C of the Inner Detector was lowered down. The remaining barrel muon chambers were also installed before closing the end of the barrel on side C. In August 2006 the field mapping of the solenoid was finished and the barrel section of the Inner Detector was installed inside the bore of the barrel cryostat. To complete the muon barrel chambers the end-cap calorimeter on side A was partially moved inside. By the end of December 2006 90 % had been installed. In January

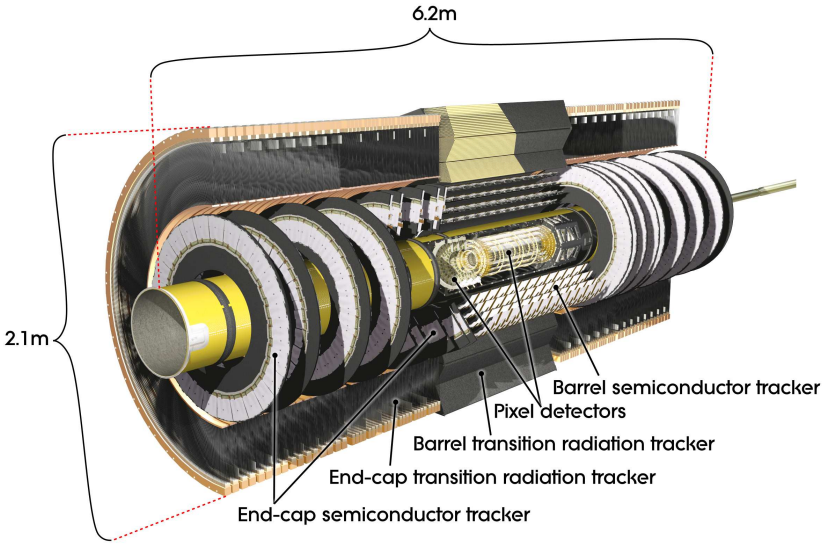

Figure 3.4.: Cut-away view of the ATLAS Inner Detector [78].

2007, the preparations for the muon big-wheel assembly started. In parallel the installation of the barrel muon chambers continued. Finally in May and June 2007, the two Inner Detector end-caps and the pixel detector together with the central VI section of the beam-pipe were installed.

- **Phase 5:** end-cap toroid magnets and muon small wheels. In June and July 2007 the two end-cap toroids were lowered down. The small wheels of the muon end-cap were assembled to the shielding disks on the surface and installed in February 2008.

- **Phase 6:** Beam-pipe and forward shielding. The beam-pipe and the forward shielding were the last elements to be installed.

Figure 3.3 shows a layout of the surface buildings and the underground infrastructure with access shafts, ATLAS cavern and counting rooms. The detector is housed in the main cavern UX15 and the main counting room is located in USA15, shielded by a 15 m thick concrete wall. The main control room resides in building SCX1.

3.2.2. Inner Detector

The purpose of the ATLAS Inner Detector (ID) is to measure the momentum with high resolution and both primary and secondary vertex of charged tracks [87, 88] . The ID covers the pseudo-rapidity range $|\eta| < 2.5$ and an energy range of 0.5 GeV to 150 GeV. The estimated vertex resolution is shown in Fig. 3.5 and the Z position and radius of the vertex is shown in Fig. 3.6.

A cylindrical envelope of $\pm$ 3512 mm and radius of 1150 mm and a solenoid field of 2 T surrounds the ID. The detector itself is 6.2 m longs and has a diameter of 2.1 m. The layout is shown in Fig. 3.4.

The ID has three independent sub-detectors, the pixel detector, Silicon Microstrips (SCT) and the straw tubes of the Transition Radiation Tracker (TRT). An overview of the Inner Detector is shown in Fig. 3.7.

Due to the high-radiation environment the Inner Detector sensors, on-detector electronics, mechanical structure and service require tight conditions. After three years of operation at design luminosity the pixel inner vertexing layer must be replaced.

To archive a very robust pattern recognition and high precision in both R-ϕ and z coordinates a combination of precision trackers at small radii with the TRT is required and the straw hits at the outer radius contribute significantly to the momentum measurement. The ID provides electron identification by enhancing the detection of transition-radiation photons in the xenon-based gas mixture of the straw tubes. For heavy-flavor and τ-lepton tagging the impact parameter measurements by the semiconductor trackers is essential. The secondary vertex measurement performance is enhanced by the innermost layer of pixels, at a radius of about 5 cm.

An overview of the intrinsic measurement accuracies and the mechanical alignment of all Inner Detector subsystems can be found in Table 3.3.

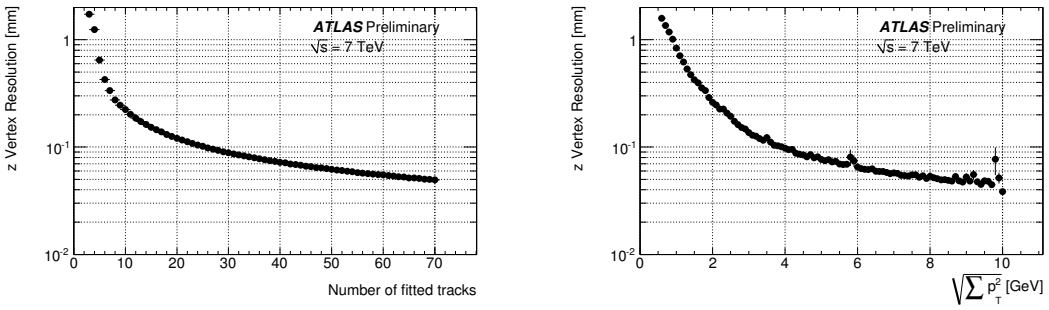

(a) (b)

Figure 3.5.: Estimated vertex resolution $\sigma_{z_{\mathrm{PV,true}}}$ in 7 TeV data as a function of the number of tracks N_{trk} (a) and as function of the value of $\sqrt{\sum_{\mathrm{trk}} p_{\mathrm{T}}^2}$ (b) [89].

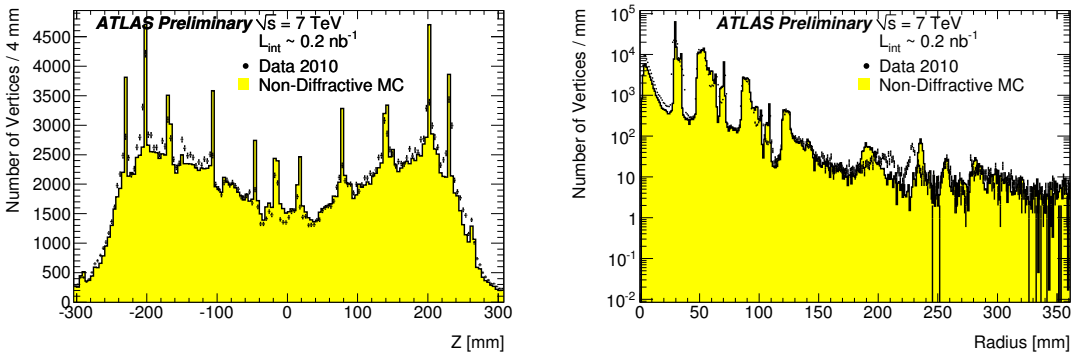

(a) (b)

Figure 3.6.: Z position (a) and Radius (b) for data (points) and MC (solid) after K^0_{S}, γ, and Λ vetoes. The Z plot is for radius at or outside the beam pipe, and the radius plot is for $|\mathrm{Z}| > 300\,\mathrm{mm}$ [99].

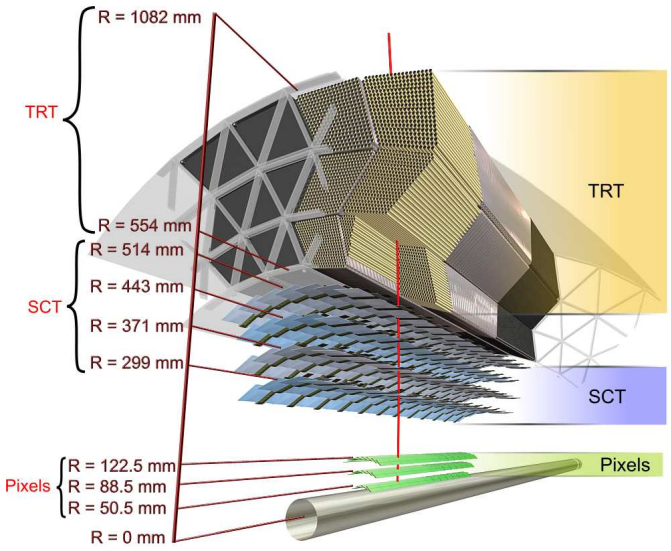

Figure 3.7.: Sensors and structural elements of the ATLAS ID [78].

Pixel Detector

The Pixel Detector is designed to provide a very high granularity and very high precision measurements as close to the interaction point as possible. It determines the impact parameter resolution and the ability of the ID to find short-lived particles such as B hadrons and τ-leptons. The Pixel Detector contains of 1744 identical pixel sensors, each 250 μm thick. About 90 % of the pixels have a size in R-ϕ of $50 \times 400\,\mu\text{m}^2$, the remaining pixels have a size of $50 \times 600\,\mu\text{m}^2$. On each sensor 47232 pixels are mounted leading to a total of 80.4 million readout channels for the Pixel Detector. The system consists of three barrels at average radii of about 4 cm, 10 cm, and, 13 cm and five disks on each side, between radii of 11 cm and 20 cm covering $|\eta| = 1.7 - 2.5$.

Semiconductor tracker

The semiconductor tracker (SCT) is designed to provide eight precision measurements per track in the intermediate radial range. These measurements contribute to the measurement of momentum, impact parameter and vertex position, as well as providing good pattern recognition by the use of high granularity. The SCT contains 61 m^2 of silicon detectors, with a total of 6.3 million readout channels. Each track crosses in average eight strip layers (four space points). In the barrel region, small-angle (40 mrad) stereo strips are used to measure both coordinates, where one set of strips in each layer is parallel to the beam direction to measure R-ϕ. In the end-cap region the detector uses a set of strips running radially and a set of stereo strips at an angle of 40 mrad. The spatial resolution of each channel is 17 μm in R-ϕ and 580 μm in z direction.

Transition radiation tracker

To operate at the very high rate expected at the LHC (typically 36 hits per track) the transition radiation tracker (TRT) is based on the use of straw tubes, which can operate on the needed rate due to the small diameter of the straws. Electron identification capability is added by employing xenon gas to detect

transition-radiation photons created in a radiator between the straws. Each straw is 4 mm in diameter and equipped with a 30 μm diameter gold-plated W-Re wire, giving a fast response. The maximum length in the barrel is 144 cm. The barrel contains about 50000 straws parallel to the beam axis, the end-cap contains 320000 radial straws leading to a total number of electronic channels of about 351000. The TRT only provides information in R-ϕ with an intrinsic accuracy of 130 μm per straw. The TRT is operated with a non-flammable gas mixture of 70 % Xe, 27 % CO_2 and 3 % O_2 with 5 – 10 mbar over-pressure.

Table 3.3.: Intrinsic measurement accuracies and mechanical alignment for the Inner Detector subsystems [78].

Item	**Intrinsic accuracy (μm)**	**Alignment tolerance (μm)**		
		Radial (R)	**Axial (z)**	**Azimuth (R-ϕ)**
Pixel				
Layer-0	10 (R-ϕ) 115 (z)	10	20	7
Layer-1 and -2	10 (R-ϕ) 115 (z)	20	20	7
Disks	10 (R-ϕ) 115 (R)	20	100	7
SCT				
Barrel	17 (R-ϕ) 580 (z)	100	50	12
Disks	17 (R-ϕ) 580 (R)	50	200	12
TRT	130			30

3.2.3. Magnet system

The ATLAS magnet system consists of four large superconducting magnets:

- One solenoid which is aligned to the beam axis. This system provides a 2 T field for the Inner Detector.
- One barrel toroid and two end-caps toroids. In the central region this system provides a 0.5 T field and a 1 T field in the end-cap region for the muon detectors.

The total length of this system is 26 m and 22 m in diameter with a stored energy of 1.6 GJ. The magnetic field is provided over a volume of 12,000 m^3 in which the volume is defined as the region in which the field exceeds 50 mT. Figure 3.8 shows the spatial arrangement of the coil windings. More details about all magnet systems can be found in [90–93].

Central solenoid

The central solenoid is designed to provide a 2 T axial field with a nominal operation current of 7.730 kA. The material in front of the calorimeter is as thin as possible to achieve the desired calorimeter performance. This results to a contribution of ~ 0.66 radiation lengths in total. The central solenoid has an inner diameter of 2.46 m and an outer diameter of 2.56 m. Its axial length is 5.8 m. The flux of the field is returned by the steel of the hadronic calorimeter. The solenoid can be charged and discharged within 30 minutes and is operated at a temperature of 4.5 K.

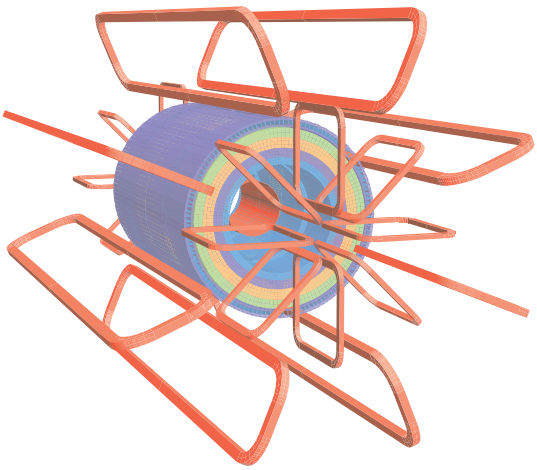

Figure 3.8.: Geometry of magnet windings and tile calorimeter steel. The solenoid winding lies inside the calorimeter volume [78].

Toroid

The barrel toroid consist of eight coils which are encased in stainless-steel vacuum vessels. It has an inner and outer diameter of 9.4 m and 20.1 m, respectively and a total length of 25.3 m. The two end-cap toroids consist each of a single cold mass built up from eight flat, square coil units and eight keystone wedges. Both, barrel and end-cap uses the same conductor and coil-winding technology where the winding is a pure Al-stabilized Nb/Ti/Cu conductor.

The toroid is operated at 4.5 K with a nominal magnet current of 20.5 kA. The total mass of the toroid barrel is 830 tonnes and 239 tonnes for each end-cap.

3.2.4. LAr and tile calorimeter

Calorimeters are used to measure the energy of final state particles. To cover the large spectrum of physics processes and requirements of the radiation environment in the large η-range of $|\eta| < 4.9$ the ATLAS calorimeters use different techniques. To provide precision measurements of electrons and photons the electromagnetic calorimeter (EM) has a fine granularity and matches to the Inner Detector over the η region. For jet reconstruction and $E_{\mathrm{T}}^{\mathrm{miss}}$ measurements a coarser granularity is sufficient.

The total thickness of the EM calorimeter is > 22 radiation lengths (X_0) in the barrel and $> 24\,\mathrm{X}_0$ in the end-caps. To provide good resolution for high energy jets the interaction lengths (λ) of the active calorimeter is $9.7\,\lambda$ in the barrel and $10\,\lambda$ in the end-caps. Including the $1.3\,\lambda$ from the outer support the total thickness is $11\,\lambda$ at $|\eta| = 0$ and is sufficient to reduce punch-through into the muon system. A cut-away view of the ATLAS calorimeter is shown in Fig. 3.9.

Electromagnetic calorimeter

The EM calorimeter uses the LAr technique and consists of three parts, the barrel ($|\eta| < 1.475$) and two end-caps ($1.375 < |\eta| < 2.5$), each housed in their own cryostat. In order to archive the demanded performance of the calorimeter the LAr calorimeter and central solenoid share a common vacuum vessel. The barrel consists of two identical half-barrels which are separated by a small gap of 4 mm at $z = 0$. Each

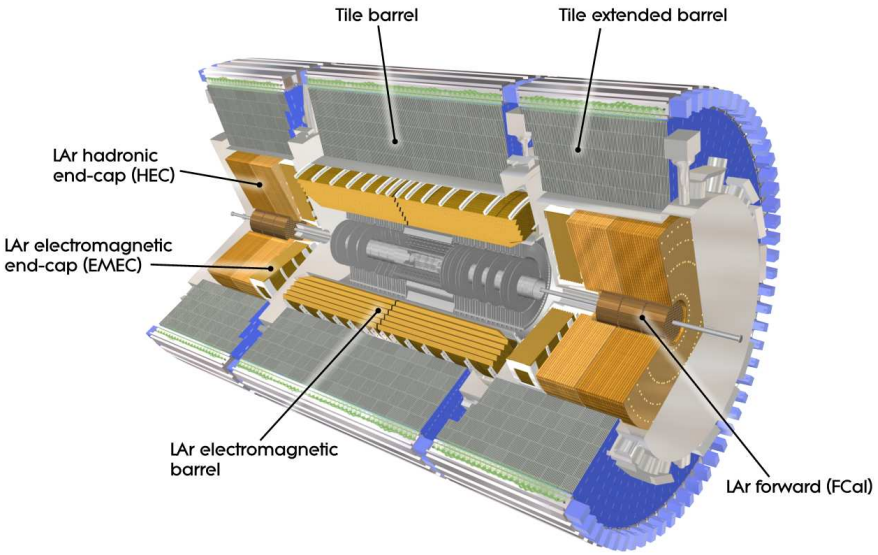

Figure 3.9.: Cut-away view of the ATLAS calorimeter [78].

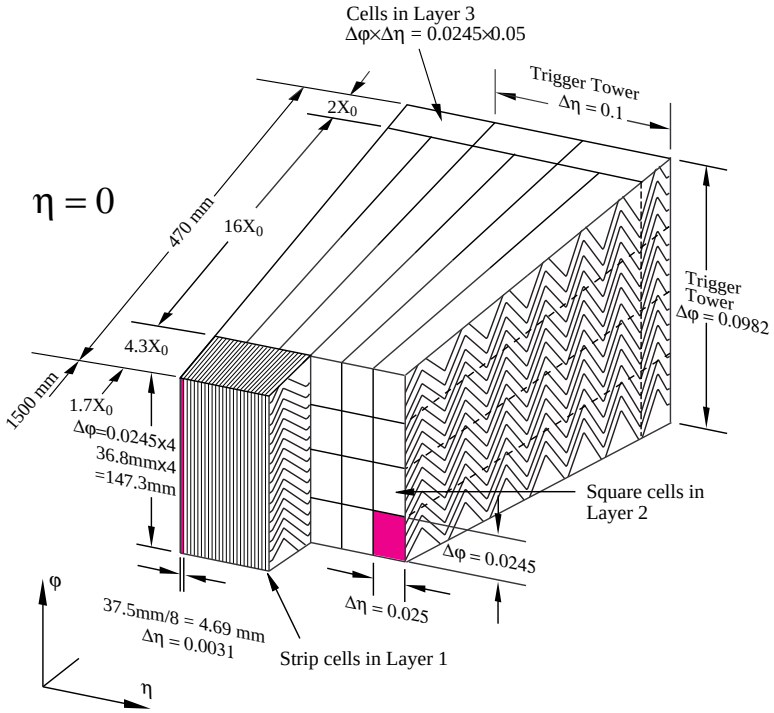

Figure 3.10.: Sketch of a barrel module of the LAr EM calorimeter [78].

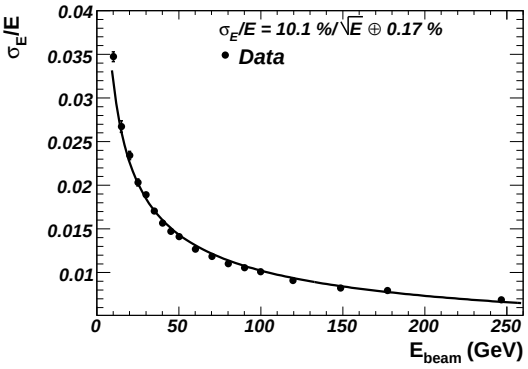

Figure 3.11.: Fractional energy resolution as a function of the electron beam energy, E_{beam} at $|\eta| = 0.687$ [78].

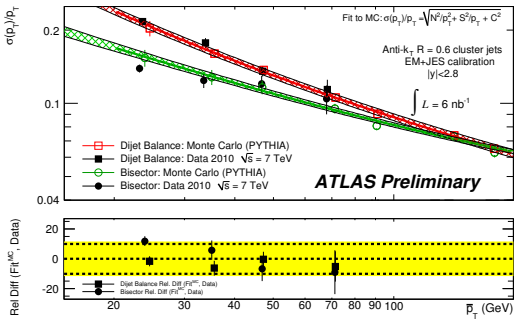

Figure 3.12.: Jet energy resolution for the dijet balance and bi-sector techniques as a function of the average jet transverse momenta. The lower plot shows the relative difference between the Monte Carlo fit and the data results. The yellow band indicates a relative uncertainty of $\pm 10\,\%$. [85].

end-cap has an outer wheel from $1.375 < |\eta| < 2.5$ and an inner wheel from $2.5 < |\eta| < 3.2$. Over its full coverage the LAr calorimeter has accordion-shaped kapton electrons and lead absorber plates as shown in Fig. 3.10. This accordion like geometry provides complete ϕ symmetry without azimuthal cracks while the lead thickness in the absorber plates has been optimized as a function of η in terms of performance in energy resolution. To provide precision measurements the EM calorimeter is segmented in three sections in depth in the region of $|\eta| < 2.5$. The end-caps are segmented only in two sections.

To correct the energy lost by electrons and photons upstream of the calorimeter in the region of $|\eta| < 1.8$, a presampler detector of active LAr layer is used. It is 1.1 cm thick in the barrel and 0.5 cm thick in the end-cap region. A complete overview of the main parameters of the EM calorimeter is given in Tab. 3.4 and Tab. 3.5.

To test the performance of the electromagnetic calorimeter several modules of barrel and end-cap have been exposed to test-beams using electron and positron beams of energy between 1 and 250 GeV. For the electron reconstruction all cells within a square of 3×3 cells around the cell with the highest energy of the middle according layer are clustered together. For all other layers all cells intersecting the projection of this square are included. The energy of the electron is given by

$$E = \text{offset} + w_0 \times E_0 + w_{01} \times \sqrt{E_0 E_1} + \lambda\,(E_1 + E_2 + E_3) + w_3 \times E_3, \tag{3.12}$$

where the offset and w_0 correct for the energy lost upstream of and in the presampler, w_{01} corrects for the energy deposition in dead material, λ corrects for the energy dependence of the sampling fraction and for lateral leakage outside the electron cluster, and w_3 corrects for the energy deposition downstream of the calorimeter. E_0 is the energy in the presampler and E_1, E_2 and E_3 are the energy in the strip, middle and back layers.

The response and the energy resolution for the barrel have been also studied. After noise subtraction the experimental measurements have been fitted with the equation

$$\frac{\sigma\,(E)}{E} = \frac{a}{\sqrt{E\,(\mathrm{GeV})}} \oplus b, \tag{3.13}$$

with a as the stochastic term and b the constant term reflecting local non-uniformities in the response of the calorimeter. From the fit in Fig. 3.11 a stochastic term of $10\,\% \cdot \sqrt{\mathrm{GeV}}$ and a constant term of $0.17\,\%$ can be obtained. With first data the jet energy resolution was measured with two different methods: the dijet balance and the bi-sector techniques. The result of these measurements is shown in Fig. 3.12. More details on both techniques can be found in [85].

Table 3.4.: Main parameters of the EM calorimeter [78].

	Barrel		**end-cap**	
EM calorimeter				
Number of layers and $\|\eta\|$ coverage				
Presampler	1	$\|\eta\| < 1.52$	1	$1.5 < \|\eta\| < 1.8$
Calorimeter	3	$\|\eta\| < 1.35$	2	$1.5 < \|\eta\| < 1.5$
	2	$1.35 < \|\eta\| < 1.475$	3	$2.5 < \|\eta\| < 3.2$
			2	$2.5 < \|\eta\| < 3.2$
Granularity $\Delta\eta \times \Delta\phi$ versus $\|\eta\|$				
Presampler	0.025×0.1	$\|\eta\| < 1.52$	0.025×0.1	$1.5 < \|\eta\| < 1.8$
Calorimeter 1st layer	$0.025/8 \times 0.1$	$\|\eta\| < 1.40$	0.050×0.1	$1.375 < \|\eta\| < 1.425$
	0.025×0.025	$1.40 < \|\eta\| < 1.475$	0.025×0.1	$1.425 < \|\eta\| < 1.5$
			$0.025/8 \times 0.1$	$1.5 < \|\eta\| < 1.8$
			$0.025/6 \times 0.1$	$1.8 < \|\eta\| < 2.0$
			$0.025/4 \times 0.1$	$2.0 < \|\eta\| < 2.4$
			0.025×0.1	$2.4 < \|\eta\| < 2.5$
			0.1×0.1	$2.5 < \|\eta\| < 3.2$
Calorimeter 2nd layer	0.025×0.025	$\|\eta\| < 1.40$	0.050×0.025	$1.375 < \|\eta\| < 1.425$
	0.075×0.025	$1.40 < \|\eta\| < 1.475$	0.050×0.025	$1.425 < \|\eta\| < 2.5$
			0.1×0.1	$2.5 < \|\eta\| < 3.2$
Calorimeter 3rd layer	0.050×0.025	$\|\eta\| < 1.35$	0.050×0.025	$1.5 < \|\eta\| < 2.5$
Number of readout channels				
Presampler	7808		1526 (both sides)	
Calorimeter	101760		62208 (both sides)	

Hadronic calorimeter

The hadronic calorimeter uses two techniques, a tile calorimeter for the barrel and the LAr technique for the hadronic end-cap and the forward calorimeter.

The tile calorimeter is placed directly outside the EM calorimeter envelope. The barrel covers the region $|\eta| < 1.0$, and two extended barrels the range from $0.8 < |\eta| < 1.7$. The tile calorimeter is a sampling calorimeter using steel as absorber and scintillating tiles as active material. Both, barrel and extended barrel, are divided azimuthally in 64 modules. The calorimeter has an inner radius of 2.28 m and an outer radius of 4.25 m. It has three layers with interaction lengths of 1.5, 4.1, and 1.8 for the barrel and 1.5, 2.6, and 3.3 for the extended barrel. At $\eta = 0$ the total thickness is 9.7 λ. The scintillating tiles are read out by wave-length shifters into two separated photomultipliers on two sides of each tile. The segmentation of the barrel and extended barrel is shown in Fig. 3.13.

Table 3.5.: Main parameters of the LAr hadronic end-cap and tile calorimeter [78].

LAr hadronic end-cap		
$\|\eta\|$ coverage		$1.5 < \|\eta\| < 3.2$
Number of layers		4
Granularity $\Delta\eta \times \Delta\phi$		0.1×0.1 $\quad 1.5 < \|\eta\| < 2.5$
		0.2×0.2 $\quad 2.5 < \|\eta\| < 3.2$
Readout channels		5632 (both sides)
Scintillator tile calorimeter		
	Barrel	Extended barrel
$\|\eta\|$ coverage	$\|\eta\| < 1.0$	$0.8 < \|\eta\| < 1.7$
Number of layers	3	3
Granularity $\Delta\eta \times \Delta\phi$	0.1×0.1	0.1×0.1
Last layer	0.2×0.1	0.2×0.1
Readout channels	5760	4092 (both sides)

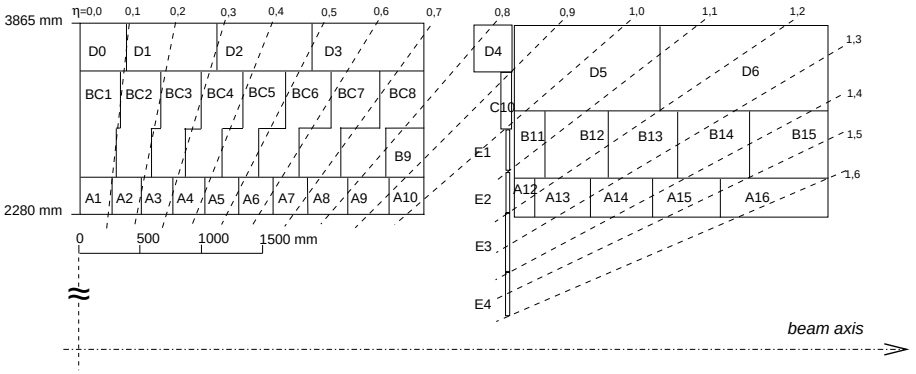

Figure 3.13.: Segmentation in depth and η of the tile-calorimeter in the central (left) and extended (right) barrel. [78].

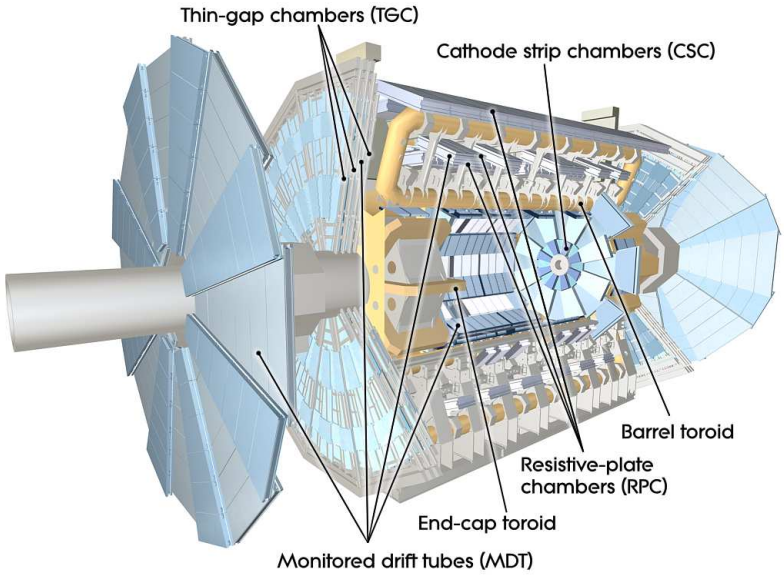

Figure 3.14.: Cut-away view of the ATLAS muon system [78].

The LAr hadronic end-cap calorimeter (HEC) consists of two independent wheels per end-cap. The HEC is located directly behind the end-cap electromagnetic calorimeter and shares the same LAr cryostat. The HEC ranges out to $|\eta| = 3.2$ to reduce the drop in material density at the transition between the end-cap and the forward calorimeter at around $|\eta| = 3.1$. The HEC also overlaps slightly with the barrel by ranging up to $|\eta| = 1.5$. Each wheel is built from 32 identical wedge-shaped modules and is divided into two segments in depth, for a total of four layers per end-cap. The HEC consists of copper plates, interleaved with LAr gaps, providing the active medium for this sampling calorimeter.

The forward calorimeter (FCal) is integrated into the end-cap cryostats to reduce the radiation background level in the muon spectrometer. To reduce the neutron albedo in the Inner Detector cavity, the front face of the FCal is recessed by about 1.2 m with respect to the EM calorimeter front face. The FCal is 10 interaction lengths deep, and consists of three modules in each end-cap. The first module is made of copper and is optimized of electromagnetic measurements. The two other modules are made of tungsten and measure the energy of hadronic interactions.

3.2.5. Muon detector

The muon spectrometer is based on the magnetic deflection of muon tracks in the superconducting air-core toroid magnets. It is instrumented with separated trigger and high-precision tracking chambers. The large barrel toroids provide the magnetic bending over the range $|\eta| < 1.4$ while the two smaller end-cap magnets provide the bending for $1.6 < |\eta| < 2.7$. For the transition region of $1.4 < |\eta| < 1.6$ magnetic deflection is provided by a combination of barrel and end-cap fields. This field is mostly orthogonal to the muon trajectories, while multiple scattering minimizes the degradation of resolution.

Tracks are measured in three layers of chambers. For the barrel region these chambers are arranged in cylindrical layers around the beam axis, while in the transition and end-cap region the chambers are installed in planes perpendicular to the beam.

An overview of the muon system is shown in Fig. 3.14.

Muon chamber types

Over most of the η-range monitored drift tubes (MDT) provide the precision measurement of the track coordinates. At large pseudo-rapidities from $2 < |\eta| < 2.7$, cathode strip chambers (CSC) with higher granularity are used. These CSC's can withstand the demanding rate and background conditions. To fulfill the stringent requirements on the relative alignment of the muon chamber layers a combination of precision mechanical-assembly techniques and optical alignment systems, both within and between muon chambers, are used.

For the trigger system resistive plate chambers (RPC) are use for the barrel and thin gap chambers (TGC) for the end-cap region. It covers the pseudo-rapidity range $|\eta| < 2.4$. The trigger chambers of the muon system have several functions: provide bunch-crossing identification, provide well-defined p_{T} thresholds, and measure the muon coordinates in the direction orthogonal to that determined by the precision-tracking chambers.

Muon chamber alignment and B-field reconstruction

The alignment of the muon chambers with respect to each other and with respect to the overall detector is responsible for the performance, particularly at the highest momenta.

A precision of 30 μm on the relative alignment of chambers both within each projective tower and between consecutive layers in immediately towers is required for a accurate stand-alone measurement of the muon momentum. Approximately 12000 precision-mounted alignment sensors monitor the internal deformations and relative positions of the MDT chambers.

To obtain adequate mass resolution in multi-muon final states an accuracy for the relative positioning of non-adjacent towers of a few millimeter is required. The relative alignment of the barrel and forward regions of the muon spectrometer, of the calorimeters, and of the Inner Detector rely on high-momentum muon trajectories.

The goal is to determine the bending power along the muon trajectories to a few parts in a thousand. To archive this the field is continuously monitored by a total of 1800 Hall sensors which are distributed throughout the spectrometer volume. Their readings are compared with magnetic-field simulations and used for reconstructing the position of the toroid coils in space, as well as to account for magnetic perturbations induced by the tile calorimeter and other nearby metallic structures.

3.2.6. Trigger and Data Acquisition

The Trigger and Data Acquisition (TDAQ) systems are separated into subsystems, typically associated with sub-detectors. The trigger system has three components: Level 1 (L1), Level 2 (L2) and the Event Filter (EF). The latter two are combined to the HLT.

The Data Acquisition system receives and buffers the event data from the detector readout electronics almost 1600 point-to-point Readout Links (ROL). The flow of the Trigger and Data Acquisition system is shown in Fig. 3.15.

The L1 Trigger

The L1 trigger [94] searches for high transverse-momentum muons, electrons, photons, jets, τ-leptons decaying into hadrons, and large missing and total transverse energy. Hence the L1 Trigger is partitioned into the calorimeter trigger and muon trigger and its selection is based on information of these two sub-detectors. The L1 Trigger uses a limited amount of the total detector information to make a decision in

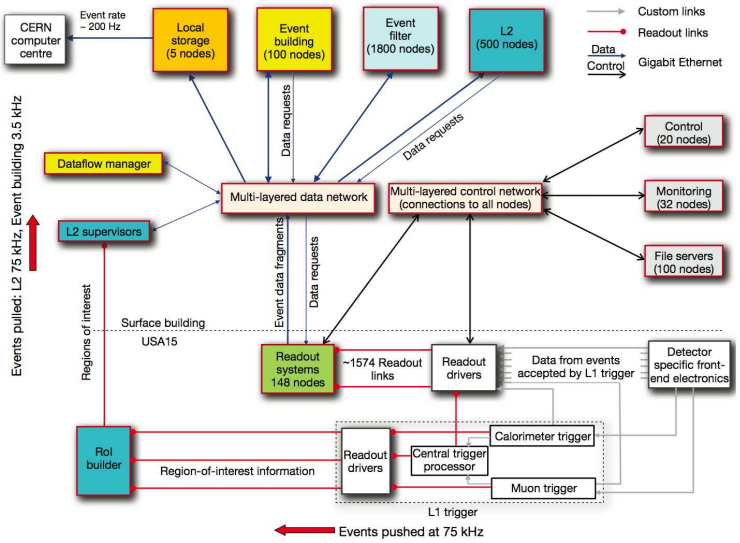

Figure 3.15.: Block diagram of the ATLAS Trigger and Data Acquisition system [78].

less than 2.5 μs reducing the incoming rate of 40 MHz to about 75 kHz. The flow of the L1 Trigger is shown in Fig. 3.16.

The L1 calorimeter trigger (L1Calo) is a pipelined digital system and searches for high-E_{T} objects like electrons and photons, jets, and hadronically decaying τ-leptons, as well as events with large $E_{\mathrm{T}}^{\mathrm{miss}}$ and large total transverse energy. To reduce the detector information a reduced granularity from the electromagnetic and hadronic calorimeter is used with about 7000 analogue trigger towers. In most parts of the detector the granularity is 0.1×0.1 in $\Delta\eta \times \Delta\phi$, but larger at higher $|\eta|$. For each LHC bunch-crossing the L1Calo triggers sends its results to the Central Trigger Processor (CTP) 1.5 μs after the event occurs.

The L1Calo trigger is located in the service cavern USA15 next to the detector cavern. The system consists of three main subsystems. The pre-processor digitizes the analogue input signals and associates them with specific bunch-crossings. Afterwards the data are transmitted to both the Cluster Processor (CP) and Jet/Energy-sum Processor (JEP). The CP identifies electron/photon and τ-lepton candidates with E_{T} above a programmable threshold and satisfying, if required, certain isolation criteria. The JEP identifies jets and produces global sums of scalar and missing transverse energy. The sum of the multiplicity of the different types of trigger objects are sent to the CTP for every bunch-crossing.

After a L1 Accept (L1A) decision from the CTP, all data from the L1Calo subsystems are read out to the Data Acquisition system to provide useful diagnostics for the LHC machine and ATLAS sub-detectors.

The L1 muon trigger based on the RPC's in the barrel and TGC's in the end-caps. These detectors have a sufficient timing accuracy to provide well-defined identification of the bunch-crossing for each muon candidate. For both, the barrel and the end-cap, the trigger is based on three trigger stations. The trigger algorithm requires coincident hits in the different trigger stations along the path of the muon from the interaction point through the detector. The width of the path is related to the p_{T} threshold

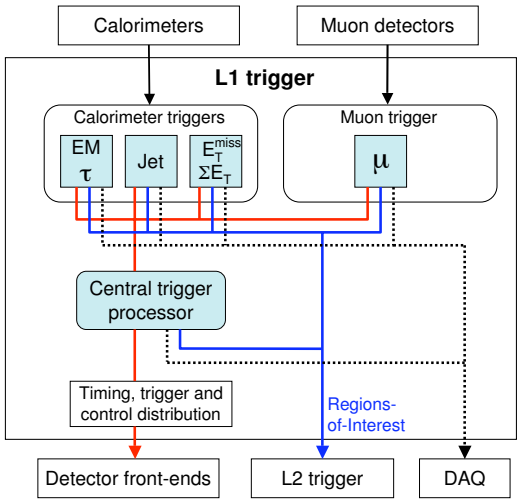

Figure 3.16.: Block diagram of the L1 trigger [78].

which is applied. Six thresholds are programmable, three associated with the low-p_{T} trigger, and three are associated with the high-p_{T} trigger. For each bunch-crossing signals from the trigger stations are combined into one set of the six threshold multiplicities and passed to the CTP.

The CTP collects information from the calorimeter trigger and the muon trigger. Using a look-up table the CTP forms trigger conditions from the input signal. If the conditions are fulfilled the CTP generates the L1A signal and sends information about the trigger decision to the L2 Trigger (Region of Interests (RoI) builder) and the Data Acquisition.

Data Acquisition system and High Level Trigger

The main components of the Data Acquisition system and High Level Trigger are readout, L2 Trigger, event-building, Event Filter, configuration, control and monitoring. During the L1 Trigger selection the event data are buffered into memories. The length of the memories defines the L1 Trigger latency of 2.5 μs. After a positive L1A the event data are transferred via 1574 Readout Links (ROL) to the DAQ/HLT. The event fragments are temporarily stored in the 1574 Readout Buffers (ROB) of the Readout System (ROS) and provided for following stages of the DAQ/HLT system.

The L2 Trigger uses information from the Region of Interests (RoI) provided by the L1 Trigger which contains $1-2\,\%$ of the full detector data. The main component of the trigger is the L2 processing farm where the event selection is executed. The results of the L2 Trigger analysis, accept or reject, is returned to the dataflow manager (DFM). Events which do not fulfill any of the L2 selection criteria are deleted from the ROS, those events which are accepted are assigned to an event-building note (SFI) by the DFM. Once the event was build the associated fragments are deleted from the ROB's. The High Level Trigger reduces the incoming rate of the L1 Trigger to about 200 Hz.

The Event Filter is a processing farm and selects events and classifies the selected events to a predetermined set of event streams. Unlike the L2 Trigger the event selection is based on standard ATLAS event reconstruction and analysis applications. If an events does not pass the event selection it will be deleted from the system. Events fulfilling the selection are being transferred to CERN's central data recording facility.

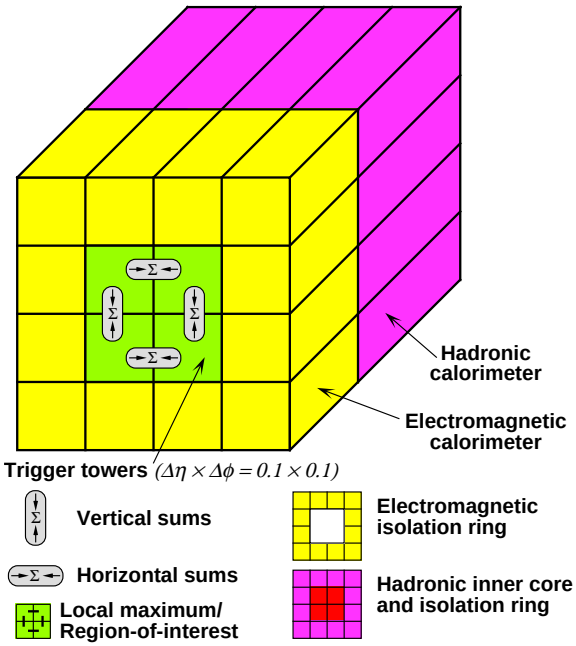

Figure 3.17.: Electron/photon and τ trigger algorithms [78].

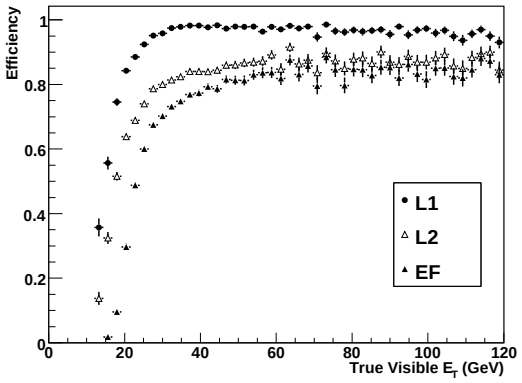

Figure 3.18.: Trigger efficiency at L1, L2 and EF for the τ20i menu item for Monte Carlo [78].

The τ trigger

For the reconstruction and identification of τ-leptons the τ trigger is mandatory. Figure 3.17 shows an example for the electron/photon and τ trigger. The τ trigger uses 2×2 clusters of trigger towers and a 12-tower surround ring as isolation veto to select narrow hadronic jets. This region of 4×4 towers build a Region of Interest and makes use of different elements. The algorithm uses the following quantities:

- The central 2×2 **core** cluster is the energy measured in the central 2×2 EM and hadronic towers.
- **TauCluster** is the energy defined by the two most energetic neighboring central towers in the EM calorimeter plus the central 2×2 hadronic towers.
- **EmIsol** is the energy in the isolation region of the 12-tower surrounding ring in the EM calorimeter.
- **HadIsol** is the energy in the isolation region of the 12-tower surrounding ring in the hadronic calorimeter.

The L1 τ trigger candidate is accepted if the core cluster is a local E_{T} maximum and additional conditions are satisfied by the **TauCluster**, **EmIsol** and **HadIsol**.

Figure 3.18 shows the efficiency for the τ20i trigger menu item. This item selects hadronic τ-decays with a true visible E_{T} larger than 20 GeV. The efficiency is shown for all three trigger levels. The drop of approximately 15 % after the L2 Trigger is mostly because of the τ-identification cuts applied. These cuts will be discussed in Chapter 6.

4. Data taking, Monte Carlo Event Generation and Detector Simulation

To understand the detector response of the ATLAS detector for the wide range of physics scenarios, predictions from Monte Carlo (MC) event generator and detailed detector simulations are used. The simulation program is integrated into the ATLAS software framework ATHENA [95], and uses a GEANT4 [96] simulation of the ATLAS detector. The output of this simulation is used to optimize the reconstruction and identification algorithms and its predictions are compared to data taken with the ATLAS detector.

In Section 4.1 the different data periods are discussed, starting with 900 GeV data taking in 2009, followed by the 2010 data taking period. As an example for a MC event generator the program HERWIG++ [97] is being discussed in Section 4.2.1, and the full detector simulation as well as an alternative fast simulation are being discussed in Section 4.2.2.

4.1. Data periods

In November 2009, the LHC single-beam commissioning started followed by the first circulating beam on November 20, 2009. Shortly after the single-beam commissioning, the ATLAS detector started recording data with a center-of-mass energy of $\sqrt{s} = 900$ GeV from November 23 to December 16. During this data taking period, the ATLAS detector recorded an integrated luminosity of $20\,\mathrm{mb}^{-1}$, from which $12\,\mathrm{mb}^{-1}$ were recorded during stable beams. The total number of collision candidates was 917,000 with 538,000 candidates recorded during stable beams. At the end of December 2009 ATLAS, also recorded 34,000 events with a center-of-mass energy of $\sqrt{s} = 2.36$ TeV.

From March 30 2010 until November 2010, the LHC was running with a center-of-mass energy of $\sqrt{s} = 7$ TeV. From that date the data are separated into different data periods according to the configuration of the detector and trigger objects. A full overview of the data periods is given in Tab. 4.1.

In ATLAS the luminosity is determined in real time approximately once per second using several detectors and algorithms [98]. The detectors are calibrated with the use of van-der-Meer beam separation method [100], where the two beams are scanned against each other in the horizontal and vertical planes to measure their overlap function. These results are displayed in the ATLAS control room and archived every two minutes. The accurate determination of the luminosity is essential for the measurement of Standard Model cross sections, which is a major goal of the ATLAS physics program for 2010. The instantaneous luminosity of proton-proton collisions can be calculated by

$$\mathcal{L} = \frac{\mu n_\mathrm{b} f_\mathrm{r}}{\sigma_\mathrm{inel}} = \frac{\mu^\mathrm{meas} n_\mathrm{b} f_\mathrm{r}}{\varepsilon \sigma_\mathrm{inel}} = \frac{\mu^\mathrm{meas} n_\mathrm{b} f_\mathrm{r}}{\sigma_\mathrm{vis}}, \tag{4.1}$$

where μ is the average number of interactions per bunch crossing (BC), n_b is the number of bunches colliding at the interaction point, f_r is the machine revolution frequency, σ_inel is the inelastic cross section, ε is the efficiency of the luminosity algorithm for a certain detector, $\mu^\mathrm{meas} = \varepsilon\mu$ is the average number of interactions per BC that pass the selection requirements of the algorithm, and σ_vis is the "visible" cross section, which is the detector calibration constant. In general this equation is only valid in case of linear

Table 4.1.: Different data periods corresponding to detector configuration and trigger objects.

Period	Subperiod	Run Range	Comment	Luminosity (nb^{-1})
A	n.a.	152166-153200	unsqueezed stable beam ($\beta^* = 10$ m)	0.4
B	B1–B2	153565-155160	first squeezed stable beams ($\beta^* = 2$ m)	9
C	C1	155228-155697	very similar to period B but higher luminosity due to more bunches in machine	9.5
	C2	156682	different configuration for L1Calo in η region near crack at $\eta = 1.45$	
D	D1-D6	158045-159224	pile-up not any more negligible: about 1.3 interactions per crossing	320
E	E1	160387-160479	new trigger menu, data now taken with Physics menu	144
	E2	160530		96
	E3	160613-160879		272
	E4	160899-160980	narrow timing gate for TGC was applied: 25 (25) ns for wire (strip) instead of the nominal 35 (45) ns	133
	E5	161118-161379	L1Calo trigger was reconfigured in the crack region	138
	E6	161407-161520		160
	E7	161562-161948		175
F	F1	162347-162577	26 colliding bunches in ATLAS	580
	F2	162620-162882		1400
G	G1	165591, 165632	bunch trains with 150 ns spacing from LHC	780
	G2	165703, 165732		1190
	G3	165767-165815		1300
	G4	165817-165818		300
	G5	165821-166143		1900
	G6	166198-166383	update to RPC timing	3600
H	H1	166466-166850	233 colliding bunches in ATLAS	6500
	H2	166856-166964	new RPC timing calibration	2800
I	I1	167575-167680	295 colliding bunches in ATLAS, only one BC contributes to L1 decision	14500
	I2	167776-167844		8500

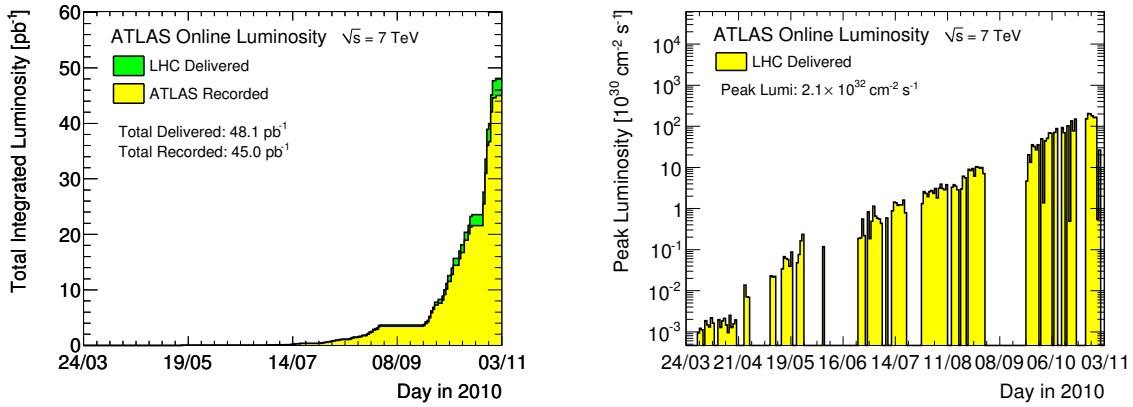

(a) (b)

Figure 4.1.: Cumulative luminosity versus day (a) delivered to (green), and recorded by ATLAS (yellow) for $\sqrt{s} = 7$ TeV and maximum instantaneous luminosity (b) versus day delivered to ATLAS recorded during stable beam periods [101].

response of the detector with respect to μ, otherwise corrections for the non linearity of the detector must be taken into account.

The luminosity delivered during the first run period 2010-2011 covers a wide range from 10^{26} cm^{-2}sec^{-1} for the first fills at $\sqrt{s} = 900$ GeV in 2009, through the highest peak luminosity obtained by the end of the 2010 proton-proton run[1] of 2.1×10^{32} cm^{-2}sec^{-1} at $\sqrt{s} = 7$ TeV. To measure this wide range of luminosity is a challenge.

The luminosity information are stored for later use in so-called *Luminosity Blocks* (LB). Each LB is approximately 2 minutes long, start and end time are set by the ATLAS DAQ system. All ATLAS data quality information and luminosity are stored in a relational database for each LB. According to these information data samples with requirements specific to the physics analysis (e.g. pixel detector ON) can be selected and the luminosity for this selection can be calculated. Since a LB is updated whenever a trigger prescale is changed, the luminosity can be corrected according to dead-time and prescale rates.

The total integrated luminosity is shown in Fig. 4.1a and the peak luminosity per day in Fig. 4.1b, both obtained at the end of the physics run 2010.

4.2. Simulation framework

The simulation chain is divided into three steps: generation of the event and immediate decays, simulation of the detector and physics interactions, and digitization [102]. The ATLAS simulation infrastructure is part of the ATLAS software framework ATHENA [95] and contains several MC event generators, a GEANT4 detector simulation, databases containing information describing the physical construction and conditions data to build the ATLAS detector geometry, and software for the digitization and reconstruction.

The flow of the ATLAS simulation software is shown in Fig. 4.2. Events are produced in standard HepMC format [103] by a generator and can be filtered at generation time according to certain properties

[1] November 3, 2010

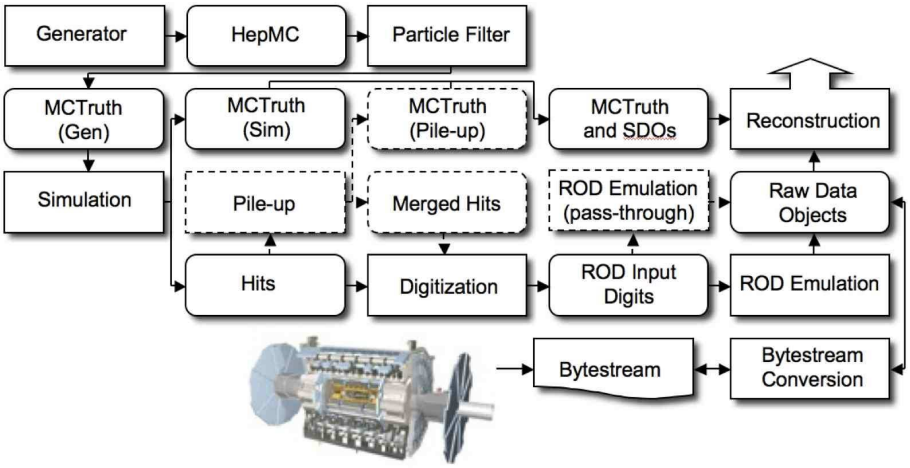

Figure 4.2.: The flow of the ATLAS simulation software, from event generators (top left) through reconstruction (top right). Algorithms are placed in square-cornered boxes and persistent data objects are placed in rounded boxes. The optional pile-up portion of the chain, used only when events are overlaid, is dashed [102].

(e.g. leptonic decay). Only particles which are "stable" and expected to propagate through a part of the detector are stored in the output datasets. A detailed description of Monte Carlo event generators is given in Section 4.2.1.

The generated events are then read into the detector simulation. Each particle is propagated through the full GEANT4 ATLAS detector simulation. Because of the complicated detector geometry and the detailed physics description, the full simulation needs several minutes per event. To achieve the required statistics faster simulations are needed. DELPHES is an open-source fast simulation [104] which can simulate different detector geometries. Both, the full GEANT4 ATLAS detector simulation and the DELPHES framework are described in Section 4.2.2.

In both event generator and detector simulation so-called "truth" information are recorded for each event. For the simulation, information like truth tracks, location of photon conversions within the inner detector or mother of each particle are kept. These truth information are further processed in the reconstruction and be used later during the analysis.

The digitization finally generates the response of the detector. It takes hit output from simulated events: hard scattering signal, minimum bias, beam halo, beam gas, and cavern background. The overlay of events (pile-up) is done during this phase and the first level trigger is simulated in a "pass" mode, i.e. no events are discard but each trigger hypothesis is evaluated and stored. The output is a Raw Data Object (RDO) which is than passed to the reconstruction software.

Due to the significant time consumption large scale production of ATLAS events cannot be completed interactively on most computers. Instead the World-wide LHC Computing Grid (WLCG or Grid) [105] is used. A single task on the Grid (e.g. simulation of 500,000 $Z \rightarrow \tau\tau$ events) is split into many jobs depending on the content and complexity of the task. The output of each jobs is registered with the ATLAS Distribution Data Management system (DDM) and DQ2 [106] is used for bookkeeping, searches for datasets on the Grid, analyze them in place, and retrieve them by the user.

4.2.1. Monte Carlo event generator

Event generation consist of the production of a set of particles which is passed to the detector simulation. Although event generation runs within the ATHENA framework most of the generators are written and maintained by external authors. Most of the well-understood generators are written in FORTRAN, hence an interface to the ATLAS software is used to transfer the FORTRAN code into an object format which can be used by the software.

Plenty of event generators are available. For the large-scale production seven generators have been used: PYTHIA [55, 56] (including an ATLAS variant, PYTHIAB [107] for the production of events with B-hadrons), HERWIG [108, 109],SHERPA [110], HIJING [111], ALPGEN [112], MC@NLO [113], and ACERMC [114]. These generators are general purpose generators which produce complete events starting from a proton-proton, proton-nucleus or nucleus-nucleus initial state and can be used standalone. There are also specialized generators used, which do not produce complete events but have to be run in combination with one of the general purpose generators. To handle τ-lepton decays and photon emission TAUOLA [115] and PHOTOS [116] are being used. EVTGEN [117] is used for B-decays, while ISAJET [118] generates supersymmetric particles in conjunction with HERWIG. Some production was also done with MADGRAPH [119] for vector boson scattering, CHARYBDIS [120] for black hole event generation, and COMPHEP [121], which is used for specific exotic physics models. The newer C++ generators PYTHIA 8 [122] and HERWIG++ [97] are also being tested. Since both produce events in the HepMC format no translation is needed and the events can be passed directly to the simulation.

Not all event generators perform hadronization. While PYTHIA and HERWIG come with their own hadronization models, SHERPA and HIJING have an interface to use the hadronization of PYTHIA, ALPGEN uses either the PYTHIA or the HERWIG hadronization, and MC@NLO has an interface to the HERWIG hadronization model.

Herwig++

HERWIG++ [97] is a general purpose generator for the simulation of high-energy lepton-lepton, lepton-hadron, and hadron-hadron collisions with emphasis on the accurate simulation of QCD radiation and the following special features:

- Initial- and final-state QCD jet evolution taking account of soft gluon interference via angular ordering
- Suppression of QCD radiation from massive particles
- The simulation of BSM physics including correlations between the production and decay of the BSM particles
- Describing the underlying event [123] via an eikonal model for multiple partonic scattering [124]
- A cluster model of the hadronization of jets based on non-perturbative gluon splitting
- A sophisticated model of hadron and tau decays using matrix elements to give the momenta of the decay products for many models and including a detailed treatment of off-shell effects and spin correlations

A generic hard, high-momentum transfer, process as it is simulated by HERWIG++ can be divided into a number of stages corresponding to increasing time and distance scale:

1. *Elementary hard subprocess.* In the hard process the incoming particles interact to produce the primary outgoing fundamental particles. In hadron-hadron-initiated process this interaction involves partons.

2. *Initial- and final-state parton showers.* In the event the colored particles are perturbatively evolved from the hard scale of the collision to the infrared cutoff. This occurs for both the initial partons involved in the collision for processes with incoming hardrons, the *initial-state shower*, and the particles produced in the collision, the *final-state shower*.

3. *Decay of heavy objects.* Massive fundamental particles such as the top quark, electroweak gauge bosons, Higgs bosons, and particles in many models of physics BSM, decay on time-scales that are shorter or comparable to that of the QCD parton shower. These particles may also initiate parton showers before and after their decay.

4. *Multiple scattering.* For high center-of-mass energies, multiple scattering is the dominant component of the underlying event that accompanies the main hard scattering. For these energies the probability of multiple scattering in the same collision becomes significant and they take place in the perturbative regime, above the infrared cutoff, and therefore give rise to additional parton showers.

5. *Hadronization.* In the final state colored partons are typically close in momentum space to partons with which they share a color index, their "color" partner. HERWIG++ uses the cluster hadronization model [125] to project these color – anti-color pairs onto singlet states called clusters, which decay to hadrons and hadron resonances.

6. *Hadron decays.* The hadron decays are simulated using matrix elements descriptions of the distributions of the decay products, and if possible the spin correlation between the different decay. For long-lived particles, this step may be re-done.

HERWIG++ is based on the Toolkit for High Energy Physics Event Generation, THEPEG [126], a framework for implementing Monte Carlo event generators. While THEPEG provides the event generator infrastructure that does not depend on the physics model, the specific models of HERWIG++ are implemented on top of these.

In HERWIG++ the matrix elements for QCD and electroweak processes are implemented as a library. Compared to its FORTRAN predecessor [108, 109] it is relatively small. For e^+e^- colliders there are only four leading order matrix elements for hard processes included. For the simulation of events in hadron colliders there is a much wider range of matrix elements available. Two of these elements have been used to validate the alternative fast detector simulation DELPHES [104] (see Section 4.2.2):

- **MEqq2gZ2ff:** Difermion production via s-channel electroweak gauge bosons. The matrix element for the production of fermion – anti-fermion pairs, interfering photons and Z^0 bosons, is implemented in the *MEqq2gZ2ff* class. Only s-channel electroweak gauge boson diagrams are included for the hadronic models.

- **MEHeavyQuark:** The matrix element for the production of top – anti-top pairs is coded in the *MEHeavyQuark* class. No approximation are made regarding the masses of the outgoing $q\bar{q}$ pair.

A small number of next-to-leading (NLO) processes are also implemented in HERWIG++.

There are also a number of matrix element generators available which can transfer their information via the original Les Houches Accord [127] or the subsequent extension [128] to HERWIG++. One of this

matrix element generators is SPHENO [129] which is used to calculated the supersymmetric spectra used for the analysis described in Chapter 7.

All event generators use Parton distribution functions as external input to describe the substructure of the proton. A detailed description of PDFs is given in Section 2.2. ATLAS uses the Les Houches Accord PDF Interface (LHAPDF [130]) library and CTEQ [131] PDFs as default.

4.2.2. Detector Simulation

Full ATLAS Geant4 simulation

The standard detector simulation of ATLAS based on the GEANT4 particle simulation toolkit [96]. GEANT4 simulates the passage of particles through matter. It includes tracking, geometry, physics models and hits, but several ATLAS specific pieces are provided as user-code. To construct the detector geometry two databases are used: one to store basic constants (the ATLAS Geometry database), and one to store various conditions data (e.g. calibrations, dead channels, misalignment) for specific runs (ATLAS Conditions database) [132]. For the geometry ATLAS uses GEOMODEL [133], a library containing basic geometrical shapes, to describe and construct the detector. GEOMODEL uses features similar to those of GEANT4.

Typically the "standard" GEANT4 simulation runs from compiled C++, which makes it necessary to recompile in order to modify any of the parameters or the geometry. To provide flexibility the framework for the ATLAS Detector Simulation (FADS) [134] uses a PYTHON interface for configuration and wraps several GEANT4 classes to allow selection and configuration without recompilation.

The numerical models, which describe the particles interactions with matter is included in "physics lists". Generally they are good for a single type of interaction and over a limited energy range. Several physics lists are used by ATLAS:

- **QGSP_BERT** is the physics list used for all simulation production after 2008. It includes the Quark-Gluon String Percompound model (QGSP) and the Bertini intranuclear cascade model (BERT) [96] as part of the hadronic physics package. The electromagnetic physics package includes step-limiting Multiple Coulomb Scattering (MSC).

- **QGSP_EMV** is the physics list used before 2008. It includes the QGSP model, but without the Bertini cascade. Since the MSC of this list is not allowed to limit the step it is labeled as electromagnetic variant (EMV).

- **QGSP_BERT_HP** is the physics list used for neutron fluence studies. Additional to the first model it contains an additional "high-precision" low-energy neutron physics model.

- **FTFP_BERT** is not an official physics list but is used for the systematic studies described in Section 5.4. The FRITIOF Precompound (FTFP) model handles the formation of strings in the initial collision of a hadron with a nucleon in the nucleus. String fragmentation into hadrons is handled by the Lund fragmentation model.

The output of the detector simulation consists of metadata, describing the configuration of the simulation, truth information, and a collection of hits for each sub-detector. These hits are records of energy deposition with position and time. At the end each event has a size of about 2 MB (for hard scattering events such as $t\bar{t}$ production).

The hits are then converted into detector response of active material by the ATLAS digitization software. Typically hits are accepted when the signal (voltage or current) on a particular readout channel

exceeds a pre-configured threshold within a particular time-window. The digits of each sub-detector are then written out as Raw Data Objects (RDOs) which are used as input for the ATLAS reconstruction software. Typically RDO files have a size of about 2.5 MB (for hard scattering event such as $t\bar{t}$ production), but the size will increase with pile-up.

Monte Carlo tunes

In order to constrain the model predictions as much as possible new MC tunes are developed by studying most recent data and new theoretical developments. The first MC tune for ATLAS is addressed to the underlying event and minimum bias description [135].

The main physics generators in ATLAS, HERWIG and PYTHIA, use the MRST LO* parton distribution functions [136] for the large scale MC production started in autumn 2009 (called MC09). For the first performance study of hadronically decaying τ-lepton described in Section 5.4, a p_{T}-ordered shower model with the interleaved shower and multi-parton interaction (MPI) model is used.

Another parameter is the fragmentation model. Until MC09, the heavy quark fragmentation function is modeled according to the Peterson fragmentation function [137], while the light quarks are treated with a symmetric Lund function [138].

For the study in Section 5.4 with $\mathcal{L} = 244\,\mathrm{nb}^{-1}$, the PYTHIA DW tune is used. This tune is a Q^2-ordered tune with more multi-parton interactions and a wider shower than the p_{T}-ordered tune. Although the p_{T}-ordered evolution has an advantage when multiple interactions are considered (and transverse momentum can be used as a common ordering variable for multiple interactions and initial state radiation, thereby allowing "interleaved evolution") the Q^2-ordered DW tune showed better agreement with data. This is probably not due to arbitrary tuning and not to the fundamental Q^2-ordered setup, but a good Q^2-ordered tune is probably better than a worse p_{T}-ordered. In Section 5.4 the DW tune is compared with the PYTHIA PERUGIA2010 tune [139]. This tune is a variant of PERUGIA0 with the amount of final-state radiation outside resonance decays increased to agree with the level inside them and should improve the description of jet shapes. For the systematic studies two different models are used, PERUGIA0 [139] as underlying event tune and PROFESSOR [140] for a different fragmentation.

4.2.3. Delphes

DELPHES [104] is a C++-based framework for fast simulation of a generic collider experiments. It includes a tracking system, embedded into a magnetic field, calorimeters, muon systems, and possible forward detectors along the beam line. DELPHES is interfaced to standard file formats, such as Les Houches Event Files [127, 128] or the HepMC file format [103]. The output is a ROOT [141] file with two branches, one containing truth information, one with observables used for analyses, such as missing transverse energy and collections of electrons and jets.

The simulation of the detector response takes the resolution of the detector into account, and reconstruction algorithms such as FASTJET [58]. To visualize the collision final states the FROG 2D/3D event display [142] is used.

DELPHES takes the event generator output to simulate the detector response, including the resolution of the sub-detector, by smearing the kinematic properties of final-state particles[2]. DELPHES includes the most essential detector features, like:

- Geometry of general central and forward detector
- Magnetic field for tracks

[2]Final-state particles are particles considered as stable by the event generator

- Reconstruction of photons, leptons, jets, b-jets, τ-jets, and missing transverse energy
- Lepton isolation
- Trigger emulation
- Event display

The framework is controlled by input cards. The detector card defines detector parameters, such as calorimeter and tracking coverage and resolution and thresholds and jet algorithm parameters. The trigger card lists the user algorithm for the simplified online preselection.

Detector simulation

The detector simulated by DELPHES corresponds to a "standard" multi-purpose detector. A central tracking system is surrounded by a electromagnetic and a hadron calorimeter. Two forward calorimeters cover the large η region for the measurement of missing transverse energy. Finally, a muon system enclose the central detector volume. The effect of a solenoid magnet field on charged particles is also simulated and affects the position at which charged particles enter the calorimeters and their corresponding tracks.

DELPHES reconstructs tracks of stable charged particles with a transverse momentum above a threshold and within the detector volume covered by the inner detector. By default a 90 % probability to reconstruct a track is assumed if the transverse momentum is higher than 0.9 GeV/c and a pseudorapidity of $|\eta| \leq 2.5$.

The energy of each stable particle is smeared with a Gaussian distribution depending on the calorimeter resolution. The resolution varies with the calorimeters (ECal, HCal, FCal). The response of each calorimeter is parametrized as a function of the energy:

$$\frac{\sigma}{E} = \frac{S}{\sqrt{E}} \oplus \frac{N}{E} \oplus C, \tag{4.2}$$

where S, N, and C are the *stochastic*, *noise* and *constant* terms, respectively, and $\oplus$ is a quadratic addition. The four momentum of the particles is smeared by DELPHES with a parametrization directly derived from typical detector designs. By default the calorimeter is assumed to cover the pseudo-rapidity range of $|\eta| \leq 3$ and has a electromagnetic and a hadronic part. The pseudo-rapidity range of $3.0 \leq |\eta| \leq 5.0$ is covered by the forward calorimeter. Muons and neutrinos are assumed not to interact with the calorimeters. While electrons and photons are smeared only with the resolution of the electromagnetic calorimeter, charged and neutral final state hadrons interact with the ECal, HCal and FCal.

More details on simulation of inner detector and calorimeter, as well as calorimetric tower and very forward detectors simulation can be found in [104].

Object reconstruction

In addition to the truth information DELPHES stores reconstructed particles ($e^{\pm}$, $\mu^{\pm}$, γ) and objects (light jets, b-jets, τ-jets, $E_{\mathrm{T}}^{\mathrm{miss}}$) in its output file. In addition further information are stored: tracks, calorimeter towers and hits in the forward detectors.

For most of the reconstructed objects their four-momentum is available (E, $\vec{p}$, p_{T}, η and ϕ) and additional properties for specific objects, such as charge and isolation status for electrons and muons or b-tagging information for jets.

Electrons and photons DELPHES reconstructs electron and photon candidates when they lie within the acceptance of the tracking system and have a transverse momentum above a certain threshold (default $p_{\mathrm{T}} > 10\,\mathrm{GeV}$). Both, electrons and photons will fire a calorimeter tower and an electron will create a track. Afterwards they will create a candidate in the jet collection. While the energy and momentum of electrons and photons is smeared fair, no eta and phi smearing is applied. Furthermore all electrons within the detector acceptance and above the threshold are identified as electron candidates although each detector is afflicted with a reconstruction and identification inefficiency. The electron collection also does not contain pions as electron fakes. The eta and phi smearing, as well as an identification efficiency and fake pions are added later with a downstream reconstruction simulation.

Muons All generator-level muons entering the detector within the acceptance of the muon system are considered as muon candidates. The acceptance consist of the transverse momentum calculated from the geometry of the detector and the magnetic field configuration (default $p_{\mathrm{T}} > 10\,\mathrm{GeV}$) and a pseudo-rapidity coverage (default $|\eta| < 2.4$). The smearing of the muon momentum depends on a Gaussian of the p_{T} variables, while eta and phi are not changed. Furthermore no pions are added to fake a muon and the reconstruction and identification inefficiency is not taken into account. As for the electrons, the eta and phi resolution as well as fake pions and a muon identification method are simulated downstream with a reconstruction simulation.

Lepton isolation In DELPHES an electron or a muon are marked as isolated if no other charged particle with a $p_{\mathrm{T}} > 10\,\mathrm{GeV}$ is found within a cone of $\Delta R < 0.5$[3]. Additionally the sum p_{T} of all tracks within the isolation cone except the lepton is provided.

Jet reconstruction To realize the jet reconstruction the FASTJET tool [58] is implemented in DELPHES. This allows a correct treatment of particles that have hadronized. Six different jet algorithms are available. Three cone algorithms and three algorithms using a sequential recombination scheme. All algorithms use calorimeter towers as input for the jet clustering. By default, the reconstruction uses a cone algorithm with $\Delta R = 0.7$. Jets are stored if their transverse energy is higher than 20 GeV. The following cone algorithm are implemented:

1. *CDF Jet Clusters* [143] This algorithm uses all towers with a E_{T} higher than a certain threshold (default $E_{\mathrm{T}} > 1\,\mathrm{GeV}$) to seed the jet candidate. It forms jets by associating towers lying within a circle (default $\Delta R = 0.7$).

2. *CDF MidPoint* [144] This algorithm was developed for the CDF Run II. By adding energy barycenter (midpoints) in the list of cone seeds it reduces infrared and collinear sensitivity compared to purely seed-based cone .

3. *Seedless Infrared Safe Cone* [145] The so called SIS-Cone algorithm is a cone algorithm, which is simultaneously insensitive to additional soft particles and collinear splittings.

The sequential recombination jet algorithms are all safe with respect to soft radiations (infrared) and collinear splitting. A detailed description of a sequential recombination jet algorithm can be found in Section 2.2.1. The difference between the three algorithms is the definition of the distances d used during the merging process:

[3] $\Delta R = \sqrt{\Delta\eta^2 + \Delta\phi^2}$

1. *Longitudinally invariant k_t jet* [146]

$$d_{i,j} = min(k_{ti}^2, k_{tj}^2)\Delta R_{ij}^2/R^2 \qquad d_{iB} = k_{ti}^2 \tag{4.3}$$

2. *Cambridge/Aachen jet* [147]

$$d_{ij} = \Delta R_{ij}^2/R^2 \qquad d_{iB} = 1 \tag{4.4}$$

3. *anti-k_t jet* [148]

$$d_{ij} = min(1/k_{ti}^2, 1/k_{tj}^2)\Delta R_{ij}^2/R^2 \qquad d_{iB} = 1/k_{ti}^2 \tag{4.5}$$

b-tagging If a jet lies in the acceptance of the tracker and is associated to a parent b-quark it is tagged as a b-jet. By default DELPHES assumes a b-tagging efficiency of 40 % and a fake b-tagging rate of 10 % for c-jets and 1 % for light jets (from u, d, and s quarks or gluons), while the b-tagging efficiency of ATLAS is about 60 % [149].

τ identification The τ identification in DELPHES follows a standard identification method in a full detector simulation. A detailed description of the ATLAS τ reconstruction and identification can be found in Chapter 5. Since DELPHES ignores all hadronically decaying τ-leptons with more than one charged hadron, the DELPHES τ identification is regarded as not useful.

Missing transverse energy In DELPHES the missing transverse energy is based on the calorimeter towers and is calculated with

$$\vec{E}_{\mathrm{T}}^{\mathrm{miss}} = -\sum_{i}^{\mathrm{towers}} \vec{E}_{\mathrm{T}}(i), \tag{4.6}$$

but muons are not taken into account for this evaluation, i.e. they need to be included during the analysis.

DELPHES validation and reconstruction and identification simulation

Every new generator or simulation needs to be validated before it can be used for analyses. DELPHES performs a fast simulation of a generic detector. Hence it is validated against ATLAS results to use DELPHES later for analyses concerning SUSY precision studies with the ATLAS experiment (see Chapter 7).

For the validation two samples, each with 500000 events, are generated with HERWIG++2.4.2 using the matrix elements *MEqq2gZ2ff* ($qq \rightarrow Z/\gamma \rightarrow f\bar{f}$) and *MEHeavyQuark* for $t\bar{t}$ production. Those events are passed trough the DELPHES detector simulation using the ATLAS detector and trigger card. The quality and validity of the output are evaluated by comparing the resolution of reconstructed data to predictions of the ATLAS detector simulation.

Reconstruction and identification simulation In the Section before the reconstruction of objects has been discussed. Electrons are reconstructed when they lie within the acceptance of the inner detector and above a p_{T} threshold. The same applies for muons when they lie in the acceptance of the muon system and above a p_{T} threshold. This corresponds to an identification efficiency of 100 % where the electrons or muons are not contamined with fakes, e.g. from pions. Therefore the simulation of fakes from pions and of identification algorithms for electrons and muons is added. For the electron identification the cut-based method with three reference cuts (loose, medium, tight) [150] is emulated. The cuts are applied in 6 p_{T} bins ranging from 0 – 10 GeV, 10 – 20 GeV, 20 – 30 GeV, 30 – 40 GeV, 40 – 50 GeV,

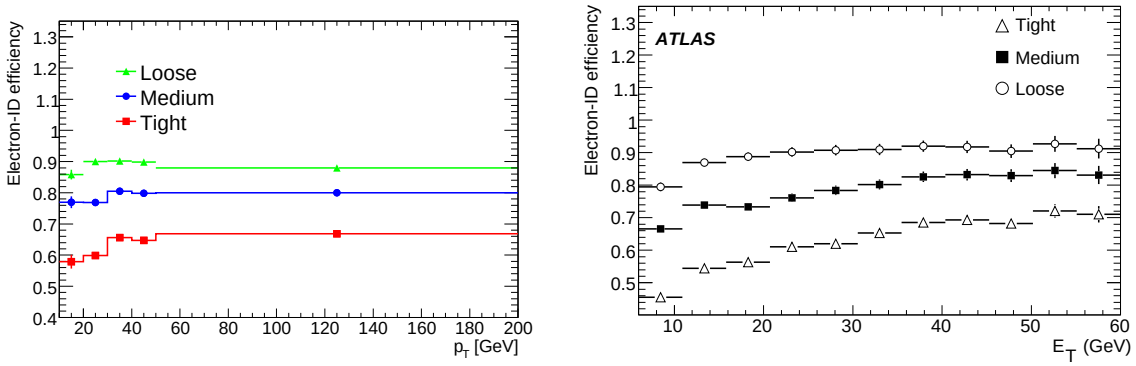

(a) (b)

Figure 4.3.: Electron efficiency for loose (green triangles), medium (blue circles), and tight (red squares) selection as function of p_{T} for p_{T} bins of $10-20\,\mathrm{GeV}$, $20-30\,\mathrm{GeV}$, $30-40\,\mathrm{GeV}$, $40-50\,\mathrm{GeV}$, and $>50\,\mathrm{GeV}$ with the DELPHES reconstruction and identification simulation (a) and electron identification efficiency as a function of E_{T} for electrons with $E_{\mathrm{T}}>5\,\mathrm{GeV}$ from the full detector simulation and reconstruction with $H\rightarrow eeee$ (b) decays taken from [150].

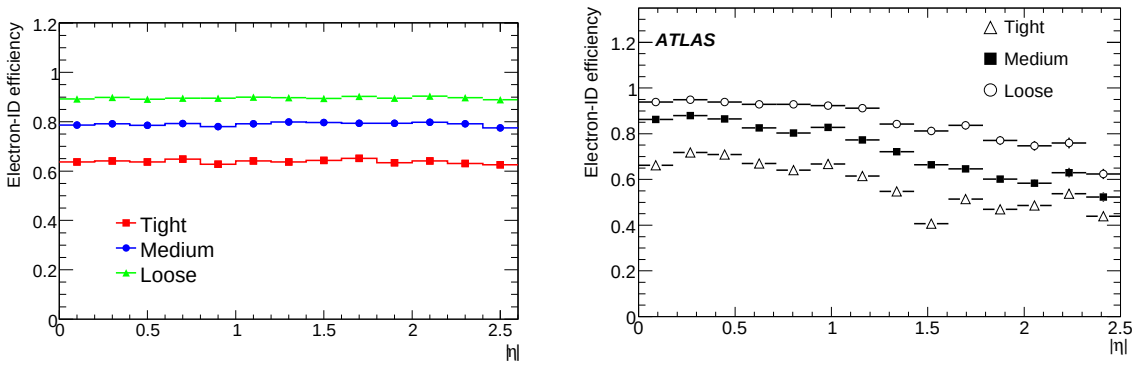

(a) (b)

Figure 4.4.: Electron efficiency for loose (green triangles), medium (blue circles), and tight (red squares) selection as function of η with the DELPHES reconstruction and identification simulation (left) and electron identification efficiency as a function of η for electrons with $E_{\mathrm{T}}>5\,\mathrm{GeV}$ from $H\rightarrow eeee$ decays taken from [150].

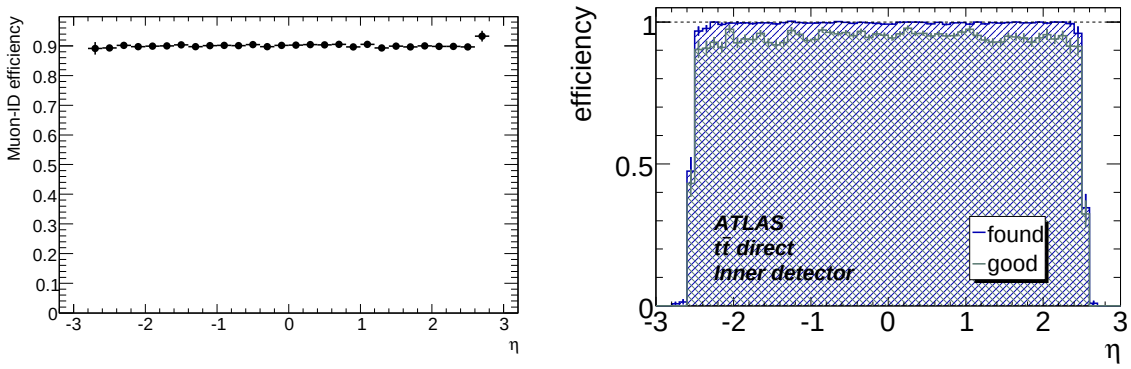

(a) (b)

Figure 4.5.: Muon identification efficiency as function of η with the DELPHES reconstruction and identification simulation (left) and inner detector $t\bar{t}$ direct muon efficiency as a function of true η for low luminosity and muons with $p_{\mathrm{T}} > 10\,\mathrm{GeV}$, taken from [151]. The blue curve is the efficiency to find the muon while the green curve additionally requires a good match between reconstructed and true track parameters.

and $> 50\,\mathrm{GeV}$ for all three reference cuts. For all three selections a flag is set for only a fraction of all reconstructed electrons being tagged as identified. The identification efficiency for electrons varies with the transverse momentum of the electron. The efficiency is shown in Fig. 4.3 and is defined as

$$\varepsilon_{\mathrm{electrons}} = \frac{\text{Number of electrons tagged as identified}}{\text{Number of all reconstructed electrons}}. \tag{4.7}$$

It is shown for all three reference cuts as a function of p_{T} with the first p_{T} bin from $0-10\,\mathrm{GeV}$ missing since DELPHES takes only electrons above $p_{\mathrm{T}} = 10\,\mathrm{GeV}$ into account. For higher p_{T} bins the assumed efficiency in DELPHES is slightly to optimistic.

The efficiency as a function of η and ϕ is shown in Fig. 4.4. Fake pions are simulated by adding true pions to the content of the electron tree. The number of pions added to the electrons depends on the cut selection, 0.176 % of all true pions are added as loose electrons, 0.046 % are added as medium electrons, and 0.0011236 % of all true pions are added as tight electrons.

For the muon identification only one cut-based selection is applied. It is sub-divided into 7 p_{T} bins with ranges from $0-2\,\mathrm{GeV}$, $2-3\,\mathrm{GeV}$, $3-4\,\mathrm{GeV}$, $4-5\,\mathrm{GeV}$, $5-6\,\mathrm{GeV}$, $6-7\,\mathrm{GeV}$, and $> 7\,\mathrm{GeV}$ [151]. Since DELPHES takes only muons with a transverse momentum of $p_{\mathrm{T}} > 10\,\mathrm{GeV}$ into account the binning has no effect on the efficiency. The overall identification efficiency for muons is shown in Fig. 4.5. The identification efficiency for muons in ATLAS is almost 90 % and only a small fraction are fakes from pions. Nevertheless this small fraction had to be added to the muon collection. A fraction of 0.08 % of true pions are added to the collection of identified muons.

As discussed above, DELPHES does not apply a smearing of eta and phi for electrons and muons. Therefore this smearing is applied consecutively. To estimate a smearing factor an official ATLAS $Z \to ee$ data sample[4] with 4758621 events is used to determine the relative resolution for theta and phi in 5 p_{T} bins. In Fig. 4.6 the relative resolution of theta in all p_{T} bins is shown. A Gauss fit is used to determine a mean value of the width of the Gauss distribution. This mean value is used to smear theta

[4]Full detector simulation and reconstruction applied

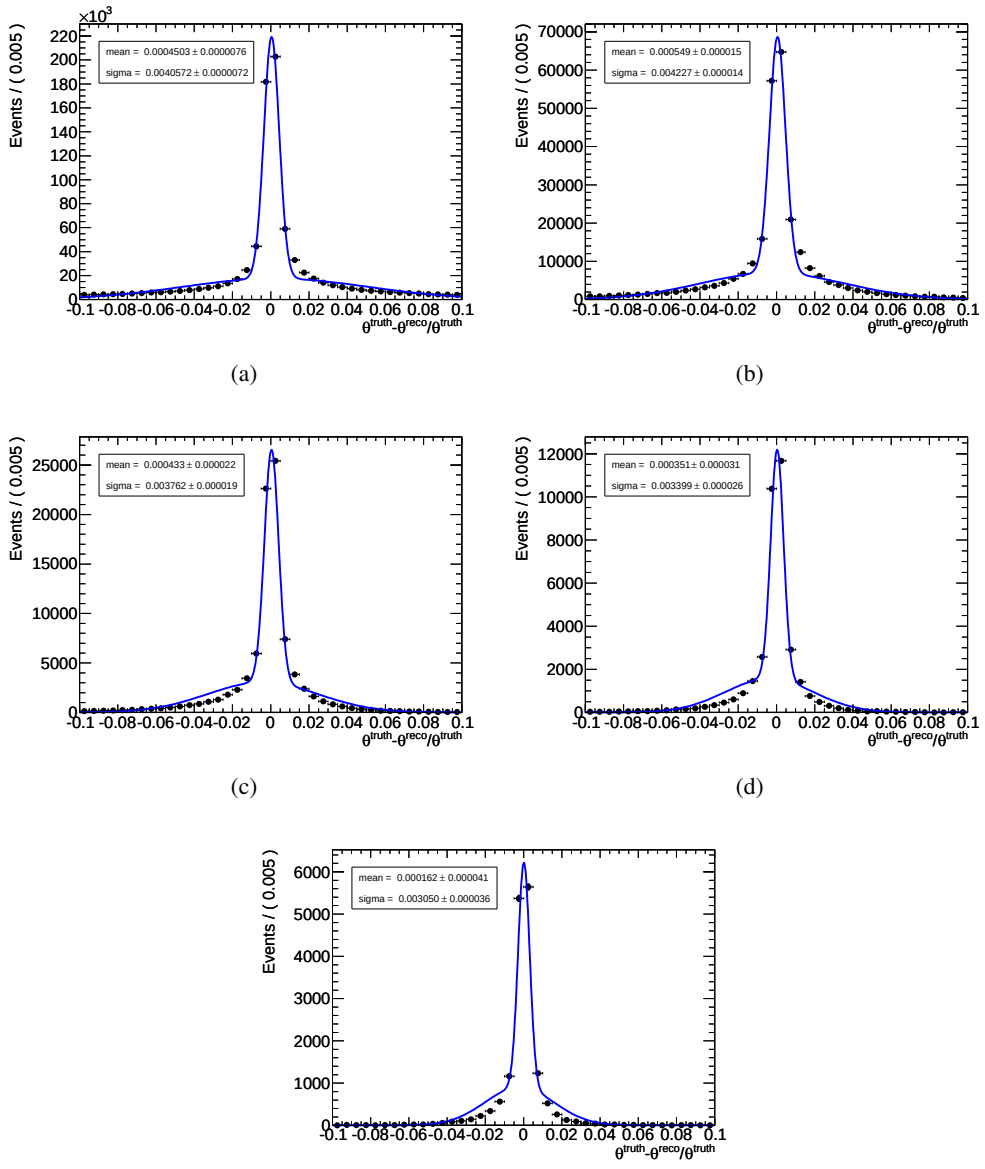

Figure 4.6.: Relative resolution of θ for the p_{T} bins 0 – 20 GeV (a), 20 – 40 GeV (b), 40 – 60 GeV (c), 60 – 80 GeV (d), and 80 – 100 GeV (e) of the full ATLAS detector simulation and reconstruction.

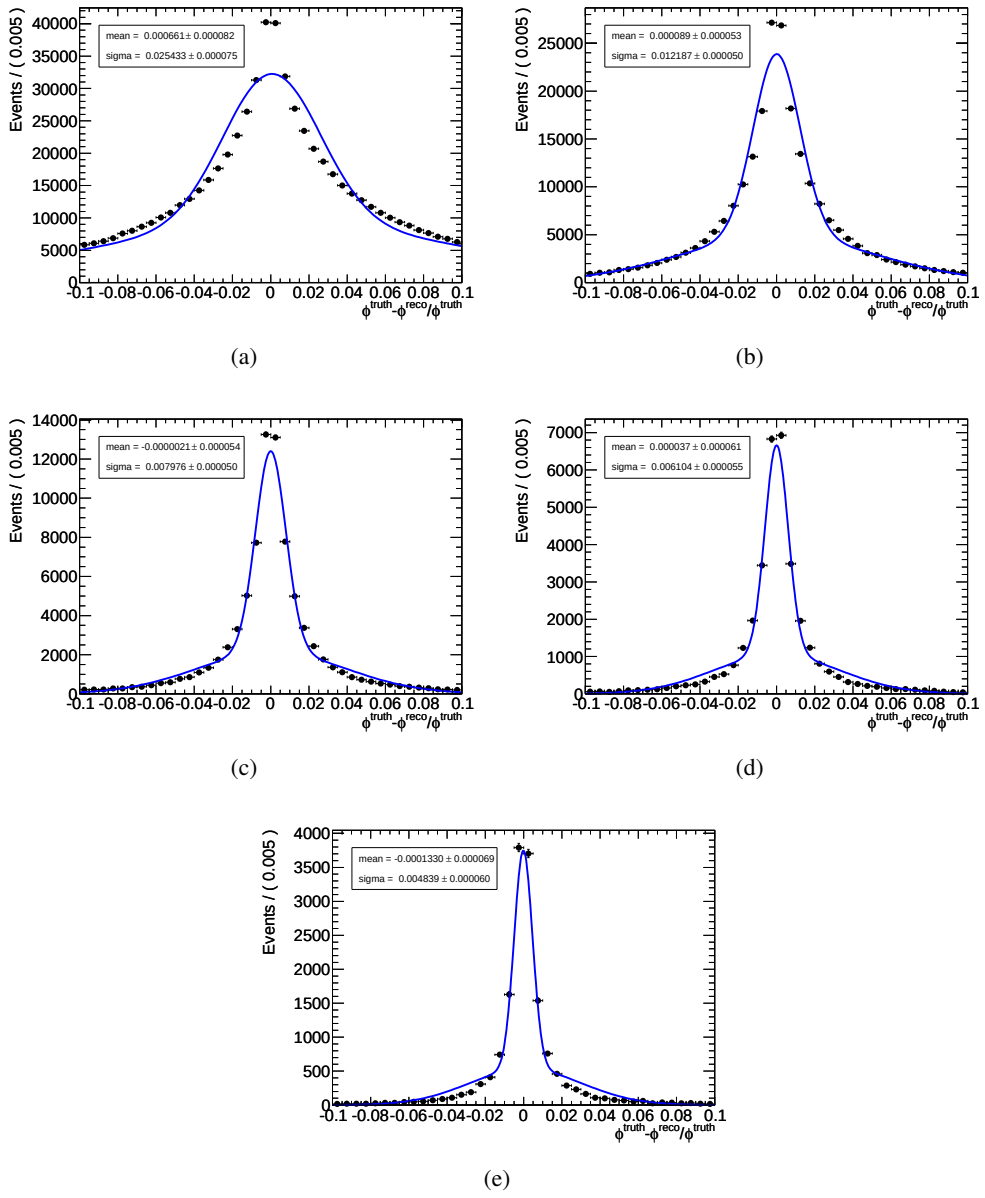

Figure 4.7.: Relative resolution of ϕ for the p_{T} bins 0 – 20 GeV (a), 20 – 40 GeV (b), 40 – 60 GeV (c), 60 – 80 GeV (d), and 80 – 100 GeV (e) of the full ATLAS detector simulation and reconstruction.

with a Gauss with the mean value as sigma. From the new theta value eta is calculated such that

$$\theta = 2 \cdot \arctan\left(\frac{1}{\exp(\eta)}\right). \tag{4.8}$$

The same procedure is applied for the phi distribution. The relative resolution of phi for all 5 p_{T} bins for the $Z \rightarrow ee$ data sample is shown in Fig. 4.7. The mean value of the width is used as sigma for a random Gauss to smear the new phi value. For the smearing of muons the same random Gauss as for the electrons is used.

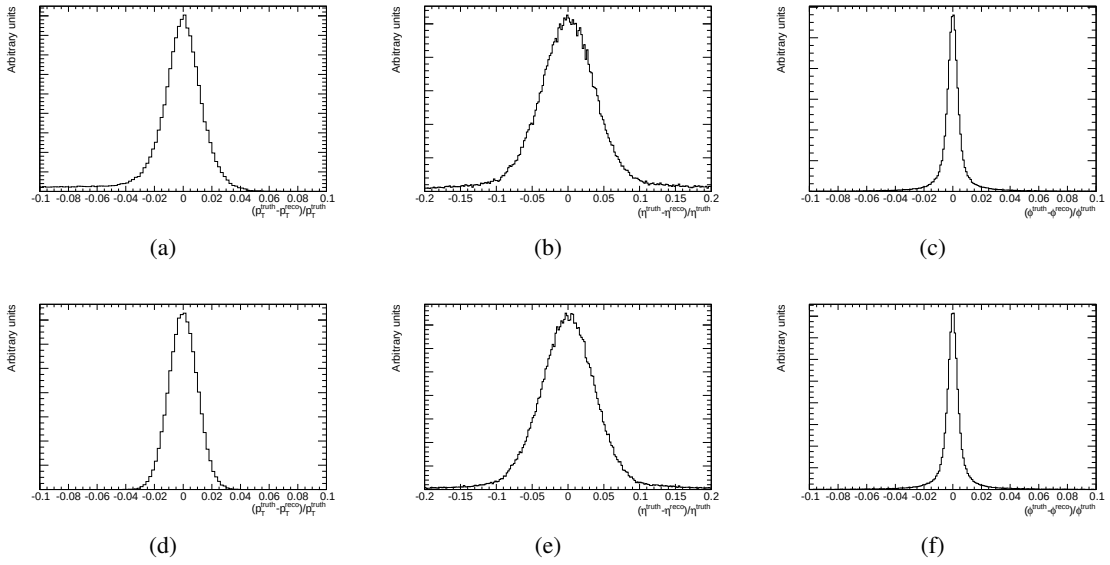

Figure 4.8.: Relative resolution of p_{T}, η, and ϕ for electrons and muons for Monte Carlo events, generated with the HERWIG++ matrix element *MEqq2gZ2ff* and passed through DELPHES and the reconstruction and identification simulation.

Validation For the validation of the detector simulation DELPHES two datasets, each with 500000 events, where generated with HERWIG++ [97]. One sample is using the matrix element *MEqq2gZ2ff*, and the other sample using the matrix element *MEHeavyQuark* for the production of heavy quarks. These samples are passed through the DELPHES detector simulation followed by the reconstruction and identification simulation.

Running DELPHES with both datasets as input provides a set of distributions which can be used to verify the quality and validity of the detector simulation. The matrix element *MEqq2gZ2ff* can be used to test the reconstruction of electrons and muons. The relative resolution as simulated by DELPHES for p_{T}, η, and ϕ for electrons and muons is shown in Fig. 4.8. Only electrons with an $E_{\mathrm{T}} > 20\,\mathrm{GeV}$ and $|\eta| < 2.5$ that match to a true electron are used[5]. For muons a $E_{\mathrm{T}} > 10\,\mathrm{GeV}$, $|\eta| < 2.5$, and a truth match is required. As expected all distributions show a certain width, i.e. the reconstructed p_{T} (η, ϕ) differs from the true value. The resolution of the fast detector simulation DELPHES (Fig. 4.8a and Fig. 4.8d) are

[5] $\Delta R < 0.2$ between MC and reconstructed particle

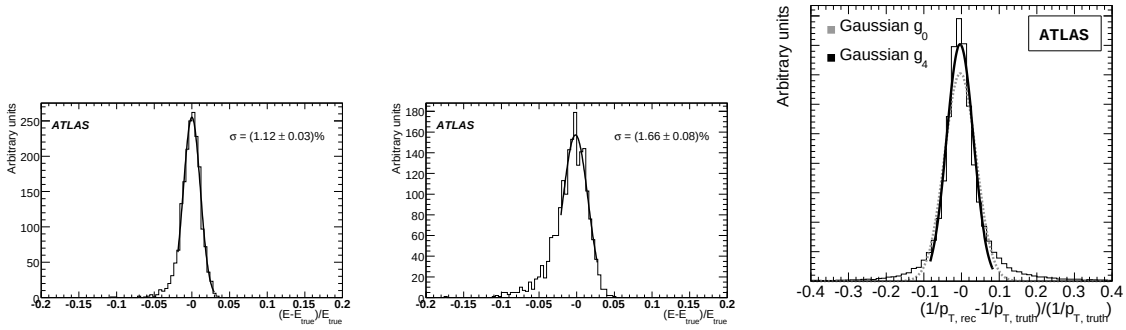

(a) (b) (c)

Figure 4.9.: Difference between measured and true energy normalized to true energy at $E = 100\,\text{GeV}$ for electrons with $|\eta| = 0.325$ (a) and $|\eta| = 1.075$ (b) (both taken from [150]) and fractional deviation of the reconstructed inverse momentum from the generated inverse momentum for muon (c). g_0 is the fitted Gaussian of iteration step 0, g_4 is the fitted Gaussian of final iteration step 4 (taken from [151]).

compared with the results of the ATLAS full detector simulation (Fig. 4.9a, Fig. 4.9b, and Fig. 4.9c). The distributions show an acceptable resolution but do not agree perfectly with the full detector simulation.

With the matrix element *MEqq2gZ2ff* a large number of Z bosons is generated, hence the reconstruction of the Z boson for the decay $Z \rightarrow ee$ and $Z \rightarrow \mu\mu$ can be checked. This is shown in Fig. 4.10 for electrons and Fig. 4.11 muons. The fit is described by a Breit-Wigner fit convoluted with a Gaussian to take the finite resolution of the electromagnetic calorimeter into account. The same distributions for the ATLAS full detector simulation are shown in Fig. 4.11. The estimated width is $\sim 2.5\,\text{GeV}$ for Fig. 4.10a and Fig. 4.10b, while for Fig. 4.11a and Fig. 4.11b the estimated width is $\sim 3.5\,\text{GeV}$. Both, $Z \rightarrow ee$ and $Z \rightarrow \mu\mu$ agree very good with the full ATLAS simulation.

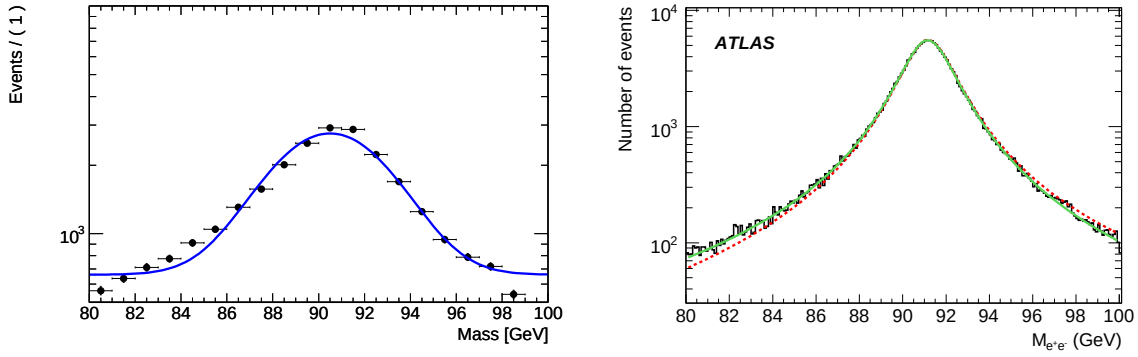

(a) (b)

Figure 4.10.: Z boson peak for the decay $Z \rightarrow ee$ for the matrix element *MEqq2gZ2ff*, simulated with DELPHES(a), and Z boson mass distribution for PYTHIA events fitted with a Breit-Wigner distribution with (solid line) and without (dashed line) the parton luminosity factor for electrons (b). The blue line in (a) represents a Breit-Wigner fit convoluted with a Gauss fit.

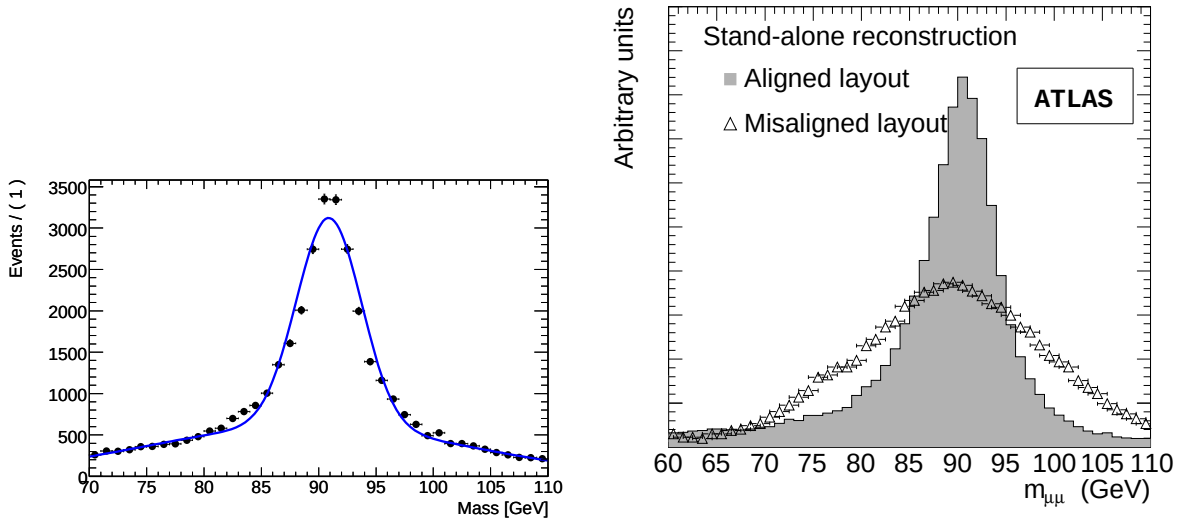

(a) (b)

Figure 4.11.: Z boson peak for the decay $Z \rightarrow \mu\mu$ for the matrix element *MEqq2gZ2ff* and reconstructed Zboson mass distribution for muons (b) [151] for an aligned and a misaligned muon spectrometer layout. The blue line in (a) represents a Breit-Wigner fit convoluted with a Gauss fit.

The matrix element *MEHeavyQuark* generates top – anti-top pairs. Since the top decays into a bottom and a W boson in almost 100 % of the time, jets, b-jets and W bosons can be used to test the validity of DELPHES.

To reconstruct the W boson the invariant mass of hadronically decaying W bosons is calculated. For the hadronically decaying W boson the invariant mass of both jets, originating from a true W is calculated. Its distribution is shown in Fig. 4.12. The peak of the distribution is shifted slightly to higher values, which originates from the resolution of the jets. The estimate width for both, Fig. 4.12a and Fig. 4.12b are ~ 9 GeV and agree very good.

The reconstruction of b-jets can be tested by checking the relative resolution of p_{T}, η, and ϕ of jets, which are tacked as b-jet. The distribution for these three relative resolutions is shown in Fig. 4.13 top and bottom left. For the b-jet a truth match to a bottom quark is required. The relative resolution for p_{T} is fine while the resolutions for η and ϕ are too narrow. This could be a hint that the smearing of η and ϕ is not well simulated by DELPHES. The bottom right plot in Fig. 4.13 shows the relative resolution of the transverse momentum for u- and d-quarks originating from true W bosons. The distribution has a smooth raising edge, while the lowering edge is steeply. The smearing of the transverse momentum is not well balanced within DELPHES which might be a reason for the shifted W peak in Fig. 4.12.

Summary

DELPHES is a framework for fast detector simulation. It includes a general multi-purpose detector, with a central tracking system, surrounded by a electromagnetic and hadron calorimeter, as well as forward calorimeters and a muon system. The framework provides a reconstruction of particles ($e^{\pm}$, $\mu^{\pm}$, γ) and objects (light jets, b-jets, τ-jets, $E_{\mathrm{T}}^{\mathrm{miss}}$).

The significance of DELPHES is analyzed and validated against ATLAS results. For a more realistic

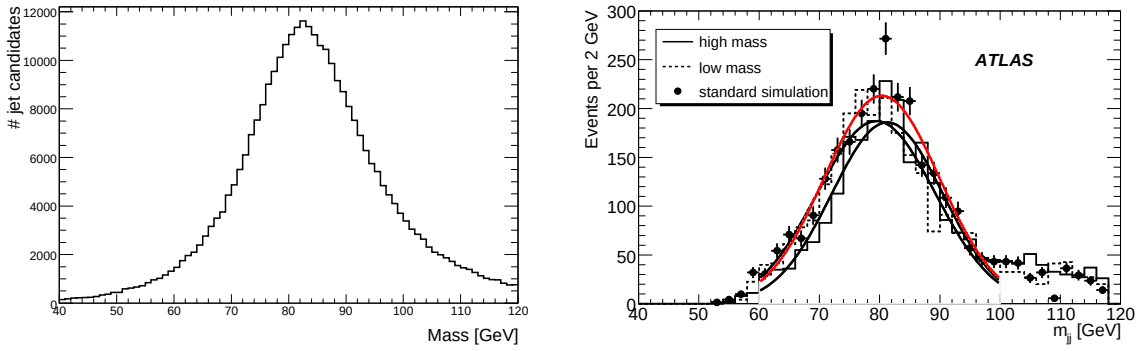

(a) (b)

Figure 4.12.: Invariant mass of two jets with a true W boson as mother for the matrix element *MEHeavyQuark*, simulated with DELPHES (a) and reconstructed W boson mass distribution in datasets with different gluon radiation settings [152] (b).

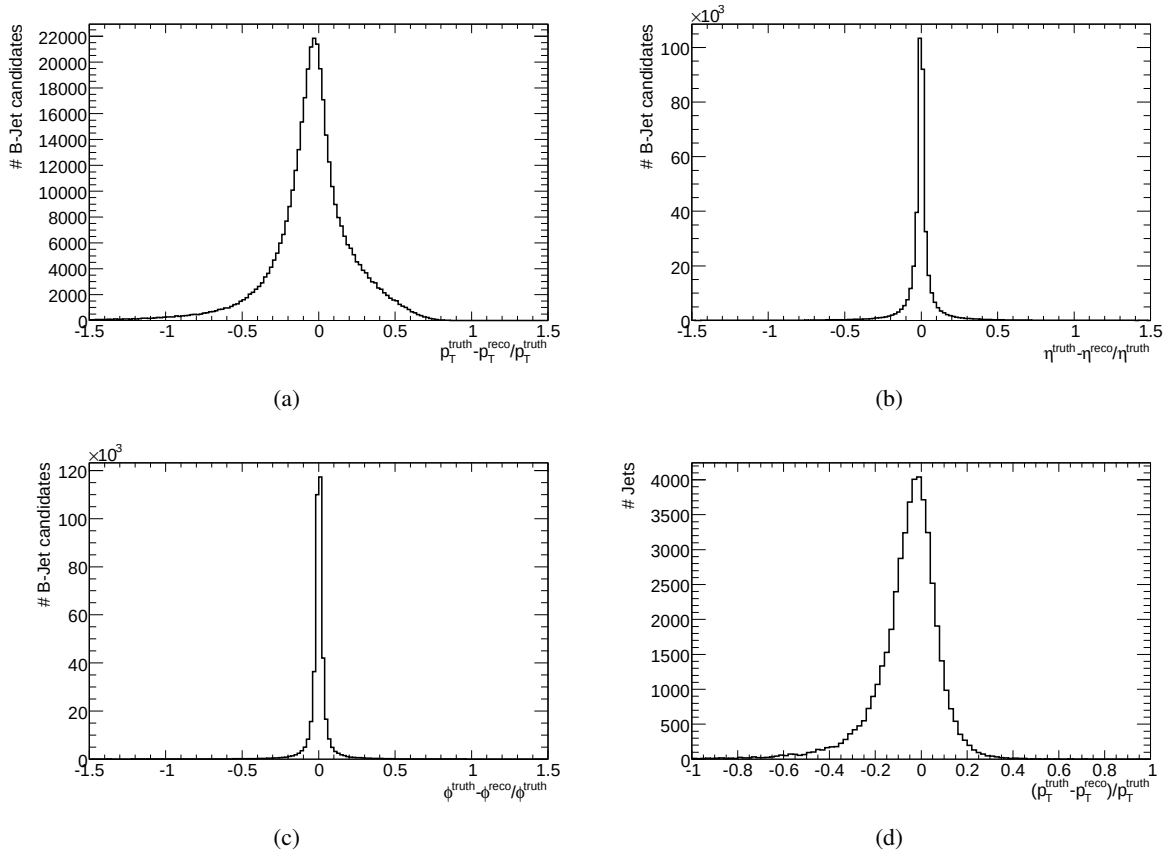

(a) (b) (c) (d)

Figure 4.13.: Relative resolution for b-jets (a) – (c) and for up- and down-quarks (d). The η and ϕ resolutions for b-jets are very narrow, the jet p_{T} resolution has a smooth raising, and a steep lowering edge.

performance of the electron and muon reconstruction, additional smearings of η and ϕ are applied, as well as identification methods are emulated.

Compared to ATLAS results the imitated identification methods show good agreement. The electron and muon resolution is consistent with ATLAS results and the reconstruction of the Z boson shows a reasonable detector resolution. The resolution of jets is cross checked by reconstructing hadronically decaying W bosons. Compared with ATLAS results the mass resolution lays within the expected detector resolution. The reconstruction and identification of τ-leptons does not assumptions predicted by the ATLAS simulation. Hence the reconstruction of τ-leptons is ignored. Except for τ's, the overall performance of the DELPHES simulation framework agree good with ATLAS results, while the resolution for electrons and muons is slightly to optimistic.

5. Reconstruction and Identification of Hadronic τ Decays

This chapter describes the reconstruction and identification methods and measurements of hadronically decaying τ-leptons.

Due to their short lifetime, τ-leptons can not be observed directly but through their decay products. Since it is difficult to distinguish leptonically decaying τ-leptons from primary electrons and muons the reconstruction at ATLAS is focused on hadronically decaying τ-leptons[1].

In Section 5.1 the phenomenology of τ-leptons and the topology of τ-leptons in LHC collisions is described. The reconstruction of τ-leptons in ATLAS is described in Section 5.2 and their identification in Section 5.3.

5.1. Phenomenology and Topology of τ-leptons

The τ-lepton is the heaviest of the three leptons and was discovered in 1975 at SLAC [153]. It has a mass of (1776.82 ± 0.16) MeV and a lifetime of $c\tau = 87.11\ \mu$m. τ-leptons decay hadronically in 64.8 % of all cases, while in $\sim$ 17.8 % of all cases they decay to electrons and in $\sim$ 17.4 % to muons. Hadronic decay modes are typically characterized by the number of charged mesons into which the τ-leptons decay, 1-prong for one charged meson and 3-prong for three charged mesons. There is also a very small fraction of 5-prong decays but they are harder to distinguish from QCD jets. A typical 3-prong τ-lepton decay with isolation cone is shown in Fig. 5.1.

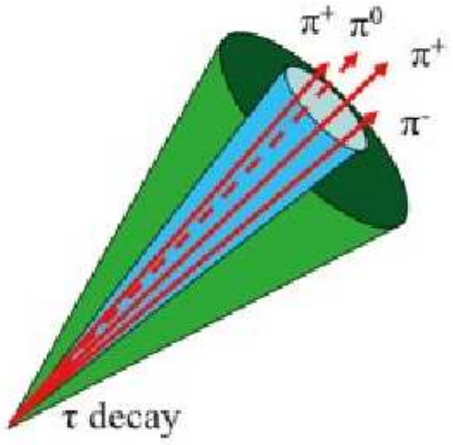

Figure 5.1.: Typical τ-lepton decay.

[1] As from now I will use τ_{had} for objects reconstructed from the visible part of the hadronic decay products of a τ-lepton.

Typically a τ-lepton decays into π's but there is a very small fraction of decays containing $K^{\pm}$ mesons which nevertheless can be identified using the same technique as for final states with $\pi^{\pm}$. There is also a very small fraction of decays with K^0_S which cannot be easily classified as 1-prong decay. A complete list of the branching ratios can be found in Tab. 5.1.

5.1.1. τ-lepton decay parameters

For leptonic decays the decay parameters (i.e. Michel parameters) are extracted from the energy spectrum of the charged daughter leptons in the decay $\tau \rightarrow l\nu_l\nu_\tau$ with $l = e,\ \mu$. If radiative corrections are ignored, terms of order $(m_l/m_\tau)^2$ and the neutrino mass is set to zero [18], the spectrum in the laboratory frame is

$$\frac{\mathrm{dT}}{dx} = \frac{G^2_{\tau l} m^5_\tau}{192\pi^3} \times \left\{ f_0(\mathrm{x}) + \rho f_1(\mathrm{x}) + \eta \frac{m_l}{m_\tau} f_2(\mathrm{x}) - P_\tau[\xi g_1(\mathrm{x}) + \xi\delta g_2(\mathrm{x})] \right\}, \tag{5.1}$$

with $f_0(x) = 2{-}6x^2{+}4x^3$, $f_1(x) = -\frac{4}{9}{+}4x^2{-}\frac{32}{9}x^3$, $f_2(x) = 12(1{-}x)^2$, $g_1(x) = -\frac{2}{3}{+}4x{-}6x^2{+}\frac{8}{3}x^3$ and $g_2(x) = \frac{4}{9} - \frac{16}{3}x + 12x^2 - \frac{64}{9}x^3$, where x is the fractional energy of the daughter lepton l and the polarization of the τ-lepton, P_τ is parametrized by the Michel parameter ρ, η, ξ, and δ. The integrated decay width is given by

$$\Gamma = \frac{G^2_{\tau l} m^5_\tau}{192\pi^3} \left(1 + 4\eta \frac{m_l}{m_\tau} \right), \tag{5.2}$$

and the matrix element

$$\frac{4G_F}{\sqrt{2}} \sum_{\substack{\gamma=S,V,T \\ \epsilon,\mu=R,T}} g^\gamma_{\epsilon,\mu} \langle \bar{e}_\epsilon | \Gamma^\gamma | (\nu_e)_n \rangle \langle (\bar{\nu}_\mu)_m | \Gamma_\gamma | \mu_\mu \rangle. \tag{5.3}$$

The matrix element in case of hadronic decays is

$$\frac{G_{\tau h}}{\sqrt{2}} \sum_{\lambda=R,L} g_\lambda \langle \bar{\Psi}_\omega(\nu_\tau) | \gamma^\mu | \Psi_\lambda(\tau) \rangle J^h_\mu, \tag{5.4}$$

with the hadronic current J^h_μ.

The incorporation of spin effects in τ-lepton decays is important. τ-leptons from decays of gauge bosons, Higgs bosons or SUSY cascade decays carry information on the polarization of the decaying resonance and information on the spin correlation in case of pair production. For $W \rightarrow \tau\nu$ and $H^{\pm} \rightarrow \tau\nu$ τ-leptons will be 100 % longitudinally polarized with P_τ = +1.0 and P_τ = -1.0 respectively. This results in different distribution of the charged to total visible energy in 1-prong decays and can be used to suppress $W \rightarrow \tau\nu$ while increasing the sensitivity to $H^{\pm} \rightarrow \tau\nu$ [154]. The polarization can also be used as a tool to discriminate between MSSM models and those with extra dimensions [155]. Since the longitudinal polarization of τ-leptons from the decay of neutral Higgs boson will be balanced with a probability of 50 %, τ-leptons from Higgs boson decays are not polarized. For Z boson decays the polarization of τ-leptons is more complicated and depends on the center-of-mass energy and the angle of the decay products [156].

The clean environment of a future linear collider or at the sLHC the sensitivity to the longitudinal and transverse spin may lead to CP measurements of the Higgs boson [157, 158].

The transverse energy spectrum of the visible decay products of τ-leptons from different processes including from Higgs boson and Z boson decays is shown in Fig. 5.2. The processes are normalized to the predicted cross sections with which they will be produced at the LHC for an integrated luminosity of 10 fb^{-1}.

Table 5.1.: Decay modes and their branching ratio of τ-lepton decays.

Decay mode	Branching ratio
$\tau \rightarrow e\nu_e\nu_\tau$	17.8 %
$\tau \rightarrow \mu\nu_\mu\nu_\tau$	17.4 %
$\tau \rightarrow h^{\pm}n\nu_\tau$ (1-prong)	49.5 %
$\tau \rightarrow \pi^{\pm}\nu_\tau$	11.1 %
$\tau \rightarrow \pi^0\pi^{\pm}\nu_\tau$	25.4 %
$\tau \rightarrow \pi^0\pi^0\pi^{\pm}\nu_\tau$	9.2 %
$\tau \rightarrow \pi^0\pi^0\pi^0\pi^{\pm}\nu_\tau$	1.1 %
$\tau \rightarrow K^{\pm}n\nu_\tau$	1.6 %
$\tau \rightarrow h^{\pm}h^{\pm}h^{\pm}n\nu_\tau$ (3-prong)	14.6 %
$\tau \rightarrow \pi^{\pm}\pi^{\pm}\pi^{\pm}\nu_\tau$	9.0 %
$\tau \rightarrow \pi^0\pi^{\pm}\pi^{\pm}\pi^{\pm}\nu_\tau$	4.3 %
$\tau \rightarrow \pi^0\pi^0\pi^{\pm}\pi^{\pm}\pi^{\pm}\nu_\tau$	0.5 %
$\tau \rightarrow \pi^0\pi^0\pi^0\pi^{\pm}\pi^{\pm}\pi^{\pm}\nu_\tau$	0.1 %
$\tau \rightarrow K^0_S X^{\pm}\nu_\tau$	0.9 %
$\tau \rightarrow (\pi^0)\pi^{\pm}\pi^{\pm}\pi^{\pm}\pi^{\pm}\pi^{\pm}\nu_\tau$ (5-prong)	0.1 %
other modes with K	1.3 %
others	0.03 %

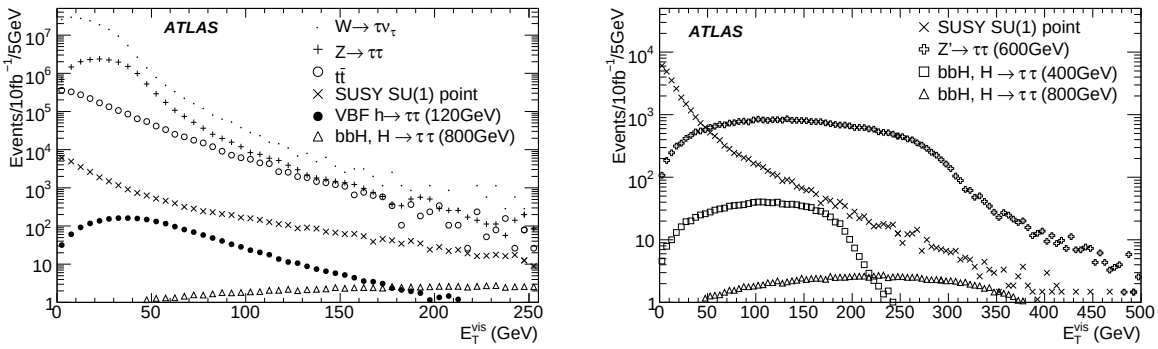

(a) (b)

Figure 5.2.: Visible transverse energy, $E_{\mathrm{T}}^{\mathrm{vis}}$, of τ-leptons from different physics processes: top quark decays, W/Z production, Standard Model vector boson fusion, Higgs boson production for $m_H = 120$ GeV (a), and τ-leptons from low energy SUSY with a light $\tilde{\tau}$ (SU1 sample), heavy Z' bosons, and heavy Higgs bosons from bbH production in the MSSM with $\tan\beta = 20(45)$ for masses of 400 GeV (800 GeV) (b) [149].

5.2. Reconstruction of τ-leptons in ATLAS

To reconstruct hadronic τ-lepton decays efficiently, information from the Inner Detector and the calorimeter are used. Only reconstruction of the visible part of the decay products is performed.

The reconstruction of hadronically decaying τ-lepton at ATLAS consists of two complementary algorithms and starts from either calorimeter or track seeds. Before each algorithm is described separately and there performance is compared, a few selected topics related to the performance of the detector are discussed.

5.2.1. Tracking and vertexing

Since the reconstruction of tracks from charged π decays is an important element of the τ_{had} reconstruction, the performance of the tracking and vertexing is discussed. The track-based algorithm (see Section 5.2.3) is seeded by one or more good quality tracks. The energy of the τ_{had} is calculated with the so called energy-flow scheme [159]. The charge of the τ_{had} candidate is determined by summing up the charges of the tracks reconstructed in the core region of the τ_{had} candidate[2]. Tracking information like the track multiplicity, the impact parameter, and the transverse flight path in case of multi-track candidates are also used for the identification of hadronic τ-leptons and to discriminate them against the background from QCD jets. Therefore the track selection should be high efficient over a broad momentum range from 1 GeV to a few hundred GeV. I will give a more detailed description of the identification methods in Section 5.3.

Reconstruction efficiency

The efficiency for the track reconstruction is defined as the probability to reconstruct a $\pi^{\pm}$ from a τ decay as a track. In [78] a standard quality selection is defined. The reconstruction efficiency of this selection for $p_{\mathrm{T}} = 1 - 50\,\mathrm{GeV}$ is shown in Fig. 5.3.

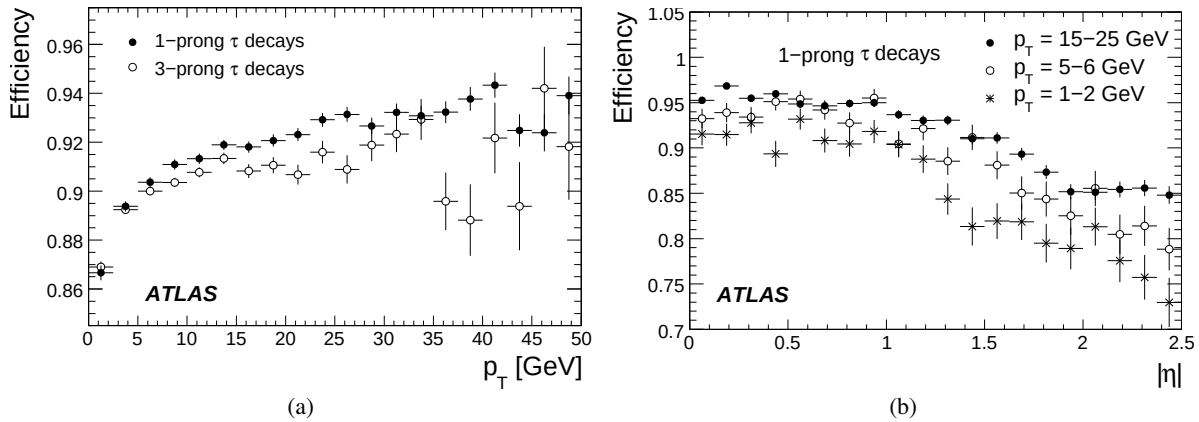

Figure 5.3.: Reconstruction efficiency for tracks from charged π's for 1-prong and 3-prong hadronic τ decays from $\mathrm{W} \rightarrow \tau\nu$ and $\mathrm{Z} \rightarrow \tau\tau$ signal samples as a function of the transverse momentum (a) and of the the pseudo-rapidity (b) of the tracks [149].

[2]The core region for the track-based (calo-based) algorithm is a cone in $(eta,\ \phi)$ with $\Delta R = \sqrt{\Delta\eta^2 + \Delta\phi^2} < 0.2$ (0.3) around the reconstructed direction of the visible decay products.

Charge mis-identification

The overall mis-identification probability is dominated by combinatorial effects: due to photon conversions or tracks from underlying events, 1-prong decays may migrate to the 3-prong category. On the other side, 3-prong decays might be reconstructed as 1-prong decays due to inefficiencies of the track reconstruction. Without additional quality cuts the overall charge mis-identification is below $\sim 3.6\,\%$. Table 5.2 shows the percentage of contamination for 1-prong and 3-prong candidates.

Table 5.2.: Percentage of 1- and 3-prong τ-lepton hadronic decays within reconstructed 1-, 2- and 3-prong τ_{had} candidates by the track algorithm, matched to true τ decays. For the leading track a $p_{\mathrm{T}} > 9\,\mathrm{GeV}$ is required (later the condition was changed to $p_{\mathrm{T}} > 6\,\mathrm{GeV}$). In addition an estimate for electron contamination and charge mis-identification is given and specific results for a subsample where no hadronic secondary interaction of primary charged π was recorded inside the Inner Detector volume. Events from $\mathrm{Z} \rightarrow \tau\tau$ and $\mathrm{W} \rightarrow \tau\nu$ samples are used [149].

Seeds for track-based τ_{had}-candidates	Reconstructed as one-prong	Reconstructed as three-prong	Reconstructed as two-prong
Electron contamination (from conversion)	1.5 %	5.7 %	2.9 %
$\tau \rightarrow \pi^{\pm} n\pi^0 \nu$	96 %	3.8 %	23.8 %
$\tau \rightarrow 3\pi^{\pm} n\pi^0 \nu$	3.9 %	96.2 %	76.2 %
Charge misid. (no. had. interact.)	1.7 % 0.4 %	3.6 % 2.1 %	

5.2.2. Reconstruction of π^0 subclusters

Table 5.3.: Fraction of 1-prong τ candidates with no, one, and two or more reconstructed π^0 subclusters [149].

decay mode	no π^0 subclusters	1 π^0 subcluster	≥ 2 π^0 subclusters
all $\tau \rightarrow h^{\pm}\nu$	32 %	35%	33 %
$\tau \rightarrow \pi\nu$	65 %	20 %	15 %
$\tau \rightarrow \rho\nu$	15 %	50 %	35 %
$\tau \rightarrow a_1(\rightarrow 2\pi^0\pi)\nu$	9 %	34 %	57 %

In 66 % of the time the decay $\tau \rightarrow \pi\nu$ is reconstructed with π^0 subclusters, where the π^0 meson creates a topocluster in the electromagnetic calorimeter with $E_{\mathrm{T}} > 1\,\mathrm{GeV}$ that is isolated from tracks. In addition more than 50 % of both $\tau^{\pm} \rightarrow \rho^{\pm}\nu \rightarrow \pi^{\pm}\pi^0\nu$ and $\tau^{\pm} \rightarrow a_1^{\pm}\nu \rightarrow \rho^{\pm}\pi^0\nu \rightarrow \pi^{\pm}\pi^0\pi^0\nu$ decays are reconstructed with one and two π^0 subclusters, respectively. In case of 1-prong decays a significant fraction of the pure electromagnetic energy, namely 55 %, is carried by the π^0.

For the identification of isolated subclusters from π^0's inside the core region of the reconstructed τ-lepton the high granularity of the electromagnetic calorimeter in ATLAS is relevant.

Reconstructed subclusters require a transverse energy of $E_{\mathrm{T}} > 1\,\mathrm{GeV}$ and must be separated by $\Delta R > 0.0375$ from the impact point of the track in the middle layer. They are accepted if their reconstructed energy in the strip plus presampler layers exceeds 10 % of their total energy. With these requirements about 50 % of satellite clusters from charged πs in the case of $\tau \rightarrow \pi\nu$ decays are removed. Table 5.3 summarizes the fraction of 1-prong candidates reconstructed with a given multiplicity of π^0subcluster.

The vector sum of the reconstructed track and the π^0 subclusters for a 1-prong decay allows the definition of the visible mass of the hadronic τ-lepton. The response and resolution for this algorithm is shown in Fig. 5.4a. The visible energy is reconstructed for decays of type $\tau \rightarrow \rho\nu$ from $\mathrm{W} \rightarrow \tau\nu$ events where at least one π^0 subclusters is reconstructed. A Gaussian fit on the left plot gives a resolution of 4.6 % with an effective shift of -2.4 %.

The invariant mass of $\tau \rightarrow \rho\nu \rightarrow \pi^0\pi\nu$ decays is shown in Fig. 5.4b. The reconstruction from the track + π^0 subcluster system is more difficult than the reconstruction of the transverse energy only since the resolution is dominated by the precision of the angle reconstruction between the charged and neutral pion.

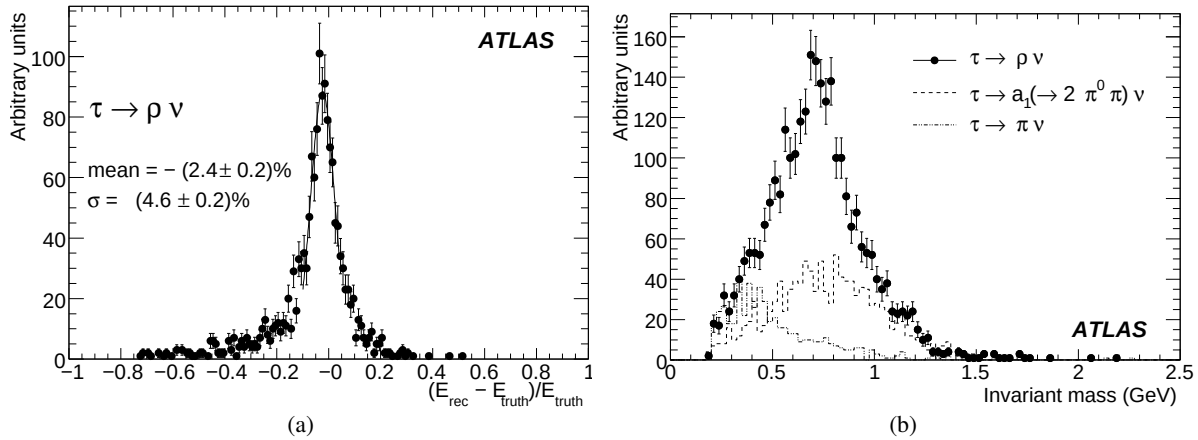

Figure 5.4.: The energy response obtained for the visible energy (a) and invariant mass of the visible decay products (b) [149].

Electron veto

For the rejection of background from $W \rightarrow e\nu$ and $Z \rightarrow ee$ an efficient rejection of tracks from isolated electrons is necessary. Therefore a dedicated algorithm to veto electrons was developed. This algorithm is based on four variables:

- The energy deposition in the hadronic calorimeter (E^{HCAL}) in the first layer of the hadronic calorimeter in a window $\Delta\phi \leq 0.2$ and $\Delta\eta \leq 0.2$ around the track extrapolation. Cutting on E^{HCAL} at 0.4 GeV (or alternatively at 0.2 GeV) already gives a good separation of electrons from hadrons.

- The energy not associated with a charged track in the strip compartment of the EM ($E^{\mathrm{max}}_{\mathrm{strip}}$). This variable is sensitive to secondary energy deposits in the EM calorimeter that are not associated to the leading track.

- The ratio of the transverse energy in the EM and the transverse track momentum ($E_{\mathrm{T}}^{\mathrm{EM}}/p_{\mathrm{T}}$). The energy is calculated in the $\Delta\eta \times \Delta\phi$ window around the impact cell of 0.075×0.3 in the presampler, 0.0475×0.3 in strips, 0.075×0.075 in the middle layer, and 1.5×0.075 in back compartment.
- The ratio of the number of high threshold to low threshold hits in the TRT ($\mathrm{N_{HT}}/\mathrm{N_{LT}}$).

The distribution of $E_{\mathrm{T}}^{\mathrm{EM}}/p_{\mathrm{T}}$ and $\mathrm{N_{HT}}/\mathrm{N_{LT}}$ for the first 15.6 nb^{-1} compared to PYTHIA QCD jets is shown in Fig. 5.5.

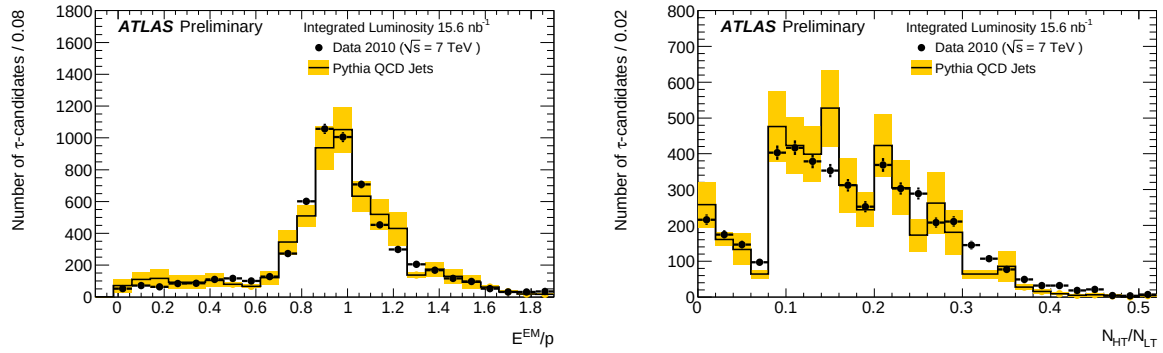

(a) (b)

Figure 5.5.: $E_{\mathrm{T}}^{\mathrm{EM}}/p_{\mathrm{T}}$ (a) and $\mathrm{N_{HT}}/\mathrm{N_{LT}}$ (b) of τ candidates matched to well identified electrons. The yellow band around the MC expectation indicates the statistical uncertainty on simulation samples. The number of τ candidates in MC samples are normalized to the number of τ candidates selected in data [160].

This algorithm rejects $\sim 95\,\%$ of all electrons from $W \rightarrow e\nu$ events with a loss of efficiency for true hadronic τ decays with track $p_{\mathrm{T}} > 6\,\mathrm{GeV}$ of less than 1.5 %.

5.2.3. Offline algorithms for τ-lepton reconstruction

Candidates reconstructed with the calorimeter-based algorithm [161] are so called *calorimeter-seeded* candidates. They consist of calorimeter jets reconstructed with the anti-$\mathrm{k_t}$ algorithm [148] (using a distance parameter $D = 0.4$) starting from topological clusters (topoclusters) [162]. The topological algorithm starts with a seed cell with energy exceeding the calorimeter noise level by $4\,\sigma$, iteratively adds associated neighboring cells to the cluster if their energy exceeds $2\,\sigma$, and finally adds all adjacent cells to the cluster. Only jets with a $p_{\mathrm{T}} > 10\,\mathrm{GeV}$ are used, calibrated with the global cell energy-density weighting (GCW) calibration scheme [163] and $|\eta| < 2.5$.

If a track is found within a cone with $\Delta R < 0.3$, it is associated to the calo-seeded τ candidate. The quality criteria for these tracks are looser than for the track-based algorithm and are shown as "loose tracks" in Tab. 5.4.

To calculate the energy of the τ candidate all cells within $\Delta R < 0.4$ around the barycenter of the cluster are summed up and calibrated with an GCW-style calibration. The cell weights are a function of the cell energy density, η and the calorimeter region. Since these weights are optimized for jets [164] and overestimate the energy for hadronic τ-leptons, so called fudge factors are applied to the corrected energy to underestimate the energy according to the position of the cell in η and ϕ and cell energy. The

mean and the sigma of a Gaussian fit to the ratio of the reconstructed and the generated energy of the visible τ decay products, $E_{\mathrm{T}}^{\tau-vis}$, in the range from 0.8 to 1.2 is shown in Fig. 5.6. The resolution is in the order of 10 % and in the energy range from 20 to 50 GeV an offset in the range of +5 % to -7 % is observed, while at large energies the offset is of the order -3 % to -5 %.

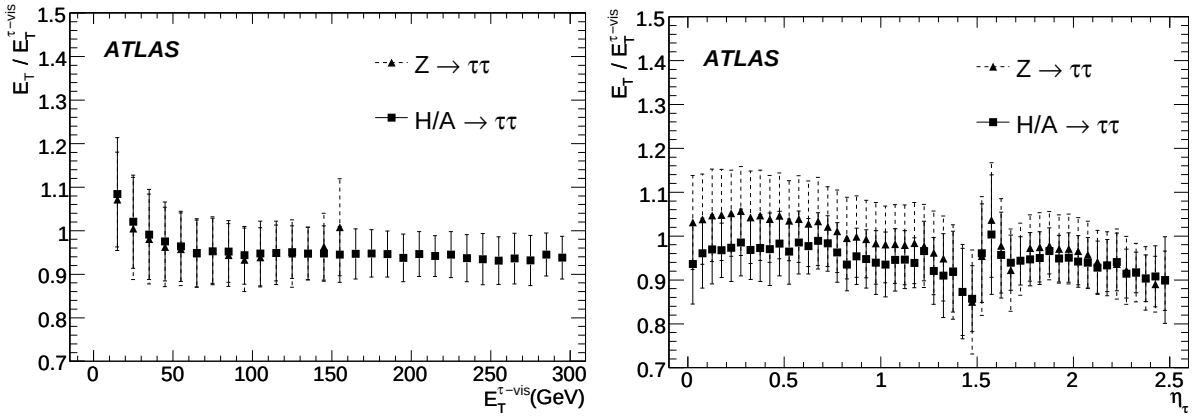

(a) (b)

Figure 5.6.: Ratio of the reconstructed (E_{T}) and the true ($E_{\mathrm{T}}^{\tau-vis}$) transverse energy of the hadronic τ decay products as function of the visible true transverse energy $E_{\mathrm{T}}^{\tau-vis}$ (a) and $|\eta|$ (b) for τ-leptons from $\mathrm{Z} \rightarrow \tau\tau$ and $\mathrm{A} \rightarrow \tau\tau$ with $m_{\mathrm{A}} = 800\,\mathrm{GeV}$ [149].

Candidates reconstructed with the track-based algorithm [165] are so called *track-seeded* candidates. This approach starts with a track with $p_{\mathrm{T}} > 6\,\mathrm{GeV}$ and passing quality criteria, which becomes a seed for building the τ candidate. The algorithm associates up to six additional tracks in the core region ($\Delta R < 0.2$) to the seed track, passing their own quality criteria. These criteria for the seed track and associated tracks are listed in Tab. 5.4.

Table 5.4.: Track quality criteria for seed tracks and associated tracks for the track-based algorithm and loose tracks for the calorimeter-based algorithm.

Track criteria	Seed track	Associated track	Loose track
p_{T} (GeV) $>$	6	1	1
$\lvert\eta\rvert <$	2.5	2.5	2.5
Impact parameter d_0 (mm) $<$	1	1	1.5
Silicon hits $N_{\mathrm{Si}} \geq$	8	8	6
TRT hits $N_{\mathrm{TRT}} \geq$	10	no cut	no cut
Normalized $\chi^2 <$	1.7	1.7	3.5
Pixel hits $N_{\mathrm{pixel}} \geq$	no cut	1	1
B-layer hits $N_{\mathrm{b\text{-}lay}} \geq$	no cut	1	no cut
High/Low threshold hit ratio $N_{\mathrm{TRT}}^{\mathrm{HT}}/N_{\mathrm{TRT}}^{\mathrm{LT}} <$	no cut	0.2	no cut

When a track-seed and a calorimeter-seed are within a distance $\Delta R < 0.2$ the τ candidate is labeled *double-seeded*. About 70 % of τ_{had} candidates which are matched to true hadronic τ's are double-seeded

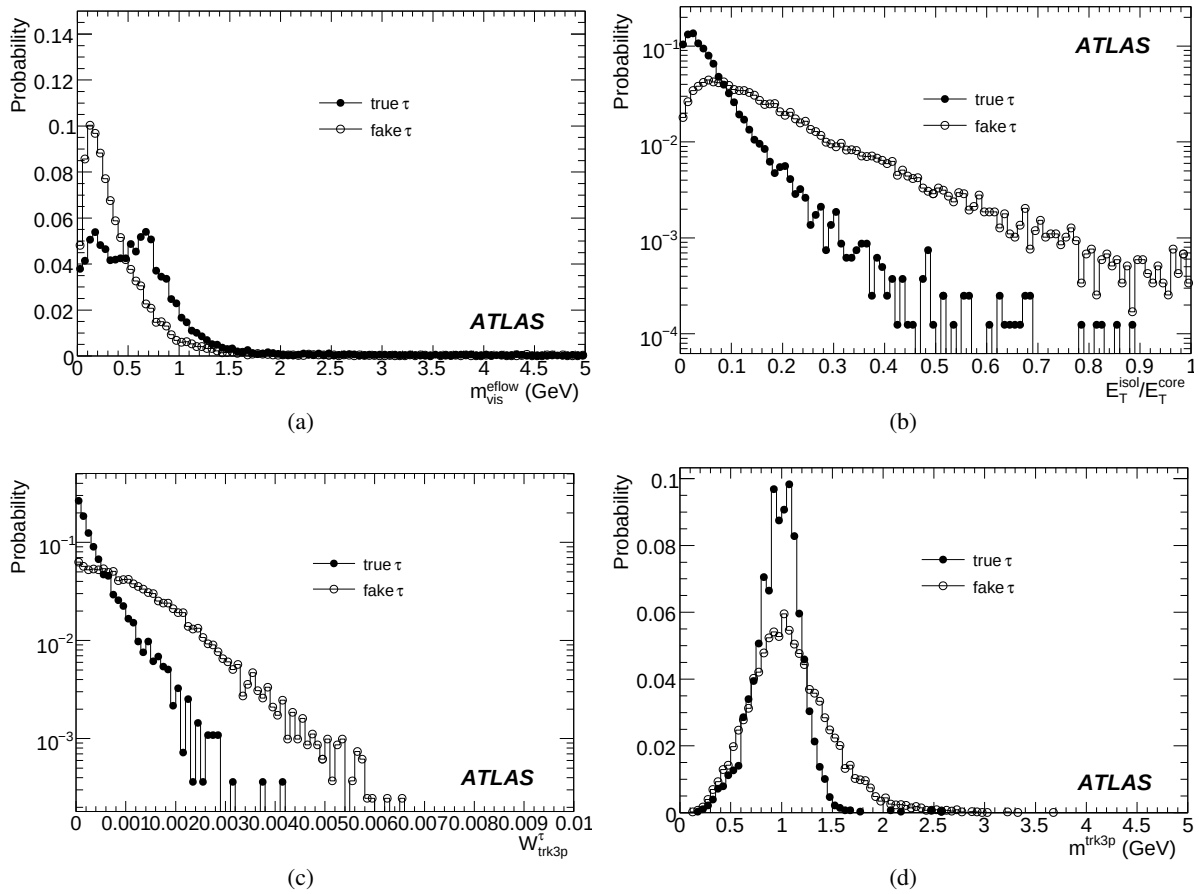

Figure 5.7.: Distribution for signal and background (with a transverse energy range of $E_{\mathrm{T}} = 20 - 40$ GeV) for the visible mass $m_{\mathrm{vis}}^{\mathrm{eflow}}$ and ratio of the transverse energy in the isolation and core region $E_{\mathrm{T}}^{\mathrm{isol}}/E_{\mathrm{T}}^{\mathrm{core}}$ for 1-prong τ candidates, and the track width $W_{\mathrm{tracks}}^{\tau}$ and the invariant mass m_{trk3p} for 3-prong τ candidates [149].

candidates, about 25 % have only a calorimeter-seed and about 5 % have only a track-seed.

The direction of the τ candidate is calculated in two ways. For track-seeded τ candidates, the η and ϕ directions are taken from the direction of the track and the primary vertex in case of 1-prong candidates, and from the p_{T}-weighted track barycenter in the case of multi-prong candidates. For candidates without a track-seed (i.e. only a calo-seed) η and ϕ are calculated based on the E_{T}-weighted barycenter of the calorimeter cells.

5.3. Identification of τ-leptons in ATLAS

The reconstruction of τ candidates provides very little rejection against the main background of QCD jets. Real rejection comes from separated identification steps. The identification is based on several discriminating variables which are used as input for identification methods based on simple cuts [166], boosted decision trees (BDT), and projective likelihood (LL). The performance of the τ identification with the first 7 TeV data is discussed in the next section, while a detailed description of the cut-based ID

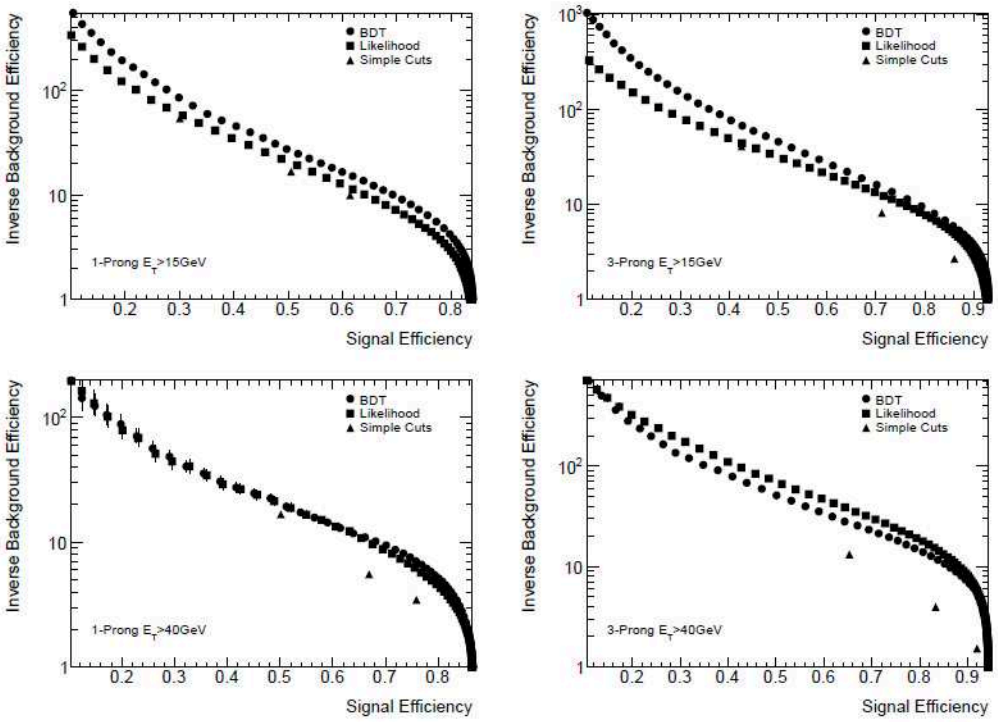

Figure 5.8.: Performance of a boosted decision tree, projective likelihood, and simple cuts for 1-prong and 3-prong τ candidates and different ranges of the transverse energy. The BDT and LL provide the most significant increase of performance over the simple cuts on 3-prong candidates due to the more limited number of variables used for the cuts [167].

method is given in Chapter 6.

Several calorimeter and tracking variables are used to discriminate a narrow, low track multiplicity τ_{had} cluster from a hadronic activity originating from quarks and gluons. If not stated otherwise, the ID quantities are calculated from cells/tracks within a core cone of $\Delta R = 0.2$ around the seed and an isolation cone is defined with $\Delta R = 0.2 - 0.4$. Please note that the selection of identification quantities given below is only a snapshot and differs from the variables used for the analysis in Section 5.4 or as input for the cut-based ID in Chapter 6.

- **Tracking quantities**
  - *Track Width:*
    The width of tracks, weighted with their transverse momentum, calculated as variance (for multi-prong candidates only)

$$W^{\tau}_{\text{tracks}} = \frac{\sum(\Delta R^{\text{track}})^2 \cdot p_{\text{T}}^{\text{track}}}{\sum p_{\text{T}}^{\text{track}}} - \frac{(\sum \Delta R^{\text{track}} \cdot p_{\text{T}}^{\text{track}})^2}{(\sum p_{\text{T}}^{\text{track}})^2}, \tag{5.5}$$

    where ΔR is the distance between the track and the τ candidate track seed in η - ϕ space, and the summation is performed over all tracks associated to the τ candidate.
  - *Track mass:*
    The invariant mass of the track system.

– *Track number:*
Number of tracks in the isolation cone.

- **Calorimetric quantities**

– *Electromagnetic radius:*
The electromagnetic radius is defined as

$$R_{\mathrm{EM}} = \frac{\sum_{\mathrm{i=1}}^{\Delta R<0.4} E_{\mathrm{T},i}^{\mathrm{EM}} \sqrt{\left(\eta_i^{\mathrm{EM}} - \eta_{\text{calo seed}}\right)^2 + \left(\phi_i^{\mathrm{EM}} - \phi_{\text{calo seed}}\right)^2}}{\sum_{i=1}^{\Delta R<0.4} E_{\mathrm{T},i}^{\mathrm{EM}}}, \tag{5.6}$$

where i runs over all cells in the associated topocluster of the τ candidate. The quantities $\eta_{\mathrm{i}}^{\mathrm{EM}}$, $\phi_{\mathrm{i}}^{\mathrm{EM}}$ and $E_{\mathrm{T,i}}^{\mathrm{EM}}$ denote the position and transverse energy of cell i, while η_{caloseed} and ϕ_{caloseed} are the coordinates for the calorimeter seeded τ candidate.

– *Number of hits in the η strip layer:*
The number of hits in η direction in the finely segmented strip detector, N_{strips}^{τ}, in the first layer of the electromagnetic barrel calorimeter. Cells in the η strip layer within $\Delta R < 0.4$ around the cluster axis are counted as hits if the energy deposits exceeds 200 MeV. In contrast to jets, a significant fraction of τ-leptons deposit nearly no energy in this layer, i.e. the number of corresponding hits is small.

– *Transverse energy width in the η strip layer:*
The transverse energy width, W_{strip}, in the η strip layer is defined as

$$W_{\text{strip}} = \sqrt{\frac{\sum_{i}^{\Delta R<0.4} E_{\mathrm{T},i}^{\text{strip}} \left(\eta_i - \eta_{\text{calo seed}}\right)^2}{\sum_{i}^{\Delta R<0.4} E_{\mathrm{T},i}^{\text{strip}}}}, \tag{5.7}$$

where the sum runs over strip cells in the associated topoclusters of the τ candidate and $E_{\mathrm{T},i}^{\text{strip}}$ is the corresponding strip transverse energy.

– *Fraction of transverse energy:*
The fraction of the transverse energy, f_{iso}, deposited in a cone of radius $0.1 < \Delta R < 0.2$ with respect to the total energy in a cone of $\Delta R = 0.2$. Cells belonging to all layers of the calorimeter are used:

$$f_{\text{iso}} = \frac{\sum E_{\mathrm{T}}^{\text{cell}}(R^{\tau,\text{cell}} < 0.2) - \sum E_{\mathrm{T}}^{\text{cell}}(R^{\tau,\text{cell}} < 0.1)}{\sum E_{\mathrm{T}}^{\text{cell}}(R^{\tau,\text{cell}} < 0.2)}. \tag{5.8}$$

– *Transverse core energy:*
The transverse energy, $E_{\mathrm{T}}^{\text{core}}$, at the EM scale, deposited inside the core cone.

– *Transverse isolation energy:*
The transverse energy, $E_{\mathrm{T}}^{\text{isol}}$ and $E_{\mathrm{T}}^{\text{isolHAD}}$, at the EM scale, deposited inside the isolation cone.

- **Tracking and calorimetric quantities**
  - *Energy ratio:*
    The ratio of transverse energy deposited in the hadronic calorimeter in the core region (at EM scale), $E_{\mathrm{T}}^{\mathrm{chrgHAD}}$, with respect to the sum of the transverse momenta of the track.
  - *Visible mass:*
    The visible mass, $m_{\mathrm{vis}}^{\mathrm{eflow}}$, calculated from cells used for the energy-flow calculation and tracks. Four multi-prong candidates the invariant mass of the track system is taken instead, since this mass is smaller than that calculated from the four-momenta of the tracks.

As an example the distributions for signal and background samples for $m_{\mathrm{vis}}^{\mathrm{eflow}}$, the ratio $E_{\mathrm{T}}^{\mathrm{isol}}/E_{\mathrm{T}}^{\mathrm{core}}$ for 1-prong candidates, $W_{\mathrm{tracks}}^{\tau}$, and the invariant mass m_{trk3p} for 3-prong candidates is shown in Fig. 5.7. The double peak structure in $m_{\mathrm{vis}}^{\mathrm{eflow}}$ comes from $\tau \to \pi^{\pm}\nu$ and $\tau \to \rho(a1)\nu$ decays.

The expected performance for a BDT and a LL compared to simple cuts is shown in Fig. 5.8. The curves describe the jet rejection versus the efficiency, separately for 1-prong and 3-prong candidates and for $E_{\mathrm{T}} > 15\,\mathrm{GeV}$ and $E_{\mathrm{T}} > 40\,\mathrm{GeV}$. The jet rejections are computed with respect to jets reconstructed from true particles in the Monte Carlo.

5.4. Performance of the ATLAS detector with 7 TeV data

The study described in this section is based on data collected with the ATLAS detector at a center-of-mass energy of $\sqrt{s} = 7\,\mathrm{TeV}$, corresponding to an integrated luminosity of approximately $\mathcal{L} = 244\,\mathrm{nb}^{-1}$ [168–170]. The data considered are required to have been taken with stable LHC beam conditions, and passed several data quality requirements for the Inner Detector and calorimeter. To select events with back-to-back jets and to enrich the sample with fake τ candidates from QCD processes that form the main background to signatures such as $\mathrm{Z} \to \tau\tau$ the following cuts have been applied:

- The Level 1 (L1) Trigger requires a τ trigger object passing a 5 GeV threshold [171].
- No "bad" jets caused by out-of-time cosmic events or sporadic noise effects in the calorimeter are present in the event [172].
- At least one vertex reconstructed with more than four tracks is present.
- At least one τ candidate wit $p_{\mathrm{T}} > 30\,\mathrm{GeV}$ (fully calibrated) and $|\eta| < 2.5$, as well as another τ candidate with $p_{\mathrm{T}} > 15\,\mathrm{GeV}$ and $|\eta| < 2.5$ (also fully calibrated). Both candidates are required to be separated by at least 2.7 radians in azimuth.

With these cuts the properties of fake τ candidates can be studied. To remove any bias due to the trigger requirement, the leading τ candidate in each event is excluded. With the cuts and requirements mentioned above the selected data samples contains 2.9 million events with 3.9 million τ candidates.

5.4.1. Identification variables

For the comparison QCD dijet MC samples are used, where the allowed range of the transverse momenta of the outgoing partons in the rest frame of the hard interaction are restricted to be between 8 and 280 GeV. These samples are generated with *PYTHIA* [56] and passed through a *GEANT4* [96] simulation of the ATLAS detector [102]. A previous study [160] used the MC09 tune [135], while this study used the DW tune [173]. The DW tune uses virtual-ordered showers and is derived to describe the CDF

II underlying event and Drell-Yan data. The DW tune seems to model the forward activity of the underlying event better than the MC09 tune, and describes jet shapes and profiles in data more accurately. A detailed description of the data taking periods and the Monte Carlo tunes is given in the previous chapter.

In the previous section the identification of τ-leptons was discussed. It is based on several discriminating variables and includes different identification methods based on simple cuts, boosted decision trees, and projective likelihood methods [174, 175]. The identification variables used for these methods have shown good separation potential in MC studies. The variables used for the identification of τ-leptons in this study differs slightly from the variables discussed in the previous section:

- **Cluster mass:**
  Invariant mass, m_{cluster}, computed from associated topoclusters.

- **Track mass:**
  Invariant mass of the track system, m_{tracks}.

- **Track radius:**
  p_{T} weighted track width
  $$R_{\text{track}} = \frac{\sum_i^{\Delta R_i<0.2} p_{\text{T},i} \Delta R_i}{\sum_i^{\Delta R_i<0.2} p_{\text{T},i}}, \tag{5.9}$$
  where i runs over all tracks associated to the τ candidate, ΔR_i is defined relative to the τ jet seed axis and $p_{\text{T},i}$ is the track transverse momentum.

- **Leading track momentum fraction:**
  $$f_{\text{trk, 1}} = \frac{p_{\text{T, 1}}^{\text{track}}}{p_{\text{T}}^{\tau}}, \tag{5.10}$$
  where $p_{\text{T, 1}}^{\text{track}}$ is the transverse momentum of the leading track of the τ candidate and p_{T}^{τ} is the transverse momentum of the τ candidate.

- **Electromagnetic radius:**
  Transverse energy weighted shower width in the EM calorimeter, as defined in (5.6).

- **Core energy fraction:**
  Fraction of transverse energy in the core ($\Delta R < 0.1$) of the τ candidate:
  $$f_{\text{core}} = \frac{\sum_i^{\Delta R<0.1} E_{\text{T},i}}{\sum_i^{\Delta R<0.4} E_{\text{T},i}}, \tag{5.11}$$
  where i runs over all cells associated to the τ candidate within ΔR_i of the τ jet seed axis.

- **Electromagnetic fraction:**
  Fraction of GCW calibrated transverse energy of the τ candidate deposited in the EM calorimeter:
  $$f_{\text{EM}} = \frac{\sum_i^{\Delta R_i<0.4} E_{\text{T},i}^{\text{GCW}}}{\sum_j^{\Delta R_i<0.4} E_{\text{T},j}^{\text{GCW}}}, \tag{5.12}$$
  where $E_{\text{T},i}$ ($E_{\text{T},j}$) is the GCW calibrated transverse energy deposited in cell i (j), and i runs over the cells in the first three layers of the EM calorimeter, while j runs over the cells in all layers of the calorimeter.

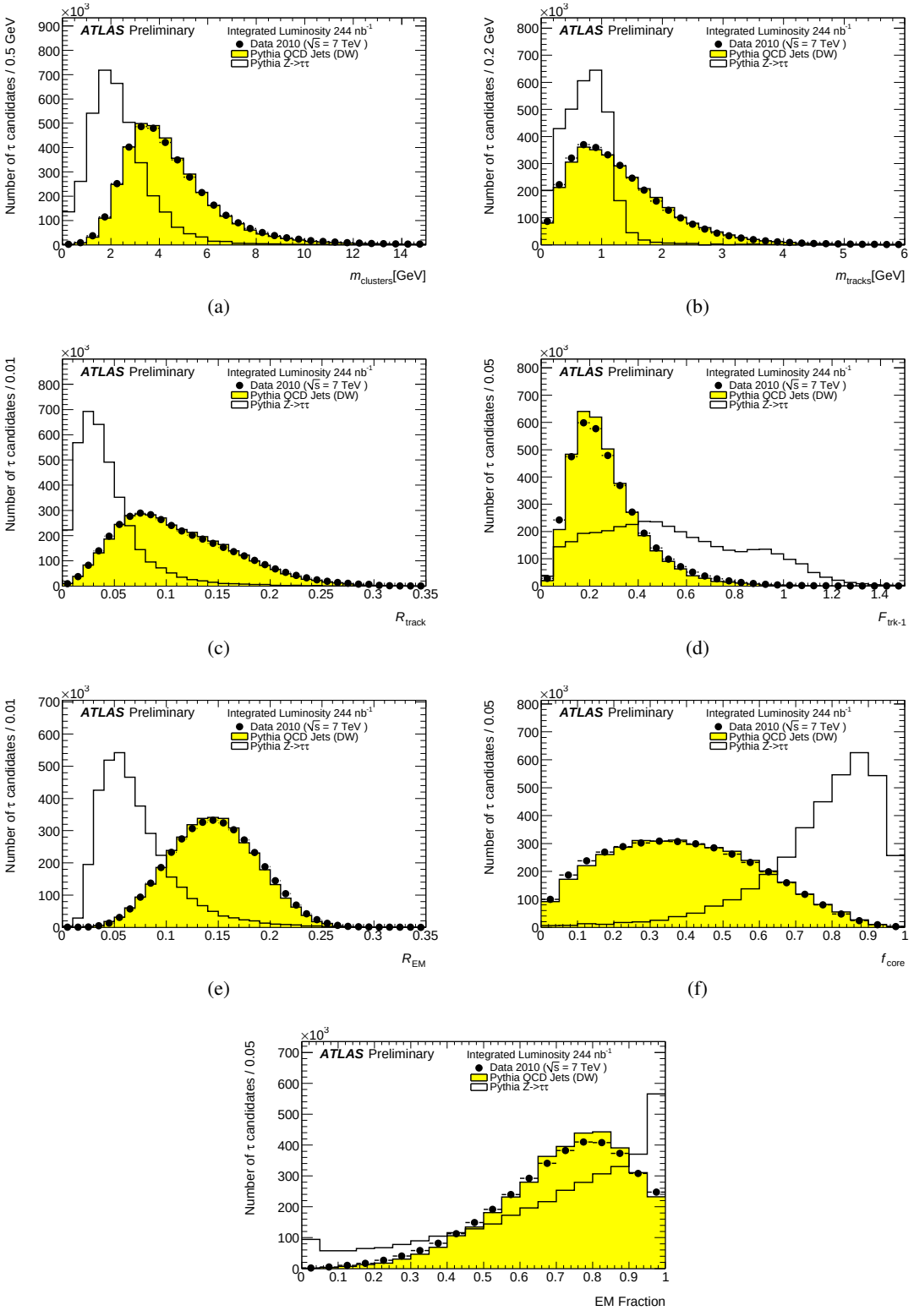

Figure 5.9.: Cluster mass, track mass, track radius, leading track momentum fraction, EM radius, core energy fraction, and EM fraction of τ candidates. The number of τ candidates in MC samples are normalized to the number of τ candidates selected in data. The statistical errors on the MC are negligible [168].

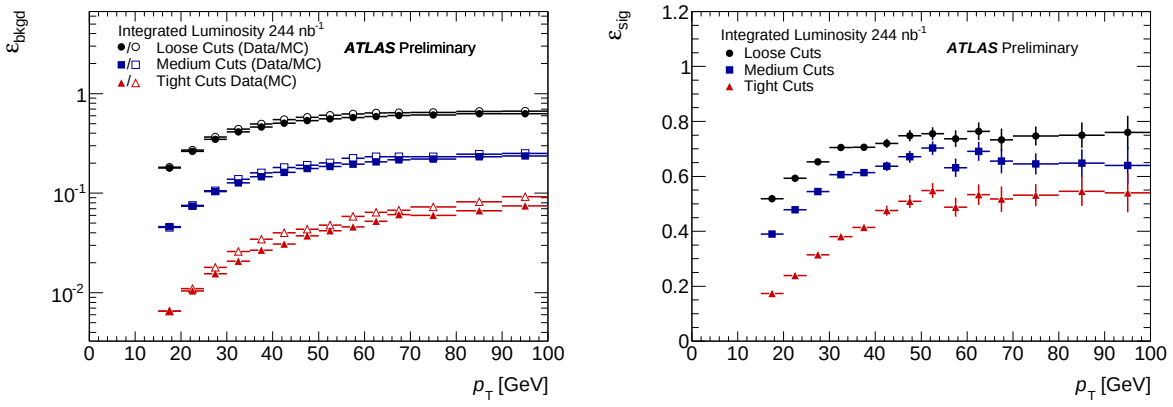

(a) (b)

Figure 5.10.: Background efficiencies obtained from data and MC samples as a function of the reconstructed p_{T}^{τ} (a) and signal efficiencies predicted by a $\mathrm{Z} \rightarrow \tau\tau$ MC sample as a function of the reconstructed p_{T}^{τ} (b) [168].

Due to the low instantaneous luminosity for the data used here, pile-up effects are expected to be small. With higher luminosity, pile-up will affect the distributions of these variables for both fake and true τ candidates.

Figure 5.9 shows the distributions for the introduced variables with data compared to DW MC tune. The shapes from τ candidates reconstructed in a signal $\mathrm{Z} \rightarrow \tau\tau$ MC09 sample and matched to true hadronically decaying τ-leptons are also overlaid to show the expected distributions of real τ-leptons. After the selection describe above, the number of τ candidates in the Monte Carlo samples are normalized to the number of τ candidates selected in data. The agreement between data and MC is quite good for all identification variables.

5.4.2. Background rejection in QCD events

The performance of the τ identification can be expressed in terms of two quantities: the signal efficiency and the background efficiency. The first is defined as

$$\varepsilon_{\mathrm{sig}} = \frac{N^{\tau}_{\mathrm{pass,match}}}{N^{\tau}_{\mathrm{match}}}, \tag{5.13}$$

where $N^{\tau}_{\mathrm{match}}$ is the number of reconstructed τ candidates matched to a true, hadronically decaying τ-lepton with visible transverse momentum $p_{\mathrm{T}}^{\mathrm{vis}} > 15\,\mathrm{GeV}$ and a visible pseudo-rapidity of $|\eta^{\mathrm{vis}}| < 2.5$ within $\Delta R < 0.2$ that are reconstructed with the correct number of associated tracks. $N^{\tau}_{\mathrm{pass,\,match}}$ is the number of these reconstructed candidates that pass the identification criteria. To evaluate the signal efficiency a $\mathrm{Z} \rightarrow \tau\tau$ MC sample is used.

The background efficiency is defined as

$$\varepsilon_{\mathrm{bkgd}} = \frac{N^{\mathrm{bkgd}}_{\mathrm{pass}}}{N^{\mathrm{bkgd}}_{\mathrm{total}}}, \tag{5.14}$$

where $N^{\mathrm{bkgd}}_{\mathrm{pass}}$ is the number of the τ candidates that pass the identification criteria, while $N^{\mathrm{bkgd}}_{\mathrm{total}}$ is the number of τ candidates.

Table 5.5.: Background efficiencies for loose, medium, and tight selection cuts. The measured background efficiencies in data are compared to the MC DW tune prediction. Uncertainties for the background efficiencies in data are from transverse momentum calibration and pile-up effects [168].

Selection	$\varepsilon_{\text{bkgd}}$ (data)	$\varepsilon_{\text{bkgd}}$ (MC)	$\varepsilon'_{\text{bkgd}}$ (data)	$\varepsilon'_{\text{bkgd}}$ (MC)
loose	$(3.2 \pm 0.2) \times 10^{-1}$	3.4×10^{-1}	$(9.4 \pm 0.6) \times 10^{-2}$	10×10^{-2}
medium	$(9.5 \pm 1.0) \times 10^{-2}$	9.9×10^{-2}	$(3.1 \pm 0.4) \times 10^{-2}$	3.3×10^{-2}
tight	$(1.6 \pm 0.3) \times 10^{-2}$	1.9×10^{-2}	$(5.6 \pm 0.9) \times 10^{-3}$	6.8×10^{-3}

The cut-based identification only uses three relatively uncorrelated variables from the quantities introduced above: R_{EM}, R_{track}, and $f_{\text{trk,1}}$. A more complex cut-based ID method will be discussed in chapter 6. The cuts are optimized on signal and background MC samples and are tuned for a minimum background efficiency at given signal efficiencies of roughly 30 % (tight), 50 % (medium), and 60 % (loose). Different cuts are applied for τ candidates with $n_{\text{track}} = 1$ and those with $n_{\text{track}} \geq 2$.

The background efficiency for data and MC samples as a function of the reconstructed p_{T}^{τ} is shown in Fig. 5.10a. The measured background efficiency in data agree well with the MC prediction ans shows a good performance with data of the cut-based identification that is optimized with MC samples. The signal efficiency obtained from the $Z \rightarrow \tau\tau$ MC sample is shown in Fig. 5.10b.

The measured background efficiency for the given data sample is listed in Tab. 5.5 together with the predictions of the Pythia DW tune. An alternative background efficiency, $\varepsilon'_{\text{bkgd}}$, is also shown, that requires in addition that τ candidates must have $n_{\text{track}} = 1$ or $n_{\text{track}} = 3$, since many analyses with hadronic τ-leptons in the final state may require this addition. The statistical uncertainties from the data are negligible, while the systematic uncertainties shown in the table a from calibration effects and pile-up effects which are being discussed later. Both effects are treated as independent.

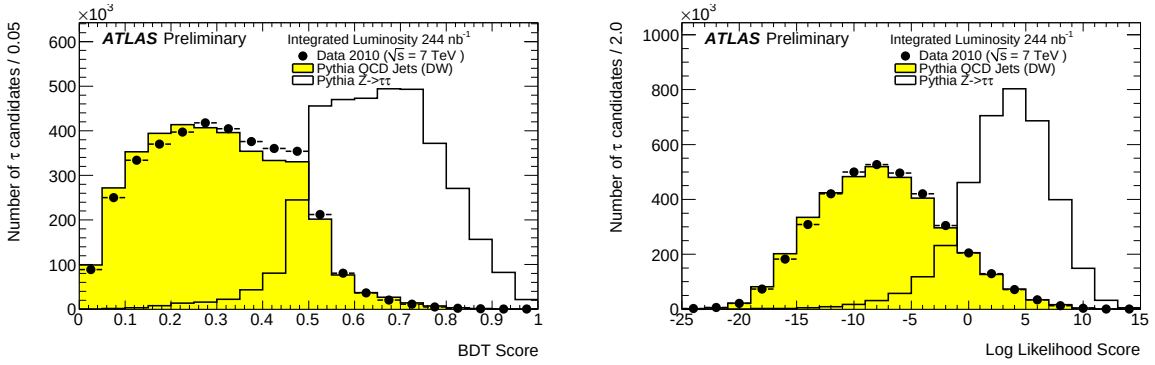

(a) (b)

Figure 5.11.: BDT jet score (a) and LL score (b) for τ candidates in data and MC samples. The number of τ candidates in the MC samples is normalized to the number of τ candidates in the data [168].

The BDT uses all seven variables listed in Section 5.4.1, while the LL uses all variables except f_{core}, due to correlations with other variables. For the training of the LL the signal and background MC samples are split in five separated p_{T} bins, while the BDT does not use split training samples. Figure 5.11 shows the distribution for the BDT score (a) and the LL score (b) for τ candidates in data compared to MC samples. The distribution for τ candidates matched to true τ-leptons in a $Z \rightarrow \tau\tau$ MC sample are also

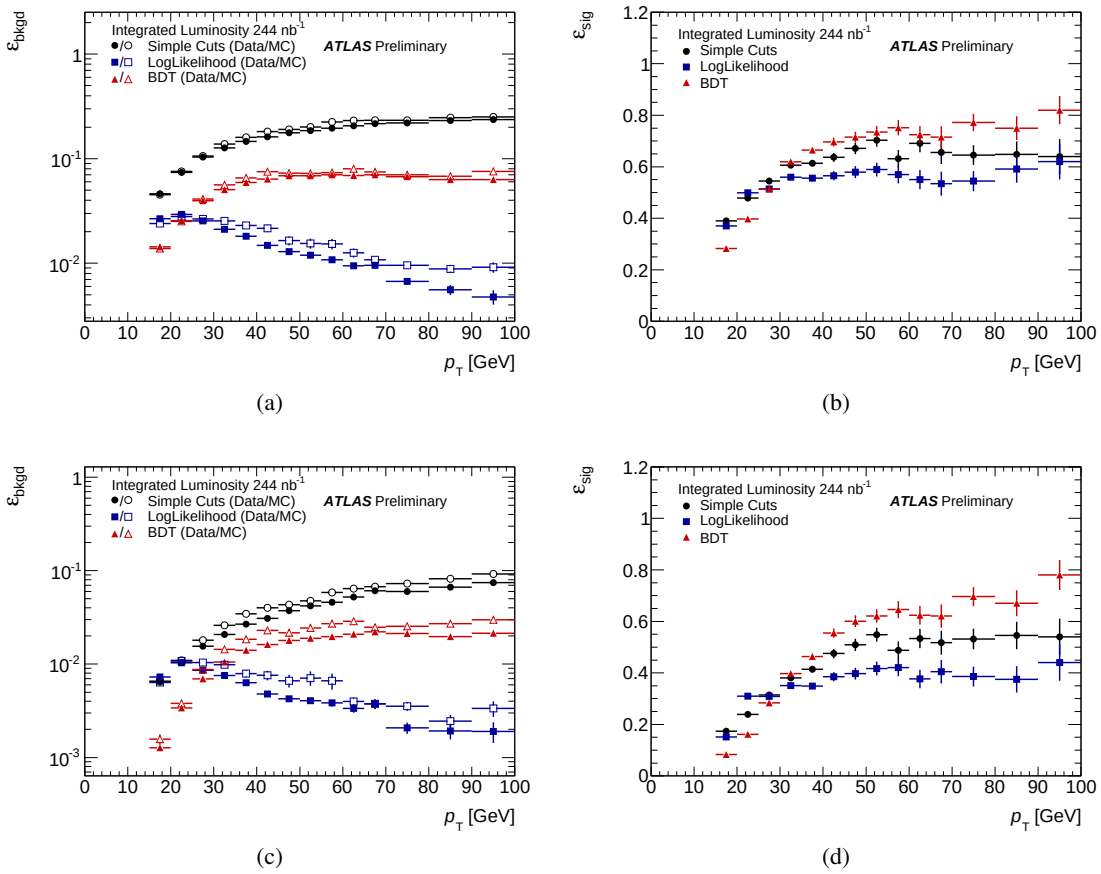

Figure 5.12.: Background efficiencies in data and MC as a function of p_{T}^{τ} with the medium selection (a) and tight selection (c) for cut-based, BDT, and LL identification and signal efficiencies from MC as a function of p_{T}^{τ} with the medium selection (b) and tight selection (d) for cut-based, BDT, and LL identification [168].

overlaid. The distributions of these multi-variate discriminants show a strong separation power, and agree reasonably well between data and the MC samples.

The background efficiencies for BDT and LL are also compared to the efficiencies of the cut-based ID method for the medium and tight selection in Fig. 5.12 (a,c) and the signal efficiency is shown in Fig. 5.12 (b,d), both as function of p_{T}^{τ}. The increased rejection power against fake τ candidates for the multi-variate discriminants against the cut-based ID is evident.

5.4.3. Systematic uncertainties

There are several systematic uncertainties associated to the variables mentioned before. Several of the variables depend on a good model of the jet width and at the time of this study, the uncertainties are dominated by the understanding of the shower shape. In the previous study [160] the MC09 tune was used, while for this study the Pythia DW tune is used, since it shows significantly better agreement between data and MC.

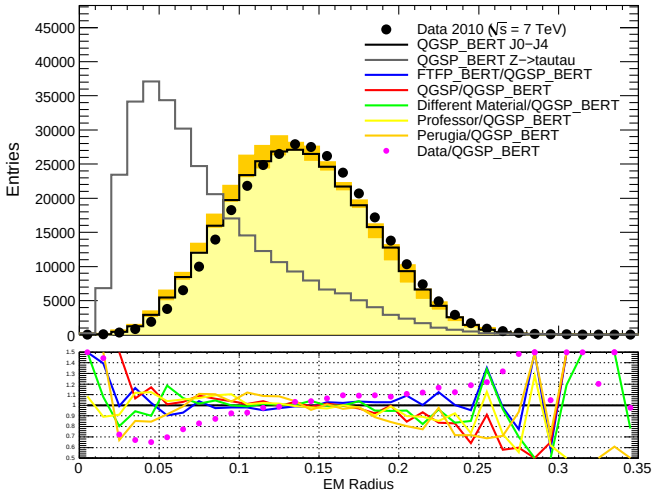

Figure 5.13.: Distribution of electromagnetic radius, showing the range of deviations from different systematic variations listed in Appendix B. The orange band in the upper plot shows the expected range of systematic uncertainties covered, while the lower plot shows the relative differences between each sample and the baseline.

Physics and detector material model

To understand the effect of different shower models Fig. 5.13 shows the distribution of R_{EM} from different systematic variations, which are listed in Tab. B obtained from the first study [160]. The total systematic uncertainty band in the upper part of Fig. 5.13 is calculated by taking the squared sum of deviations between the baseline sample and the different shower models, different underlying event tunes, different fragmentation models and different detector material distributions. Where several different alternatives exist in the same category, the maximum deviation is used. All deviations are determined separately for positive and negative deviations from the baseline. In this case the baseline was the MC09 tune while for later studies the Pythia DW tune is used. For this study Fig. 5.14 shows all seven discriminating variables with the Pythia DW tune as baseline, overlaid by data. The uncertainty band is derived from using a sample generated with Perugia2010. The Pythia DW tune gives the best description of jet widths of any ATLAS dijet sample. Perguia2010 does not describe the jet widths as well, but is still a significant improvement compared to the default MC09 tune and is the recommended tune by the ATLAS MC tuning group. The effect of different shower models for the multi-variate discriminants is shown in Fig. 5.15a for the BDT score and in Fig. 5.15c for the LL score.

Another source of uncertainty is the detector material model. It can also effect several of the τ discriminating variables. The effect of changing the detector material is shown in Fig. 5.16. Special samples with additional detector material have been produced with the following changes:

- 5 % X0 between barrel and strip,
- 20 % X0 in barrel cryostat before the presampler, and
- 20 % X0 in cryostat after the LAr calorimeter.

Since these alternative samples only exist for the MC09 tune the relative difference to the standard MC09

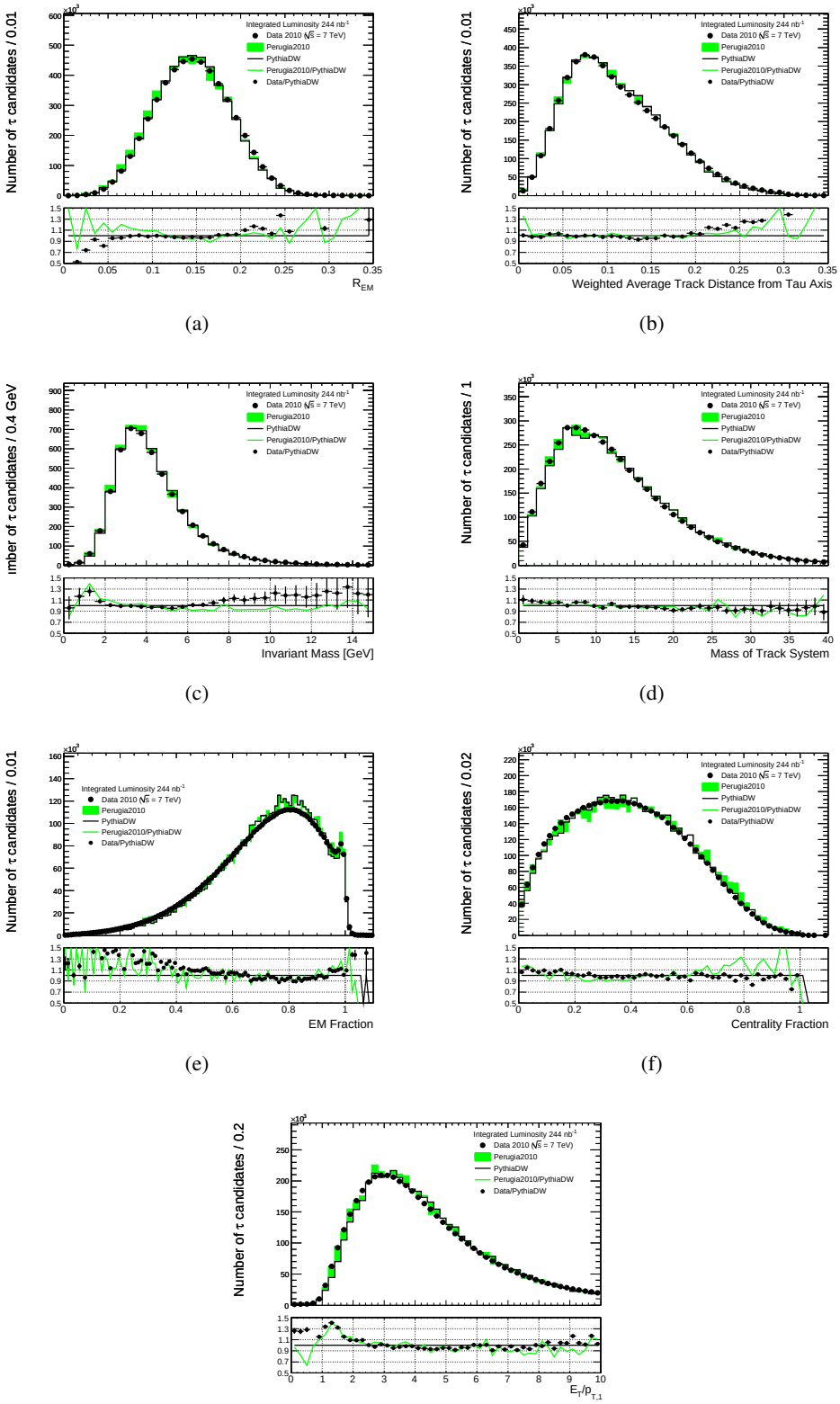

Figure 5.14.: Systematic uncertainties from choice of Pythia tune. DW is chosen as baseline and is compared to Perugia2010.

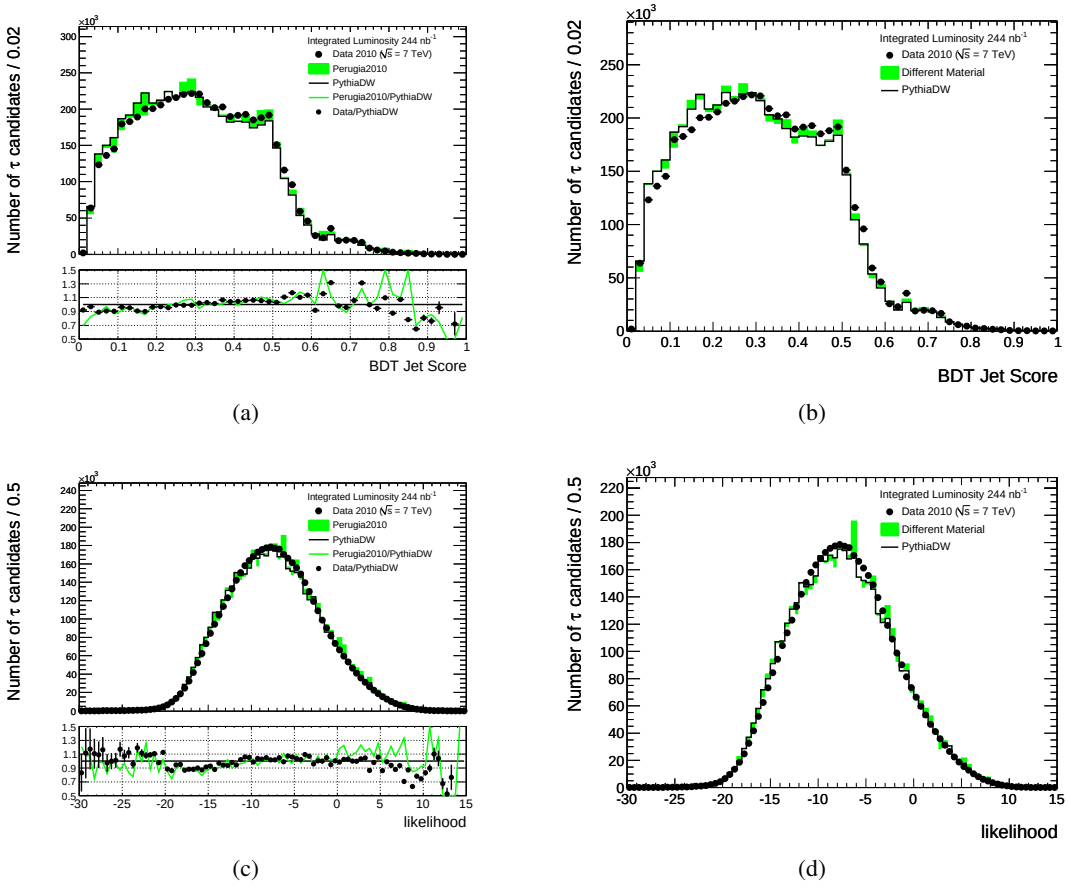

Figure 5.15.: The systematic uncertainty obtained from varying the Pythia tune (left) and the detector material model (right) on the BDT (top) and LL (bottom) output.

tune is calculated and then applied to the baseline DW tune. The effect of additional detector material for the multi-variate discriminants is shown in Fig. 5.15b for the BDT score and in Fig. 5.15d for the LL score.

Energy scale and different beam conditions

Two other effects of systematic uncertainties on the measured background efficiency come from the transverse momentum calibration and pile-up effects due to varying beam conditions.

The transverse momentum calibrations presented in this study are based on the global cell energy-density weighting (GCW) calibration scheme. To study the effect of different calibration schemes, a simple p_{T} and η dependent calibration (EM+JES) [176] is studied and the variation of the background efficiency is determined by comparing the calibration of τ candidates using the GCW scheme with the EM+JES scheme.

Three of the seven identification variables are effected by using different calibration schemes: m_{cluster}, f_{EM}, and $f_{\mathrm{trk,1}}$, where the cut-based ID only uses the last variable. The relative difference in the background efficiency for the cut-based ID method using the two calibration schemes is shown in Fig. 5.17a as a function of p_{T}^{τ}. When using the EM+JES calibration scheme, the background efficiency drops by

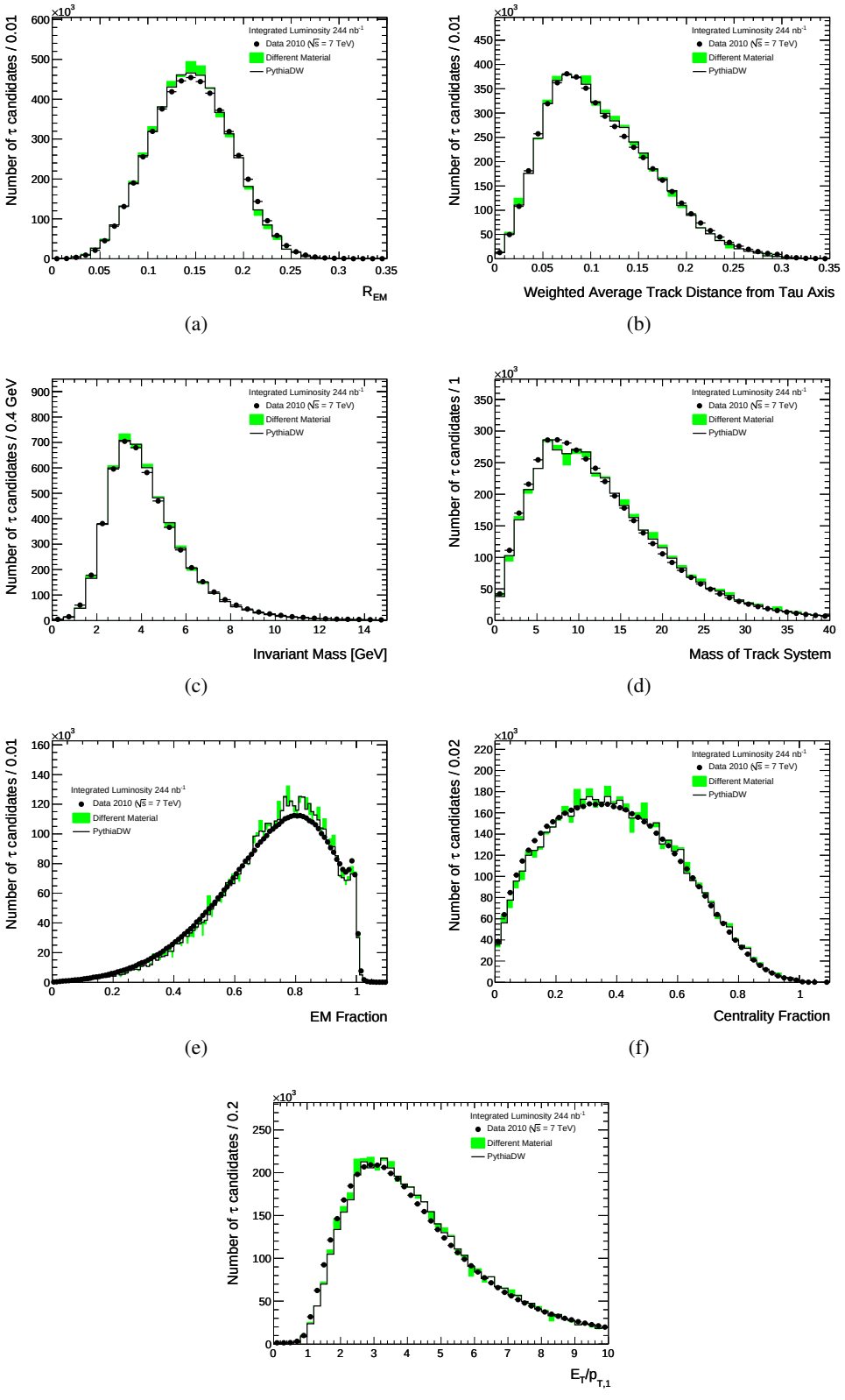

Figure 5.16.: Systematic uncertainties from different ATLAS material model are shown for each of the 7 discriminating variables. Since these alternative samples only exist for the MC09 tune the relative difference to the standard MC09 tune is calculated and then applied to the baseline DW tune.

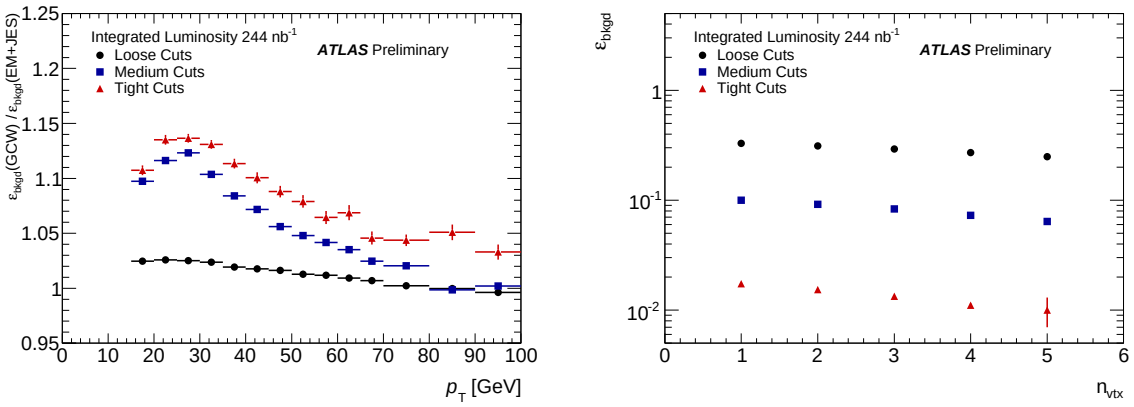

(a) (b)

Figure 5.17.: Ratio of background efficiencies using EM+JES and GCW calibrations as a function of p_{T}^{τ} (a) and background efficiencies as a function of n_{vtx} (b) [168].

2.1 %, 8.5 %, and 9.6 % for the loose, medium, and tight selections, respectively.

Since the start of the 7 TeV collisions the beam intensity has been increase nearly by a factor of 3 orders of magnitude (luminosity is proportional to beam intensity^2. According to these changes, the data taking period is divided into categories. As listed in Tab. 4.1 in Chapter 4, the biggest change occurs in period D, where large luminosity enhancement compared to the previous periods can bee seen.

The increased beam intensities lead to different pile-up conditions that also effect the distribution of the identification variables. The average total number of particles will increase, which can affect the measured shower shape. Since the number of vertices n_{vtx} is highly correlated with pile-up activity, the background efficiency is evaluated as a function of n_{vtx} for the cut-based identification method. This is shown in Figure 5.17b.

The systematic uncertainty can be determined by taking the mean difference of the background efficiency in events with $n_{\mathrm{vtx}} = 1$ and $n_{\mathrm{vtx}} > 1$. The resulting uncertainties are 5.7 %, 9.3 %, and 14.5 % for the loose, medium, and tight selection, respectively.

Beam spot variations, the impact of calorimeter noise, and detector alignment are other sources of systematic uncertainties. Their affect is found to be small.

5.4.4. First τ candidates in ATLAS

In May 2010 the first candidate for a $\mathrm{W} \rightarrow \tau\nu$ decay with a hadronically decaying τ-lepton has been observed. The display of this event is shown in Fig. 5.18. The first $\mathrm{Z} \rightarrow \tau\tau$ candidate with the decay $Z \rightarrow \tau^+\tau^- \rightarrow \mu^+\nu\nu\tau_h^-\nu$, where τ_h denotes a hadronic τ decay has been observed in August 2010. The display is shown in Fig. 5.19. The hadronic τ candidate has three well defined tracks, and the μ and the τ have opposite sign reconstructed charges.

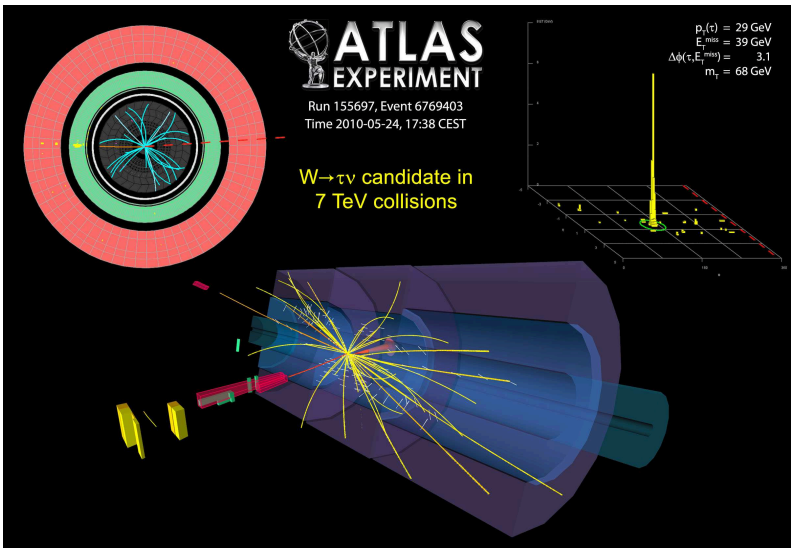

Figure 5.18.: W $\rightarrow \tau\nu$ event display, with a hadronically decaying τ-lepton. No additional object (electron, muon, or jet) was found in the event [177].

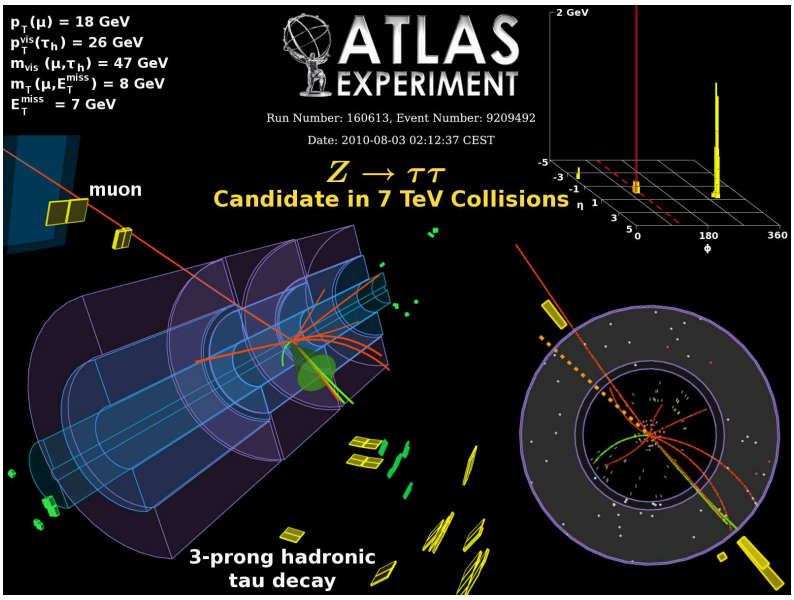

Figure 5.19.: Z $\rightarrow \tau\tau$ event display, with a hadronically decaying τ-lepton [177].

6. Cut-based Identification of Hadronic τ Decays

In the previous chapter the reconstruction and general identification of hadronic τ-lepton decays was discussed. To distinguish candidates originating from hadronically decaying τ-leptons and those originating from jets, an identification after the reconstruction step must be performed.

Multivariate techniques like logarithmic likelihood (LL) or boosted decision trees (BDT) are complex methods, based on several input variables and returning one value per event (see Fig. 5.11). The LL consists of building a model out of probability density functions (PDF) that reproduces the input variables for signal and background. Correlations among the variables are ignored. A decision tree is a binary tree structured classifier repeating yes/no decisions on a single variable at a time until some stop criteria is reached. The boosting of the tree represents an extension to a single tree decision. Several decision trees (called forest) are combined to form a classifier which is given by a (weighted) majority vote of the individual decision trees. Due to their complexity multivariate techniques are sensitive to uncertainties and calibration, which makes them less preferred choice for early data taking phases.

Hence the cut-based identification method presented in this chapter uses only a reduced number of variables that will be well understood in the early data taking phases (robust variables). Therefore some variables are avoided, including those based on: precision tracking (i.e. variable depending on secondary vertex reconstruction or impact parameter significances), π^0 reconstruction, energy-flow calculations, number of cells in the η-strip layer that exceeds 200 MeV, τ specific energy calibrations, and the number of tracks that are found in an isolation region (outside ΔR[1] > 0.2).

Two cut-based methods have been implemented in the ATLAS offline reconstruction software ATHENA [166], one method (calorimeter identification method) uses variables that are derived from calorimetric energy deposits only, and can be used in case the tracking detectors are not well understood. The other method (calorimeter+tracking method) extends the number of variables used, to include information from tracks associated to the τ candidates (within $\Delta R < 0.2$). The variables of each method and the optimization procedure is discussed in Section 6.1. The performance of each method is discussed in Section 6.2.

6.1. Cut-based method for τ Identification

Currently three types of optimization for both methods are defined: tight, medium, and loose, corresponding to efficiencies of approximately 0.3, 0.5, and 0.7. The efficiencies are calculated with respect to the number of true hadronically decaying τ-leptons with $E_{\mathrm{T}}^{\mathrm{vis}} > 10\,\mathrm{GeV}$ and $|\eta| < 2.5$.

These cuts are separately optimized for τ candidates with one or zero tracks and those with two or more tracks. In addition, the optimization is performed in reconstructed $E_{\mathrm{T}}^{\mathrm{vis}}$ bins. The optimization of the calorimeter identification method is performed on all τ candidates with a calo-seed, while the calorimeter+tracking identification method is optimized on τ candidates with both, track and calo-seeds.

[1] $\Delta R = \sqrt{\Delta\eta^2 + \Delta\phi^2}$

The data samples used for the optimization come from the central ATLAS CSC production. Official Raw Data Object (RDO) files are reconstructed with release 14.2.0 and the resulting ntuples are analyzed. The optimization is performed using Pythia samples [55] of Z $\rightarrow \tau\tau$ and $bbA \rightarrow \tau\tau$ (m_A = 800 GeV, to give high E_{T} τ-leptons) events for signal and Pythia dijet events with a momentum transfer at hard scatter ranging from 17 – 140 GeV for background. The physics event samples are listed in Tab. 6.1 and Tab. 6.2.

Table 6.1.: 14 TeV signal samples

Dataset ID	channel	number of events	x-section
005188	$Z \rightarrow \tau\tau$	131500	$1.64{\cdot}10^3$ pb
005862	$bbA \rightarrow \tau\tau$	66750	0.0152 pb

Table 6.2.: 14 TeV background samples

Dataset ID	channel	number of events	x-section
005010	Dijet J1 (17 – 35 GeV)	78500	$1.38{\cdot}10^9$ pb
005011	Dijet J2 (35 – 70 GeV)	141000	$93.3{\cdot}10^6$ pb
005012	Dijet J3 (70 – 140 GeV)	123950	$5.88{\cdot}10^6$ pb

6.1.1. Variables for the calorimeter identification method

This method applies selection criteria on calorimeter seeded τ candidates. It uses a selection of four calorimetric variables. The following variables are used:

- **Electromagnetic radius**
  The electromagnetic radius R_{EM} is defined as

$$R_{\mathrm{EM}} = \frac{\sum_{i=1}^{\Delta R<0.4} E_{\mathrm{T},i}^{\mathrm{EM}} \sqrt{\left(\eta_i^{\mathrm{EM}} - \eta_{\text{calo seed}}\right)^2 + \left(\phi_i^{\mathrm{EM}} - \phi_{\text{calo seed}}\right)^2}}{\sum_{i=1}^{\Delta R<0.4} E_{\mathrm{T},i}^{\mathrm{EM}}},$$

  where i runs over all cells in the associated topoclusters of the τ candidate. The quantities $\eta_{\mathrm{i}}^{\mathrm{EM}}$, $\phi_{\mathrm{i}}^{\mathrm{EM}}$ and $E_{\mathrm{T,i}}^{\mathrm{EM}}$ denote the position and transverse energy of cell i, while $\eta_{\text{calo seed}}$ and $\phi_{\text{calo seed}}$ are the coordinates for the calorimeter seeded τ candidate.

- **Transverse energy width in the η strip layer**

The transverse energy width W_{strip} in the η strip layer is defined as

$$W_{\text{strip}} = \sqrt{\frac{\sum_{i}^{\Delta R<0.4} E_{\text{T},i}^{\text{strip}} \left(\eta_i - \eta_{\text{calo seed}}\right)^2}{\sum_{i}^{\Delta R<0.4} E_{\text{T},i}^{\text{strip}}}},$$

where the sum runs over strip cells in the associated topoclusters of the τ candidate and $E_{\text{T},i}^{\text{strip}}$ is the corresponding strip transverse energy.

- **Isolation in the calorimeter**
  The isolation fraction f_{iso} is defined as

$$f_{\text{iso}} = \frac{\sum_{i}^{0.1<\Delta R<0.2} E_{\text{T},i}^{\text{EM}}}{\sum_{j}^{\Delta R<0.4} E_{\text{T},j}^{\text{EM}}},$$

  where the indices i and j run over the electromagnetic cell transverse energies $E_{\text{T},i}^{\text{EM}}$ and $E_{\text{T},j}^{\text{EM}}$ in the associated topoclusters of the τ candidate.

- **Ratio of EM energy and total energy**
  The ratio $\frac{E_{\text{T}}^{\text{EM}}}{E_{\text{T}}^{\text{total}}}$ is defined as

$$\frac{E_{\text{T}}^{\text{EM}}}{E_{\text{T}}^{\text{total}}} = \frac{\sum_{i}^{\Delta R<0.4} E_{\text{T},i}^{\text{EM}}}{\sum_{i}^{\Delta R<0.4} E_{\text{T,i}}^{\text{EM}} + \sum_{j}^{\Delta R<0.4} E_{\text{T},j}^{\text{Had}}},$$

  where the sums run over all cells in the associated topoclusters of the τ candidate, $E_{\text{T},i}^{\text{EM}}$ is the cell energy in the electromagnetic calorimeter and $E_{\text{T},j}^{\text{Had}}$ the energy in the hadronic calorimeter, both taken after the global cell weighting calibration.

The distributions for these variables are shown in Fig. 6.1 for 1-prong τ candidates within a $E_{\text{T}}^{\text{vis}}$ range of 25 – 45 GeV and for 3-prong τ candidates in the same $E_{\text{T}}^{\text{vis}}$ range in Fig. 6.2. The distributions for the remaining $E_{\text{T}}^{\text{vis}}$ ranges can be found in Section A.1.

6.1.2. Variables for the calorimeter+track identification method

The calorimeter+track identification method applies selection criteria on τ candidates seeded by both, a calorimeter jet and a track. It combines the four variables of the calorimeter-based identification method described in Section 6.1.1 with five variables that involve tracking. This method gives a better performance due to a larger number of variables providing additional information. For these variables the energies of cells associated to the τ candidate within $\Delta R < 0.4$ of the track seed direction are considered.

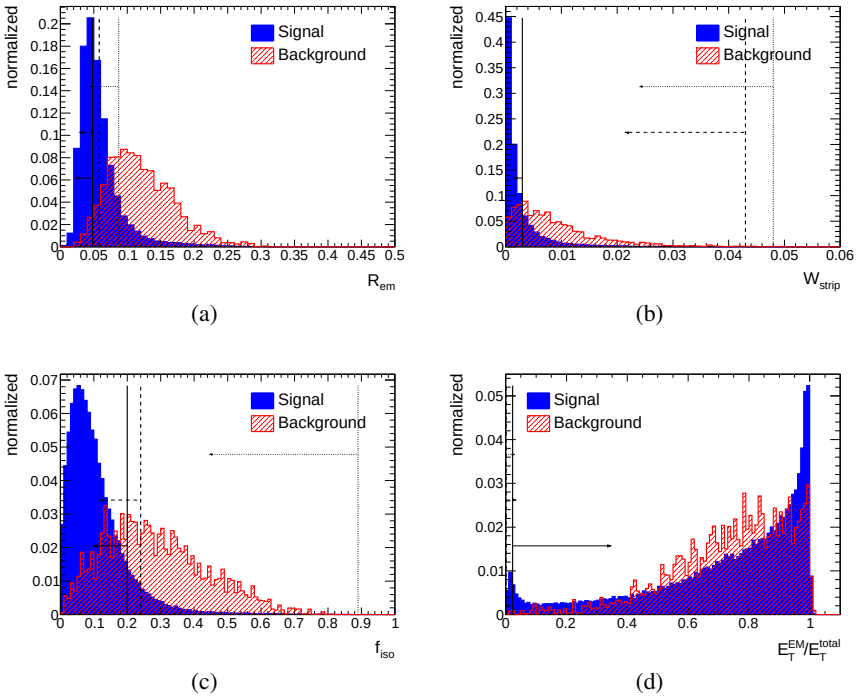

Figure 6.1.: Distribution of calorimeter variables for 1-prong τ-lepton candidates within a $E_{\mathrm{T}}^{\mathrm{vis}}$ range of 25 – 45 GeV, position of tight (solid line), medium (dashed line), and loose (dotted line) cuts are shown.

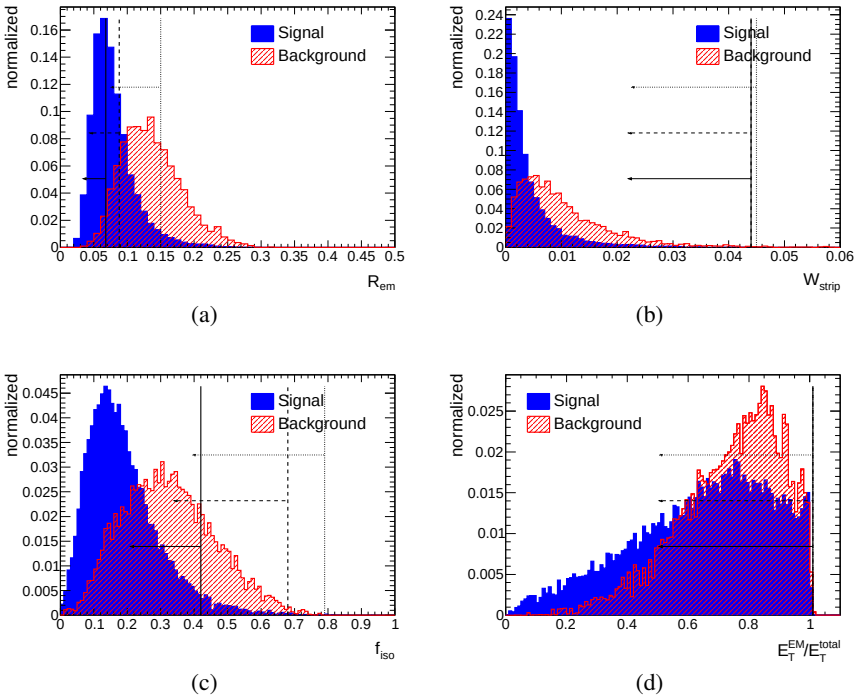

Figure 6.2.: Distribution of calorimeter variables for 3-prong τ-lepton candidates within a $E_{\mathrm{T}}^{\mathrm{vis}}$ range of 25 – 45 GeV, position of tight (solid line), medium (dashed line), and loose (dotted line) cuts are shown.

- **E_{T} over p_{T} of the leading track**
  The ratio $E_{\mathrm{T}}/p_{\mathrm{T1}}$ is defined as

$$\frac{E_{\mathrm{T}}}{p_{\mathrm{T1}}} = \frac{\sum_i E_{\mathrm{T},i}^{\mathrm{EM}} + \sum_i E_{\mathrm{T},i}^{\mathrm{Had}}}{p_{\mathrm{T1}}},$$

  where $E_{\mathrm{T},i}^{\mathrm{EM}}$ and $E_{\mathrm{T},i}^{\mathrm{Had}}$ are the globally weighted transverse energies of the cells associated to the τ candidate in the EM and hadronic calorimeters, respectively, and p_{T1} is the transverse momentum of the leading track.

- **Ratio of EM energy and sum of p_{T} of tracks**
  The variable $\frac{E_{\mathrm{T}}^{\mathrm{EM}}}{p_{\mathrm{T}}^{\mathrm{total}}}$ is defined as

$$\frac{E_{\mathrm{T}}^{\mathrm{EM}}}{p_{\mathrm{T}}^{\mathrm{total}}} = \frac{\sum_i E_{\mathrm{T},i}^{\mathrm{EM}}}{\sum_{j=1}^{N} p_{\mathrm{T},j}^{track}},$$

  where $E_{\mathrm{T},i}^{\mathrm{EM}}$ is the energy after global cell weighting calibration in cell i and the sum in the denominator runs over the transverse momenta $p_{\mathrm{T}}^{\mathrm{track}}$ of the $N = \min(\mathrm{n}, 3)$ highest p_{T} tracks associated to the n-prong τ candidate.

- **Ratio of hadronic energy and sum of p_{T} of tracks**
  The ratio $\frac{E_{\mathrm{T}}^{\mathrm{Had}}}{p_{\mathrm{T}}^{\mathrm{total}}}$ is defined as

$$\frac{E_{\mathrm{T}}^{\mathrm{Had}}}{p_{\mathrm{T}}^{\mathrm{total}}} = \frac{\sum_i E_{\mathrm{T},i}^{\mathrm{Had}}}{\sum_{j=1}^{N} p_{\mathrm{T},j}^{\mathrm{track}}},$$

  where $E_{\mathrm{T},i}^{\mathrm{Had}}$ is the energy in cell i after global cell weighting calibration and the sums in the denominator run over the transverse momenta $p_{\mathrm{T}}^{\mathrm{track}}$ of the $N = \min(\mathrm{n},3)$ highest p_{T} tracks associated to the τ candidate.

- **Ratio of sum of p_{T} of tracks and total energy**
  The ratio $\frac{p_{\mathrm{T}}^{\mathrm{total}}}{E_{\mathrm{T}}^{\mathrm{total}}}$ is defined as

$$\frac{p_{\mathrm{T}}^{\mathrm{total}}}{E_{\mathrm{T}}^{\mathrm{total}}} = \frac{\sum_{k=1}^{N} p_{\mathrm{T},k}^{\mathrm{track}}}{\sum_i E_{\mathrm{T},i}^{\mathrm{EM}} + \sum_j E_{\mathrm{T},j}^{\mathrm{Had}}},$$

  where the sum in the numerator runs over the transverse momentum $p_{\mathrm{T}}^{\mathrm{track}}$ of the $N = \min(\mathrm{n}, 3)$ leading tracks associated to the n-prong τ candidate. $E_{\mathrm{T},i}^{\mathrm{EM}}$ is the cell energy in the electromagnetic calorimeter and $E_{\mathrm{T},j}^{\mathrm{Had}}$ the cell energy in the hadronic calorimeter, with cell energies being taken after global cell weighting calibration. This variable is the reciprocal of $E_{\mathrm{T}}^{\mathrm{total}}/p_{\mathrm{T1}}$ for 1-prong τ candidates.

- **Track spread**
  The spread of tracks in η, ϕ-space, weighted with their transverse momentum, $\mathrm{W}_{\mathrm{track}}^{\tau}$, for multi-track candidates is defined as

$$W_{\mathrm{track}}^{\tau} = \frac{\sum \left(\Delta R^{\mathrm{track}}\right)^2 \cdot p_{\mathrm{T}}^{\mathrm{track}}}{\sum p_{\mathrm{T}}^{\mathrm{track}}} - \frac{\left(\sum \Delta R^{\mathrm{track}} \cdot p_{\mathrm{T}}^{\mathrm{track}}\right)^2}{\left(\sum p_{\mathrm{T}}^{\mathrm{track}}\right)^2},$$

  where $\Delta R^{\mathrm{track}}$ is the distance between the track and the τ candidate track seed in $\eta - \phi$ space, and the summation is performed over all tracks associated to the τ candidate.

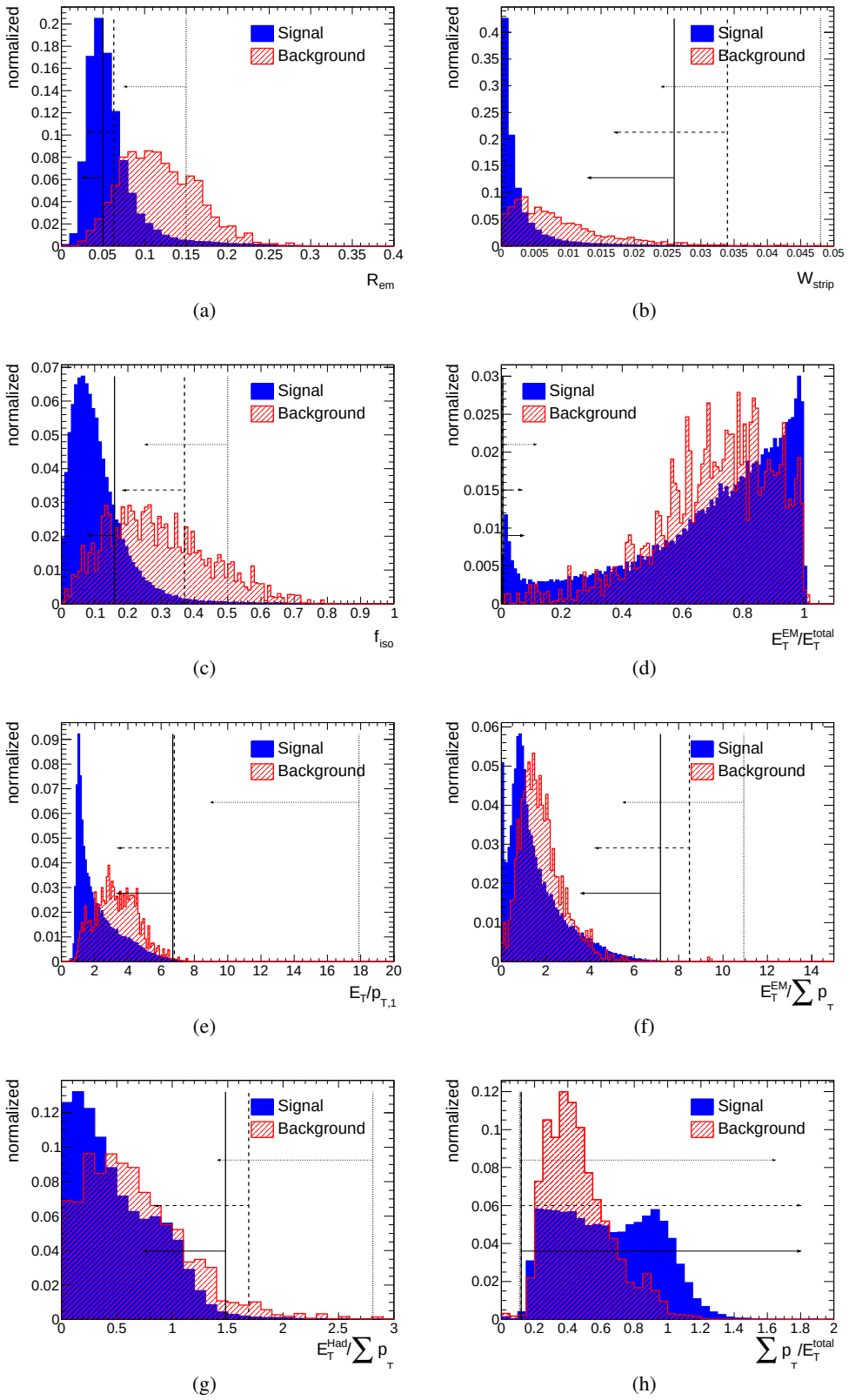

Figure 6.3.: Distribution of calorimeter and tracking variables for 1-prong τ-lepton candidates within a E_T^{vis} range of 25 – 45 GeV, position of tight (solid line), medium (dashed line), and loose (dotted line) cuts are shown.

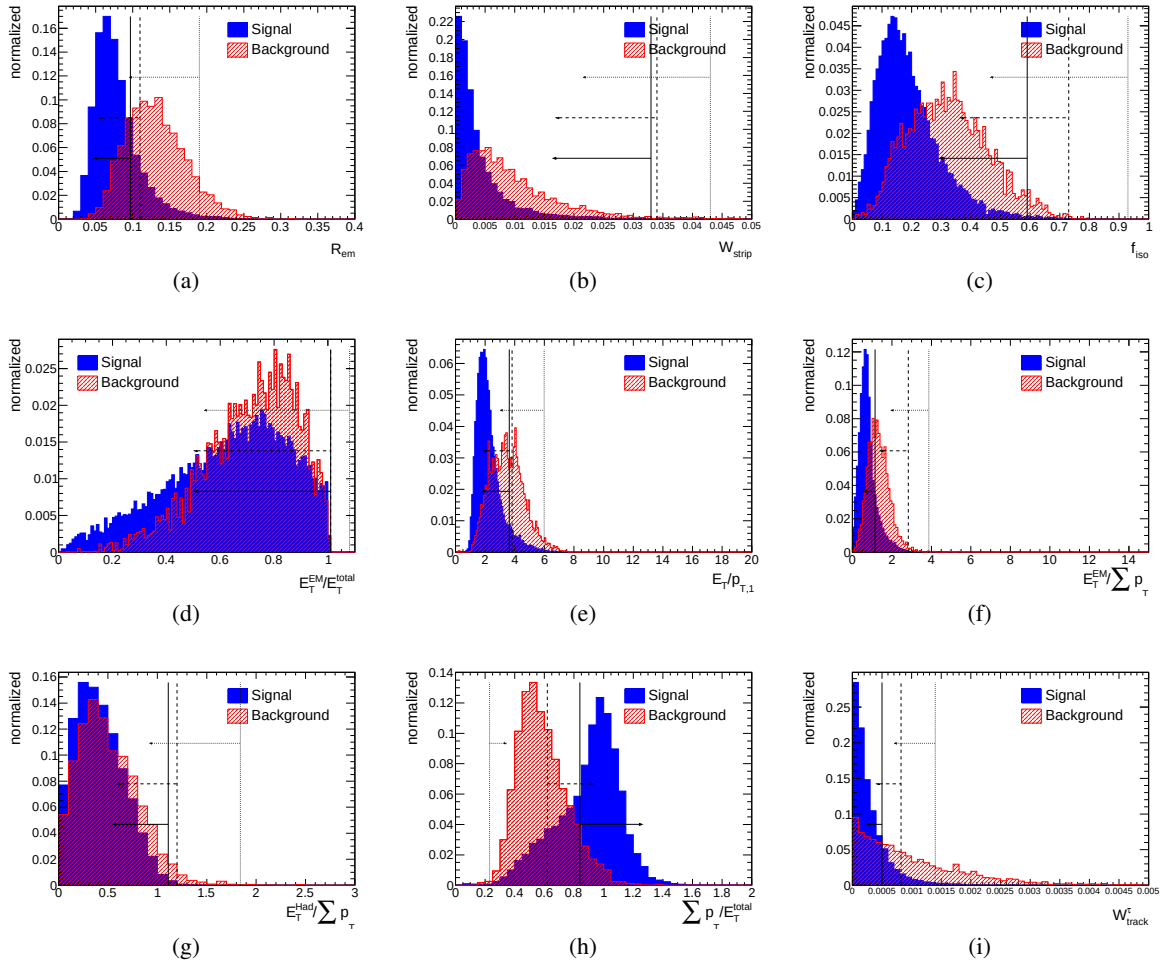

Figure 6.4.: Distribution of calorimeter and tracking variables for 3-prong τ-lepton candidates within a $E_{\mathrm{T}}^{\mathrm{vis}}$ range of 25 – 45 GeV, position of tight (solid line), medium (dashed line), and loose (dotted line) cuts are shown.

The distributions described above are shown in Fig. 6.3 for 1-prong τ candidates in the $E_{\mathrm{T}}^{\mathrm{vis}}$ range of 25 – 45 GeV and for 3-prong τ candidates in the same $E_{\mathrm{T}}^{\mathrm{vis}}$ range in Fig. 6.4. The distributions for the remaining $E_{\mathrm{T}}^{\mathrm{vis}}$ ranges are shown in Section A.2.

6.1.3. Optimization procedure

Since many physics processes have a small production cross section, compared to those from different production mechanism it is essential to develop methods, which classify events as those that have a higher probability to come from the physical process of interest (signal) and those that have a higher probability to come from other processes (background). Multivariate classification methods based on machine learning techniques are one possible solution. The cut-based identification method is a compromise between using as much information as possible on one side and being robust against uncertainties in the first phase of data taking on the other side. Hence this identification method does not use multivariate methods but less complex rectangular cuts and uses only variables declared to be robust.

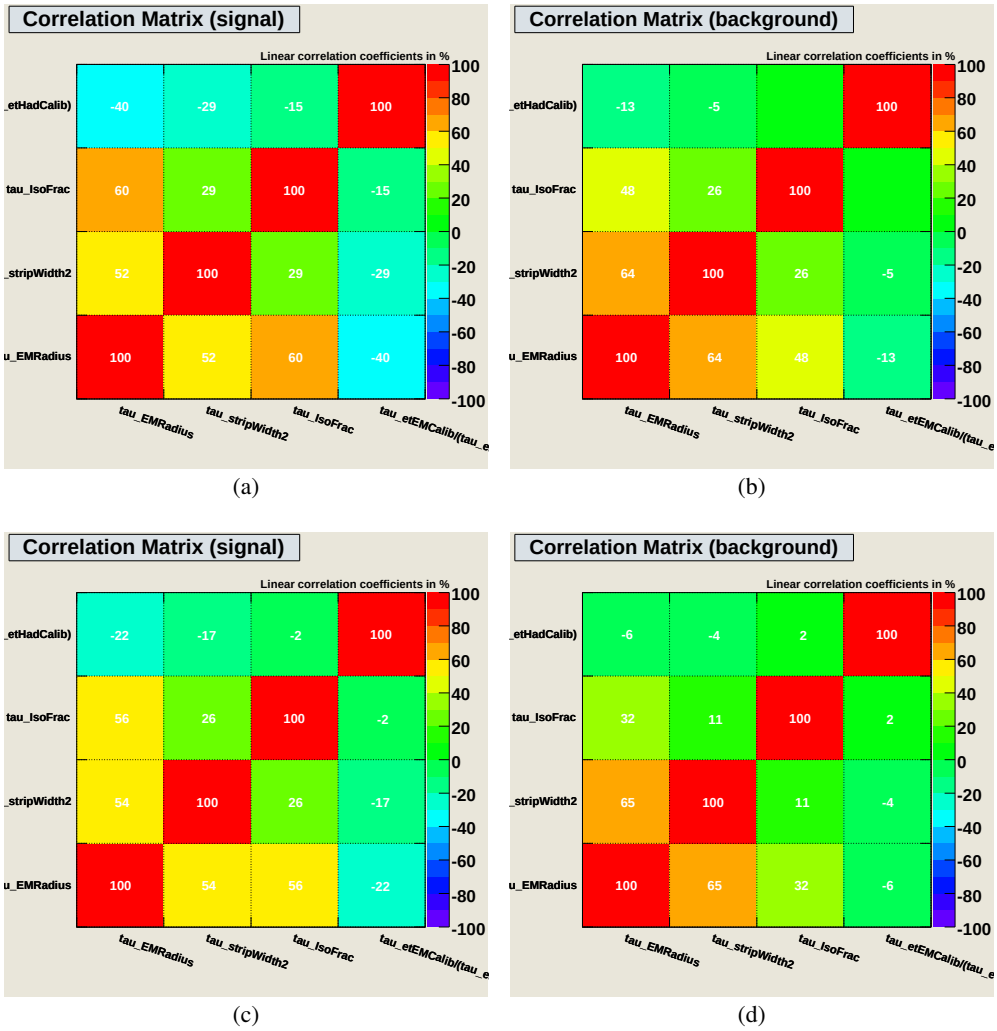

Figure 6.5.: Correlation matrix of calorimeter-based approach for 1-prong τ candidates and multi-prong τ candidates for signal (a, c) and background (b, d) for a $E_{\mathrm{T}}^{\mathrm{vis}}$ range of 25 – 45 GeV.

For the first phase of optimization TMVA, a Toolkit for Multivariate Data Analysis [178] is used. TMVA provides a ROOT-integrated environment for the processing and parallel evaluation of sophisticated multivariate classification techniques as well as rectangular cut optimization based on a genetic algorithm. The optimization is performed in two steps: training and testing together with visualizing the performance. A detailed description of the TMVA package can be found in [178].

The optimization for the cut-based selections is performed in multiple steps for five $E_{\mathrm{T}}^{\mathrm{vis}}$-bins (10 – 25 GeV, 25 – 45 GeV, 45 – 70 GeV, 70 – 100 GeV and >100 GeV) and for 1-prong and 3-prong τ-lepton candidates separately. For the training and testing the data composition of the samples must be known (event classification). By using separate signal and background samples as defined in Tab. 6.1 for signal and Tab. 6.2 for the background, a unique event classification is ensured. For performance reasons the samples are split into samples with only 1-prong τ candidates and only 3-prong τ candidates. TMVA splits the input samples into training samples and testing samples. The number of training events can be

chosen by the user, while the remaining events are used for testing. For the optimization of the cut-based identification the ratio is 1:1.

All variables classified as safe variables are used as input for a rectangular cut optimization which is the most simplest and most common classifier for selecting signal events. Unlike to all other TMVA classifiers it returns a binary response (signal or background). The optimization maximizes the background rejection at a given signal efficiency, and scans over the full range of the latter quantity.

The genetic algorithm (GA) is used as optimization method. It is a technique to find approximate solutions to optimization or search problems. The problem is modeled by a group (*population*) of abstract representations (*genomes*) of possible solutions (*individuals*). By applying means the individuals of the population should evolve towards and optimal solution of the problem. Apart from the abstract representation of the solution domain, a fitness function must be defined. This fitness function depends on the problem. It either returns a value representing the goodness of an individual or it compares two individuals and indicates which of them performs better. In the rectangular cut optimization it is given by good background rejection combined with high signal efficiency.

During initialization, all parameters of all individuals (cut ensembles from the previous defined variables) are chosen randomly. The individuals are evaluated in terms of their background and signal efficiency using the fitness function. Each cut ensemble that gives an improvement in the background rejection for a specific signal efficiency bin is stored. The fitness of each individual is assessed, where the fitness is determined by the difference of the best found background rejection for a given signal efficiency and the value produced by the current individual. Hence the algorithm is forced to focus on the region where the potential of improvement is the highest. Individuals with a good fitness are selected to produce the next generation. New individuals are created by crossover and mutated afterwards. The mutation changes some values of some parameters of some individuals randomly according to a Gaussian distribution function. This process can be controlled with parameters.

Before starting the optimization several configuration options can be set. First the cut boundaries for all input variables listed in Section 6.1 are defined. From Fig. 6.3 it becomes clear that for the variables R_{EM}, W_{strip}, f_{iso}, $E_{\mathrm{T}}^{\mathrm{total}}/p_{\mathrm{T1}}$, $\frac{E_{\mathrm{T}}^{\mathrm{EM}}}{p_{\mathrm{T}}^{\mathrm{total}}}$, and $\frac{E_{\mathrm{T}}^{\mathrm{Had}}}{p_{\mathrm{T}}^{\mathrm{total}}}$ smaller cuts need to be applied to separate signal and background, while for the variables $\frac{E_{\mathrm{T}}^{\mathrm{EM}}}{E_{\mathrm{T}}^{\mathrm{total}}}$ and $\frac{p_{\mathrm{T}}^{\mathrm{total}}}{E_{\mathrm{T}}^{\mathrm{total}}}$ greater cuts need to be applied. This option is set for each selection, calorimeter or calorimeter+track method, and 1-prong or 3-prong τ candidates separately.

The optimization is performed in several steps. A so-called "constrained method" is used to guarantee a consistent identification of the τ-lepton between the three types of optimization; i.e. τ-leptons identified with the tight selection must be identified with the medium and loose selection, too, and τ-leptons identified with the medium selection must be identified with the loose selection. Five iteration steps of signal efficiency from $0.9 \rightarrow 0.7 \rightarrow 0.5 \rightarrow 0.3 \rightarrow 0.1$ are performed. For the first iteration step no cut range on the input variables is defined. The cut values for a given signal efficiency of 0.9 are used to define a minimum or maximum (depending on the cut boundaries of the variable) of allowed cut ranges for each variable for the second iteration. Consequently τ-leptons fulfilling the criteria for a signal efficiency of 0.9 are required to fulfill the criteria for a signal efficiency of 0.7. From the second iteration the cut values for a given signal efficiency of 0.7 are used as maximum or minimum cut ranges for the fourth iteration step and the same procedure is applied to last iteration step.

Finally five sets of cut values for both methods, calorimeter-based and calorimeter+track-based, as well as for 1-prong and 3-prong τ candidates are established. The cut values for a given efficiency of 0.9 and 0.1 are only used to show the performance of the cut-based identification method compared to multivariate techniques. This comparison is discussed in the next Section. The results with a signal efficiency of 0.7, 0.5, and 0.3 (iteration steps two to four) are used as cut values for the selections loose,

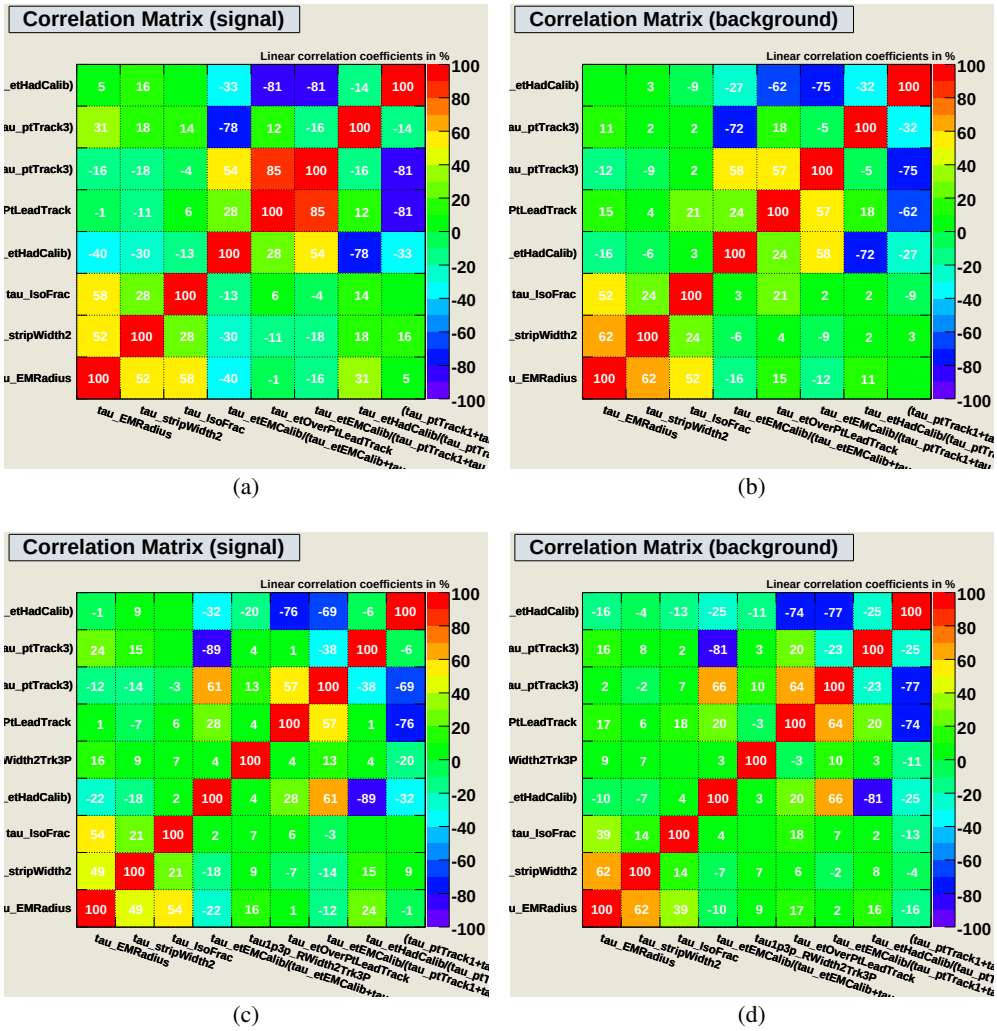

(a) (b)

(c) (d)

Figure 6.6.: Correlation matrix of calorimeter+track-based approach for 1-prong τ candidates and multi-prong τ candidates for signal (a, c) and background (b, d) for a $E_{\mathrm{T}}^{\mathrm{vis}}$ range of 25 – 45 GeV.

medium, and tight.

Besides the cut value TMVA provides further results and histograms. An order of the input variables ranging from the variable with the highest separation power to the variable with the lowest separation power is provided. The independence of the optimization performed by TMVA from the order of the input variables given to it is also verified. A modification of the order of the input variables did not yield to a significantly better performance.

TMVA also evaluates the linear correlation of the input variables and presents them in a correlation matrix. For the calorimeter-based method the correlation matrices are shown in Fig. 6.5 and for the calorimeter+track based method in Fig. 6.6. In each case the linear correlation is shown for signal and background datasets and 1-prong and 3-prong τ candidates with an $E_{\mathrm{T}}^{\mathrm{vis}}$ range of 25 – 45 GeV separately. These plots help to identify variables which are highly correlated. Figure 6.5 shows correlation of R_{EM} with W_{strip} and f_{iso}, while Fig. 6.6 shows correlation between variables containing the sum of the p_{T}

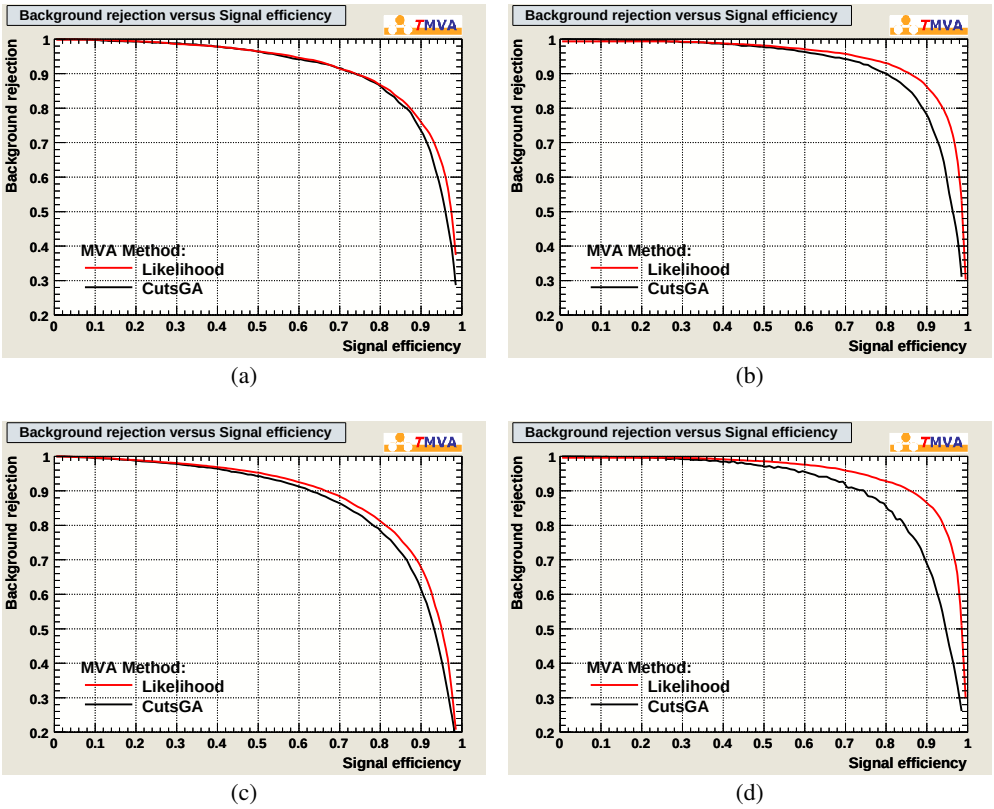

Figure 6.7.: Background rejection versus signal efficiency for the calorimeter-based identification method (left) and calorimeter+track-based identification method (right) for 1-prong (a, b) and multi-prong (c, d) τ candidates within a $E_{\mathrm{T}}^{\mathrm{vis}}$ range of 25 – 45 GeV. The performance is shown for the rectangular cut optimization with the genetic algorithm (black) and a projective likelihood estimator (red).

of tracks. For the next optimization round it is considered to remove one or more of these variable and replace where appropriate. Since R_{EM} is the variable with the highest separation power W_{strip} or f_{iso} can be removed without significant loss of performance.

An other histogram provided by TMVA shows the background rejection as function of the signal efficiency for all classifiers that are used for the training. TMVA can run multiple classifiers parallel. Hence a likelihood is trained at the same time with the rectangular cut optimization to provide a comparison of the performance of a complex multivariate technique with the cut optimization. The likelihood uses the same variables that are used for the rectangular cut optimization. It builds a model out of probability density functions (PDFs) that reproduces the input variables for signal and background. For a given event, the likelihood for being a signal type is obtained by multiplying the signal probability densities of all input variables, and normalizing this by the sum of the signal and background likelihoods. The comparison plots are shown in Fig. 6.7 for both, the calorimeter-based and calorimeter+track-based identification method and for 1-prong and 3-prong τ candidates within an $E_{\mathrm{T}}^{\mathrm{vis}}$ range of 25 – 45 GeV separately. In all cases the likelihood method performance slightly better. It is obvious that the performance increases with the number of variables, at it is the case for the calorimeter+track method and shown on the left plots

of Fig. 6.7. The background rejection versus signal efficiency is almost the same for the likelihood and the cut-based identification method in case of the calorimeter-based method. For the calorimeter+track method, the likelihood classifier has an advantage with a higher number of variables. The maximum of input variables for the cut-based ID method to perform reasonable is eight variables in case of 1-prong τ candidates and nine variables in case of 3-prong τ candidates, respectively.

For the second phase, the TMVA output is used as a starting point for the cut values. The final cut values are rounded to two significant digits and if the automated cut choice given by TMVA is not deemed to be appropriate, this cut value is adjusted by hand. Such an adjustment is made only if the assigned TMVA cut is placed in a clearly ineffective position (i.e. in the negligible tails of both signal and background distributions), and is made tighter without compromising any signal efficiency.

From release 15 these cut selections are implemented in the `taurec` package of the ATHENA software.

6.2. Performance of the cut-based selection

To assess the performance of the cut-based identification, both methods are compared with a projective logarithmic likelihood method for both the calorimeter and calorimeter+track identification methods. In contrast to the likelihood shown in Fig. 6.7, this likelihood is tuned on a broader selection of discriminant variables that is not restricted to the robust variables used for the cut-based ID. This likelihood method is intended to be used when the τ identification variables are more fully understood, and thus uses as many variables as possible to maximize discrimination power. The performance of both methods is tested using statistically independent events from the same samples as used in the optimization phase.

The performance is presented in the background rejection versus signal efficiency plane. For the signal efficiency, $\epsilon_\tau^{\text{n-prong}}$, τ candidates are matched to Monte Carlo τ-leptons with $E_{\text{T}}^{\text{vis}} > 10\,\text{GeV}$ and $|\eta| < 2.5$ within a cone of $\Delta R = 0.2$. The efficiency is calculated for all five $E_{\text{T}}^{\text{vis}}$ bins and both decay modes and is defined as

$$\epsilon_\tau^{\text{n-prong}} = \frac{\text{number of matched reconstructed n-prong } \tau \text{ candidates passing cuts}}{\text{number of true hadronically decaying n-prong } \tau \text{ leptons}}, \tag{6.1}$$

for n = 1 or 3.

The background rejection r, which gives the ratio of rejected candidates to accepted candidates is defined as

$$r = \frac{1}{\epsilon_{\text{bkg}}} - 1, \tag{6.2}$$

where the background efficiency, ϵ_{bkg}, is defined as

$$\epsilon_{\text{bkg}} = \frac{\text{number of reconstructed } \tau \text{ candidates passing cuts}}{\text{number of all reconstructed } \tau \text{ candidates}}. \tag{6.3}$$

6.2.1. Performance of the calorimeter identification method

The performance of the calorimeter identification method as described in Section 6.1.1 is shown in Fig. 6.8 for 1-prong candidates, the performance for 3-prong candidates is shown in Fig. 6.9. For comparison reason the efficiency versus rejection curve of the cut-based ID method shows not only the rejection rate for the loose (0.7), medium (0.5), and tight (0.3) but also for efficiencies at approximately 0.1 and 0.9. For the likelihood the efficiencies and rejections for cuts on the likelihood values are plotted.

For both decay modes, a calorimeter seed is required. Table 6.3 shows the efficiencies and rejection rates for the loose, medium, and tight cuts for 1-prong and 3-prong τ candidates using the calorimeter identification method.

The performance for 1-prong candidates is better than that for 3-prong candidates. The efficiencies for loose, medium, and tight cut thresholds deviate from the target efficiencies of 70 %, 50 %, and 30 % respectively since they are computed requiring that the signal τ candidates are reconstructed with the correct number of tracks, whereas the optimization does not have such a requirement.

Table 6.3.: Efficiencies for hadronically decaying τ leptons and rejection rates against jets for the cut-based selection using the calorimeter identification method. The uncertainties shown are due to Monte Carlo statistics, no systematic uncertainties are determined at this point in time. No track multiplicity on the τ candidates is required for the rejection.

Selection	$E_{\mathrm{T}}^{\mathrm{vis}}$-range (GeV)	efficiency 1-prong	efficiency 3-prong	rejection
Loose	10-25	0.715 ± 0.001	0.637 ± 0.003	0.443 ± 0.006
	25-45	0.757 ± 0.002	0.680 ± 0.002	0.73 ± 0.02
	45-70	0.828 ± 0.003	0.733 ± 0.005	1.78 ± 0.02
	70-100	0.868 ± 0.003	0.909 ± 0.006	0.131 ± 0.005
	>100	0.950 ± 0.001	0.698 ± 0.003	2.96 ± 0.05
Medium	10-25	0.482 ± 0.001	0.578 ± 0.003	2.28 ± 0.02
	25-45	0.538 ± 0.001	0.501 ± 0.002	8.7 ± 0.2
	45-70	0.618 ± 0.003	0.565 ± 0.005	11.8 ± 0.2
	70-100	0.606 ± 0.004	0.621 ± 0.008	13.8 ± 0.2
	>100	0.639 ± 0.002	0.663 ± 0.003	6.6 ± 0.1
Tight	10-25	0.295 ± 0.001	0.333 ± 0.002	15.9 ± 0.2
	25-45	0.343 ± 0.001	0.309 ± 0.002	31 ± 2
	45-70	0.347 ± 0.002	0.319 ± 0.003	54 ± 2
	70-100	0.375 ± 0.003	0.420 ± 0.007	49 ± 1
	>100	0.374 ± 0.001	0.354 ± 0.002	140 ± 10

6.2.2. Performance of the calorimeter+track identification method

Figure 6.10 shows the performance for the calorimeter+track identification method as described in Section 6.1.2 for 1-prong candidates, and in Fig. 6.11 for 3-prong candidates. For both cases the τ candidates are reconstructed from both calorimeter and track seeds. Like for the calorimeter-based method the curve of the cut-based method is extended by two additional efficiencies at approximately 0.1 and 0.9. The efficiency and rejection rates for the loose, medium, and tight cuts for both decay modes are shown in Tab. 6.4.

As expected, the calorimeter+track identification method has a rejection considerably higher for a given efficiency than the calorimeter identification method. In both methods, the performance for 1-prong candidates is also much higher than for 3-prong candidates. The calorimeter+track identification method, although rejecting jets at a lower rate than for the likelihood-based identification, still has good discrimination power against jets.

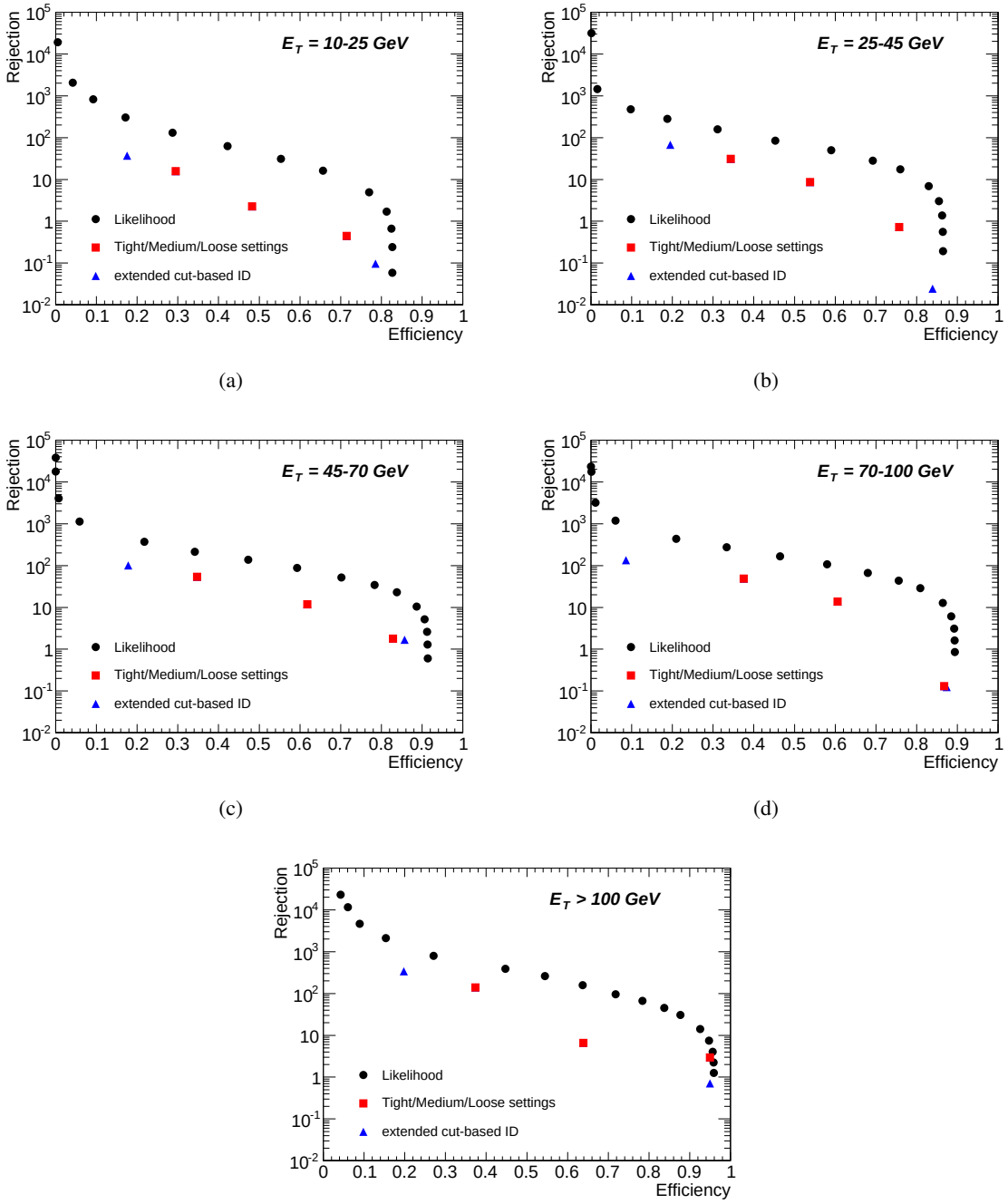

(a) (b) (c) (d) (e)

Figure 6.8.: Efficiency vs. rejection of calorimeter-based identification method compared with the likelihood for 1-prong τ candidates for the $E_{\mathrm{T}}^{\mathrm{vis}}$ ranges 10 – 25 GeV, 25 – 45 GeV, 45 – 70 GeV, 70 – 100 GeV, and >100 GeV. The efficiency is for true 1-prong τ candidates, and the rejection is for jets in QCD dijet samples. For the calorimeter identification tight, medium, and loose are shown in squares while the triangle extend the cut-based ID method by two additional efficiencies.

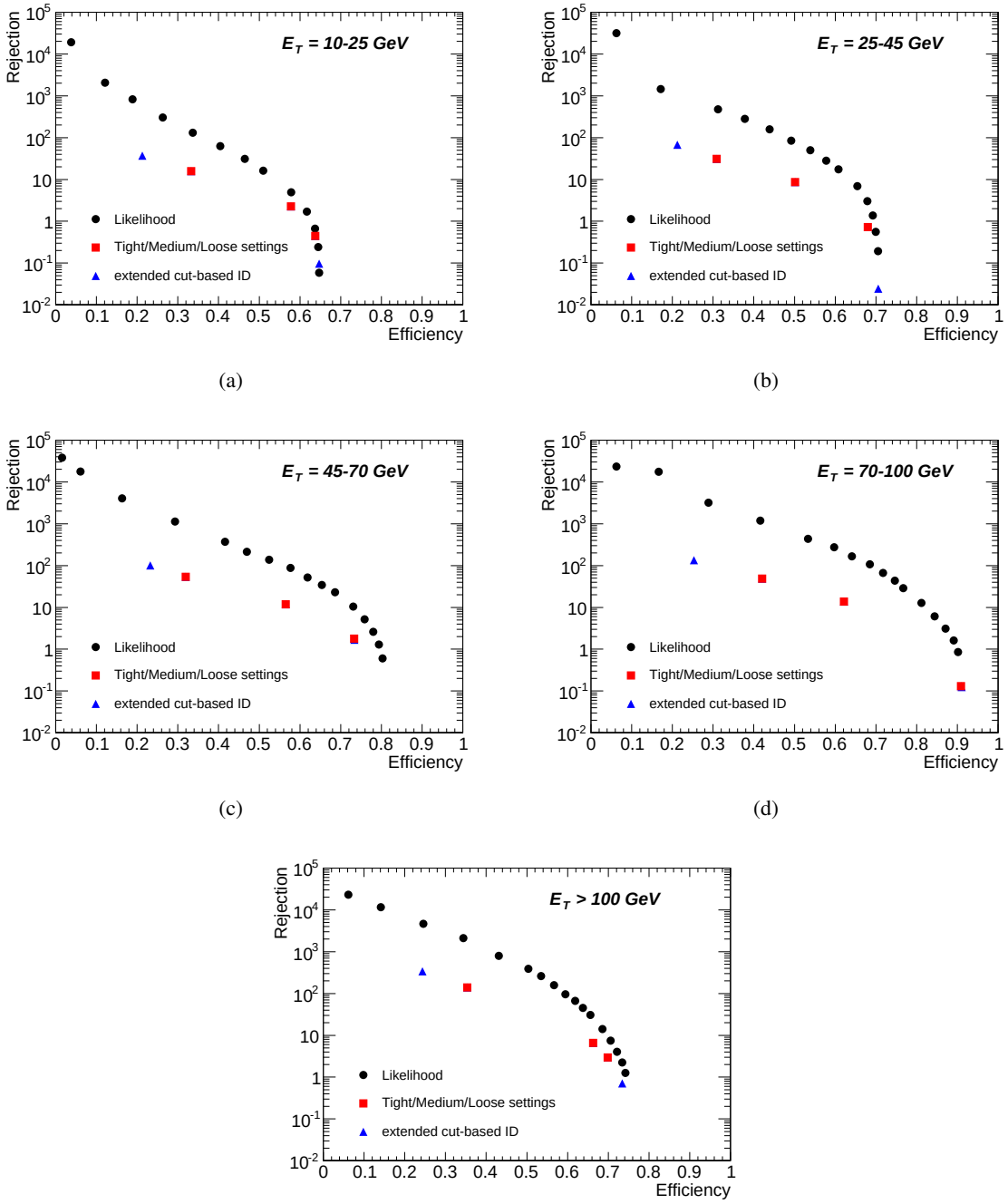

Figure 6.9.: Efficiency vs. rejection of calorimeter-based identification method compared with the likelihood for 3-prong τ candidates for the $E_{\mathrm{T}}^{\mathrm{vis}}$ ranges 10 – 25 GeV, 25 – 45 GeV, 45 – 70 GeV, 70 – 100 GeV, and >100 GeV. The efficiency is for true 1-prong τ candidates, and the rejection is for jets in QCD dijet samples. For the calorimeter identification tight, medium, and loose are shown in squares while the triangle extend the cut-based ID method by two additional efficiencies.

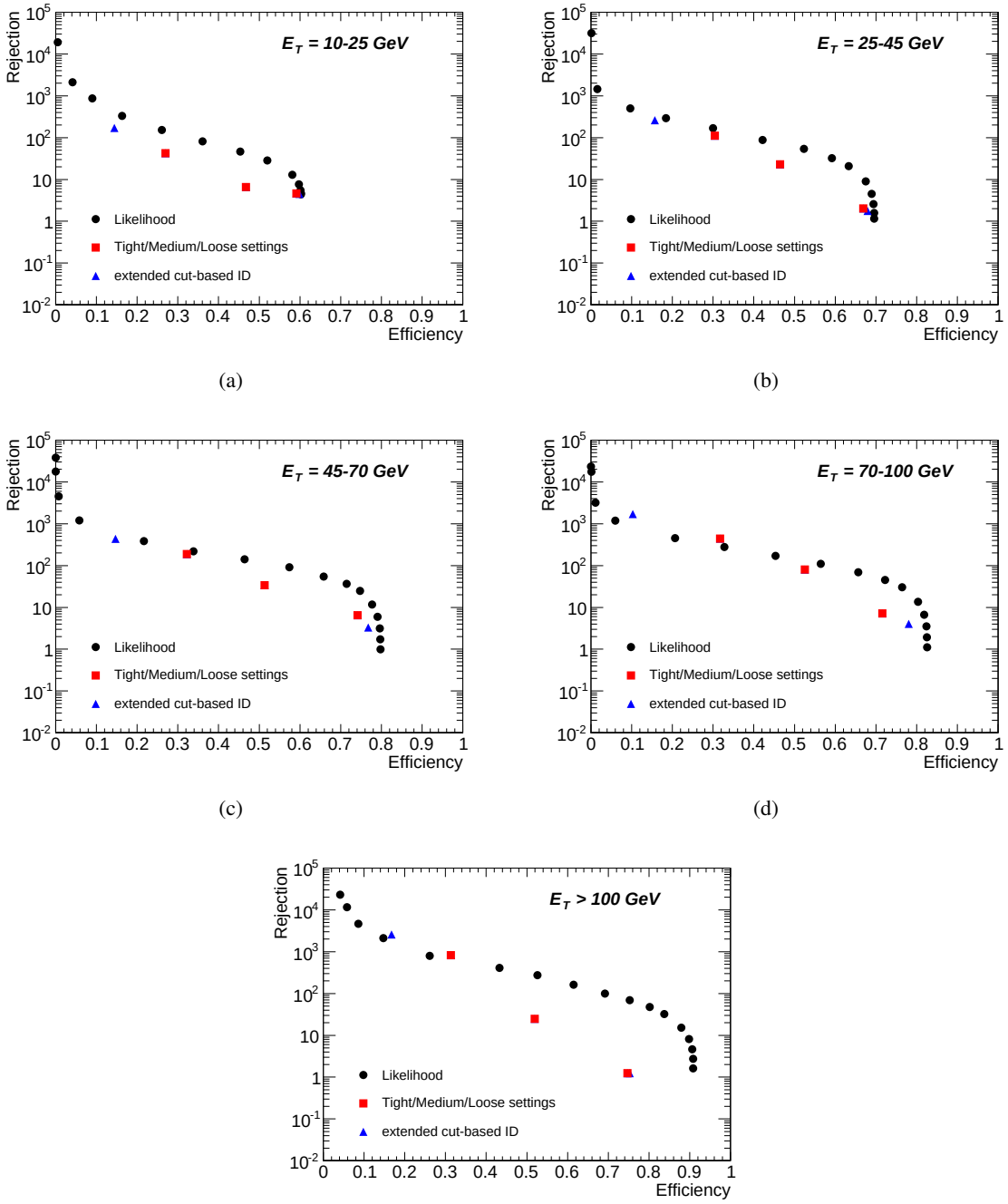

(a) (b) (c) (d) (e)

Figure 6.10.: Efficiency vs. rejection of calorimeter+track-based identification method compared with the likelihood for 1-prong τ candidates for the $E_{\mathrm{T}}^{\mathrm{vis}}$ ranges 10 – 25 GeV, 25 – 45 GeV, 45 – 70 GeV, 70 – 100 GeV, and $>$ 100 GeV. The efficiency is for true 1-prong τ candidates, and the rejection is for jets in QCD dijet samples. For the calorimeter identification tight, medium, and loose are shown in squares while the triangle extend the cut-based ID method by two additional efficiencies.

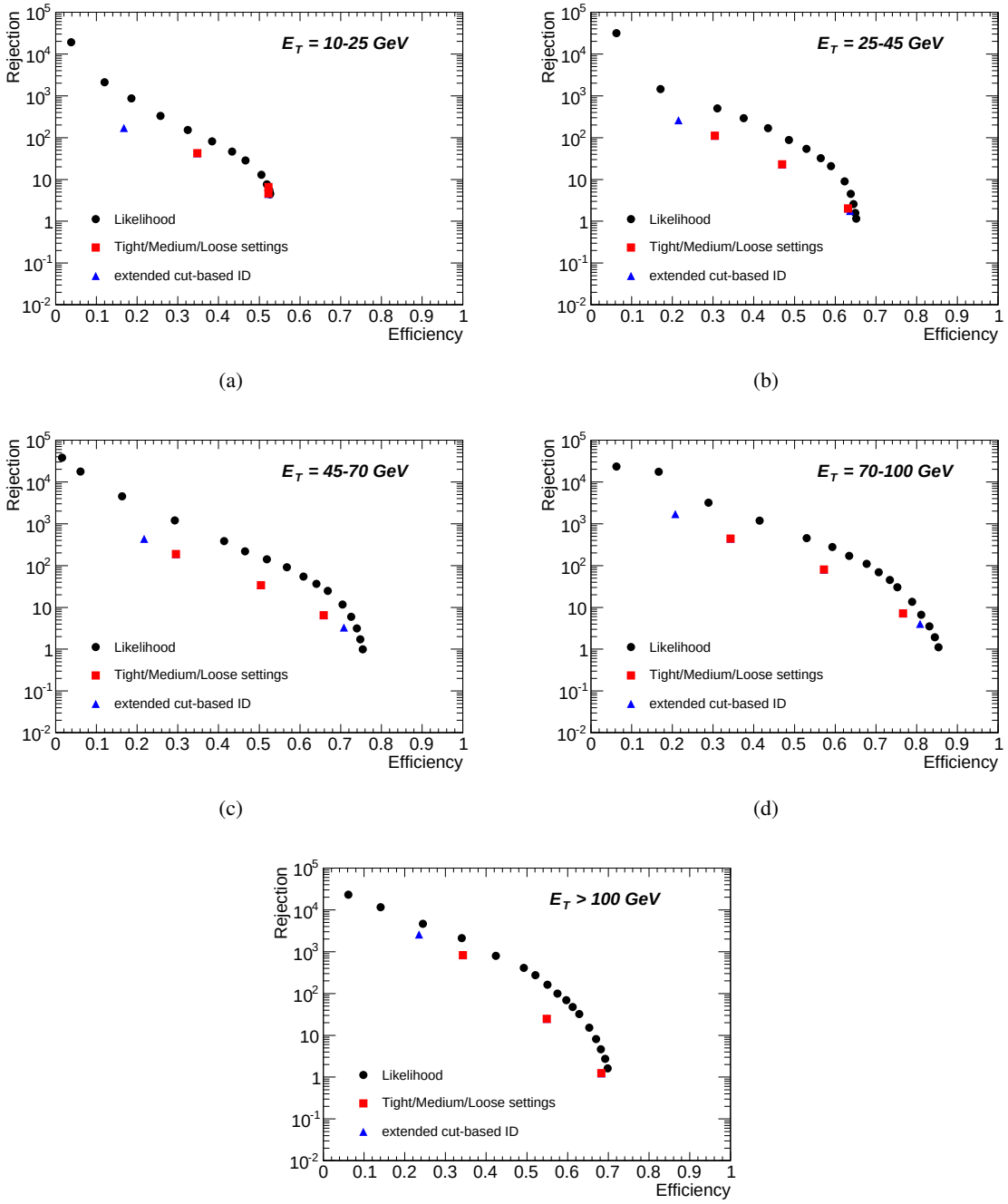

Figure 6.11.: Efficiency vs. rejection of calorimeter+track-based identification method compared with the likelihood for 3-prong τ candidates for the $E_{\mathrm{T}}^{\mathrm{vis}}$ ranges 10 – 25 GeV, 25 – 45 GeV, 45 – 70 GeV, 70 – 100 GeV, and $>$ 100 GeV. The efficiency is for true 1-prong τ candidates, and the rejection is for jets in QCD dijet samples. For the calorimeter identification tight, medium, and loose are shown in squares while the triangle extend the cut-based ID method by two additional efficiencies.

Table 6.4.: Efficiencies for hadronically decaying τ leptons and rejection rate against jets for the cut-based selection using the calorimeter+track identification method. The uncertainties shown are due to Monte Carlo statistics, no systematic uncertainties are determined at this point in time. No track multiplicity on the τ candidates is required for the rejection.

Selection	$E_{\mathrm{T}}^{\mathrm{vis}}$-range (GeV)	efficiency 1-prong	efficiency 3-prong	rejection
Loose	10-25	0.591 ± 0.001	0.523 ± 0.003	4.66 ± 0.05
	25-45	0.669 ± 0.002	0.631 ± 0.002	2.02 ± 0.04
	45-70	0.742 ± 0.003	0.658 ± 0.005	6.5 ± 0.1
	70-100	0.716 ± 0.004	0.766 ± 0.008	7.20 ± 0.09
	>100	0.747 ± 0.002	0.683 ± 0.003	1.25 ± 0.02
Medium	10-25	0.467 ± 0.001	0.523 ± 0.003	6.57 ± 0.07
	25-45	0.465 ± 0.001	0.470 ± 0.002	22.9 ± 1.0
	45-70	0.513 ± 0.003	0.504 ± 0.004	34 ± 1
	70-100	0.525 ± 0.004	0.572 ± 0.008	80 ± 3
	>100	0.519 ± 0.002	0.549 ± 0.003	24.9 ± 0.9
Tight	10-25	0.270 ± 0.001	0.348 ± 0.002	42.5 ± 1.0
	25-45	0.304 ± 0.001	0.304 ± 0.002	110 ± 10
	45-70	0.322 ± 0.002	0.295 ± 0.003	190 ± 10
	70-100	0.317 ± 0.003	0.343 ± 0.006	440 ± 40
	>100	0.313 ± 0.001	0.343 ± 0.002	830 ± 160

6.3. Outlook on cut-based identification methods

From release 15 the cut-based identification method is implemented in the `taurec` package of the ATHENA software. After first experience with analyses of Monte Carlo and data events using the cut-based ID method, adaptations according to the requirements must be performed. The binning of $E_{\mathrm{T}}^{\mathrm{vis}}$ is reduced from five bins down to 2 bins with the $E_{\mathrm{T}}^{\mathrm{vis}}$ range 20 – 60 GeV and >60 GeV. The former binning with five $E_{\mathrm{T}}^{\mathrm{vis}}$ bins led to a stepped p_{T} distribution for τ-leptons passing the loose, medium, or tight selection according to the bin steps of 10 – 25 GeV, 25 – 45 GeV, 45 – 70 GeV, 70 – 100 GeV, and >100 GeV. As an option the binning in η with the range $|\eta| < 1.1$ and $|\eta| > 1.1$ is investigated to have separated cuts for barrel and crack region.

The number and choice of variables is also updated. For the calorimeter-based method the following variables are used:

- **Electromagnetic radius** as defined in Section 6.1.1.
- **Isolation in the calorimeter** as defined in Section 6.1.1.
- **Core energy fraction** as defined in Section 5.4.1.
- **Number of effective cluster** is defined as

$$N_{\mathrm{eff}} = \frac{(\sum_i E_i)^2}{\sum_i E_i^2}, \tag{6.4}$$

  where i runs over all clusters associated to the τ candidate.

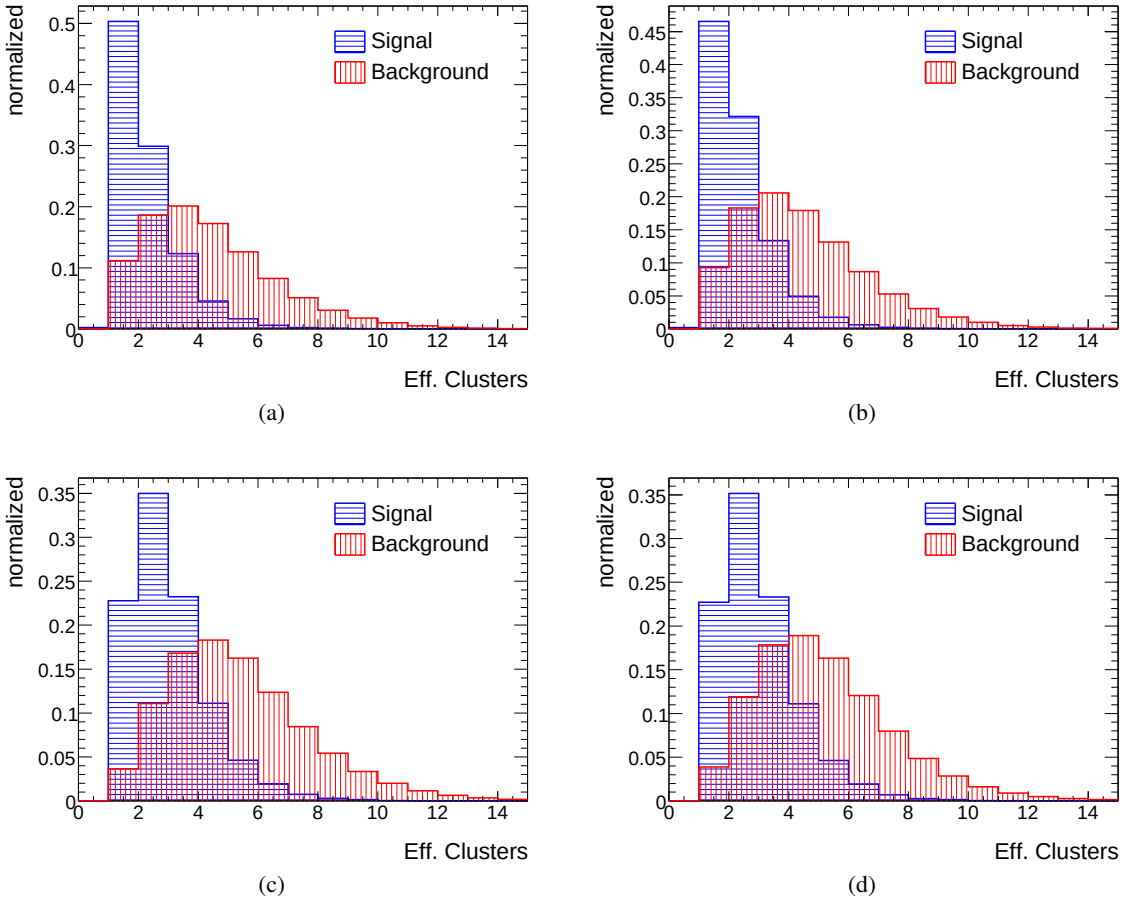

Figure 6.12.: Distribution of number of effective cluster for the calorimeter-based identification method (left) and the calorimeter+track-based identification method (right) for 1-prong τ candidates (a, b) and multi-prong τ candidates (c, d) within a $E_{\mathrm{T}}^{\mathrm{vis}}$ range of 20 – 60 GeV.

The number of additional variables for the calorimeter+track-based method is reduced to the following variables:

- E_{T} **over** p_{T} **of the leading track** as defined in Section 6.1.2.
- **Ratio of EM energy and sum of** p_{T} **of tracks** as defined in Section 6.1.2.
- **Ratio of Had energy and sum of** p_{T} **of tracks** as defined in Section 6.1.2.
- **Track spread** for multi-track τ candidates, as defined in Section 6.1.2.

The distribution for the new variables are shown in Fig. 6.12 for the number of effective clusters and in Fig. 6.13 for the core energy fraction, for both methods and decay modes within a $E_{\mathrm{T}}^{\mathrm{vis}}$ range of 20 – 60 GeV. From the distributions of both variables, good separation power between signal and background can be predicted.

As for the previous cut-based method the cuts are optimized separately for 1-prong and 3-prong τ candidates, with the subset of signal τ candidates of:

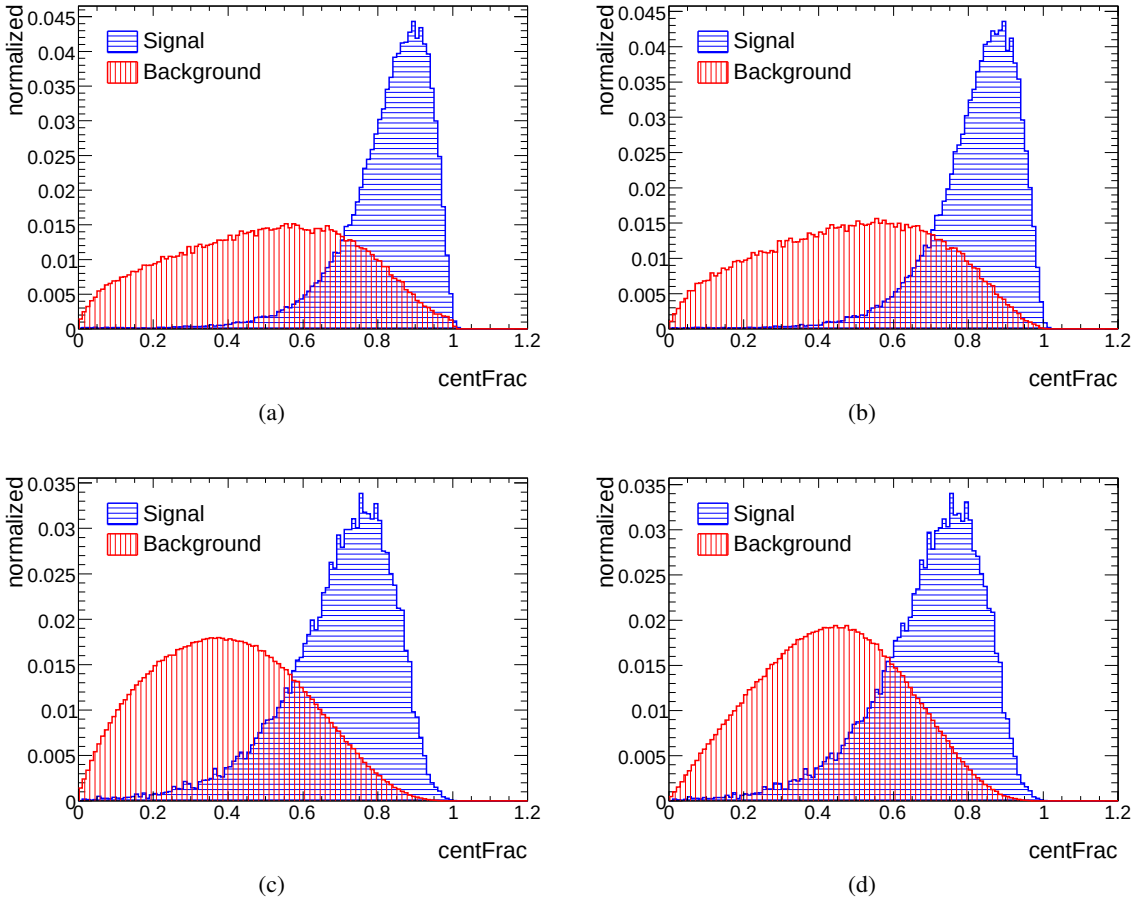

Figure 6.13.: Distribution of the core energy fraction for the calorimeter-based identification method (left) and the calorimeter+track-based identification method (right) for 1-prong τ candidates (a, b) and multi-prong τ candidates (c, d) within a $E_{\mathrm{T}}^{\mathrm{vis}}$ range of 20 – 60 GeV.

- reconstructed 1-track τ candidates matched to truth 1-prong τ-leptons in the signal sample vs. reconstructed 1-track τ candidates in the background sample.
- reconstructed 3-track τ candidates matched to truth 3-prong τ-leptons in the signal sample vs. reconstructed 3-track τ candidates in the background sample.

For the optimization 0, 2, 4, etc. track τ candidates are not considered but the cuts for 1-prong τ candidates are being applied on all τ candidates with < 2 tracks and the cuts for 3-prong τ candidates are used for all τ candidates with more than 2 tracks. The selection of 30 %, 50 %, and 70 % for loose, medium, and tight is kept.

Starting with release 15.7.x anti-k_t4 [148] jets are used as seed instead of Cone4Topo jets. Hence existing RDOs are re-reconstructed with the newer release 15.6.3.3 to produce samples using the anti-k_t4 jet-finding algorithm. The samples used for the new optimization come from the central ATLAS Monte Carlo production from 2008 (called MC08) with a center-of-mass energy of $\sqrt{s} = 10\,\mathrm{TeV}$ [2]. The re-

[2] Although the LHC run with a center-of-mass energy of $\sqrt{s} = 7\,\mathrm{TeV}$, 10 TeV samples are used for the optimization since no

Table 6.5.: $\sqrt{s} = 10\,\text{TeV}$ signal samples using the anti-k_t4 algorithm.

Dataset ID	channel	number of events	x-section (nb)
106052	$Z \rightarrow \tau\tau$	598616	1.12505
109007	$A \rightarrow \tau\tau(200\,\text{GeV})$	3000	0.00419247
109222	$A \rightarrow \tau\tau(300\,\text{GeV})$	3000	0.000720968
106573	$bAA \rightarrow \tau\tau(800\,\text{GeV})$	11000	0.00000485426

sulting ntuples are analyzed. Datasets used for signal samples are summarized in Tab. 6.5, dataset for background samples are summarized in Tab. 6.6.

Table 6.6.: $\sqrt{s} = 10\,\text{TeV}$ background samples using the anti-k_t4 algorithm.

Dataset ID	channel	number of events	x-section (nb)
005010	Dijet J1 (17-35 GeV)	989225	859436
005011	Dijet J2 (35-70 GeV)	927175	56152.2
005012	Dijet J3 (70-140 GeV)	1005886	3241.57
005013	Dijet J4 (140 – 560 GeV)	1108728	150.9

The procedure of the optimization is identical to the procedure described in Section 6.1.3. Parallel to the rectangular cut optimization using the genetic algorithm a likelihood is trained to compare both methods. The results of this comparison is shown in the background rejection versus signal efficiency plane in Fig. 6.14. The performance is shown for both identification methods and decay modes within a $E_{\text{T}}^{\text{vis}}$ range of 20 – 60 GeV. The performance of the rectangular cut optimization and the likelihood is almost identical except for the calorimeter+track-based method in case of multi-prong τ candidates. Since the statistic is low in this case the gain of multivariate techniques when using more variables becomes obvious.

Afterwards the performance of the new cut-based ID method is compared with the old cut-based method and the same logarithmic likelihood that is used for the comparison in Section 6.2 and that is trained on a broader selection of variables. In Fig. 6.15 the performance is shown in the efficiency versus rejection plane. The signal efficiency is defined as in (6.1) and the rejection is defined as in (6.2). The performance is shown for both methods and decay modes each in the $E_{\text{T}}^{\text{vis}}$ bin of 20 – 60 GeV. As for the previous optimization the performance decreases with the number of tracks. For the calorimeter-based method this effect is more significant than for the calorimeter+track-based method that uses more discriminant variables. Although the new cut-based optimization is trained to efficiencies of 30 %, 50 %, and 70 % they are shifted to lower efficiencies but higher rejections compared to the previous cut-based method.

The main difference between the first and second cut-based identification method are the different collections of variables and the different $E_{\text{T}}^{\text{vis}}$ bins. Compared to the first optimization two variables that are highly correlated are removed and/or replaced. Those variables are

7 TeV samples using the anti-k_t4 algorithm are available at the time of the optimization. It is expected that the replacement of the jet-finding algorithm has a more significant effect than the use of 10 TeV samples instead of 7 TeV

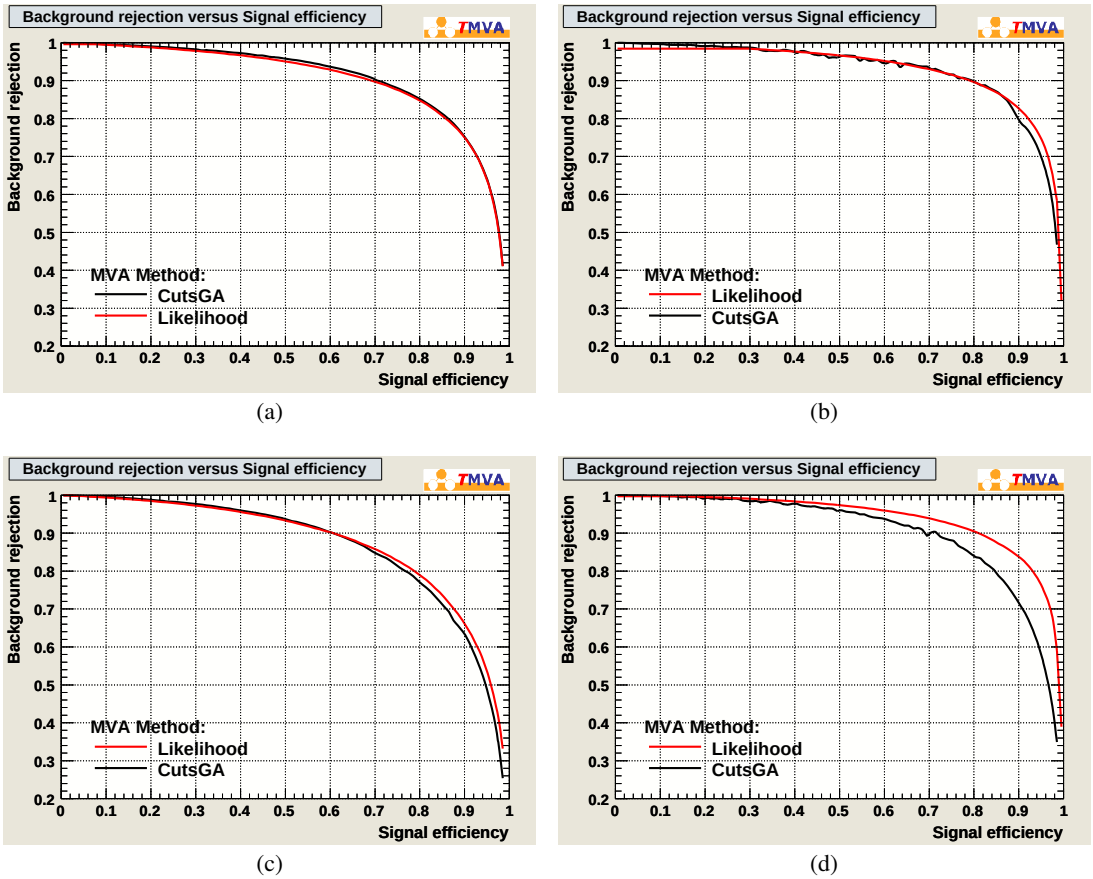

Figure 6.14.: Background rejection versus signal efficiency for the calorimeter-based identification method (left) and calorimeter+track-based identification method (right) for 1-prong (a, b) and multi-prong (c, d) τ candidates within a $E_{\mathrm{T}}^{\mathrm{vis}}$ range of 20 – 60 GeV. The performance is shown for the rectangular cut optimization with the genetic algorithm (black) and a projective likelihood estimator (red).

- The transverse energy width in the η strip layer, that is correlated to the electromagnetic radius.
- The ratio of sum of p_{T} of tracks and total energy, that is correlated to the ratio of EM (hadronic) energy and sum of p_{T} of tracks.

Furthermore the number of E_{T} bins is reduced from five to two. The first $E_{\mathrm{T}}^{\mathrm{vis}}$ bin from 20 – 60 GeV is focused on the main signal source of τ-lepton decays like $\mathrm{Z} \rightarrow \tau\tau$, while the second $E_{\mathrm{T}}^{\mathrm{vis}}$ bin with > 60 GeV covers all high-p_{T} τ-leptons.

Further optimization will focus on new variables like those presented in Section 5.4, that provide better separation power and are well understood. Based on variables used for the cut-based identification method, likelihood and boosted decision trees are being developed and tested. For complex analyses performed with multivariate techniques, cut-based methods using the same variables can be used as cross checks.

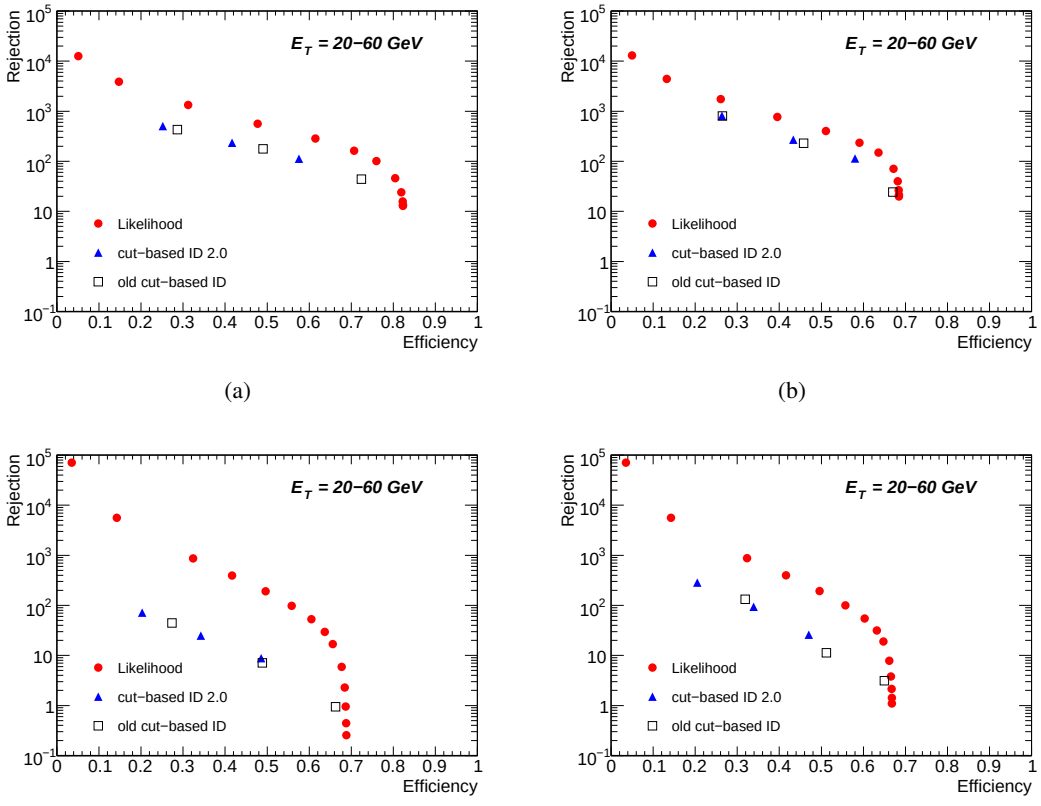

Figure 6.15.: Background rejection versus signal efficiency for the calorimeter-based identification method (left) and calorimeter+track-based identification method (right) for 1-prong (a, b) and multi-prong (c, d) τ candidates within a $E_{\mathrm{T}}^{\mathrm{vis}}$ range of 20 – 60 GeV. The performance is shown for the new cut-based identification method (blue triangles), the old cut-based identification method (open squares) and a logarithmic likelihood (red dots).

7. Experimental study of CP-violation in the stop sector

In this chapter the potential to observe CP-violating effects in SUSY $\tilde{t}_1$-cascade decay chains with the ATLAS experiment is discussed. As discussed in Chapter 2, the asymmetries of triple products of the final state particles momenta are sensitive to CP-violating effects. To reconstruct all momenta in the decay chains, all particle masses in the cascade decay must be known. A fully hadronic study with 500 fb^{-1} has been performed to define the areas of the mSUGRA parameter space.

The formalism for this study and the processes involved are described in Section 7.1. In Section 7.2 the momentum reconstruction and the reconstruction procedure from data is described. Concluding the results are discussed in Section 7.3

7.1. Formalism

7.1.1. Structure of the T-odd asymmetry

The general structure of the T-odd asymmetry was already discussed in Section 2.3.4. The two triple products used for this study are

$$\mathcal{T}_{\ell_N} = \vec{p}_{\ell_N} \cdot (\vec{p}_W \times \vec{p}_t), \tag{7.1}$$

$$\mathcal{T}_{\ell\ell} = \vec{p}_b \cdot (\vec{p}_{\ell^+} \times \vec{p}_{\ell^-}), \tag{7.2}$$

where ℓ^+ and ℓ^- are the two leptons produced in the $\tilde{\chi}_2^0$ cascade decay and the T-odd asymmetry is defined as

$$\mathcal{A}_T = \frac{N_{\mathcal{T}_+} - N_{\mathcal{T}_-}}{N_{\mathcal{T}_+} + N_{\mathcal{T}_-}} = \frac{\int \text{sign}\{\mathcal{T}_f\}|T|^2 d\text{lips}}{\int |T|^2 d\text{lips}}, \tag{7.3}$$

where $f = \ell_N$ or $\ell\ell$, $d$lips denotes Lorentz invariant phase space and $N_{\mathcal{T}_+}$ ($N_{\mathcal{T}_-}$) are the numbers of events for which the triple product $\mathcal{T}$ is positive (negative). The denominator in (7.3), $\int |T|^2 d\text{lips}$, is proportional to the cross section of the combined production and decay processes. The T-odd asymmetry for both triple products is shown in Fig. 2.10. For Eq. (7.2) the identification of the near and far lepton is not required.

While the covariant product of (2.53) is Lorentz invariant, the triple products are not. Since the rest frame of the $\tilde{\chi}_2^0$ and the $\tilde{t}_1$ are equivalent ($p_{\tilde{t}} = p_{\tilde{\chi}_2^0} + p_t$) the covariant product for the triple product in (7.1) can be written as

$$\epsilon_{\mu\nu\rho\sigma} p^\mu_{\tilde{\chi}_2^0} p^\nu_{\ell_N} p^\rho_W p^\sigma_t = \epsilon_{\mu\nu\rho\sigma} p^\mu_{\tilde{t}_1} p^\nu_{\ell_N} p^\rho_W p^\sigma_t \,. \tag{7.4}$$

If momentum conservation is exploited ($p_{\tilde{\chi}_2^0} = p_{\tilde{\ell}} + p_{\ell_N},\ p_{\tilde{\ell}} = p_{\ell_F} + p_{\tilde{\chi}_1^0},\ p_W = p_t + p_b$), the covariant product of the triple product in (7.2) can be written as

$$\epsilon_{\mu\nu\rho\sigma} p^\mu_{\tilde{\chi}_2^0} p^\nu_{\ell_N} p^\rho_W p^\sigma_t = \epsilon_{\mu\nu\rho\sigma} (p_{\ell_F} + p_{\tilde{\chi}_1^0})^\mu p^\nu_{\ell_N} p^\rho_W p^\sigma_b \,. \tag{7.5}$$

If the momentum of the unstable particles in the decay chain are known, the triple products originating from (7.4) and (7.5) can now be exploit and maximized. Therefore a momentum reconstruction is performed, which is described in Section 7.2.

A change of the decaying $\tilde{t}_1$ to a $\tilde{t}_1^*$ or changing the charge of the near lepton ℓ_N reverses the sign of the covariant product. Hence the charge of both, the $\tilde{t}_1$ and the ℓ_N have to be known otherwise any asymmetry will cancel. By demanding that the opposite cascade produces a single lepton, the charge of the opposite $\tilde{t}_1$ can be found. This results in tri-lepton final states. To distinguish the near and far lepton the momentum reconstruction technique will be used.

7.1.2. Scenario: spectrum and decay modes

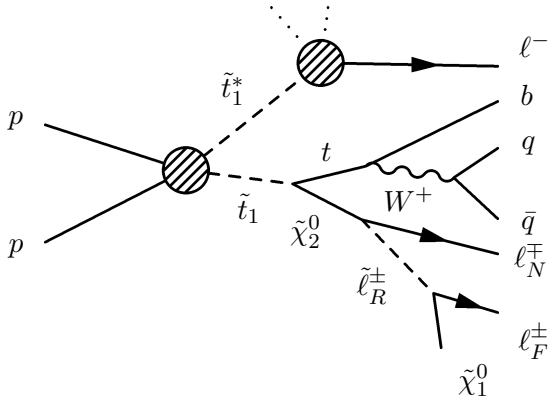

Figure 7.1.: Stop cascade decay process studied for the momentum reconstruction.

Table 7.1.: mSUGRA benchmark scenario (masses in GeV).

Parameter	m_0	$m_{1/2}$	$\tan\beta$	sign(μ)	A_0
Value	65	210	5	+	0

For the study described in this chapter the $\tilde{t}$ production process

$$pp \to \tilde{t}_1 \tilde{t}_1^* \tag{7.6}$$

with the following two-body decays is considered:

$$\tilde{t}_1 \to \tilde{\chi}_2^0 t, \qquad \tilde{\chi}_2^0 \to \tilde{\ell}\ell_{\mathrm{N}}, \qquad \tilde{\ell} \to \tilde{\chi}_1^0 \ell_{\mathrm{F}}, \qquad t \to b + W, \tag{7.7}$$

where ℓ_{N} and ℓ_{F} denote the near and far leptons respectively. The process is shown in Fig. 7.1. It is generated in the mSUGRA scenario with the parameters given in Tab. 7.1 and with an added CP-phase to the trilinear coupling ϕ_{A_t}. The spectrum at the electroweak scale has been derived by using the RGE code SPHENO 2.2.3 [129], except for the masses and the mixing of the $\tilde{t}_i$'s which are calculated by using the low energy soft SUSY breaking parameters and the phase of the trilinear coupling ϕ_{A_t} (see Eq. (2.46)

Table 7.2.: Gaugino masses (in GeV).

Particle	$m_{\tilde{\chi}_1^0}$	$m_{\tilde{\chi}_2^0}$	$m_{\tilde{\chi}_3^0}$	$m_{\tilde{\chi}_4^0}$	$m_{\tilde{\chi}_1^\pm}$	$m_{\tilde{\chi}_2^\pm}$	$m_{\tilde{g}}$
Mass (GeV)	77.7	142.4	305.1	330.3	140.7	329.9	514.116

Table 7.3.: Squark masses (in GeV) except for the $\tilde{t}_i$.

Particle	$m_{\tilde{t}_1}$	$m_{\tilde{t}_2}$	$m_{\tilde{b}_1}$	$m_{\tilde{b}_2}$	$m_{\tilde{q}_{dL}}$	$m_{\tilde{q}_{dR}}$	$m_{\tilde{q}_{uL}}$	$m_{\tilde{q}_{uR}}$
Mass (GeV)	345.7	497.8	443.4	466.0	484.7	465.2	478.7	464.9

and Appendix A in [77]). For this scenario the phase of the trilinear coupling is set to $\phi_{A_t} = 0.8\pi$. The masses of the gauginos are shown in Tab. 7.2, of the squarks in Tab. 7.3, and of the sleptons in Tab. 7.4.

The mass hierarchy of the SUSY spectrum required for this analysis is

$$m_{\tilde{t}_1} + m_t > m_{\tilde{\chi}_2^0} > m_{\tilde{\ell}_R^\pm} > m_{\tilde{\chi}_1^0}, \tag{7.8}$$

to allow full momentum reconstruction.

Since the feasibility of the study depends heavily on the integrated luminosity, the prediction on the cross section for the decay chain

$$\sigma = \sigma(pp \to \tilde{t}_1\tilde{t}_1^*) \times \text{BR}(\tilde{t}_1 \to t\tilde{\chi}_2^0) \times \text{BR}(\tilde{\chi}_2^0 \to \tilde{\ell}^\pm\ell^\mp) \times \text{BR}(\tilde{\ell}^\pm \to \tilde{\chi}_1^0\ell^\pm) \times \text{BR}(t \to q_u\bar{q}_d b), \tag{7.9}$$

is important. The corresponding branching ratios are summarized in Tab. 7.5. Since the charge of the stop in the opposite decay chain has to be known, the decay products must contain a single lepton. The dominant process for the production of single leptons is via the channel $\tilde{t}_1 \to \tilde{\chi}_1^+ b$. Table 7.5 shows that the decay $\tilde{\chi}_1^+ \to \tilde{\tau}_1^+\nu_\tau$ is the dominate process[1]. Applying of a τ identification might be very promising for this study. Unfortunately the performance of the τ-lepton identification in DELPHES is significant meanly compared to the performance of the full ATLAS detector simulation(see Section 4.2.3). Therefore the study is performed without a τ-lepton identification.

Table 7.4.: Slepton masses (in GeV).

Particle	$m_{\tilde{\ell}_L}$	$m_{\tilde{\ell}_R}$	$m_{\tilde{\tau}_2}$	$m_{\tilde{\tau}_1}$
Mass (GeV)	163.4	110.8	164.9	108.0

The dependence of ϕ_{A_t} on the parton level asymmetry, (7.3) is shown in Fig. 7.2 for both triple products $\mathcal{T}_{\ell_N}$ and $\mathcal{T}_{\ell\ell}$. From Fig. 7.2 (a) the largest asymmetry occurs for the triple product $\mathcal{T}_{\ell_N}$ with a maximum asymmetry of $|\mathcal{A}_{\ell_N}|_{\max} \approx 15\,\%$ at $\phi_{A_t} \approx 0.8\,\pi$. The phase used for this study is indicated with a vertical line. Since the "true" CP triple product correlation can only partially be measured, the asymmetry for $\mathcal{T}_{\ell\ell}$ is smaller at $|\mathcal{A}_{\ell\ell}|_{\max} \approx 6.5\,\%$.

[1] since only the right sleptons and the bino-like $\tilde{\chi}_1^0$ are lighter than the wino-like $\tilde{\chi}_1^+$, the decay of the $\tilde{\chi}_1^+$ is via mixing terms or Yukawa couplings

Table 7.5.: Branching ration (in %) for various decays with phase $\phi_{A_t} = |\frac{4}{5}\pi|$. The last row gives the cross section for stop pair production at the LHC with $\sqrt{s} = 14\,\text{TeV}$ at leading order from HERWIG++ [77].

Parameter	Value
BR($\tilde{t}_1 \to \tilde{\chi}_1^0 t$)	34.6
BR($\tilde{t}_1 \to \tilde{\chi}_2^0 t$)	7.5
BR($\tilde{t}_1 \to \tilde{\chi}_1^+ b$)	50.1
BR($\tilde{t}_1 \to \tilde{\chi}_2^+ b$)	7.8
BR($\tilde{\chi}_2^0 \to \tilde{\mu}_R^+ \mu^- / \tilde{e}_R^+ e^-$)	11.6
BR($\tilde{\chi}_1^+ \to \tilde{\tau}_1^+ \nu_\tau$)	95.1
$\sigma(pp \to \tilde{t}_1 \tilde{t}_1^*)$ [pb]	3.44

If the dominant production process at the LHC ($gg \to \tilde{t}_1 \tilde{t}_1^*$) and relevant parton distribution functions (`MRST 2004LO` [179]) are included the asymmetries drop down (Fig. 7.2 (b)). For the triple product $\mathcal{T}_{\ell_N}$ the asymmetry decreases to $|\mathcal{A}_{\ell_N}|_{\text{max}} \approx 4.5\,\%$. The reduction results from the boosted frame of the produced $\tilde{t}_1$ as discussed in Section 2.3.4. For the triple product $\mathcal{T}_{\ell\ell}$ the asymmetry is reduced far less to $|\mathcal{A}_{\ell\ell}|_{\text{max}} \approx 3.8\,\%$, because the triple product relies on the ℓ_F being correlated with the ℓ by the intrinsic boost of the $\tilde{\chi}_2^0$, $\tilde{\ell}$ system. This system already has a boost, even when the $\tilde{t}_1$ is at rest. If the $\tilde{t}_1$ is boosted, the boost of the system $\tilde{\chi}_2^0$, $\tilde{\ell}$ is proportionally less, since the momenentum of the $\tilde{t}_1$ is distributed throughout the decay chain.

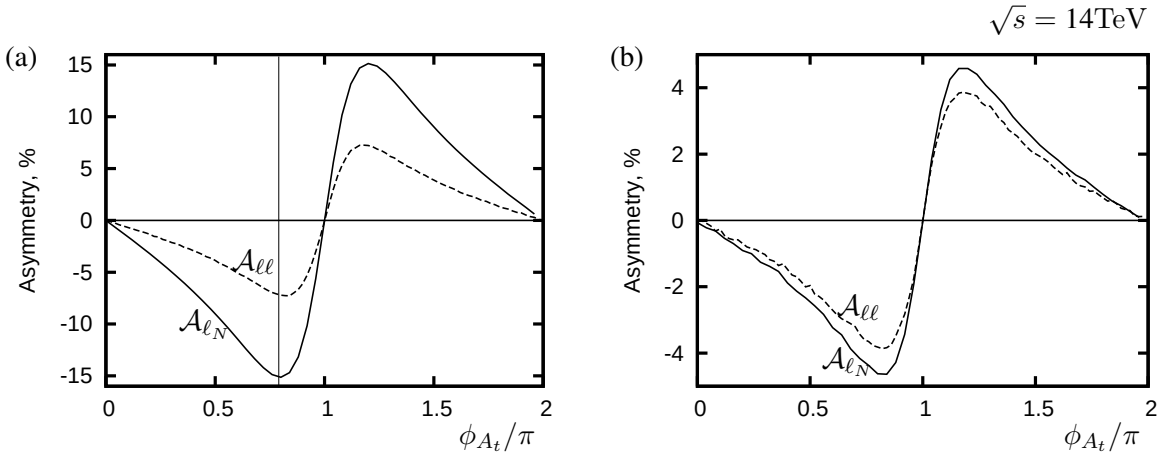

Figure 7.2.: The asymmetry $\mathcal{A}_{\text{T}}$, Eq. (7.3), in the rest frame of $\tilde{t}_1$ as a function of ϕ_{A_t} (a) and the asymmetry $\mathcal{A}_{\text{T}}$ in the laboratory frame as a function of ϕ_{A_t} (b) at the LHC at $\sqrt{s} = 14\,\text{TeV}$. The solid line is the asymmetry for the triple product $\mathcal{T}_{\ell_N}$, Eq. (7.1), the dotted line is for the triple product $\mathcal{T}_{\ell\ell}$, Eq. (7.2). The vertical line in (a) indicates the phase used for this study [77].

7.2. Momentum Reconstruction

The previous section showed, that the triple product that is reconstructed from the momenta in the laboratory frame at the LHC is reduced by a factor ~ 4. This is described by (7.5), where the lab frame is boosted with respect to the rest frame of the $\tilde{\chi}_2^0$ or $\tilde{t}_1$ (for a more detailed discussion see [75]). The dilution of the asymmetry in the laboratory frame for the $\tilde{t}_1$ production with varying initial momenta is shown in Fig. 2.10. If the momenta of the $\tilde{t}_1$ can be reconstructed a Lorentz transformation of all momenta in the triple product into the rest frame of the $\tilde{t}_1$ can be performed and the full asymmetry can be recovered. Since only the triple product $\mathcal{T}_{\ell_N}$, (7.1) calculated in the reconstructed rest frame of the $\tilde{t}_1$ is observable with high significance at the LHC, this study concentrates only on this triple product.

7.2.1. Reconstruction procedure

The momenta of the $\tilde{\chi}_1^0$ can be reconstructed with the two-body decay chain:

$$\tilde{t} \to t + \tilde{\chi}_2^0 \to t + \tilde{\ell}^{\pm} + \ell_N^{\mp} \to t + \tilde{\chi}_1^0 + \ell_N^{\mp} + \ell_F^{\pm}. \tag{7.10}$$

The following mass constraints are assumed:

$$m^2_{\tilde{\chi}_1^0} = (p_{\tilde{\chi}_1^0})^2, \tag{7.11}$$

$$m^2_{\tilde{\ell}^{\pm}} = (p_{\tilde{\chi}_1^0} + p_{\ell_F^{\pm}})^2, \tag{7.12}$$

$$m^2_{\tilde{\chi}_2^0} = (p_{\tilde{\ell}^{\pm}} + p_{l_N^{\mp}})^2 = (p_{\tilde{\chi}_1^0} + p_{\ell_F^{\pm}} + p_{l_N^{\mp}})^2, \tag{7.13}$$

$$m^2_{\tilde{t}_1} = (p_{\tilde{\chi}_2^0} + p_t)^2 = (p_{\tilde{\chi}_1^0} + p_{\ell_F^{\pm}} + p_{l_N^{\mp}} + p_t)^2, \tag{7.14}$$

where p is the four momentum of the respective particles. The final state momenta $p_{\ell_F^{\pm}}$, $p_{\ell_N^{\mp}}$, and p_t can be measured and the unknown $p_{\tilde{\chi}_1^0}$ can be expanded to

$$\vec{p}_{\tilde{\chi}_1^0} = a\vec{p}_{\ell_F^{\pm}} + b\vec{p}_{\ell_N^{\mp}} + c\vec{p}_t. \tag{7.15}$$

The system of 3 linear equations with the unknown $a,\ b,\ c$ can be solved by calculating $\vec{p}_{\tilde{\chi}_1^0} \cdot \vec{p}_{\ell_F^{\pm}}$, $\vec{p}_{\tilde{\chi}_1^0} \cdot \vec{p}_{\ell_N^{\mp}}$, and $\vec{p}_{\tilde{\chi}_1^0} \cdot \vec{p}_t$. Inserting (7.15) and utilizing (7.12) – (7.14) forms the system of equation:

$$\mathcal{M} \begin{pmatrix} a \\ b \\ c \end{pmatrix} = \begin{pmatrix} \frac{1}{2}(m^2_{\tilde{\chi}_1^0} - m^2_{\tilde{\ell}}) + E_{\tilde{\chi}_1^0} E_{\ell_F} \\ \frac{1}{2}(m^2_{\tilde{\ell}} - m^2_{\tilde{\chi}_2^0}) + p_{\ell_F} \cdot p_{\ell_N} + E_{\tilde{\chi}_1^0} E_{\ell_N} \\ \frac{1}{2}(m^2_{\tilde{\chi}_2^0} + m^2_t - m^2_{\tilde{t}_1}) + p_{\ell_F} \cdot p_t + p_{\ell_N} \cdot p_t + E_{\tilde{\chi}_1^0} E_t \end{pmatrix}, \tag{7.16}$$

with

$$\mathcal{M} = \begin{pmatrix} \vec{p}_{\ell_F} \cdot \vec{p}_{\ell_F} & \vec{p}_{\ell_F} \cdot \vec{p}_{\ell_N} & \vec{p}_{\ell_F} \cdot \vec{p}_t \\ \vec{p}_{\ell_N} \cdot \vec{p}_{\ell_F} & \vec{p}_{\ell_N} \cdot \vec{p}_{\ell_N} & \vec{p}_{\ell_N} \cdot \vec{p}_t \\ \vec{p}_t \cdot \vec{p}_{\ell_F} & \vec{p}_t \cdot \vec{p}_{\ell_N} & \vec{p}_t \cdot \vec{p}_t \end{pmatrix}. \tag{7.17}$$

By inverting the matrix $\mathcal{M}$, solutions for $a,\ b,$ and c in terms of constants and the free parameter $E_{\tilde{\chi}_1^0}$ can be found. The on-shell mass condition for the $\tilde{\chi}_1^0$, (7.11), can be written as

$$E^2_{\tilde{\chi}_1^0} = (a, b, c)\mathcal{M} \begin{pmatrix} a \\ b \\ c \end{pmatrix} + m^2_{\tilde{\chi}_1^0}. \tag{7.18}$$

Since the above equation is quadratic, the result has two solutions. The solutions are re-substituted into (7.15) to find all components of the $\tilde{t}_1$ momentum on an event-by-event basis.

Since Eq. (7.11) is quadratic, each reconstructed event has two solutions for $p_{\tilde{\chi}_1^0}$. But there is no extra information on the decay chain to determine which solution is physically correct and it can not be distinguished which solution corresponds to the physically correct configuration. Hence the $\tilde{t}_1$ momentum of both configurations is calculated and all final state particles in the triple product are boosted in the rest frame of the reconstructed $\tilde{t}_1$. The event is accepted if the sign of both triple products are the same, otherwise the event is rejected. The disadvantage of this method is the loss of events and therefore statistical significance.

Another problem is the effect of combinatorics. For the reconstruction of the decay chain the near and far lepton have to be identified correctly to compute the triple product $\mathcal{T}_{\ell_N}$ (this information is not required for $\mathcal{T}_{\ell\ell}$). Furthermore a third lepton is required to determine the charge of the opposite $\tilde{t}$. If the third lepton has the same flavor as those of the triple product, it contributes to the reconstruction of the $\tilde{\chi}_2^0$. These combinatorial effects are removed by again demanding that all calculated triple products are of the same sign.

7.3. Results

The study described below is performed for an integrated luminosity of 500 fb^{-1}. Signal and background events are generated using the event generator HERWIG++2.4.2. The generator calculates all matrix elements in the process, the initial hard interaction, the subsequent SUSY particle decays, the parton showers, and the hadronization (see Chapter 4). Since HERWIG++ calculates the spin correlations in SUSY cascade decays, it allows the input of complex mixing matrices. The SUSY mass spectrum has been derived from SPHENO 2.2.3. Afterwards the generated events are passed through the detector simulation DELPHES and the subsequent reconstruction and identification simulation, which is described in Section 4.2.3.

For the signal, about 1.7 $\times 10^6$ $pp \to \tilde{t}_1\tilde{t}_1^*$ events with a cross section of 3.44 pb have been generated. The process of interest is

$$\begin{aligned} \tilde{t} &\to t + \tilde{\chi}_2^0 \\ \tilde{\chi}_2^0 &\to \ell_N^{\mp} + \tilde{\ell}^{\pm} \\ \tilde{\ell}^{\pm} &\to \ell_F^{\pm} + \tilde{\chi}_1^0. \end{aligned} \tag{7.19}$$

In the mSUGRA scenario many other SUSY particles will be produced, hence the main background for this process is SUSY itself. Therefore about 40 $\times 10^6$ SUSY events with a cross section of 80.1 pb have been generated to study the separation of the considerable SUSY background.

In [77] the following Standard Model backgrounds were generated with HERWIG++: $t\bar{t}$, Drell-Yan gauge boson production (Z,γ,W), W + jet, WW, WZ, ZZ, and $W\gamma$. In addition $t\bar{t}\ell^+\ell^-$ events were generated with MADGRAPH [119] and HERWIG++ for parton shower and hadronization. It was found that the only background to pass the triple product is $t\bar{t}\ell^+\ell^-$ with a very low rate of 0.03 events/fb^{-1}, corresponding to only ≈ 1 % of the signal processes. Hence the Standard Model background is neglected for this study.

The event selection is discussed in Section 7.3.1. To validate the momentum reconstruction, the method is first applied on truth level. The comparison of the reconstructed momentum with the true momentum of the MC $\tilde{\chi}_1^0$, as well as the triple product asymmetry on truth level is shown in Section 7.3.2. Finally the momentum reconstruction is applied on detector level. The reconstruction of the $\tilde{\chi}_1^0$ and the calculation of the triple product asymmetry is described in Section 7.3.3.

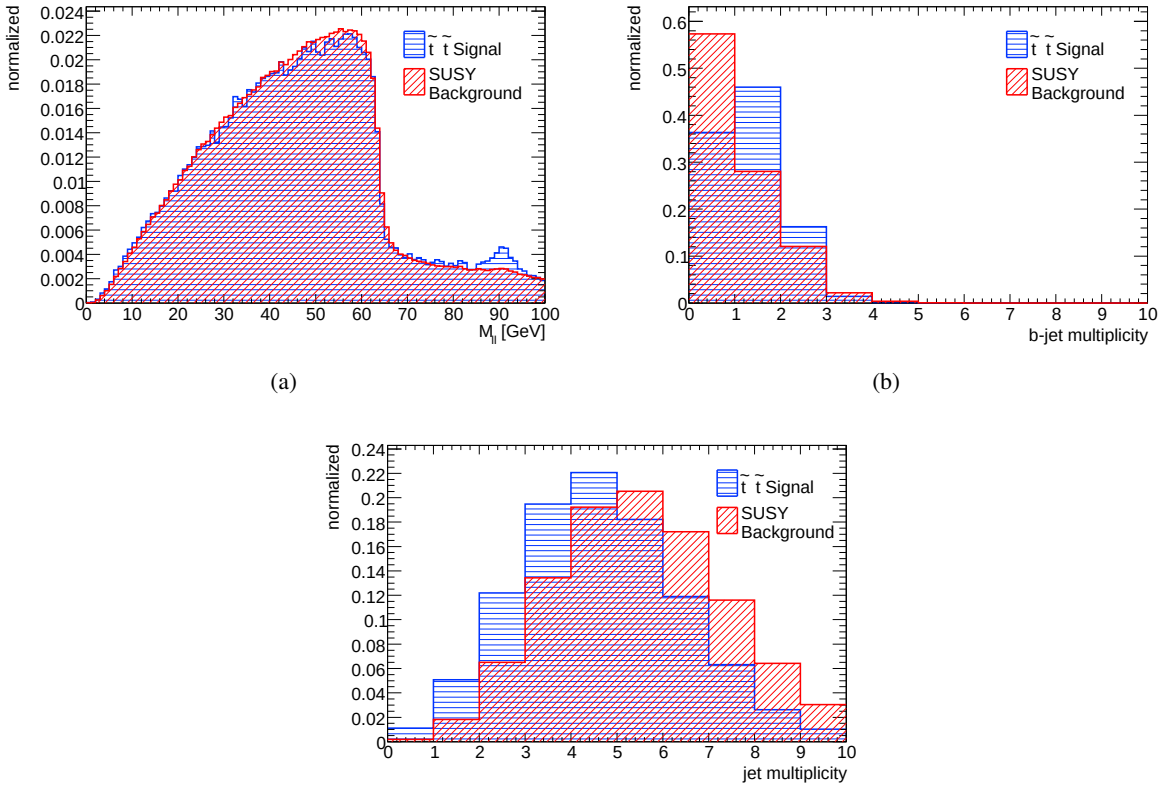

Figure 7.3.: Distributions of the variables used for the event selection. The invariant mass $M_{\ell^+\ell^-}$ (a) is shown after the lepton cut and OSSF cut have been applied. The b-jet multiplicity (b) is shown after the $M_{\ell^+\ell^-}$ has been applied, and the jet multiplicity (c) is shown after the b-jet cut has been applied. The distributions are shown for signal (blue) and background (red) and are normalized.

7.3.1. Event selection

For the calculation of all triple products of the decay chain the reconstruction of the near lepton, far lepton, and the top is required. A third lepton is required, to determine the charge of the opposite decay chain. Reconstructed lepton candidates are provided by the detector simulation while the top is reconstructed from its decay products.

Almost 100 % of the tops decay via a b and a W boson. The W boson is reconstructed by 2 jets (no b-jets) with an invariant mass of 70 GeV $< M_{jj} <$ 90 GeV. All possible combinations are taken into account. A t is reconstructed if the invariant mass of a reconstructed W and a b-jet lies in the range of 150 GeV $< M_{W^\pm b} <$ 190 GeV.

The jet reconstruction used the anti-k_t jet algorithm with $\Delta R^2 = 0.5$. For the event selection the following cuts are applied:

- Three isolated charged leptons, each with $p_T > 10$ GeV and $|\eta| < 2.5$.

[2] $\Delta R = \sqrt{\Delta\eta^2 + \Delta\phi^2}$

Table 7.6.: Cross section, number of events and triple product for the true decay chain at the LHC with $\sqrt{s} = 14$ TeV.

	$\tilde{t}_1\tilde{t}_1^*$
Cross section [pb]	3.44
Events with 500 fb^{-1}	1698619
Events with 500 fb^{-1} with decay chain	111610 ± 334.1
Events with 500 fb^{-1} passing triple product N_{total}	46939 ± 216.7
N_{asym}	6929 ± 216.1

- Two leptons with opposite sign and same flavor (OSSF).
- An invariant mass of the OSSF leptons of $M_{\ell^+\ell^-} > 10$ GeV.
- At least one b-jet with $p_{\text{T}} > 20$ GeV and $|\eta| < 3.5$.
- At least two additional jets (no b-jet) with $p_{\text{T}} > 20$ GeV and $|\eta| < 3.5$.

Exact three leptons in the final state are required. One pair of these leptons must be OSSF, originating from the decay of the $\tilde{\chi}_2^0$. The third lepton is required to identify the charge of the opposite $\tilde{t}_1$. Hence the sum of the charge of all three leptons gives the charge of the opposite $\tilde{t}_1$. Since a b-jet is produced in almost all t decays, at least one b-jet is required in the final state. For a full reconstruction of the t, at least two additional jets in the final state are required.

The distributions of the invariant mass $M_{\ell^+\ell^-}$, b-jet multiplicity and jet multiplicity are shown in Fig. 7.3. Each distribution is shown with the previous cuts applied. Apart from selecting events with at least one b-jet, the b-jet multiplicity cut has a good separation power of signal and background.

The additional jets are used to reconstruct the W boson. All possible b-jet and W boson combinations are used for a full reconstruction of the t. Only combinations in the range $150\,\text{GeV} < M_{W^\pm b} < 190\,\text{GeV}$ are used for kinematical reconstruction described in Section 7.2. Any t's and OSSF leptons combinations in the final state are used for the momentum reconstruction. If the particles satisfy the kinematic constraints from (7.11) – (7.14) the momentum of the $\tilde{\chi}_1^0$ will have at least two solutions. For each solution the relevant rest frame triple product is calculated. If all triple products have the same sign, the event is accepted, otherwise the event is rejected.

7.3.2. Momentum reconstruction on truth level

The study starts with the momentum reconstruction and calculation of the triple product asymmetry on truth level. First the decay chain of interest

$$\tilde{t} \to t + \tilde{\chi}_2^0 \to t + \ell_N^\mp + \tilde{\ell}^\pm \to t + \ell_N^\mp + \ell_F^\pm + \tilde{\chi}_1^0, \tag{7.20}$$

is identified. For the triple product the b and W boson associated to the t are determined.

The triple product of the top and both leptons is calculated and only decay chains with all triple products having the same sign are accepted. All other decay chains are rejected. Since the charge of the $\tilde{t}_1$ is known, the charge of the opposite $\tilde{t}_1$ is known, too. The asymmetry is defined as

$$\mathcal{A}_T = \frac{N_{\text{asym}}}{N_{\text{total}}}, \tag{7.21}$$

where N_{total} is the number of events with all triple products having the same sign and N_{asym} is defined as

$$\mathcal{N}_{\text{asym}} = \begin{cases} + = charge\ \tilde{t}_1, & \text{if the sign of all triple products } \mathcal{T} \text{ is positive,} \\ - = charge\ \tilde{t}_1, & \text{if the sign of all triple products } \mathcal{T} \text{ is negative.} \end{cases} \tag{7.22}$$

Values for the total number of events, total number of decay chains, decay chains passing the triple product, and the asymmetry value can be found in Tab. 7.6.

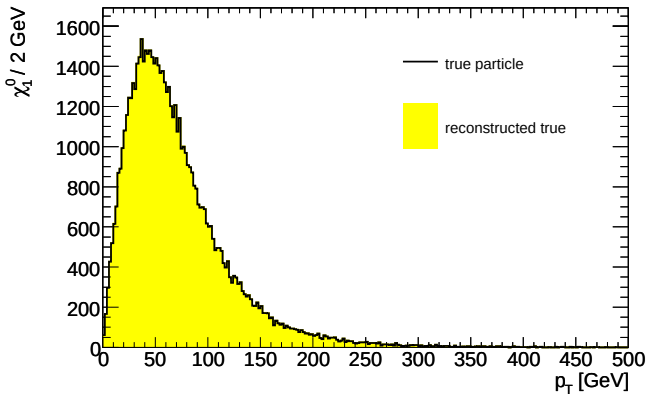

Figure 7.4.: 4-momentum (black) and reconstructed p_{T} (yellow) of the true $\tilde{\chi}_1^0$ for 500 fb^{-1} at the LHC with $\sqrt{s}$ = 14 TeV.

This yields to an asymmetry of $\mathcal{A} = 6929 \pm 216.1/46939 \pm 216.1 = 0.148 \pm 0.005$, which corresponds to the asymmetry predicted in [77] (see also Fig. 7.2).

The result of the momentum reconstruction of the $\tilde{\chi}_1^0$ on truth level is shown in Fig. 7.4. The black line shows the distribution of the true 4-momentum of all MC $\tilde{\chi}_1^0$ of the decay chain in (7.19), while the yellow area shows the distribution of the reconstructed momentum of the MC $\tilde{\chi}_1^0$ using true top and leptons. As shown in Fig. 7.4 both distributions are perfectly consistent. The reconstructed momentum agrees perfect with the true 4-momentum of the MC $\tilde{\chi}_1^0$.

The momentum reconstruction assumes that all masses are known (see Eq. (7.11) – (7.14)). If the masses defined by the scenario (see Tab. 7.2 – Tab. 7.4) are used instead of the MC masses a deviation in both distributions shown in Fig. 7.4 will occur. This is due to mass uncertainties produced by the generator and the natural width of the t. The mass spectrum of the $\tilde{\chi}_1^0$, $\tilde{\chi}_2^0$, $\tilde{t}$, the $\tilde{\ell}$, and the t are shown in Fig. 7.5. For the momentum reconstruction of the MC $\tilde{\chi}_1^0$ the 4-vector masses of the corresponding true MC sparticles can be used. At reconstruction level, masses defined by the scenario from Tab. 7.2 – Tab. 7.4 and from the reconstructed t, respectively must be used. The deviations of the true mass and the model mass causes uncertainties in the momentum reconstruction.

7.3.3. Momentum reconstruction and background separation

The separation of the large background and isolation of the $\tilde{t}_1\tilde{t}_1^*$ process is a challenge. In a first step the event selection, described in Section 7.3.1 is applied. These cuts reduce the signal at 98.2 % while the background is reduced at 99.15 %.

The second step is the reconstruction of W's to perform a full reconstruction of the t's. All two-jet combinations (no b-jets) that satisfy the invariant mass condition 70 GeV $< M_{jj} <$ 90 GeV are used

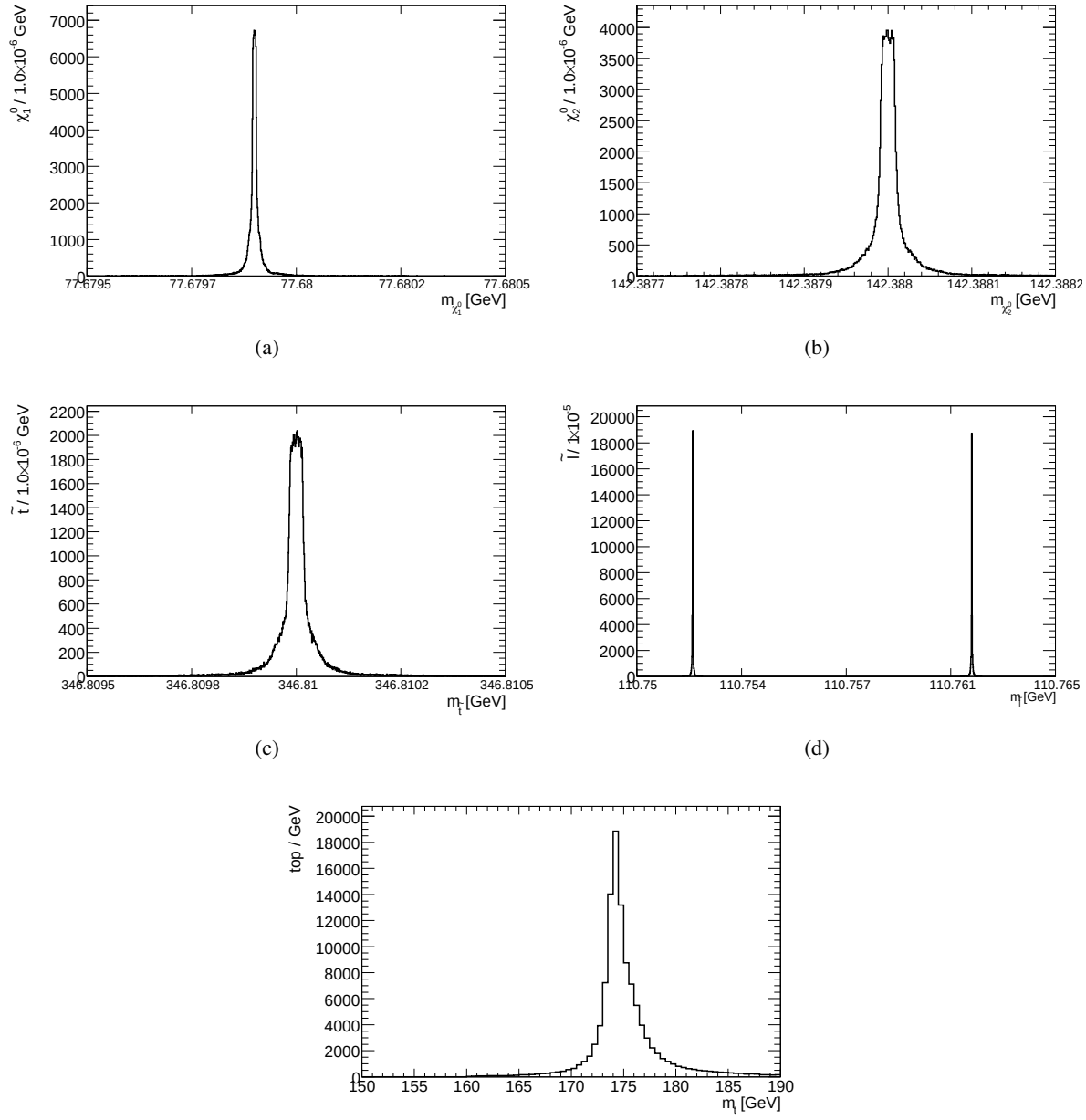

Figure 7.5.: Masses of the $\tilde{\chi}_1^0$ (a), $\tilde{\chi}_2^0$ (b), $\tilde{t}$ (c), $\tilde{\ell}$ (d), and the t (e). All masses show a certain width. Since the generator produces an uncertainty on the sparticle masses the real 4-vector mass must be used for the momentum reconstruction of the true $\tilde{\chi}_1^0$. The distribution for the $\tilde{\ell}$ mass shows two peaks, one for the selectron (left) and one for the smuon (right)

Table 7.7.: Cross section, cut-flow and signal to background ratio at the LHC with $\sqrt{s} = 14$ TeV for both, the production channel $\tilde{t}_1\tilde{t}_1^*$ and inclusive SUSY production.

	$\tilde{t}_1\tilde{t}_1^*$	SUSY background	signal/background
Cross section [pb]	3.44	80.1	
Events with 500 fb^{-1}	1698619	39498688	
Events with 500 fb^{-1} after initial selection	30453 ± 175.4	333905 ± 577.8	0.0912 ± 0.0005
Events with 500 fb^{-1} after W reconstruction	19436 ± 139.4	204198 ± 451.9	0.0952 ± 0.0007
Events with 500 fb^{-1} after t reconstruction	9771 ± 98.8	88839 ± 298.1	0.110 ± 0.001
Events with 500 fb^{-1} after momentum reconstruction	6191 ± 78.7	34488 ± 185.7	0.180 ± 0.002
Events with 500 fb^{-1} after triple product	1256 ± 35.4	6618 ± 81.4	0.190 ± 0.006

as W boson candidate. A t is found if the invariant mass of any b-jet and reconstructed W satisfy $150\,\text{GeV} < M_{W^\pm b} < 190\,\text{GeV}$. Events with no reconstructed t are rejected.

The last step contains the momentum reconstruction and calculation of the triple product of any t and OSSF lepton combination as described in Section 7.2. Events with no solution found for the momentum reconstruction are rejected and only events with all triple products having the same sign are accepted. The charge of the opposite decaying $\tilde{t}_1$ is determined by summing the charges of the three leptons.

In Tab. 7.7 the cut-flow of events for both, the production channel $\tilde{t}_1\tilde{t}_1^*$ and inclusive SUSY production is summarized. The signal to background ratio increases from 0.0912 ± 0.0005 after the initial event selection to 0.19 ± 0.006 after the requirement, that all triple product of the event have the same sign. Although the number of background events is reduced by a factor of almost 6000, the signal to background ratio may still be too low. With $N_{\text{total}} = 1256 \pm 35.4$ and $N_{\text{asym}} = 28 \pm 35.4$ inserted in (7.21) the asymmetry adds up to $\mathcal{A}_T = 0.0223 \pm 0.0282$.

Further cuts are required to distinguish signal from background. The largest background in mSUGRA comes from $\tilde{g}$ production with a dominant decay to sbottom, $\tilde{g} \to \tilde{b}_i b$ with a branching ratio of $\approx 30\,\%$. The $\tilde{b}_i$ decays mainly to $\tilde{\chi}_2^0 b$ or $\tilde{\chi}_1^+ t$ which have a very similar final state as the signal process. The difference of the signal and background process is that the $\tilde{g}$ and first and second generation $\tilde{q}$ have a higher mass. Furthermore a gluino has one or more decay vertex in the cascade decay, which produces another hard jet. That means, that the average p_{T} of the particles produced in the background event will be higher and the number of jet will be greater. Besides events with higher missing transverse energy are produced in mSUGRA background processes. Therefore three additional cuts can be introduced after the initial selection:

- Missing transverse energy $E_{\text{T}}^{\text{miss}} < 300\,\text{GeV}$.
- Number of jets < 9.
- Number of b-jets < 3.

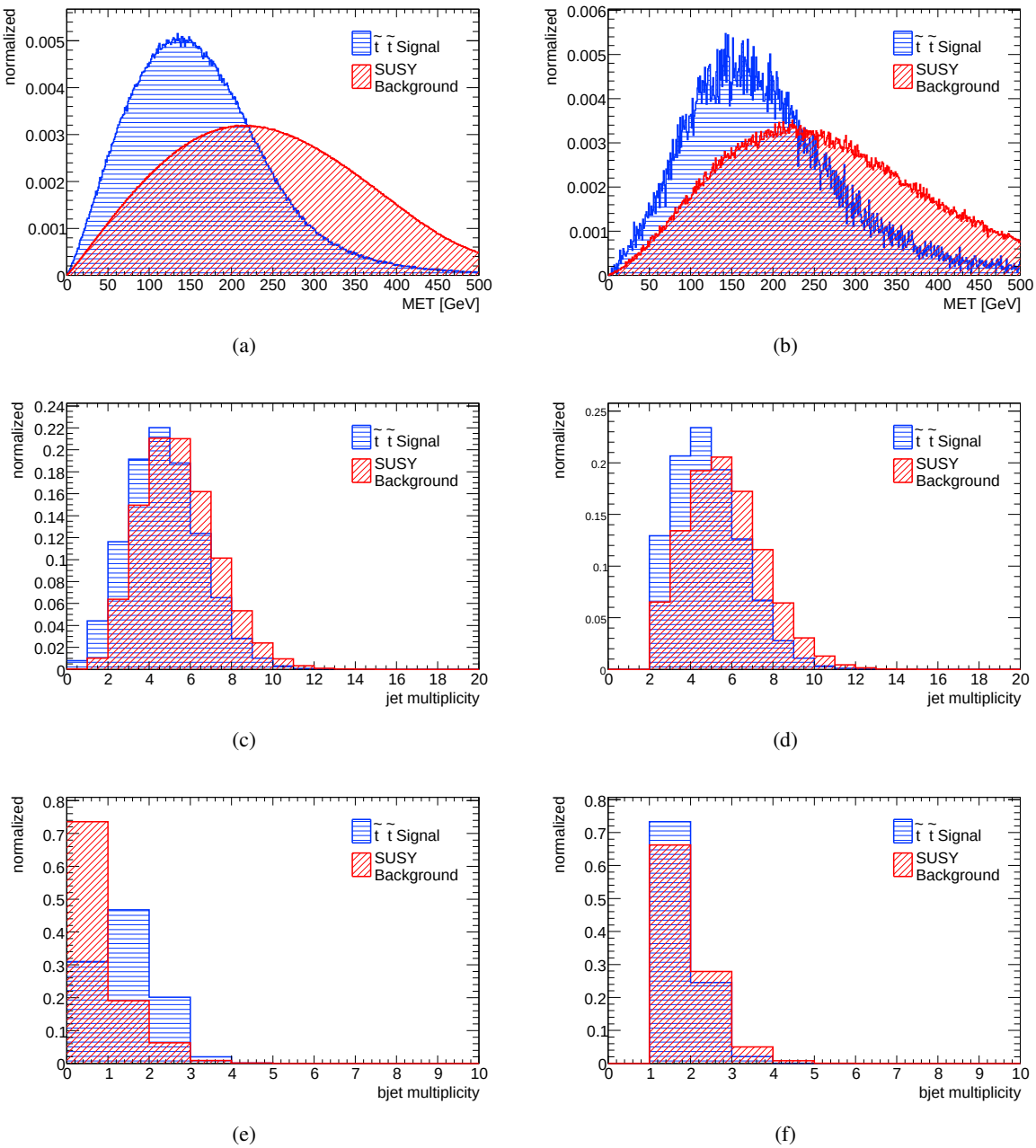

Figure 7.6.: Signal (blue) and background (red) distributions of $E_{\mathrm{T}}^{\mathrm{miss}}$ (top), jet multiplicity N_{jet} (middle), and b-jet multiplicity $N_{b-\mathrm{jet}}$ (bottom) before (left column) and after (right column) the initial cuts are applied.

Table 7.8.: Number of events with additional cuts, and signal to background ratio for both, the production channel $\tilde{t}_1\tilde{t}_1^*$ and inclusive SUSY production at the LHC with $\sqrt{s} = 14\,\text{TeV}$.

	$\tilde{t}_1\tilde{t}_1^*$	SUSY background	signal/background
Events with $500\,\text{fb}^{-1}$ after triple product and additional cuts	1104 ± 33.2	4197 ± 64.8	0.263 ± 0.009

The distributions of these three variables are shown on Fig. 7.6 for both, before and after the initial cut selection.

With the additional cuts the signal to background ratio increases by 40 % (see Tab. 7.8) to 0.263 ± 0.009, i.e. with the current cut selection no significant separation between signal and background can be achived.

Furthermore the background contributes to the triple product. Although no overall asymmetry is expected in the background, the increased number of N_{total} dilutes the asymmetry $\mathcal{A}_T$ and increases the sensitivity to discover the CP violation at the LHC.

With the additional cuts the number of events with all triple products having the same sign is $N_{\text{total}} = 1104 \pm 33.2$. With $N_{\text{asym}} = 20 \pm 33.2$ the asymmetry is $\mathcal{A}_T = 0.0181 \pm 0.0301$. Although the asymmetry value is smaller than without the additional cuts, these cuts increase the signal to background ratio significantly. Since the background has no overall asymmetry it will dilutes the asymmetry. Therefore a good background suppression is mandatory.

In Fig. 7.7 the asymmetry $\mathcal{A}_T$ is shown as function of the phase ϕ_{A_t}. The lines show the amount of integrated luminosity at which a $3\,\sigma$ observation is possible. The asymmetry can be seen where the asymmetry curve lies outside the luminosity band. With an asymmetry maximum of $|\mathcal{A}_t|_{\text{max}} \approx 2.23\,\%$ the study lies not within the $3\,\sigma$ observation limit for $1\,\text{ab}^{-1}$. To be sensitive to a phase between $|0.6|\pi < \phi_{A_t} < |0.85\pi|$ an asymmetry of $|\mathcal{A}_t|_{\text{max}} \approx 6.5\,\%$ is required.

In Section 7.3.2 it was discussed that different masses for the constraints of Eq. (7.11) – (7.14) influ-

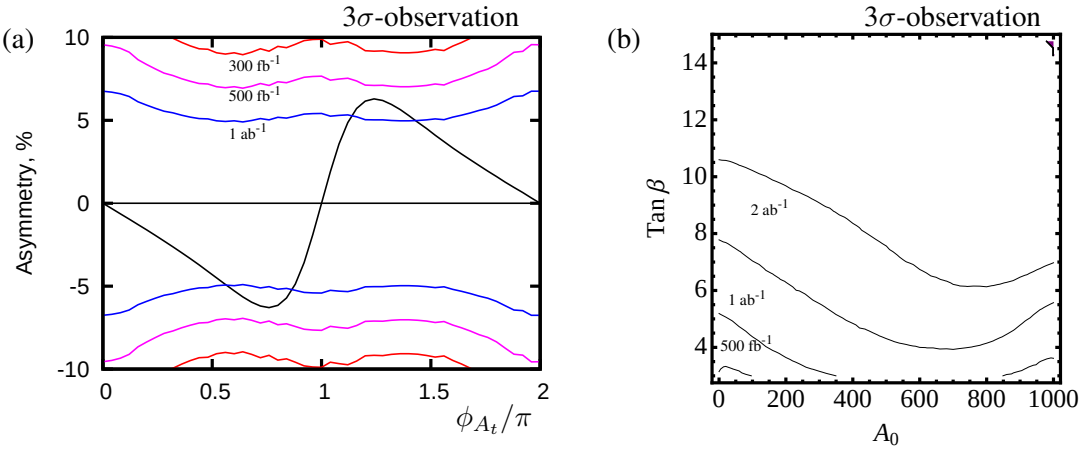

Figure 7.7.: General SUSY production for the asymmetry $\mathcal{A}_{\ell_N}$. τ identification is included in both plots. Asymmetry, $\mathcal{A}_{\ell_N}$, at reference point with 3σ-luminosity lines shown (a), and minimum luminosity required for 3σ-discovery in $\tan\beta, A_0$ plane when asymmetry, $\mathcal{A}_{\ell_N}$, is maximal (b) [77].

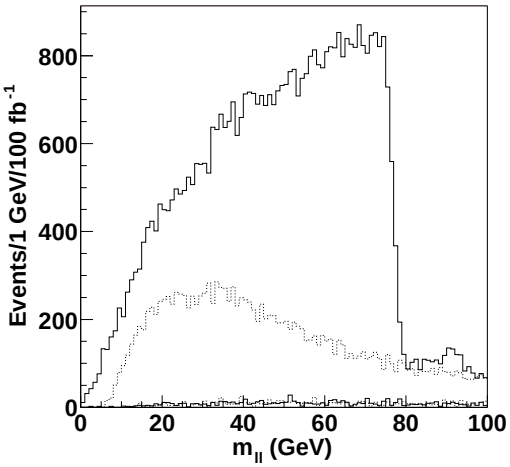

Figure 7.8.: Invariant mass $m_{\ell\ell}$ for an integrated luminosity of 100 fb^{-1} [180].

ences the momentum reconstruction. In case of truth level momentum reconstruction the true MC masses of the $\tilde{\chi}_1^0$, $\tilde{\chi}_2^0$, $\tilde{t}$, $\tilde{\ell}$, and t are used. At reconstruction level the MC masses are not available. The method is based on the assumption that the masses of all particles are known. Therefore the masses defined by the scenario (Tab. 7.2 – Tab. 7.4) are used.

To investigate the effect of different masses the momentum reconstruction for the true $\tilde{\chi}_1^0$ and reconstructed $\tilde{\chi}_1^0$ is performed with varying masses. For the true $\tilde{\chi}_2^0$ the model masses, defined by the scenario and the MC masses are used. Figure 7.5 shows that the true masses of all sparticles have a certain width. If the true masses or the model masses are used for the momentum reconstruction of the true $\tilde{\chi}_1^0$ the relative resolution of the reconstructed p_{T} and true 4-vector p_{T} shows are sharp peak at zero (see Fig. 7.10 red lines). For the reconstructed $\tilde{\chi}_1^0$ the model masses, true MC masses extracted from the decay chain, and smeared masses are used for the momentum reconstruction. The masses of $\tilde{\chi}_1^0$, $\tilde{\chi}_2^0$, $\tilde{\ell}$, and $\tilde{t}$ are smeared within their mass uncertainties. The uncertainties are extracted from the SPS 1a benchmark scenario [180]. The mass of the $\tilde{\chi}_2^0$ and $\tilde{\ell}$ depend on the mass of the $\tilde{\chi}_1^0$, while the mass of the $\tilde{t}$ is independent. The following mass constraints are used

$$m_{\tilde{\chi}_1^0} = (77.68 \pm 3.88)\mathrm{GeV}, \tag{7.23}$$

$$m_{\tilde{\chi}_2^0} = 66.49 + 0.977 \cdot m_{\tilde{\chi}_1^0}, \tag{7.24}$$

$$m_{\tilde{\ell}} = \frac{0.93(m_{\tilde{\chi}_1^0} + m_{\tilde{\chi}_2^0})}{2}, \tag{7.25}$$

$$m_{\tilde{t}_1} = (346.81 \pm 6.4)\mathrm{GeV}. \tag{7.26}$$

The masses of the $\tilde{\chi}_1^0$ and the $\tilde{t}_1$ are smeared with a Gauss distribution while the masses of the $\tilde{\chi}_2^0$ and $\tilde{\ell}$ are calculated with respect to $m_{\tilde{\chi}_1^0}$. The relative resolution for the p_{T} of the reconstructed $\tilde{\chi}_1^0$ is shown in Fig. 7.9. All three resolutions are significant expanded than both resolutions of the true $\tilde{\chi}_1^0$. With a maximum of RMS = 0.618 ± 0.016 for the smeared mass, the uncertainty on the p_{T} resolution is more than 50 %. For both truth momenta the RMS is very close to zero, even if the model mass is

Table 7.9.: Number of events after momentum reconstruction and triple product with additional cuts for both, masses defined by the model and with mass uncertainties at the LHC with $\sqrt{s} = 14\,\text{TeV}$.

	Scenario masses	Smeared masses
Events with $500\,\text{fb}^{-1}$ after momentum reconstruction and additional cuts	5363 ± 73.2	5280 ± 72.7
Events with $500\,\text{fb}^{-1}$ after triple product and additional cuts	1104 ± 33.2	1094 ± 33.1
Difference of $N_{\mathcal{T}+}$ and $N_{\mathcal{T}-}$ (N_{asym})	$+20 \pm 33.2$	$+88 \pm 33.1$

used instead of the true MC mass. Within the three resolutions of the reconstructed $\tilde{\chi}_1^0$ the quality of the relative resolution decreases from true MC masse to the smeared masse. In Tab. 7.9 the number of events after the momentum reconstruction, triple product and the difference $N_{\mathcal{T}+} - N_{\mathcal{T}-}$ for both mass spectra is summarized. The number of events does not show any significant variations, whereas asymmetry value, N_{asym} differs significantly. If uncertainties on the masses are included, the asymmetry value is $\mathcal{A}_T = 8.04\,\%$. This shows that, mass uncertainties have a large effect on the triple product. Hence a proper knowledge of the masses of the $\tilde{\chi}_1^0$, $\tilde{\chi}_2^0$, $\tilde{t}_1$, and $\tilde{\ell}$ is required for this study. At the LHC no precise mass measurements can be performed while the mass difference can be measured very accurate. The mass is measured with the analysis of kinematic edges. In Fig. 7.8 the invariant mass of two leptons in a process involving $\tilde{\chi}_2^0 \to \tilde{\ell}_R \ell$ is shown. The mass of the $\tilde{\chi}_2^0$is determind by the endpoint of the edge.

The reconstructed momentum of the $\tilde{\chi}_1^0$ is shown in Fig. 7.10. The black lines shows the distribution for all events, accepted by the event selection and with all triple products having the same sign. The blue lines represents the distribution with all events rejected which do not contain the decay chain of interest (7.19). The number of reconstructed momenta is slightly less. That means, that a small fraction of the reconstructed momenta in the black distribution originate from the wrong decay chain. The red line shows the p_{T} distribution when the t, ℓ_N, and ℓ_F that are used for the triple product match to a MC t and MC leptons from the decay chain. This conditions reduces the statistic significant and shows that a large fraction of the particles, used for the momentum reconstruction are not originating from the same decay chain. As already mentioned one problem of the reconstruction procedure are combinatorics. In Fig. 7.11 the mass and p_{T} of the reconstructed t's are shown. The distributions satisfy several constraints. While the black distribution contain all events, for the red distribution only event which contain the decay chain are accepted. This constrain reduces the number of reconstructed t's slightly and shows that a small fraction of reconstructed t candidates are not originating from the interesting decay chain. The blue distribution requires that the W used for the reconstruction of the t has a truth match[3], while the yellow distribution requires a truth match of both, W and t. Both constraints dilutes the number of t candidates significant, i.e. a large fraction of t candidates are mis-identified. These "fake" t's increase the number of combinations for the momentum reconstruction and enhance the chance of triple products with different signs.

[3] $\Delta R \leq 0.2$ for the reconstructed and truth W.

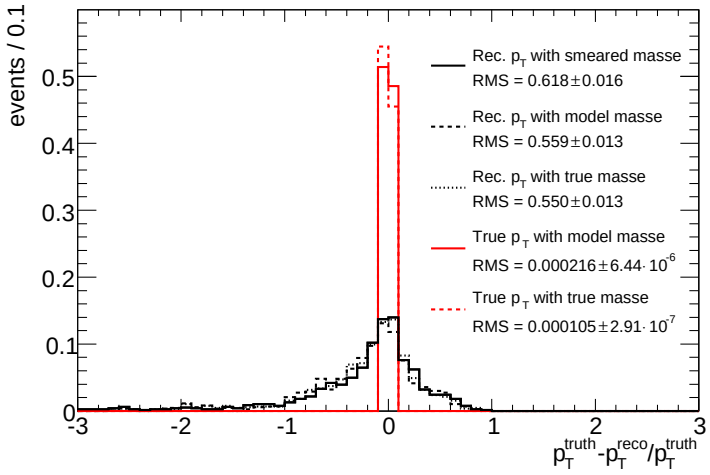

Figure 7.9.: Relative resolution of the p_{T} of the reconstructed $\tilde{\chi}_1^0$ (black) and true MC $\tilde{\chi}_1^0$ (red) for 500 fb^{-1} at the LHC with $\sqrt{s} = 14$ TeV. For the reconstructed neutralino masses defined by the scenario in Tab. 7.2 – Tab. 7.4 (dashed), true masses of the decay chain (dotted), and masses smeared according to the mass uncertainties of the SPS 1a benchmark scenario (solid) are used. For the true MC $\tilde{\chi}_1^0$ masses given by the model (solid) and true masses are used.

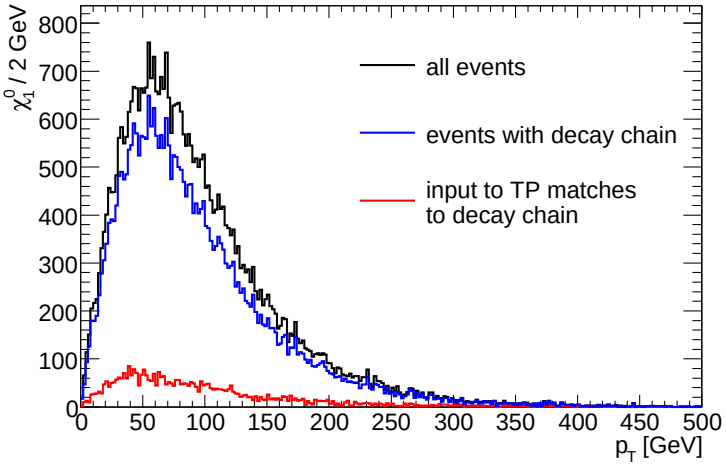

Figure 7.10.: Reconstructed p_{T} of the $\tilde{\chi}_1^0$ for 500 fb^{-1} at the LHC with $\sqrt{s} = 14$ TeV, for all events (black), only events that contain the decay chain (7.19) (blue), and for the case that t and both leptons ℓ_N and ℓ_F satisfy a truth match to the MC particles of the decay chain (red).

7.4. Conclusions

This study analyzes the possibility to observe CP-violating effects in SUSY at the LHC. The study is performed on a $\tilde{t}_1\tilde{t}_1^*$ production process followed by a two-body decay. Triple product correlations that are formed from the final state particles are sensitive to potential complex phases in the model. Since

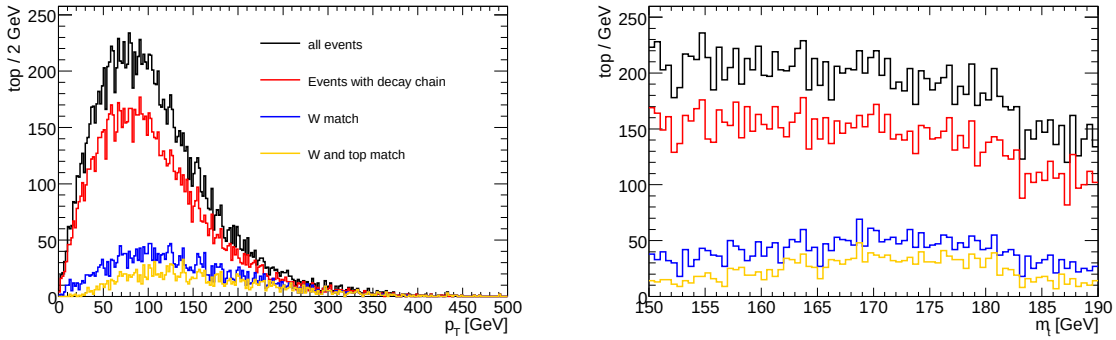

(a) (b)

Figure 7.11.: Reconstructed top momentum (a) and reconstructed top mass m_t (b).

triple products depend on the spin correlation, they are sensitive to CP-odd observables.

The process that is investigated is the $\tilde{t}_1$ decay into a t and $\tilde{\chi}_2^0$, followed by a two-body decay. Events have been generated with HERWIG++2.4.2, while the mSUGRA parameter space has been derived with SPHENO 2.2.3. Afterwards the generated events are passed through the ATLAS like simulation of the DELPHES detector simulation framework. In the mSUGRA scenario an asymmetry in the triple product distribution of up to 15 % can be expected. The source of the CP violation in this scenario is the phase of the trilinear coupling A_t that obtains a value of $\phi_{A_t} \sim 0.8$ for a maximum asymmetry.

Since the LHC is a hadron collider, precision measurements will be difficult. The rest frame of the CP-odd asymmetry is diluted due to the high boost of the produced particles, which is a challenge for observations. To get access to the rest frame of the $\tilde{t}_1$, a momentum reconstruction of the invisible LSPs is performed. The study shows that a full reconstruction of the production and decay process is possible, but as shown in Fig. 7.9 the momentum reconstruction is very sensitive to uncertainties of the sparticle masses. Therefore an accurate knowledge of all masses is required. With the full reconstructed events the momenta of particles can be boosted back into the rest frame of the $\tilde{t}_1$. The momentum reconstruction involves a decrease of the background and improves the signal to background ratio.

The study shows that after the detector simulation only an asymmetry of 2.23 % can be measured which is outside the 3 σ observation. The momentum reconstruction and background separation involves a hifh loss statistics. Furthermore the current DELPHES version does not allow significant τ-lepton identification. With increased $\tan\beta$ the branching ratio $\tilde{\chi}_2^0 \rightarrow \tilde{\ell}^{\pm}\ell^{\mp}$ is reduced and $\tilde{\tau}$'s are becoming more mixed which increases the left handed component of the lighter $\tilde{\tau}$. Therefore, the $\tilde{\tau}_1$ couples more strongly to the $\tilde{\chi}_2^0$ and becomes more dominant in this decay channel. The absence of the τ-lepton identification reduces the statistics. However, the implementation of a τ-lepton identification would induce larger missing transverse energy from the τ neutrinos. The large $E_{\mathrm{T}}^{\mathrm{miss}}$ again would corrupt the momentum reconstruction.

In the current study the signal to background ration is increased only up to 0.263 ± 0.034. The high background dilutes the asymmetry although it contains no overall asymmetry. Hence the background rejection has to be improved to become more sensitive to asymmetries in the triple product. Even with a maximum asymmetry of $\sim$6.5 % a 3 σ effect at the LHC would require an integrated luminosity of $\mathcal{L} = 1$ ab^{-1} of data and would only be sensitive in the range of $|0.6\pi| \lesssim \phi_{A_t} \lesssim |0.85\pi|$. With an asymmetry of $\mathcal{A}_T = 2.23$ %, CP-violating effects induced by a phase in the trilinear coupling of $\phi_{A_t} = 0.8\pi$ can

not be measured with an integrated luminosity of $500\,\mathrm{nb}^{-1}$.

With an instantaneous luminosity of $\mathcal{L} = 10^{35}\mathrm{cm}^{-2}\mathrm{s}^{-1}$ the upgrade of the LHC to s(uper)LHC [181] might be able to access this parameter space and becomes more sensitive to the asymmetry in a wider range of the phase of the trilinear coupling. In the clean environment of future linear collider, such as the ILC [182] or CLIC [183] it will be more easier to isolate the kinematic region of the asymmetry. Besides the masses of the sparticles can be measured more precisely which allows a more accurate calculation of the triple product.

The effect of CP violation in SUSY at the LHC can also be studied on further channels such as

$$\tilde{g} \to \tilde{t} + t \to \tilde{\chi}_1^+ + b + t \to \tilde{\chi}_1^0 \ell^+ \nu_\ell + b + t \tag{7.27}$$

as described in [184]. In this case the source of the CP violation is the phase of the bino mass parameter M_1. A $3\,\sigma$ effect can be expected after a few years of LHC running at high luminosity. In this case the sensitivity to the phase is expected in the range $0.2\,\pi \lesssim \phi_1 \lesssim 0.85\,\pi$.

8. Summary and Outlook

8.1. Summary and Conclusion

With the start of the LHC in 2010 a new energy range in pp collisions with a center-of-mass energy of $\sqrt{s} = 7$ TeV is explored for the first time. The first goal of the LHC will be the re-discovery and validation of the Standard Model, like the Z boson and the identification of the top quark. As already mentioned in this thesis the Standard Model is not complete and poses many questions. The Higgs mechanism distributes mass to particles and comes together with a new particle, the Higgs boson. If the Higgs boson exists, its mass will lie in the discovery potential of the LHC. The idea of supersymmetry provides many solutions to further problems, such as the hierarchy problem when all running couplings converge in one point at the GUT scale. New sources for dark matter are provided by several supersymmetric models where the lightest supersymmetric particle (LSP) serves as a good dark matter candidate.

The first data taking phase was focused on a profound understanding of the detector. Particularly analyses involving supersymmetric scenarios use of a comprehensive choice of reconstructed objects, such as missing transverse energy, jet, leptons, and photons. All facets of the reconstruction and identification have to be understood. This includes a detailed understanding of the varied backgrounds to perform a good separation against the signal.

In searches for new physics τ-leptons play an important role. In the decay of gauge bosons, Higgs bosons, or SUSY cascade decays they carry information on the polarization of the decaying resonance. The polarization can also be used to discriminate between MSSM models and those with extra dimension. In this thesis the reconstruction and identification performance of τ-leptons at 7 TeV with the ATLAS detector has been shown. For an integrated luminosity of $\mathcal{L} = 244\,\text{nb}^{-1}$ no τ-leptons are expected but at proton-proton colliders τ-leptons form jets that are very close to QCD background. The reconstruction and identification relies to a large fraction on shower shape variables. The extensive dijet background has been used to compare the distribution of these variables with predictions from Monte Carlo simulation. Thereby the systematic uncertainties were investigated by using different shower models, different underlying event tunes, different fragmentation models, and different detector material. The identification performance has been tested by using a boosted decision tree (BDT) and a projective likelihood method (LL). It has been shown that the distributions in data agree very well with the simulation within systematic uncertainties and that they provide a good separation power of τ-leptons against QCD dijet background. The first τ candidates from the decay of a W boson and a Z boson have been presented presented.

The identification of τ-leptons based on the separation power of varied discriminating variables build during the reconstruction. Complex multivariate techniques such as BDT or LL require a good understanding of the detector response and variables. This thesis presents the development of a cut-based identification method, that uses a small selection of well understood variables to distinguish between signal and background. Since the reconstruction of tracks and vertices needs a good detector alignment, two methods have been developed: one method trusts only calorimeter variables to avoid uncertainties in the inner detector alignment, while the second, more advanced method combines calorimeter and tracking information. In contrast to multivariate techniques, the cut-based method is more transparent concerning signal and background separation. Both cut-based methods were optimized separately for 1-prong and

3-prong τ candidates, as well as for 5 different E_{T}-bins. Compared to a likelihood the performance of the cut-based methods are smaller but for an expected efficiency of 30 % and 50 % they show a good separartion power against QCD dijet background. Both cut-based methods have been used to study the reconstruction and identification performance of τ-leptons with $\mathcal{L} = 244\,\mathrm{nb}^{-1}$ and build the basis for more advanced algorithms.

Finally the potential to observe CP-violating effects in SUSY at the LHC has been observed for the first time. The CP violation observed in the Standard Model is not sufficient to explain the matter – anti-matter asymmetry in the universe, hence new source of CP violation are required. In this study the effect of CP violation in the stop sector inside the MSSM scenario for 500 fb^{-1} at 14 TeV has been investigated. Instead of using the official ATLAS detector simulation the fast simulation framework DELPHES has been used to simulate an ATLAS like detector. In this scenario the CP violation occurs via a complex phase in the trilinear coupling. For this study the phase has been set to $\phi_{A_t} = 0.8\pi$. The phase in the trilinear coupling induces a T-odd asymmetry in the triple products of the final state. As production process the two-body decay chain

$$\tilde{t} \rightarrow t + \tilde{\chi}_2^0 \rightarrow t + \tilde{\ell}^{\pm} + \ell_N^{\mp} \rightarrow t + \tilde{\chi}_1^0 + \ell_N^{\mp} + \ell_F^{\pm}$$

has been chosen and the triple product

$$\mathcal{T}_{\ell_N} = \vec{p}_{\ell_N} \cdot (\vec{p}_W \times \vec{p}_t)$$

has been investigated. The triple product has to be calculated in the rest frame of the decay $\tilde{t}$, hence a full reconstruction of all final state particle momenta is essential. The momentum reconstruction of the $\tilde{\chi}_1^0$ and the calculation of the triple product asymmetry has been presented. The momentum reconstruction is restricted by a large fraction of combinatorics originating from the W boson and top reconstruction, as well as from the correct identification of the near and far lepton. Therefore a significant fraction of the reconstructed momenta can not be allocated to the $\tilde{\chi}_1^0$ of the observed decay chain. With a phase of $\phi_{A_t} = 0.8\pi$ the induced maximum asymmetry was $|\mathcal{A}_{\ell_N}|_{\mathrm{max}} \approx 15\,\%$, while the measured triple product asymmetry was $\mathcal{A}_T = 2.23 \pm 2.28\,\%$. The study has been shown that a clear separation of signal and the large background needs further effords. A significant measurement of the asymmetry only using electrons and muons as final state leptons is not possible.

8.2. Outlook

Whereas the focus of the first year of data taking was due to the understanding of the detector response and of the reconstruction and identification algorithm, the run of 2011 will be used for detailed studies, such as τ analyses, search for Standard Model and new physics, as well as for developing of advanced identification methods. Studies on the performance of the τ-lepton identification helped to identify variables with a better separation power against QCD background and which are more robust against systematic uncertainties. These variables can be used to modify the cut-based method to make it more stable against uncertainties. A well calibrated inner detector is essential for the identification and reconstruction of primary and secondary vertices. Since a displaced secondary vertex is characteristical for τ-leptons, an accurate vertex reconstruction will improve the separation of τ-leptons from their QCD background.

With a well performing cut-based method more advanced techniques can be evolved, such as BDT and LL. By using the same collection of variables all methods can be used as cross check against each other. Eventually τ-leptons will give a large contribution in many analyses of new physics.

It has been pointed out that the measurement of the triple product asymmetry in case of a phase in the trilinear coupling is not possible. Due to a faint τ reconstruction of the simulation framework

DELPHES, no τ-leptons have been used for the study presented in this thesis. As shown in Tab. 7.5 the dominant decay process is $\tilde{\chi}_1^+ \rightarrow \tilde{\tau}_1^+ \nu_\tau$, hence the implementation of τ-leptons could increase the statistic significantly. Further improvement of the W boson and top quark reconstruction, as well as an improved lepton identification would reduce combinatorics and increase the signal to background ratio.

As shown, the momentum reconstruction responds very sensitive on the sparticle masses. At the LHC precise mass measurements of new particles will be a challenge, while the mass differences can be measure very precisely. Even if CP violation in the MSSM scenario is not found at the LHC, it can probably be measured at a future collider, if CP violation in the MSSM exists. A lepton collider with high energy provides a very clean environment and has the advantage of a know initial state of the collision. Hence the kinematic region of the signal process can be isolated and a good separation against the background can be performed and the effect of combinatorics can be minimized. Precise mass measurements of SUSY particles will also improve the momentum reconstruction.

A. Additional figures

A.1. Calorimeter identification variables

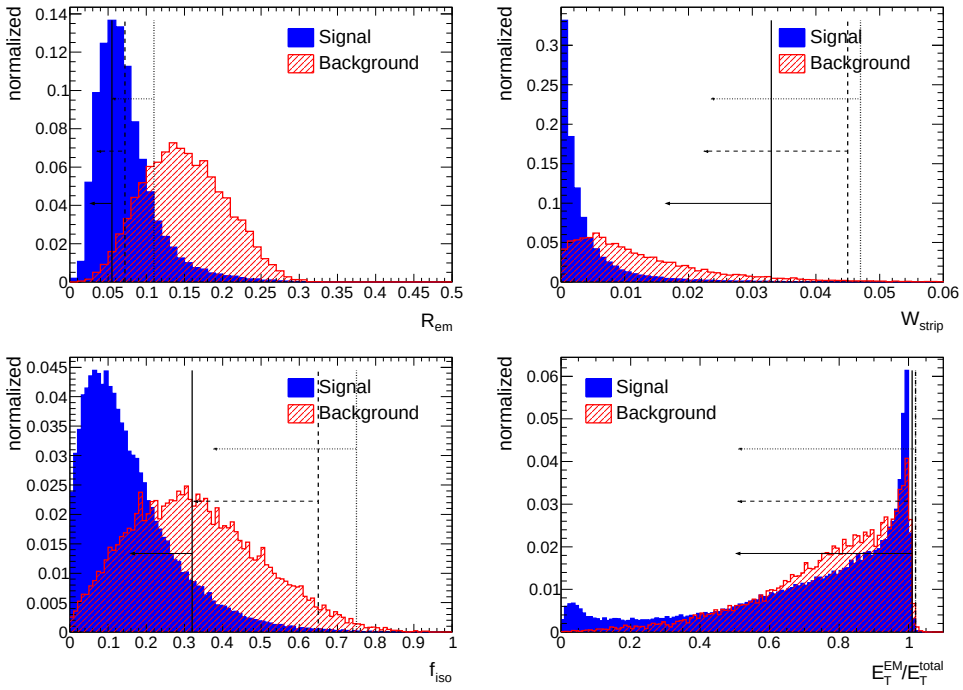

Figure A.1.: Distribution of calorimeter variables for 1-prong τ-lepton candidates within a p_{T} range of 10 – 25 GeV, position of tight (solid line), medium (dashed line), and loose (dotted line) cuts are shown.

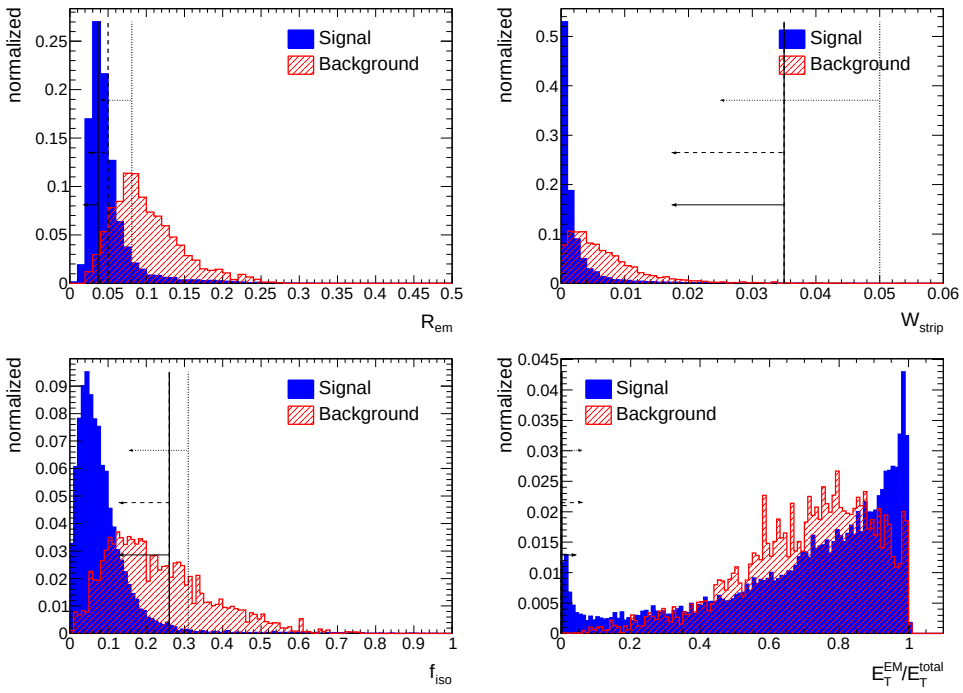

Figure A.2.: Distribution of calorimeter variables for 1-prong τ-lepton candidates within a p_T range of 45 – 70 GeV, position of tight (solid line), medium (dashed line), and loose (dotted line) cuts are shown.

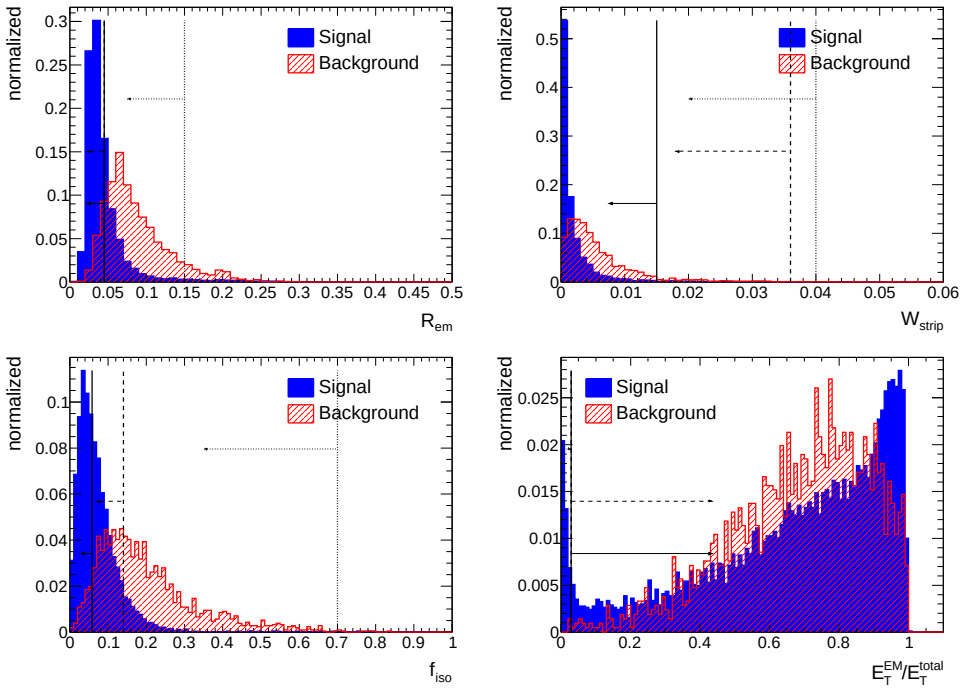

Figure A.3.: Distribution of calorimeter variables for 1-prong τ-lepton candidates within a p_T range of 70 – 100 GeV, position of tight (solid line), medium (dashed line), and loose (dotted line) cuts are shown.

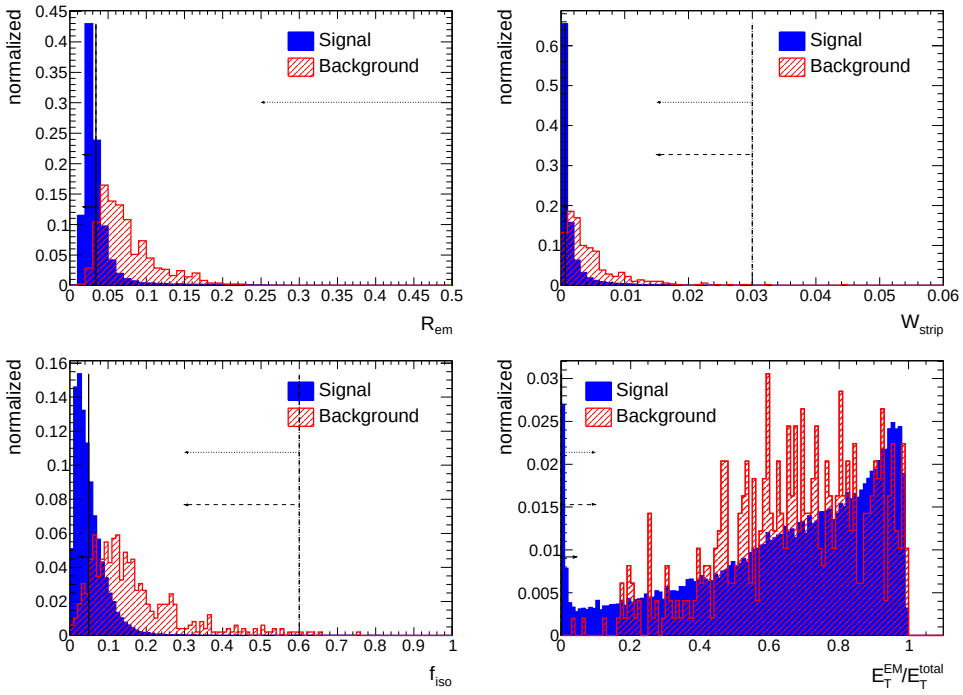

Figure A.4.: Distribution of calorimeter variables for 1-prong τ-lepton candidates within a p_T range of > 100 GeV, position of tight (solid line), medium (dashed line), and loose (dotted line) cuts are shown.

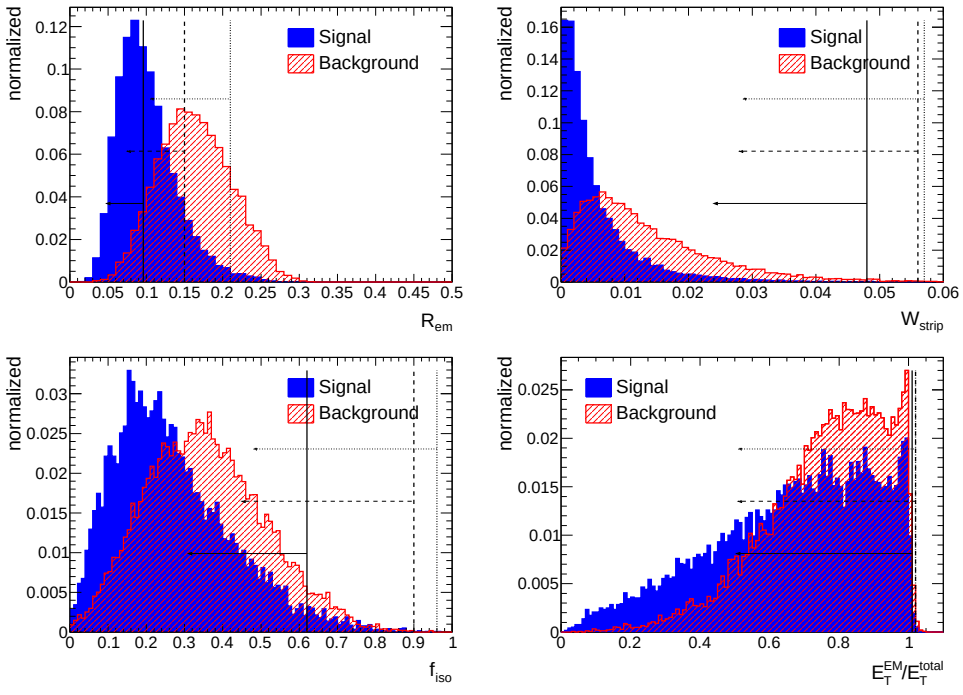

Figure A.5.: Distribution of calorimeter variables for 3-prong τ-lepton candidates within a p_T range of 10 – 25 GeV, position of tight (solid line), medium (dashed line), and loose (dotted line) cuts are shown.

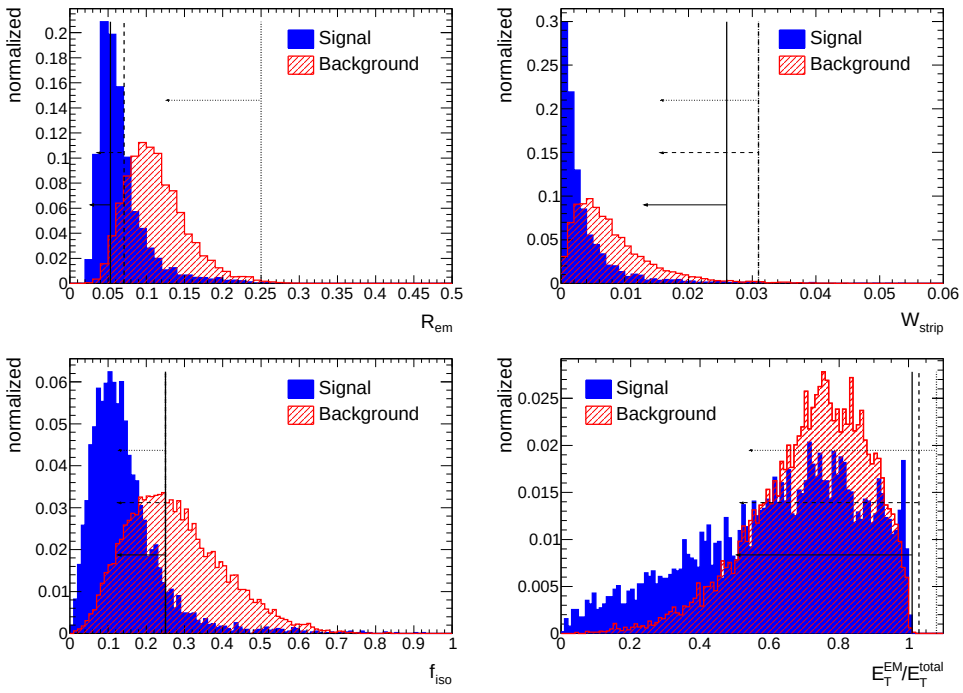

Figure A.6.: Distribution of calorimeter variables for 3-prong τ-lepton candidates within a p_{T} range of 45 – 70 GeV, position of tight (solid line), medium (dashed line), and loose (dotted line) cuts are shown.

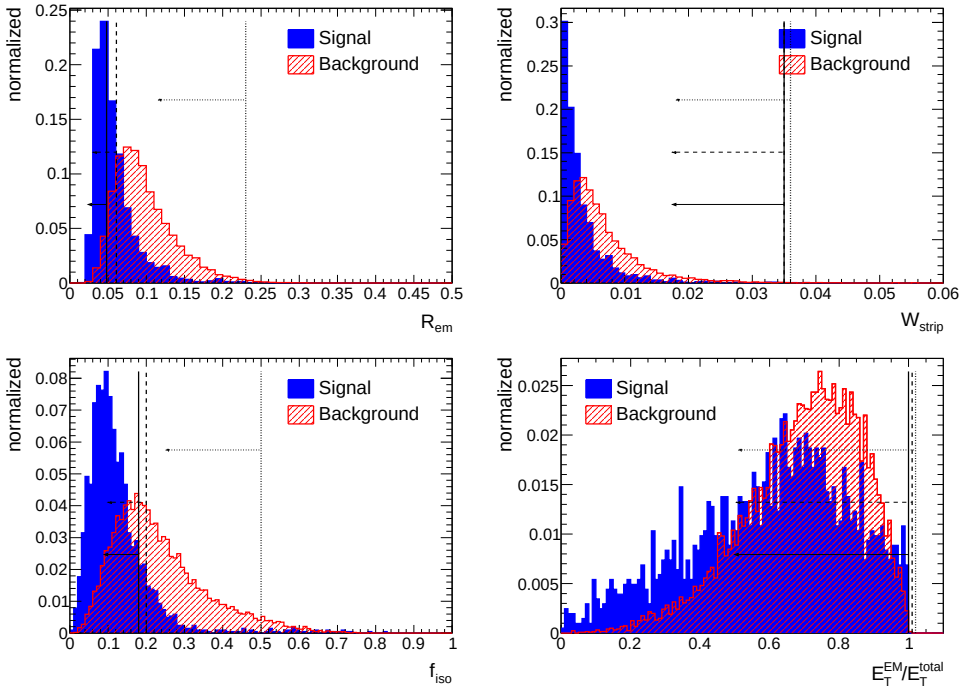

Figure A.7.: Distribution of calorimeter variables for 3-prong τ-lepton candidates within a p_{T} range of 70 – 100 GeV, position of tight (solid line), medium (dashed line), and loose (dotted line) cuts are shown.

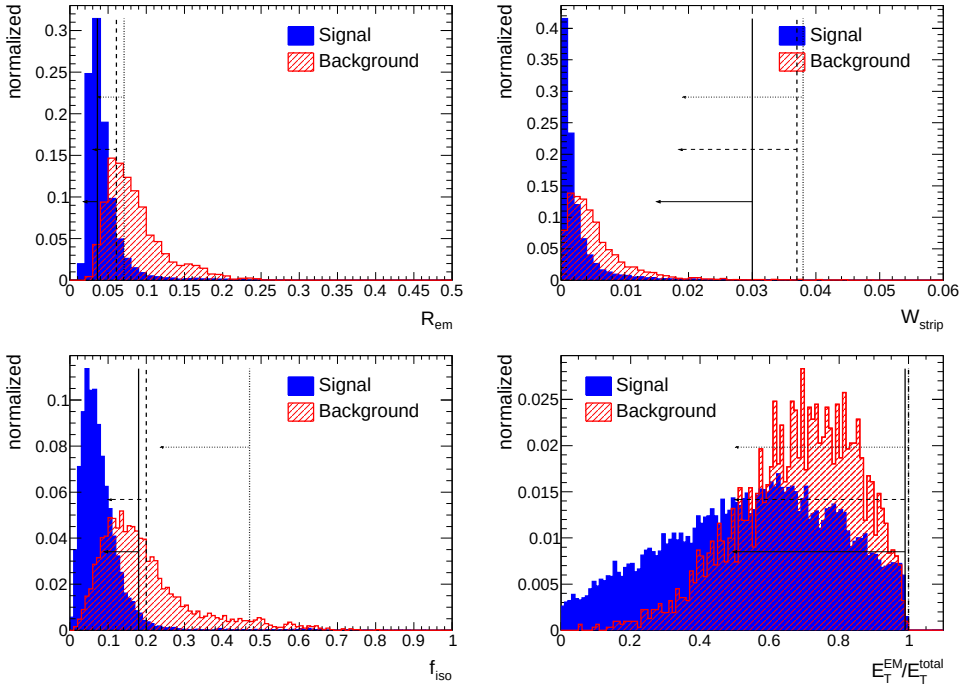

Figure A.8.: Distribution of calorimeter variables for 3-prong τ-lepton candidates within a p_{T} range of $> 100\,\mathrm{GeV}$, position of tight (solid line), medium (dashed line), and loose (dotted line) cuts are shown.

A.2. Calorimeter+tracking identification variables

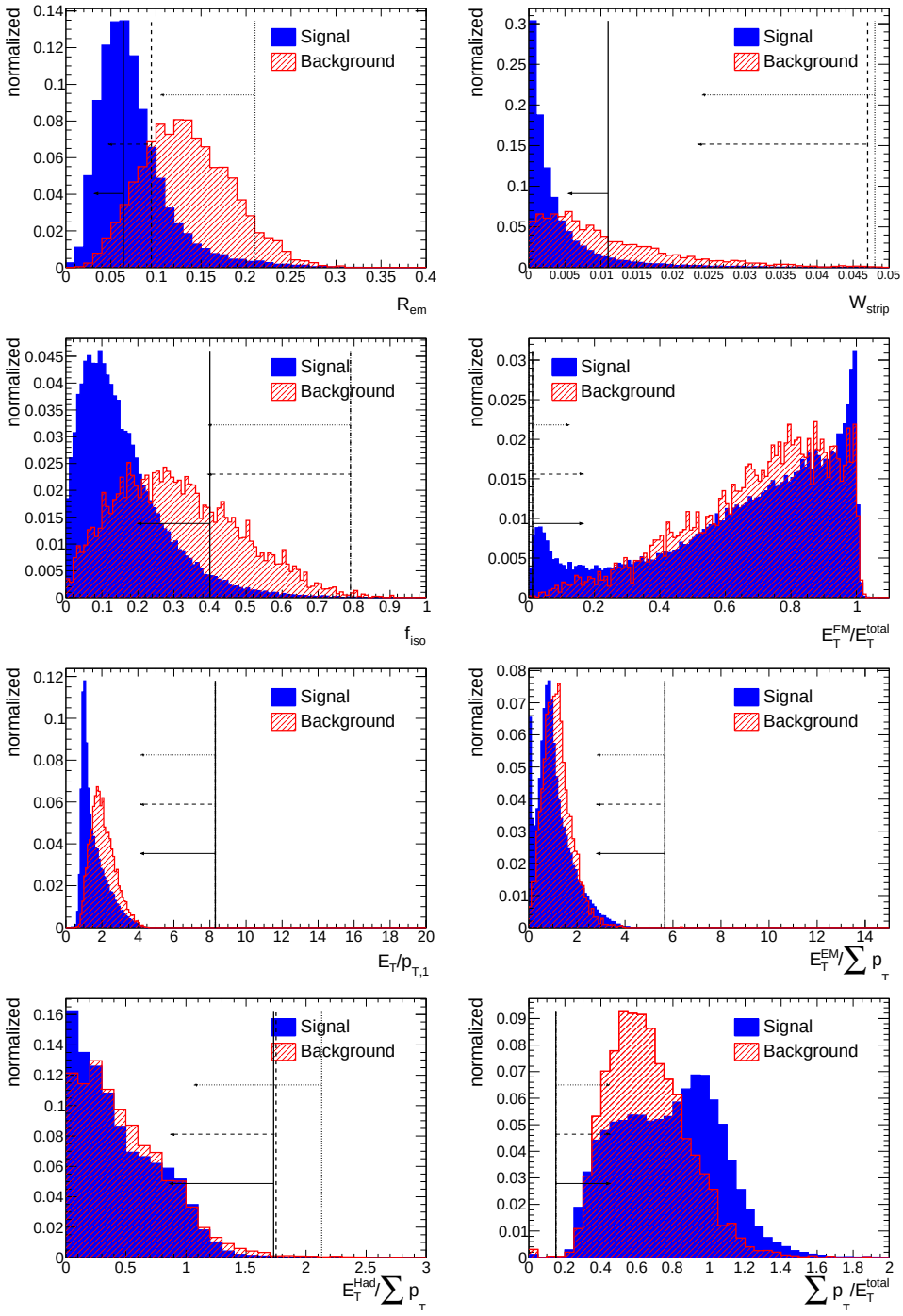

Figure A.9.: Distribution of calorimeter and tracking variables for 1-prong τ-lepton candidates within a p_{T} range of 10 – 25 GeV, position of tight (solid line), medium (dashed line), and loose (dotted line) cuts are shown.

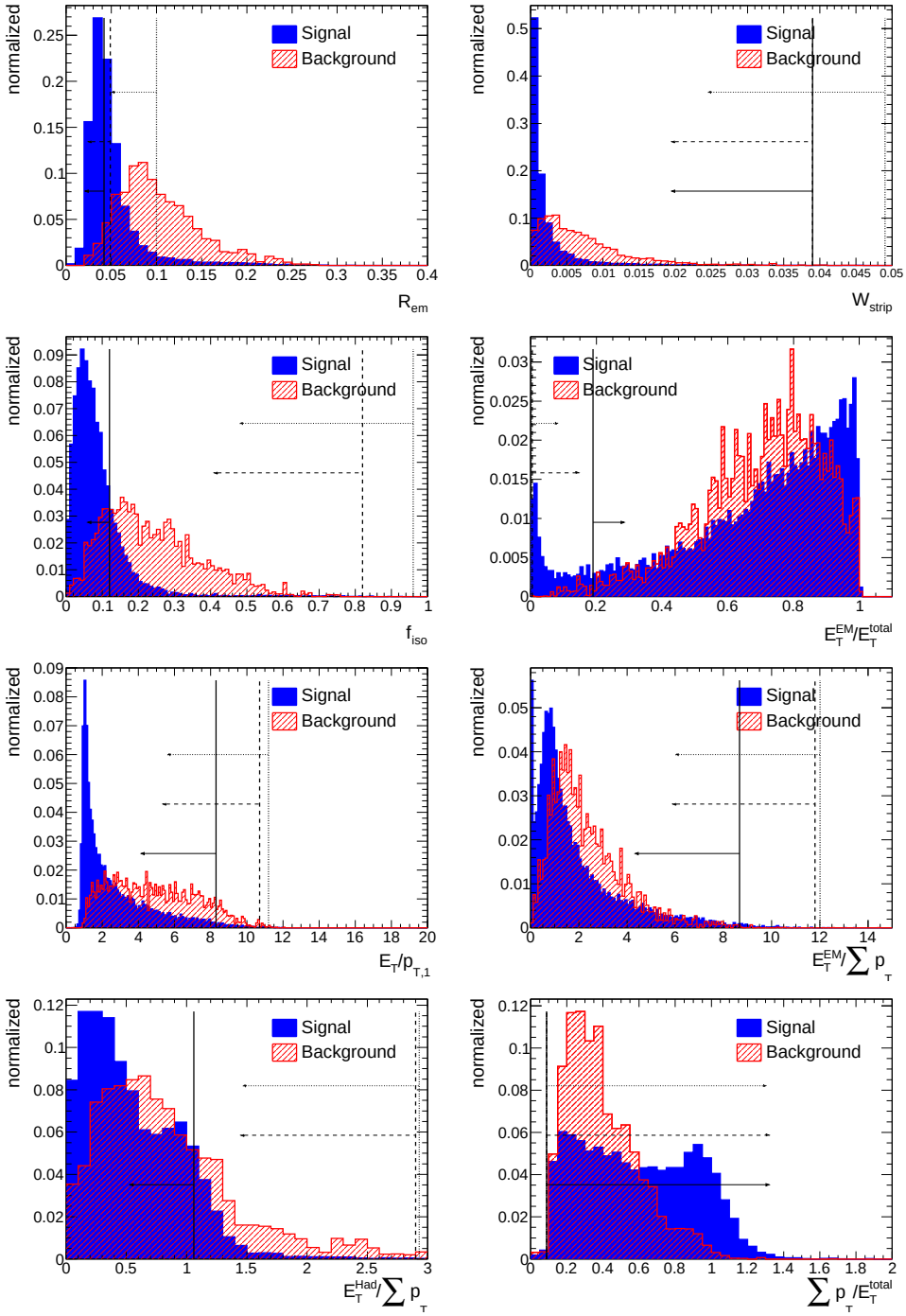

Figure A.10.: Distribution of calorimeter and tracking variables for 1-prong τ-lepton candidates within a p_{T} range of 45 – 70 GeV, position of tight (solid line), medium (dashed line), and loose (dotted line) cuts are shown.

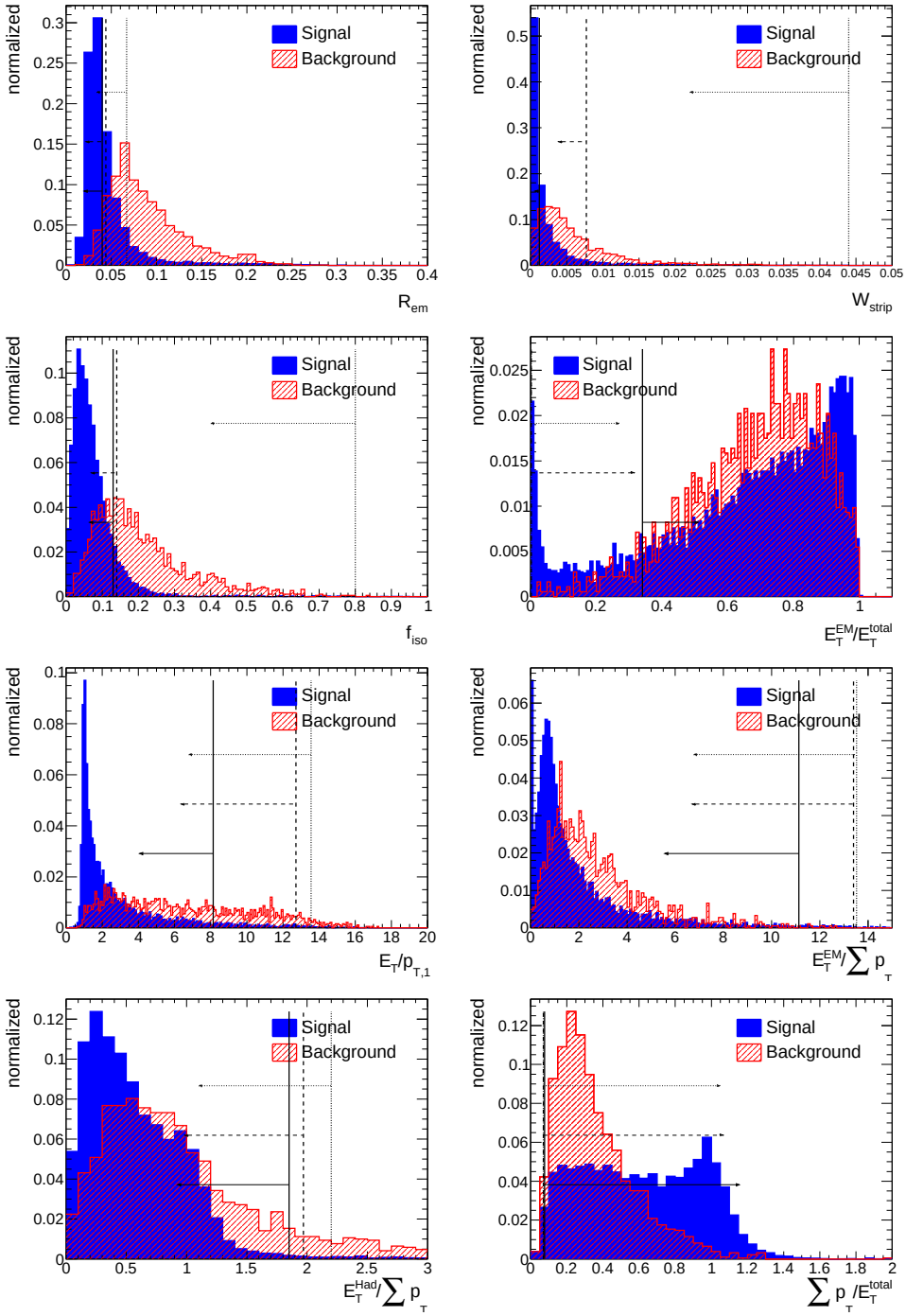

Figure A.11.: Distribution of calorimeter and tracking variables for 1-prong τ-lepton candidates within a p_{T} range of 70 – 100 GeV, position of tight (solid line), medium (dashed line), and loose (dotted line) cuts are shown.

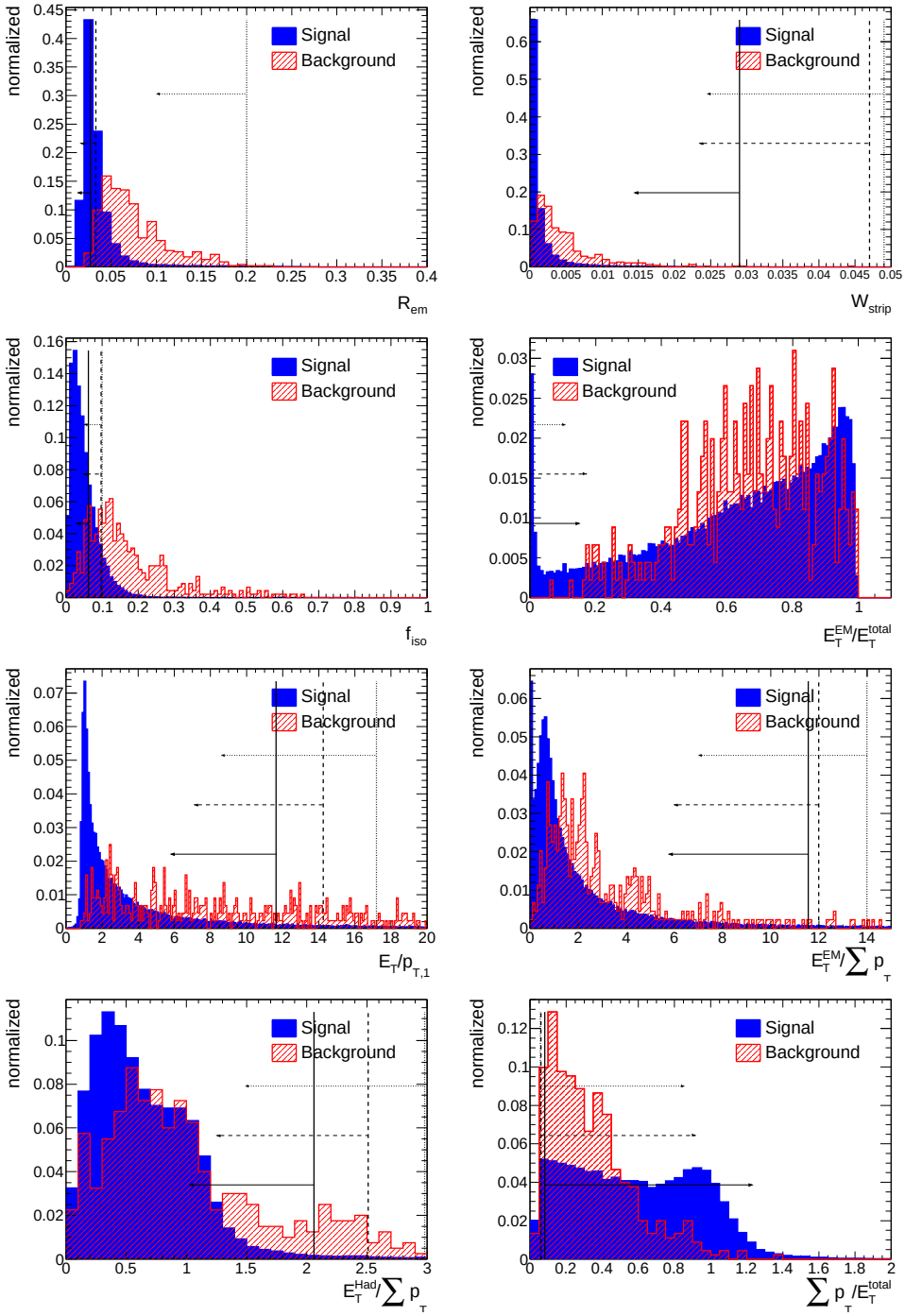

Figure A.12.: Distribution of calorimeter and tracking variables for 1-prong τ-lepton candidates within a p_{T} range of $> 100\,\mathrm{GeV}$, position of tight (solid line), medium (dashed line), and loose (dotted line) cuts are shown.

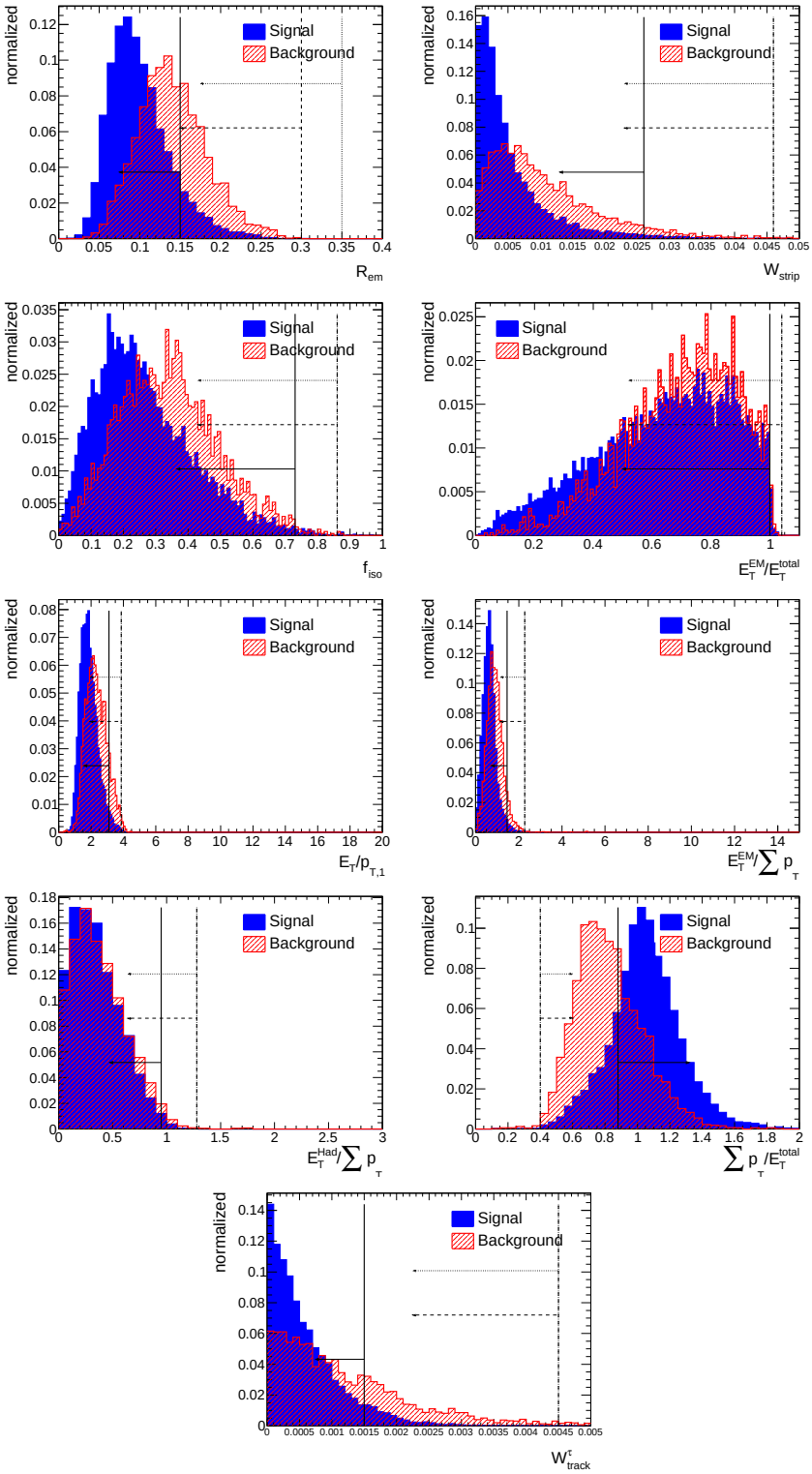

Figure A.13.: Distribution of calorimeter and tracking variables for 3-prong τ-lepton candidates within a p_{T} range of 10 – 25 GeV, position of tight (solid line), medium (dashed line), and loose (dotted line) cuts are shown.

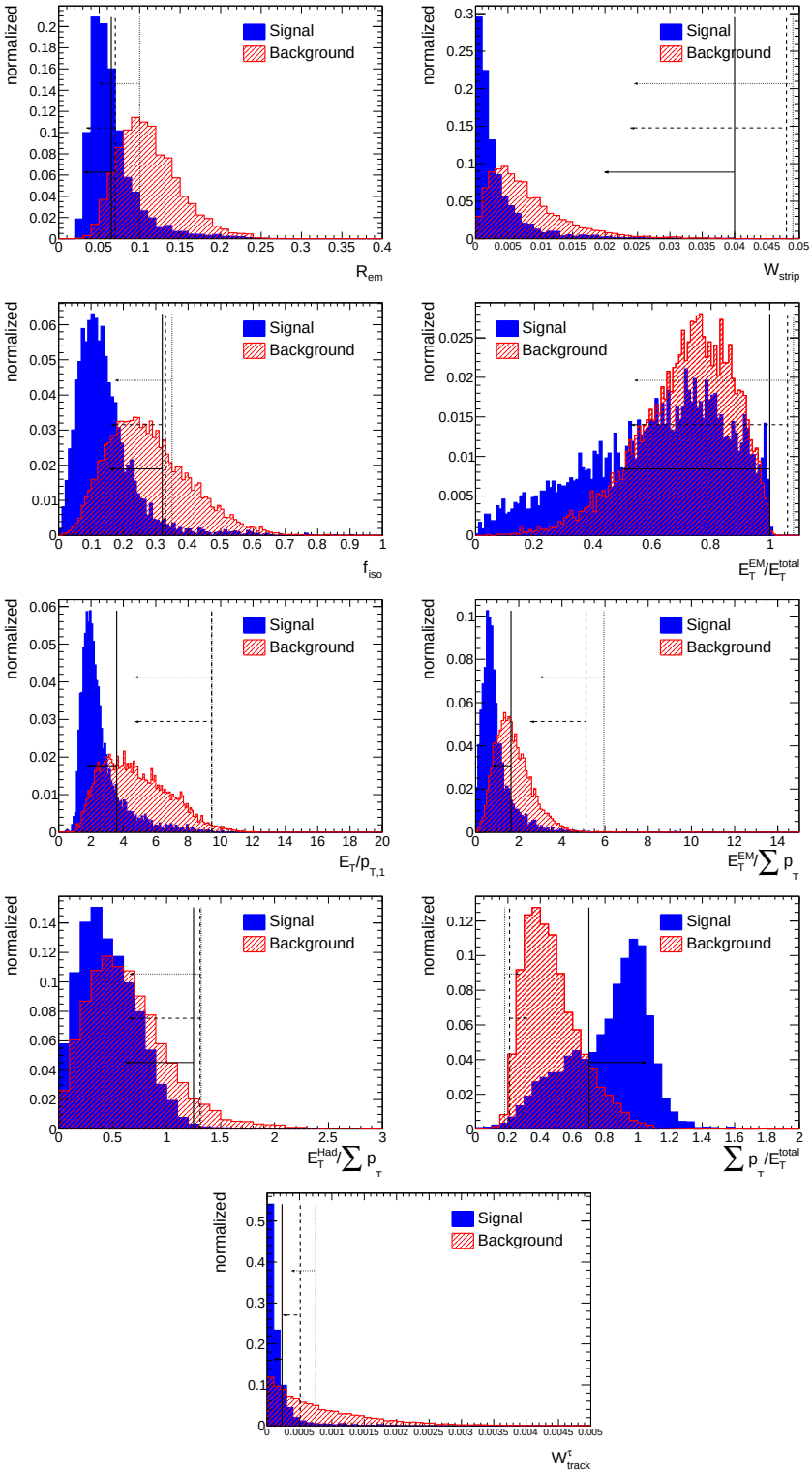

Figure A.14.: Distribution of calorimeter and tracking variables for 3-prong τ-lepton candidates within a p_{T} range of 45 – 70 GeV, position of tight (solid line), medium (dashed line), and loose (dotted line) cuts are shown.

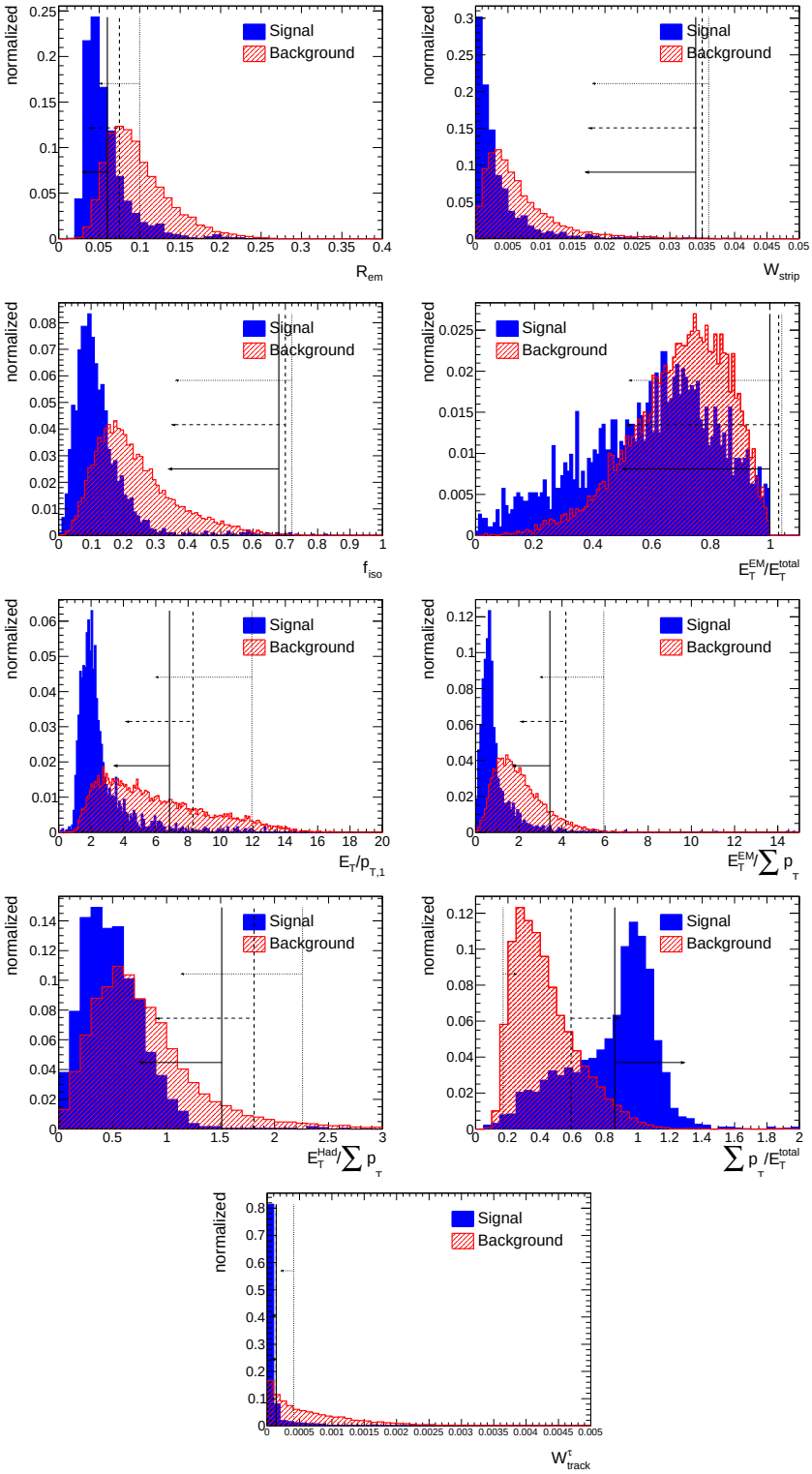

Figure A.15.: Distribution of calorimeter and tracking variables for 3-prong τ-lepton candidates within a p_{T} range of 70 – 100 GeV, position of tight (solid line), medium (dashed line), and loose (dotted line) cuts are shown.

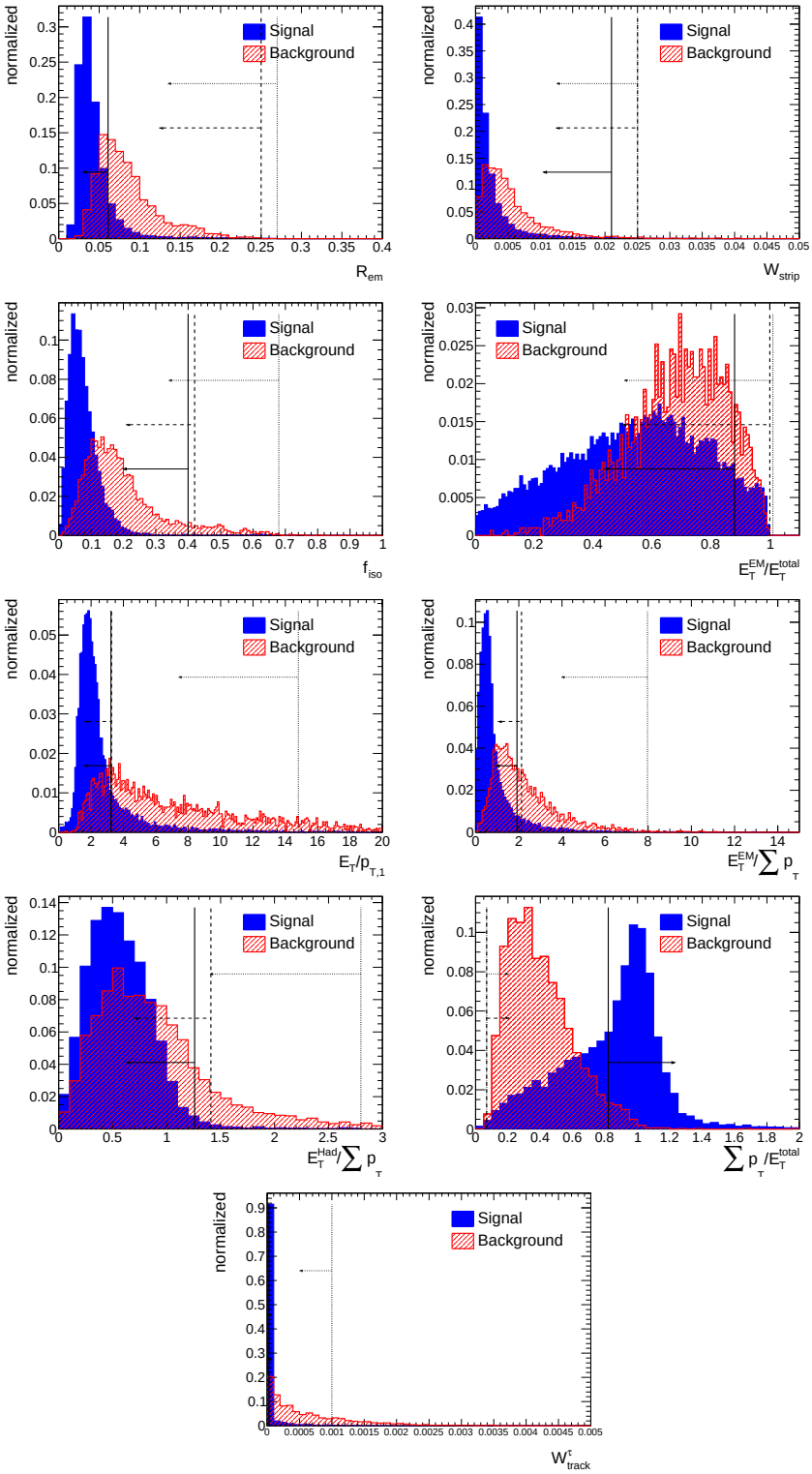

Figure A.16.: Distribution of calorimeter and tracking variables for 3-prong τ-lepton candidates within a p_{T} range of $> 100\,\mathrm{GeV}$, position of tight (solid line), medium (dashed line), and loose (dotted line) cuts are shown.

B. Additional tables

Table B.1.: Configuration options for the TMVA cut optimisation. Values given are default. If predefined categories exist, the default category is marked by a '*'.

Option	Values	Description
`FitMethod`	`MC, GA*, SA`	Optimisation method
`EffMethod`	`EffSel, EffPDF`	Selection method
`VarProp[i]`	`NotEnforced*, FMax, FMin, FSmart`	Variable properties that can be used to inject prior information on cut boundaries per variable `[i]`; if no index is given, the selection applies to all variables
`CutRangeMin[i]`	`-1`	Minimum of allowed cut range for variable `[i]`; if no index is given, the value applies to all variables
`CutRangeMax[i]`	`-1`	Maximum of allowed cut range for variable `[i]` (see above); if `CutRangeMin=CutRangeMax`, the natural ranges of the input variables are used as cut range

Table B.2.: Monte Carlo datasets. The baseline samples are e468_s766_s767_r1303. The others are used for the systematic uncertainty evaluation.

MC dataset ID	Simulation tag	Events	Description
105009	e468_s766_s767_r1303	1388184	Baseline
105010	e468_s766_s767_r1303	1354485	
105011	e468_s766_s767_r1303	1388079	
105012	e468_s766_s767_r1303	1387430	
105013	e468_s766_s767_r1303	1397401	
105014	e468_s766_s767_r1303	1391612	
105009	e468_s774_s767_r1302	99938	Different shower model
105010	e468_s774_s767_r1302	99837	(FTFP_BERT)
105011	e468_s774_s767_r1302	99940	
105012	e468_s774_s767_r1302	99908	
105013	e468_s774_s767_r1302	99834	
105009	e468_s775_s767_r1302	99896	Different shower model
105010	e468_s775_s767_r1302	88995	(QGSP)
105011	e468_s775_s767_r1302	99995	
105012	e468_s775_s767_r1302	98877	
105013	e468_s775_s767_r1302	99896	
105009	e468_s790_s791_r1304	99600	Different material
105010	e468_s790_s791_r1304	99947	(5% X0 between barrel and strip,
105011	e468_s790_s791_r1304	99748	20% X0 in barrel cryostat before the presampler
105012	e468_s790_s791_r1304	73900	20% X0 in cryostat after the LAr calorimeter)
105013	e468_s790_s791_r1304	99549	20% X0 in cryostat after the LAr calorimeter)
115019	e530_s766_s767_r1303	99950	Different fragmentation model
115020	e530_s766_s767_r1303	99748	(Professor model)
115021	e530_s766_s767_r1303	99950	
115022	e530_s766_s767_r1303	99798	
115023	e530_s766_s767_r1303	99898	
115029	e534_s766_s767_r1303	99848	Different underlying event model
115030	e534_s766_s767_r1303	99749	(Perugia0 tune)
115031	e534_s766_s767_r1303	99749	
115032	e534_s766_s767_r1303	97847	
115033	e534_s766_s767_r1303	99799	
106052	e468_s765_s767_r1302	201971	$Z \rightarrow \tau\tau$ dataset used as reference

Table B.3.: Cut values for calorimeter-based identification method

$E_{\mathrm{T}}^{\mathrm{vis}}$-bin (GeV)	Variable	1-prong			3-prong		
		tight	medium	loose	tight	medium	loose
10 – 25	R_{EM}	≤ 0.55	≤ 0.72	≤ 0.11	≤ 0.096	≤ 0.15	≤ 0.28
	W_{strip}	≤ 0.033	≤ 0.045	≤ 0.047	≤ 0.048	≤ 0.056	≤ 0.057
	f_{iso}	≤ 0.32	≤ 0.65	≤ 0.75	≤ 0.62	≤ 0.90	≤ 0.96
	$\frac{E_{\mathrm{T}}^{\mathrm{EM}}}{E_{\mathrm{T}}^{\mathrm{total}}}$	≤ 1.01	≤ 1.02	≤ 1.02	≤ 1.01	≤ 1.02	≤ 1.02
25 – 45	R_{EM}	≤ 0.048	≤ 0.058	≤ 0.087	≤ 0.068	≤ 0.088	≤ 0.15
	W_{strip}	≤ 0.0030	≤ 0.043	≤ 0.048	≤ 0.044	≤ 0.044	≤ 0.045
	f_{iso}	≤ 0.20	≤ 0.24	≤ 0.89	≤ 0.42	≤ 0.68	≤ 0.79
	$\frac{E_{\mathrm{T}}^{\mathrm{EM}}}{E_{\mathrm{T}}^{\mathrm{total}}}$	> 0.023	> 0.0011	> 0.0010	≤ 1.01	≤ 1.01	≤ 1.01
45 – 70	R_{EM}	≤ 0.037	≤ 0.050	≤ 0.10	≤ 0.053	≤ 0.071	≤ 0.25
	W_{strip}	≤ 0.035	≤ 0.035	≤ 0.050	≤ 0.026	≤ 0.031	≤ 0.031
	f_{iso}	≤ 0.26	≤ 0.26	≤ 0.31	≤ 0.25	≤ 0.25	≤ 0.25
	$\frac{E_{\mathrm{T}}^{\mathrm{EM}}}{E_{\mathrm{T}}^{\mathrm{total}}}$	> 0.0028	> 0.00040	> 0.00040	≤ 1.01	≤ 1.03	≤ 1.08
70 – 100	R_{EM}	≤ 0.045	≤ 0.045	≤ 0.15	≤ 0.048	≤ 0.061	≤ 0.23
	W_{strip}	≤ 0.015	≤ 0.036	≤ 0.040	≤ 0.035	≤ 0.035	≤ 0.036
	f_{iso}	≤ 0.058	≤ 0.14	≤ 0.70	≤ 0.18	≤ 0.20	≤ 0.50
	$\frac{E_{\mathrm{T}}^{\mathrm{EM}}}{E_{\mathrm{T}}^{\mathrm{total}}}$	> 0.0029	> 0.029	> 0.0010	≤ 1.00	≤ 1.01	≤ 1.02
> 100	R_{EM}	≤ 0.034	≤ 0.034	≤ 0.50	≤ 0.036	≤ 0.061	≤ 0.071
	W_{strip}	≤ 0.00069	≤ 0.030	≤ 0.030	≤ 0.030	≤ 0.037	≤ 0.038
	f_{iso}	≤ 0.049	≤ 0.60	≤ 0.60	≤ 0.18	≤ 0.20	≤ 0.47
	$\frac{E_{\mathrm{T}}^{\mathrm{EM}}}{E_{\mathrm{T}}^{\mathrm{total}}}$	> 0.0015	> 0.00033	> 0.00033	≤ 0.99	≤ 1.00	≤ 1.00

Table B.4.: Cut values for calorimeter+track-based identification method

$E_{\mathrm{T}}^{\mathrm{vis}}$-bin (GeV)	Variable	1-prong			3-prong		
		tight	medium	loose	tight	medium	loose
10 – 25	R_{EM}	≤ 0.064	≤ 0.095	≤ 0.30	≤ 0.15	≤ 0.30	≤ 0.35
	W_{strip}	≤ 0.011	≤ 0.047	≤ 0.048	≤ 0.026	≤ 0.046	≤ 0.046
	f_{iso}	≤ 0.40	≤ 0.79	≤ 0.79	≤ 0.73	≤ 0.86	≤ 0.86
	$\frac{E_{\mathrm{T}}^{\mathrm{EM}}}{E_{\mathrm{T}}^{\mathrm{total}}}$	> 0.011	> 0.011	> 0.00083	≤ 1.00	≤ 1.04	≤ 1.04
	$E_{\mathrm{T}}^{\mathrm{total}}/p_{\mathrm{T1}}$	≤ 8.30	≤ 8.30	≤ 10.88	≤ 3.10	≤ 3.87	≤ 3.87
	$\frac{E_{\mathrm{T}}^{\mathrm{EM}}}{p_{\mathrm{T}}^{\mathrm{total}}}$	≤ 5.66	≤ 5.66	≤ 10.14	≤ 1.46	≤ 2.28	≤ 2.28
	$\frac{E_{\mathrm{T}}^{\mathrm{Had}}}{p_{\mathrm{T}}^{\mathrm{total}}}$	≤ 1.73	≤ 1.75	≤ 2.13	≤ 0.95	≤ 1.28	≤ 1.28
	$\frac{p_{\mathrm{T}}^{\mathrm{total}}}{E_{\mathrm{T}}^{\mathrm{total}}}$	> 0.15	> 0.15	> 0.088	> 0.88	> 0.40	> 0.40
	$W_{\mathrm{track}}^{\tau}$	–	–	–	≤ 0.0015	≤ 0.0045	≤ 0.0045
25 – 45	R_{EM}	≤ 0.050	≤ 0.063	≤ 0.20	≤ 0.097	≤ 0.11	≤ 0.19
	W_{strip}	≤ 0.026	≤ 0.034	≤ 0.048	≤ 0.033	≤ 0.034	≤ 0.043
	f_{iso}	≤ 0.16	≤ 0.37	≤ 0.50	≤ 0.59	≤ 0.73	≤ 0.93
	$\frac{E_{\mathrm{T}}^{\mathrm{EM}}}{E_{\mathrm{T}}^{\mathrm{total}}}$	> 0.0049	> 0.0045	> 0.00078	≤ 1.01	≤ 1.01	≤ 1.08
	$E_{\mathrm{T}}^{\mathrm{total}}/p_{\mathrm{T1}}$	≤ 6.70	≤ 6.79	≤ 17.90	≤ 3.63	≤ 3.82	≤ 5.99
	$\frac{E_{\mathrm{T}}^{\mathrm{EM}}}{p_{\mathrm{T}}^{\mathrm{total}}}$	≤ 7.18	≤ 8.48	≤ 10.94	≤ 1.15	≤ 2.83	≤ 3.87
	$\frac{E_{\mathrm{T}}^{\mathrm{Had}}}{p_{\mathrm{T}}^{\mathrm{total}}}$	≤ 1.48	≤ 1.69	≤ 2.81	≤ 1.11	≤ 1.20	≤ 1.84
	$\frac{p_{\mathrm{T}}^{\mathrm{total}}}{E_{\mathrm{T}}^{\mathrm{total}}}$	> 0.12	> 0.12	> 0.11	> 0.84	> 0.62	> 0.23
	$W_{\mathrm{track}}^{\tau}$	–	–	–	≤ 0.00050	≤ 0.00082	≤ 0.0014
45 – 70	R_{EM}	≤ 0.042	≤ 0.049	≤ 0.10	≤ 0.065	≤ 0.070	≤ 0.10
	W_{strip}	≤ 0.039	≤ 0.039	≤ 0.049	≤ 0.040	≤ 0.048	≤ 0.049
	f_{iso}	≤ 0.12	≤ 0.82	≤ 0.96	≤ 0.32	≤ 0.33	≤ 0.35
	$\frac{E_{\mathrm{T}}^{\mathrm{EM}}}{E_{\mathrm{T}}^{\mathrm{total}}}$	> 0.19	> 0.0049	> 0.0028	≤ 1.00	≤ 1.06	≤ 10.8
	$E_{\mathrm{T}}^{\mathrm{total}}/p_{\mathrm{T1}}$	≤ 8.30	≤ 10.71	≤ 11.20	≤ 3.58	≤ 9.45	≤ 9.46
	$\frac{E_{\mathrm{T}}^{\mathrm{EM}}}{p_{\mathrm{T}}^{\mathrm{total}}}$	≤ 8.67	≤ 11.80	≤ 12.01	≤ 1.64	≤ 5.12	≤ 5.95
	$\frac{E_{\mathrm{T}}^{\mathrm{Had}}}{p_{\mathrm{T}}^{\mathrm{total}}}$	≤ 1.06	≤ 2.90	≤ 2.93	≤ 1.25	≤ 1.31	≤ 1.32
	$\frac{p_{\mathrm{T}}^{\mathrm{total}}}{E_{\mathrm{T}}^{\mathrm{total}}}$	> 0.088	> 0.088	> 0.087	> 0.70	> 0.21	> 0.18
	$W_{\mathrm{track}}^{\tau}$	–	–	–	≤ 0.00023	≤ 0.00051	≤ 0.00075

Table B.5.: Cut values for calorimeter+track-based identification method

$E_{\mathrm{T}}^{\mathrm{vis}}$-bin (GeV)	Variable	1-prong			3-prong		
		tight	medium	loose	tight	medium	loose
70 – 100	R_{EM}	≤ 0.040	≤ 0.044	≤ 0.067	≤ 0.060	≤ 0.075	≤ 0.10
	W_{strip}	≤ 0.0012	≤ 0.0077	≤ 0.044	≤ 0.034	≤ 0.035	≤ 0.036
	f_{iso}	≤ 0.13	≤ 0.14	≤ 0.80	≤ 0.68	≤ 0.70	≤ 0.72
	$\frac{E_{\mathrm{T}}^{\mathrm{EM}}}{E_{\mathrm{T}}^{\mathrm{total}}}$	> 0.34	> 0.0021	> 0.0018	≤ 1.00	≤ 1.03	≤ 1.04
	$E_{\mathrm{T}}^{\mathrm{total}}/p_{\mathrm{T1}}$	≤ 8.14	≤ 12.72	≤ 13.56	≤ 6.85	≤ 8.30	≤ 11.94
	$\frac{E_{\mathrm{T}}^{\mathrm{EM}}}{p_{\mathrm{T}}^{\mathrm{total}}}$	≤ 11.13	≤ 13.40	≤ 13.52	≤ 3.44	≤ 4.18	≤ 5.94
	$\frac{E_{\mathrm{T}}^{\mathrm{Had}}}{p_{\mathrm{T}}^{\mathrm{total}}}$	≤ 1.85	≤ 1.97	≤ 2.20	≤ 1.51	≤ 1.81	≤ 2.26
	$\frac{p_{\mathrm{T}}^{\mathrm{total}}}{E_{\mathrm{T}}^{\mathrm{total}}}$	> 0.077	> 0.071	> 0.070	> 0.86	> 0.59	> 0.17
	$W_{\mathrm{track}}^{\tau}$	–	–	–	≤ 0.00014	≤ 0.00014	≤ 0.00041
> 100	R_{EM}	≤ 0.027	≤ 0.033	≤ 0.20	≤ 0.061	≤ 0.25	≤ 0.27
	W_{strip}	≤ 0.029	≤ 0.047	≤ 0.049	≤ 0.021	≤ 0.025	≤ 0.025
	f_{iso}	≤ 0.062	≤ 0.097	≤ 0.10	≤ 0.40	≤ 0.42	≤ 0.68
	$\frac{E_{\mathrm{T}}^{\mathrm{EM}}}{E_{\mathrm{T}}^{\mathrm{total}}}$	> 0.0010	> 0.00057	> 0.00036	≤ 0.88	≤ 1.00	≤ 1.01
	$E_{\mathrm{T}}^{\mathrm{total}}/p_{\mathrm{T1}}$	≤ 11.63	≤ 14.25	≤ 17.19	≤ 3.23	≤ 3.26	≤ 14.81
	$\frac{E_{\mathrm{T}}^{\mathrm{EM}}}{p_{\mathrm{T}}^{\mathrm{total}}}$	≤ 11.56	≤ 11.99	≤ 13.99	≤ 1.92	≤ 2.13	≤ 7.96
	$\frac{E_{\mathrm{T}}^{\mathrm{Had}}}{p_{\mathrm{T}}^{\mathrm{total}}}$	≤ 2.06	≤ 2.51	≤ 2.98	≤ 1.26	≤ 1.41	≤ 2.80
	$\frac{p_{\mathrm{T}}^{\mathrm{total}}}{E_{\mathrm{T}}^{\mathrm{total}}}$	> 0.082	> 0.061	> 0.057	> 0.82	> 0.068	> 0.068
	$W_{\mathrm{track}}^{\tau}$	–	–	–	≤ 0.000028	≤ 0.000033	≤ 0.0010

List of Figures

List of Tables

Bibliography

[1] A. Motte, *The mathematical principles of natural philosophy*, London 1729 (Translation of the third edition of 1726), Reprint Amherst 1995.

[2] A. Einstein, *Zur Elektrodynamik bewegter Körper*, AdP **17**, 891-921 (1905).

[3] A. Einstein, *Die Grundlage der allgemeinen Relativitätstheorie*, AdP *49*, 769-822 (1916).

[4] J.J. Thomson, *Cathode Rays*, Philosophical Magazine **44**, 293 (1897).

[5] M. Gell-Mann, *A schematic model of baryons and mesons*, Phys. Lett. **8**, 214-215 (1964).

[6] CDF Collaboration, F. Abe et al., *Observation of Top Quarks in $\bar{p}p$ Collisions*, Phys. Rev. Lett. **74**, 2626-2631 (1995).

[7] D0 Collaboration, S. Abachi et al., *Search for High Mass Top Quark Production in $\bar{p}p$ Collisions at $sqrts$ = 1.8 TeV*, Phys. Rev. Lett. **74**, 2422-2426 (1995).

[8] DONUT Collaboration, K. Kodama et al., *Observation of tau neutrino interactions*, Phys. Lett. B **504**, 218-224 (2001).

[9] F. Englert and R. Brout, *Broken Symmetry and the Mass of Gauge Vector Mesons*, Phys. Rev. Lett. **13**, 321-323 (1964).

[10] P. W. Higgs, *Broken Symmetries and the Masses of Gauge Bosons*, Phys. Rev. Lett. **13**, 508-509 (1964).

[11] N. Cabibbo, *Unitary Symmetry and Leptonic Decays*, Phys. Rev. Lett. **10**, 531-533 (1963).

[12] M. Kobayashi and T. Maskawa, *CP-Violation in the Renormalizable Theory of Weak Interaction*, Prog. Theor. Phys. **49**, 652-657 (1973).

[13] V. Trimble, *Existence and Nature of Dark Matter in the Universe*, Ann. Rev. Astron. Astrophys. **25**, 425-472 (1987).

[14] W. Hollik, *Quantum field theory and the Standard Model*, Proceedings of 2009 European School of High-Energy Physics, CERN-2010-002 (2010).

[15] E. Fermi, *Sulla quantizzazione del gas perfetto monoatomico*, Rend. Lincei **3**, 145-149 (1926), translated as *On the Quantization of the Monoatomic ideal gas*, arXiv:cond-mat/9912229v1.

[16] P.A.M. Dirac, *On the Theory of Qunatum Mechanics*, Proceedings of the Royal Society, Series **A112**, 661-677 (1926).

[17] W. Pauli, *Exclusion Principle and Quantum Mechanics*, Nobel Lecture, Physics 1942-1962, http://nobelprize.org/nobel_prizes/physics/laureates/1945/pauli-lecture.html.

[18] K. Nakamura et al. (Particle Data Group), *Review of Particle Physics*, J. Phys. **G37**, 075021 (2010).

[19] D.J. Gross and F. Wilczek, *Ultraviolet Behavior of Non-Abelian Gauge Theories*, Phys. Rev. Lett. **30**, 1343-1346 (1973).

[20] H.D. Politzer, *Reliable Perturbative Results for Strong Interactions?*, Phys. Rev. Lett. **30**, 1346-1349 (1973).

[21] H. Fritzsch, M. Gell-Mann and H. Leutwyler, *Advantages of the color octet gluon picture*, Phys. Lett. **B47**, 365-368 (1973).

[22] S.L. Glashow, *Partial-symmetries of weak interactions*, Nucl. Phys. **B22**, 579-588 (1961).

[23] S. Weinberg, *A Model of Leptons*, Phys. Rev. Lett. **19**, 1264-1266 (1967).

[24] S.L. Glashow, J. Iliopoulos and L. Maiani, *Weak Interactions with Lepton-Hadron Symmetry*, Phys. Rev. **D2**, 1285-1292 (1970).

[25] The LEP Working Group for Higgs Boson Searches, *Search for the Standard Model Higgs Boson at LEP*, Phys. Lett. **B565**, 61-75 (2003).

[26] Tevatron New Phenomena, Higgs working group, *Combined CDF and DZero Upper Limits on Standard Model Higgs-Boson Production with up to 6.7 fb-1 of Data*, arXiv:1007.4587v1(2010).

[27] H. Flächer, M. Goebel, J. Haller, A. Höcker, K. Mönig, J. Stelzer, *Revisiting the Global Electroweak Fit of the Standard Model and Beyond with Gfitter*, Eur. Phys. J. **C60**, 543 (2009).

[28] H. Georgi and S.L. Glashow, *Unity of All Elementary-Particle Forces*, Phys. Rev. Lett. **32**, 438-441 (1974).

[29] S. Weinberg, *Implications of dynamical symmetry breaking*, Phys. Rev. **D13**, 974-996 (1976).

[30] S. Weinberg, *Implications of dynamical symmetry breaking: An addendum*, Phys. Rev. **D19**, 1277-1280 (1979).

[31] M. B. Einhorn, *Confinement, form factors, and deep-inelastic scattering in two-dimensional quantum chromodynamics*, Phys. Rev. **D14**, 3451-3471 (1976).

[32] L. Susskind, *Dynamics of spontaneous symmetry breaking in the Weinberg-Salam theory*, Phys. Rev. **D20**, 2619-2625 (1979).

[33] H. P. Nilles, *Supersymmetry, supergravity and particle physics*, Phys. Rept. **110**, 1-162 (1984).

[34] H. E. Haber, G. L. Kane, *The search for supersymmetry: Probing physics beyond the standard model*, Phys. Rept. **117**, 75-263, (1985).

[35] S. Martin, *S Supersymmetry Primer*, arXiv:hep-ph/9709356v5 (2008).

[36] WMAP Collaboration, E. Komatsu et al., *Five-Year Wilkinson Microwave Anisotropy Probe (WMAP) Observations: Cosmological Interpretation.*, Astophys. J. Suppl. **180**, 330-376 (2009), arXiv:0803.0547v2 [astro-ph].

[37] A.D. Sakharov, *Violation of CP invariance, C asymmetry, and baryon asymmetry in the universe*, JETP Lett. **5**, 24-27 (1967).

[38] A.G. Cohen, D.B. Kaplan and A.E. Nelson, *Progress in Electroweak Baryogenesis*, Ann. Rev. Nucl. Part. Sci. **43**, 27-70 (1993), arXiv:hep-ph/9302210v1.

[39] M.B. Gavela, P. Hernandez, J. Orloff, O. Pene and C. Quimbay, *Standard Model CP-violation and Baryon asymmetry Part II: Finite Temperature*, Nucl. Phys. **B430**, 382-426 (1994), arXiv:hep-ph/9406289v2.

[40] G. P. Salam, *Elements of QCD for hadron colliders*, Proceedings of 2009 European School of High-Energy Physics, CERN-2010-002 (2010).

[41] S. Catani et al., *QCD*, arXiv:hep-ph/0005025v1 (2000).

[42] The H1, ZEUS Collaborations, *Combined Measurment and QCD Analysis of the Inclusive ep Scattering Cross Sections at HERA*, arXiv:0911.0884v2, (2010).

[43] A.D. Martin, R. G. Roberts, W. J. Stirling and R. S. Thorne, *Parton Distribution and the LHC: W and Z Production*, Eur.Phys.J. **C14**, 133-145 (2000).

[44] J. Ellis, M.K. Gaillard and G.G. Ross, *Search for gluons in e^+e^- annihilation*, Nucl. Phys. **B111**, 253-271 (1976).

[45] L.W. Garland, T. Gehrmann, E.W.N. Glover, A. Koukoutsakis and E. Remiddi, *The two-loop QCD matrix element for $e^+e^- \to 3$ jets*, Nucl. Phys. **B627**, 107-188 (2002).

[46] K. Hagiwara and D. Zeppenfeld, *Amplitudes for multi-parton processes involving a current at e^+e^-, $e^\pm p$, and hadron colliders*, Nucl. Phys. **B313**, 560-594 (1989).

[47] B. Andersson, G. Gustafson and T. Sjöstrand, *A model for baryon production in quark and gluon jets*, Nucl. Phys. **B197**, 45-54 (1982).

[48] B. Andersson, G. Gustafson and T. Sjöstrand, *Baryon Production in Jet Fragmentation and γ-Decay*, Phys. Scr. **32**, 574 (1985).

[49] R.D. Field and R.P. Feynman, *A parametrization of the properties of quark jets*, Phys. Nucl. **B136**, 1-76 (1978).

[50] D. Amati and G. Veneziano, *Preconfinement as a property of perturbative QCD*, Phys. Lett. **B83**, 87-92 (1979).

[51] A. Bassetto, M. Ciafaloni and G. Marchesini, *Inelastic distributions and color structure in pertubative QCD*, Nucl. Phys. **B163**, 477-518 (1980).

[52] X. Artru and G. Mennessier, *String model and multiproduction*, Nucl. Phys. **B70**, 93-115 (1974).

[53] B. Andersson, G. Gustafson, G. Ingelman and T. Sjöstrand, *Parton fragmentation and string dynamics*, Phys. Rept. **97**, 31-145 (1983).

[54] T. Sjöstrand, *High-energy-physics event generation with PYTHIA 5.7 and JETSET 7.4*, Comp. Phys. Comm. **82**, 74-89 (1994).

[55] T. Sjöstrand et al., *High-Energy-Physics Event Generation with PYTHIA 6.1*, Comp. Phys. Commun. **135**, 238-259 (2001), arXiv:hep-ph/0010017v1.

[56] T. Sjostrand, S. Mrenna and P.Z. Skands, *PYTHIA 6.4 Physics and Manual*, JHEP **05**, 026 (2006).

[57] G.P. Salam, *Towards Jetography*, arXiv:0906.1833v2 [hep-ph] (2009).

[58] M. Cacciari and G.P. Salam, *Dispelling the N^3 myth for the Kt jet-finder*, Phys. Lett. **B641**, 57-61 (2006).

[59] W.d. Boer and C. Sander, *Global Electroweak Fits and Gauge Coupling Unification*, Phys. Lett. **B585**, 276-286 (2004), arXiv:hep-ph/0307049v1.

[60] S. Coleman and J. Mandula, *All Possible Symmetries of the S Matrix*, Phys Rev. **159**, 1251-1256 (1967).

[61] G. 't Hooft, *Symmetry Breaking through Bell-Jackiw Anomalies*, Phys. Rev. Lett. **37**, 8-11 (1976).

[62] R. Barbier et al., *R-parity violating supersymmetry*, Phys. Rept. **420**, 1-202 (2005), arXiv:hep-ph/0406039v2.

[63] M. Kuroda, *Complete Lagrangian of MSSM*, arXiv:hep-ph/9902340v3 (2005).

[64] L. O'Raifeartaigh, *Spontaneous symmetry breaking for chirals scalar superfields*, Nucl. Phys. **B96**, 331-352 (1975).

[65] SNO Collaboration, Q. R. Ahmad et al., *Direct Evidence for Neutrino Flavor Transformation from Neutral-Current Interactions in the Sudbury Neutrino Observatory*, Phys. Rev. Lett. 89:011301 (2002).

[66] V.A. Rubakov and M.E. Shaposhnikov, *Electroweak baryon number non-conservation in the early univers and in high-energy collisions*, Usp. Fiz. Nauk **166**, 493-537 (1996), arXiv:hep-ph/9603208.

[67] S. Dimopoulos and D.W. Sutter, *The Supersymmetric Flavor Problem*, Nucl. Phys. **B452**, 496-512 (1995), arXiv:hep-ph/9504415.

[68] T. Ibrahim and P. Nath, *CP violation from standard model to strings*, Rev. Mod. Phys. **80**, 577-631 (2008), arXiv:0705.2008 [hep-ph].

[69] A. Pilaftsis, *Higgs Scalar-Pseudoscalar Mixing int the Minimal Supersymmetric Standard Model*, Phys. Lett. **B435**, 88-100 (1998), arXiv:hep-ph/9805373v1.

[70] D.A. Demir, *Effects of the supersymmetric phases on the neutral Higgs sector*, Phys. Rev. **D60**, (1999), arXiv:hep-ph/9901389v1.

[71] A. Pilaftsis and C.E.M. Wagner, *Higgs Bosons in the Minimal Supersymmetric Standard Model with Explicit CP Violation*, Nucl. Phys. **B553**, 3-42 (1999), arXiv:hep-ph/9902371v4.

[72] M. Carena, J. Ellis, A. Pilaftsis and C.E.M. Wagner, *CP-Violating MSSM Higgs Bosons in the Light of LEP 2*, Phys. Lett. **B495**, 155-163 (2000), arXiv:hep-ph/0009212v1.

[73] ALEPH, DELPHI, L3, OPAL Collaboration, The LEP Working Group "for Higgs Boson Searches", *Search for Neutral MSSM Higgs Bosons at LEP*, Eur. Phys. J. **C47**, 547-587 (2006), arXiv:hep-ex/0602042v1.

[74] M. Schumacher, *Investigation of the Discovery Potential for Higgs Bosons of the Minimal Supersymmetric Extension of the Standard Model (MSSM) with ATLAS*, arXiv:hep-ph/0410112v1.

[75] J. Ellis, F. Moortgat, G. Moortgat-Pick, J.M. Smillie and J. Tattersall, *Measurement of CP Violation in Stop Cascade Decays at the LHC*, Eur. Phys. J. **C60**, 633-651 (2009), arXiv:0809.1607 [hep-ph].

[76] F. Deppisch and O. Kittel, *Probing SUSY CP Violation in Two-Body Stop Decays at the LHC*, arXiv:0905.3088 [hep-ph] (2009).

[77] G. Moortgat-Pick, K. Rolbiecki and J. Tattersall, *Momentum reconstruction at the LHC for probing CP-violation in the stop sector*, arXiv:1008.2206v1 [hep-ph] (2010).

[78] The ATLAS Collaboration, G. Aad et al., *The ATLAS Experiment at the CERN Large Hadron Collidor*, JINST **3** (2008) S08003.

[79] *LHC Design Report*, cernrep/2004-003-v1, (2004).

[80] K. Wille, *The Physics of Particle Accelerator*, Oxford University Press (2000).

[81] CERN, *CAS - CERN Accelerator School: 5th Advanced Accelerator Physics Course*, CERN 95-06 (1995).

[82] The ATLAS Collaboration, G. Aad et al., *Detector and physics performance technical design report Vol. 1*, CERN/LHCC/99-014 (1999); *Detector and physics performance technical design report Vol. 2*, CERN/LHCC/99-015 (1999).

[83] The ATLAS Collaboration, G. Aad et al., *The ATLAS Inner Detector commissioning and calibration*, Eur. Phys. J. **C70**, 787-821 (2010), arXiv:1004.5293v2 [physics.ins-det].

[84] The ATLAS Collaboration, G. Aad et al., *Electron and photon reconstruction and identification in ATLAS: expected performance at high energy and results at 900 GeV*, ATLAS Note, ATLAS-CONF-2010-005 (2010).

[85] The ATLAS Collaboration, G. Aad et al., *Jet energy resolution and reconstruction efficiencies from in-situ techniques with the ATLAS Detector Using Proton-Proton Collisions at a Center of Mass Energy sqrts = 7 TeV*, ATLAS Note, ATLAS-CONF-2010-054 (2010).

[86] The ATLAS Collaboration, G. Aad et al., *Muon Reconstruction Performance*, ATLAS Note, ATLAS-CONF-2010-064.

[87] The ATLAS Collaboration, G. Aad et al., *ATLAS Inner detector: technical design report Vol. 1*, CERN-LHCC-97-016 (1997); *ATLAS Inner detector: technical design report Vol. 2*, CERN-LHCC-97-017 (1997).

[88] The ATLAS Collaboration, G. Aad et al., *ATLAS pixel detector: technical desig report*, CERN-LHCC-98-013 (1998).

[89] The ATLAS Collaboration, G. Aad et al., *Performance of primary vertex reconstruction in proton-proton collisions at sqrt(s) = 7 TeV in the ATLAS experiment*, ATLAS Note, ATLAS-CONF-2010-069 (2010).

[90] The ATLAS Collaboration, G. Aad et at, *Magent system technical design report*, CERN-LHCC-97-018 (1997).

[91] A. Yamamoto et al., *The ATLAS central solenoid*, Nucl. Instrum. Meth. **A584** (2008) 53.

[92] The ATLAS Collaboration, G. Aad et al., *Barrel toroid technical design report*, CERN-LHCC-97-019 (1997).

[93] The ATLAS Collaboration, G. Aad et al., *End-cap toroid technical design report*, CERN-LHCC-97-020 (1997).

[94] The ATLAS Collaboration, G. Aad et al., *Level-1 Trigger*, CERN-LHCC-98-14 (1998).

[95] The ATLAS Collaboration, G. Aad et al., *ATLAS Computing*, ATLAS-TDR-017, CERN-LHCC-2005-022 (2005).

[96] GEANT4 Collaboration, S. Agostinelli et at., *GEANT4: A simulation toolkit*, Nucl. Inst. and Meth. **A506**, 250-303 (2003).

[97] M. Bähr, S. Gieseke, M. A. Gigg, D. Grellscheid, K. Hamilton, O. Latunde-Dada, S. Plätzer, P. Richardson, M. H. Seymour, A. Sherstnev, J. Tully, B. R. Webber, *Herwig++ Physics and Manual*, Eur. Phys. J. **C58**, 639-707 (2008).

[98] The ATLAS Collaboration, G. Aad et al., *Luminosity Determination Using the ATLAS Detector*, ATLAS Note, ATLAS-CONF-2010-060 (2010).

[99] The ATLAS Collaboration, G. Aad et al., *Mapping the material in the ATLAS Inner Detector using secondary hadronic interactions in 7 TeV collisions*. ATLAS Note, ATLAS-CONF-2010-058 (2010).

[100] S. van der Meer, *Calibration of the effective beam height in the ISR*, CERN-ISR-PO-68-31 (1968).

[101] https://twiki.cern.ch/twiki/bin/view/Atlas/RunStatsPublicResults2010

[102] The ATLAS Collaboration, G. Aad et al., *The ATLAS Simulation Infrastructure*, arXiv:1005.4568v1 [physics.ins-det] (2010).

[103] M. Dobbs and J.B. Hansen, *The HepMC C++ Monte Carlo event record for High Energy Physics*, Comput. Phys. Commun. **134**, 41-46 (2001).

[104] S. Ovyn, X. Rouby and V. Lemaitre, *Delphes, a framewokr for fast simulation of a generic collider experiment*, arXiv:0903.2225v3 [ehp-ph] (2009).

[105] I. Bird (ed.) et al., *LHC computing Grid*, Technical Design Report, CERN-LHCC-2005-024 (2005).

[106] M. Branco et al., *Managing ATLAS data on a petabyte-scale with DQ2*, J. Phys.: Conf. Ser. **119** 062017, (2008).

[107] M. Smizanska, S.P. Baranov, J. Hrivnac and E. Kneringer, *Overview of Monte Carlo simulations for ATLAS B-physics in the period 1996-1999*, ATL-PHYS-2000-025 (2000).

[108] G. Marchesini, B.R. Webber, G. Abbiendi, I.G. Knowles, M.H. Seymour and L. Stanco *HERWIG: A Monte Carlo event generator for simulating hadron emission reactions with interfering gluons*, Comput. Phys. Commun. **67**, 465 (1992).

[109] G. Corcella, I.G. Knowles, G. Marchesini, S. Moretti, K. Odagiri, P. Richardson, M.H. Seymour and B.R. Webber, *HERWIG 6.5: an event generator for Hadron Emission Reactions With Interfering Gluons (including supersymmetric processes)*, JHEP **01** (2001) (010), arXiv:hep-ph/0011363.

[110] T. Gleisberg, S. Hoeche, F. Krauss, A. Schaelicke, S. Schumann, J. Winter, *SHERPA 1.alpha, a proof-of-concept version*, JHEP **02** (2004) 056, arXiv:hep-ph/0311263.

[111] X. Wang and M. Gyulassy, *HIJING 1.0: A Monte Carlo Program for Parton and Particle Production in High Energy Hadronic and Nuclear Collisions*, Comput. Phys. Commun. **83** (1994) 307, arXiv:nucl-th/9502021v1.

[112] M.L. Mangano, M. Moretti, F. Piccinini, R. Pittau and A.D. Polosa, *ALPGEN, a generator for hard multiparton processes in hadronic collisions*, JHEP **07** (2003) 001, arXiv:hep-ph/0206293v2.

[113] S. Frixione, P. Nason and B.R. Webber, *Matching NLO QCD and parton showers in heavy flavour production*, JHEP **08** (2003) 007, arXiv:hep-ph/0305252v2.

[114] B. P. Kersevan and E. Richter-Was, *The Monte Carlo Event Generator AcerMC 2.0 with Interfaces to PYTHIA 6.2 and HERWIG 6.5*, arXiv:hep-ph/0405247v1 (2004).

[115] S. Jadach, J. H. Kuhn and Z. Was, *TAUOLA: A Library of Monte Carlo programs to simulate decays of polarized tau leptons*, Comput. Phys. Commun. **64**, 275-299 (1990).

[116] E. Barberio, B. van Eijk and Z. Was, *PHOTOS: A Universal Monte Carlo for QED radiative corrections in decays*, Coomput. Phys. Commun. *66*, 115-128 (1991).

[117] D.J. Lange, *The EvtGen particle decay simulation package*, Nucl. Instrum. Meth. **A462**, 152-155 (2001).

[118] F.E. Paige, S.D. Protopopescu, H. Baer and X. Tata, *ISAJET 7.69: A Monte Carlo Event Generator for pp, $\bar{p}p$, and e^+e^- Reactions*, arXiv:hep-ph/0312045v1 (2003).

[119] T. Stelzer and W.F. Long, *Automatic Generation of Tree Level Helicity Amplitudes*, Comput. Phys. Commun. **81**, 357-371 (1994), arXiv:hep-ph/9401258v1.

[120] C.M. Harris, P. Richardson and B.R. Webber, *CHARYBDIS: A Black Hole Event Generator*, JHEP **08**, (2003) 033, arXiv:hep-ph/0307305v2.

[121] The CompHEP Collaboration, E. Boos et al., *CompHEP 4.4 - Automatic Computations from Lagrangians to Events*, Nucl. Instrum. Meth. **A534**, 250 (2004), arXiv:hep-ph/0403113v1.

[122] T. Sjöstrand, S. Mrenna and P. Skands, *A Brief Introduction to PYTHIA 8.1*, Comput. Phys. Commun. **178**, 852-867 (2008), arXiv:0710.3820v1.

[123] M. Bähr, S. Gieseke and M. H. Seymour, *Simulation of multiple partonic interactions in Herwig++*, arXiv:0803.3633v2 [hep-ph] (2008).

[124] I. Borozan and M.H. Seymour, *An eikonal model for multiparticle production in hadron-hadron interactions*, JHEP **09**, 015 (2002), arXiv:hep-ph/0207283.

[125] B. R. Webber, *A QCD Model for Jet Fragmentation including Soft Gluon Interference*, Nucl. Phys. **B238** (1984) 492.

[126] L. Lönnblad, *ThePEG, PYTHIA7, Herwig++ and ARIADNE*, Nucl. Instrum. Meth. **A559**, 246-248 (2006).

[127] E. Boos et al., *Generic User Process Interface for Event Generators*, arXiv:hep-ph/0109068v1 (2001).

[128] J. Alwall et al., *A standard format for Les Houches Event Files*, Comput. Phys. Commun. **176**, 300-304 (2007), arXiv:hep-ph/0609017.

[129] W. Porod, *SPheno, a program for calculating supersymmetric spectra, SUSY particle decays and SUSY particle production at e^+e^- colliders*, Comput. Phys. Commun. **153**, 275-315 (2003), arXiv:hep-ph/0301101v4.

[130] D. Bourilkov, R.C. Group and M.R. Whalleyu, *LHAPDF: PDF use from the Tevatron to the LHC*, arXiv:hep-ph/0605240, (2006).

[131] W.K. Tung, H.L. Lai, J. Pumplin, P. Nadolsky and C.-P. Yuan, *Global QCD Analysis and Collider Phenomenology–CTEQ*, arXiv:0707.0275 [hep-ph], (2007).

[132] F. Viegas, R. Hawkings and G. Dimitrov, *Relational database for conditions data and event selection in ATLAS*, in Proceedings for Computing in High Energy and Nuclear Physics 2007 (CHEP2007), Victoria, BC, Canada, J. Phys.: Conf. Ser. 119 (2008).

[133] J. Boudreau and V. Tsulaia, *The GeoModel Toolkit for Detector Description*, in Computing in High Energy and Nuclear Physics 2004 (CHEP2004), Interlaken, Switzerland.

[134] A. Dell'Acqua et al., *Development of the ATLAS Simulation Framework*, in Computing in High Energy and Nuclear Physics 2001 (CHEP2001), Bejing, China.

[135] The ATLAS Collaboration, G. Aad et al., *ATLAS Monte Carlo tunes for MC09*, ATLAS Note, ATL-PHYS-PUB-2010-002 (2010).

[136] A. Sherstnev and R.S. Thorne, *Parton Distribution for LO Generators*, Eur. Phys. J. **C55**, 553-575 (2008), arXiv:0711.2473 [hep-ph] (2008).

[137] C. Peterson, D. Schlatter, I. Schmitt and P.M. Zerwas, *Scaling Violations in Inclusive e^+e^- Annihilation Spectra*, Phys. Rev. **D27**, 105-111 (1983).

[138] B. Andersson, G. Gustafson and B. Söderberg, *A General Model for Jet Fragmentation*, Z. Phys. **C20**, 317-329 (1983).

[139] P.Z. Skands, *Tuning Monte Carlo Generators: The Perugia Tunes*, arXiv:1005.3457v2 [hep-ph] (2010).

[140] A. Buckley, H. Hoeth, H. Lacker, H.Schulz and J.E. von Seggern, *Systematic event generator tuning for the LHC*, Eur. Phys. J. **C65**, 331-357 (2010), arXiv:0907.2973 [hep-ph].

[141] *ROOT An Object-Oriented Data Analysis Framework*, http://root.cern.ch

[142] L. Quertenmont and V. Roberfroid, *FROG: The Fast & Realistic OPENGL Displayer*, arXiv:0901.2718v1 [hep-ex] (2009).

[143] CDF Collaboration, F. Abe et al., *Topology of three-jet events in $p\bar{p}$ collisions at $\sqrt{s} = 1.8\,TeV$*, Phys. Rev. **D45**, 1448-1458 (1992).

[144] G.C. Blazey et al., *Run II Jet Physics: Proceedings of the Run II QCD and Weak Boson Physics Workshop*, arXiv:hep-ex/0005012v2 (2000).

[145] G.P. Salam and G. Soyes, *A practical seedless infrared-safe cone jet algorithm*, JHEP **05**, 086 (2007).

[146] S. Ctani, Y.L. Dokshitzer, M.H. Seymour and B.R. Webber, *Longitudinally-invariant k_t-clustering algorithms for hadron-hadron collisions*, Nucl. Phys. **B406**, 187-224 (1993).

[147] M. Wobisch and T. Wengler, *Hadronization Corrections to Jet Cross Sections in Deep-Inelastic Scattering*, arXiv:hep-ph/9907280v1 (1999).

[148] M. Cacciari, G. P. Salam and G. Soyez, *The anti-k_t jet clustering algorithm*, JHEP **04** (2008) 063.

[149] The ATLAS Collaboration, G. Aad et al., *Expected Performance of the ATLAS Experiment*, CERN-OPEN-2008-020 (2008).

[150] The ATLAS Collaboration, G. Aad et al., *Expected Performance of the ATLAS Experiment*, CERN-OPEN-2008-020, 44-93 (2008).

[151] The ATLAS Collaboration, G. Aad et al., *Expected Performance of the ATLAS Experiment*, CERN-OPEN-2008-020, 162-228 (2008).

[152] The ATLAS Collaboration, G. Aad et al., *Expected Performance of the ATLAS Experiment*, CERN-OPEN-2008-020, 898-924 (2008).

[153] M. L. Perl, *Evidence for Anomalous Lepton Production in e+-e- Annihilation*, Phys. Rev. **35**, 1489-1492 (1975).

[154] K. Assamagan and Y. Coadou, *The hadronic tau decay of a heavy charged Higgs in ATLAS*, ATLAS Note, ATL-PHYS-2000-031 (2000).

[155] K. Assamagan and A. Deansdrea, *The hadronic τ decay of heavy charged Higgs in models with singlet neutrino in large extra dimension*, ATLAS Note, ATL-PHYS-2001-019 (2001).

[156] T. Pierzchala, E. Richter-Was, Z. Was and M. Worek, *Spin effects in tau-lepton pair production at LHC*, Acta Phys. Polon **B32**, 1277-1296 (2001).

[157] G. R. Bower, T. Pierzchala, Z. Was and M. Worek, *Measuring the Higgs boson's parity using tau $\rightarrow$ rho nu*, Phys. Lett. **B543**, 227-234 (2002).

[158] K. Desch, A. Imhof, Z. Was and M. Worek, *Probing the CP nature of the Higgs boson at linear colliders with tau spin correlations; the case of mixed scalar–pseudoscalar couplings*, Phys. Lett. **B579**, 157-164 (2004).

[159] The ATLAS Collaboration, G. Aad et al., *Expected Performance of the ATLAS Experiment*, CERN-OPEN-2008-020, 242-248 (2008).

[160] The ATLAS Collaboration, G. Aad et al., *Reconstruction of hadronic tau candidates in QCD events at ATLAS with 7 TeV proton-proton collisions*, ATLAS Note, ATLAS-CONF-2010-059 (2010).

[161] M. Heldmann and D. Cavalli, *An improved tau-Identification for the ATLAS experiment*, ATLAS Note, ATL-PHYS-PUB-2006-008 (2006).

[162] The ATLAS Collaboration, *Calorimeter Clustering Algorithms: Description and Performance*, ATLAS Note, ATL-LARG-PUB-2008-002 (2008).

[163] The ATLAS Collaboration, *Properties of Jets and Inputs to Jet Reconstruction and Calibration with the ATLAS Detector Using Proton-Proton Collisions at* $\sqrt{s}$ *= 7 TeV*, ATLAS Note, ATLAS-CONF-2010-053 (2010).

[164] The ATLAS Collaboration, G. Aad et al., *Expected Performance of the ATLAS Experiment*, CERN-OPEN-2008-020, 298-326 (2008).

[165] E. Richter-Was and T. Szymocha, *Hadronic tau identification with track based approach: the* $Z \rightarrow \tau\tau$, $W \rightarrow \tau\nu$ *and di-jet events from DC1 data samples*, ATLAS Note, ATL-PHYS-PUB-2005-005 (2005).

[166] The ATLAS Collaboration, G. Aad et al., *Cut-based Identification of Hadronic* τ *Decays in Early ATLAS Data*, ATLAS Note, ATL-PHYS-PUB-2010-001 (2010).

[167] The ATLAS Collaboration, G. Aad et al., *Using Boosted Decision Trees for Hadronic Tau Identification*, ATLAS Note, ATL-COM-PHYS-2010-603 (2010).

[168] The ATLAS Collaboration, G. Aad et at., *Tau Reconstruction and Identification Performance in ATLAS*, ATLAS Note, ATLAS-CONF-2010-086 (2010).

[169] Björn Gosdzik, *Tau Reconstruction and Identification Performance at ATLAS*, Proceeding 21st Hadron Collider Physics Symposium (HCP 2010), Toronto, arXiv:1009.6135v1 [hep-ex] (2010).

[170] The ATLAS Collaboration, G. Aad et al., *Luminosity Determination Using the ATLAS DEtector*, ATLAS Note, ATLAS-CONF-2010-060 (2010).

[171] The ATLAS Collaboration, G. Aad et al., *Performance of the ATLAS tau trigger in p-p collisions at* $\sqrt{s}$ *= 7 TeV*, ATLAS Note, ATLAS-CONF-2010-090 (2010).

[172] The ATLAS Collaboration, G. Aad et al., *Data-Quality Requirements and Event Cleaning for Jets and Missing Transverse Energy Reconstruction with the ATLAS Detector in Proton-Proton Collisions at a Center-of-Mass Energy of* $\sqrt{s}$ *= 7 TeV*, ATLAS Note, ATLAS-CONF-2010-038 (2010).

[173] R. Field, *CDF Run 2 Monte-Carlo Tunes*, talk presented at the Fermilab MC Tuning Workshop (Oct 2002). http://www-cdf.fnal.gov/physics/conferences/cdf8547_RDF_TeV4LHC.pdf

[174] L. Breiman, J. Friedman, C. Stone and R. Olshen, *Classification and Regression Trees*, Chapman & Hall, (1984).

[175] Y. Freund and R. Shapire, *Experiments with a New Boosting Algorithm*, Proceedings 13th International Conference on Machine Learning, (1996).

[176] The ATLAS Collaboration, G. Aad et al., *Jet energy scale and its systematic uncertainty for jets produced in proton-proton collisions at* $\sqrt{s}$ *= 7 TeV and measured with the ATLAS detector*, ATLAS Note, ATLAS-CONF-2010-056 (2010).

[177] https://twiki.cern.ch/twiki/bin/view/AtlasPublic/EventDisplayPublicResults

[178] A. Höcker et al., *TMVA - Toolkit for Multivariate Data Analysis with ROOT*, CERN-OPEN-2007-007, arXiv:physics/0703039v5 (2007).

[179] A.D. Martin, W.J. Stirling, R.S. Thorne and G. Watt, *Update of Parton Distribution at NNLO*, Phys. Lett. **B652**, 292-299 (2007), arXiv:0706.0459 [hep-ph].

[180] LHC/LC Study Group, *Physics Interplay of the LHC and the ILC*, arXiv:hep-ph/0410364v1 (2004).

[181] F. Gianotti et al., *Physics Potential and experimental challenges of the LHC luminosity upgrade*, Eur. Phys. J. **C39**, 293-333 (2005), arXiv:hep-ph/0204087v1.

[182] The ILC Collaboration, G. Aarons et al., *International Linear Collider Reference Design Report Volume 2: PHYSICS AT THE ILC*, arXiv:0709.1893v1 [hep-ph] (2007).

[183] CLIC Study Team Collaboration, H. Braun et al., *CLIC 2008 Parameters*, CERN-OPEN-2008-021, CLIC-Note-764 (2008).

[184] G. Moortgat-Pick, K. Rolbiecki, J. Tattersall and P. Wienemann, *Probing CP Violation with and without Momentum Reconstruction at the LHC*, JHEP **01** 004 (2010), arXiv:0908.2631v2 [hep-ph].

Danksagung

Nach erfolgreicher Disputation möchte ich an dieser Stelle all den Menschen danken, die mich während meiner Zeit als Doktorand und der Entstehungsphase dieser Arbeit begleitet und motiviert haben. Sie alle habe mich dabei tatkräftigt unterstützt und dazu beigetragen, diese Phase meines Lebens erfolgreich zu beenden. Während meiner Zeit beim ATLAS Experiment habe ich viele nette Menschen kennen gelernt und die Erfahrungen die ich gesammelt habe sind unschätzbar wertvoll.

An erster Stelle möchte ich Philip dafür danken, daß er mir die Möglichkeit gegeben hat bei ihm zu promovieren. Seine schier unerschöpfliche Energie und Enthusiasmus, seine Gabe immer weiter zu motivieren und niemals die Hoffnung zu verlieren, daß alles Gut wird, selbst bei größten technischen Unwegsamkeiten ist phänomenal. Er hat mir stets mit gutem Rat zur Seite gestanden. Danke!

Viele Dank auch an Prof. Dr. Peter Schleper, der sich bereiterklärt hat mein Zweitgutacher für die Dissertation zu sein.

Ein großes Danke geht an Stan, der mich geduldig in die Welt der τ-leptonen eingeführt hat. Sein unglaubliches Wissen und seine Hilfsbereitschaft sind inspirierend für jeden. Es hat große Freude gemacht, mit ihm zusammen zu arbeiten, gell?

Ein großes Dankeschön geht auch an Gudi. Immer ein Augenzwinkern auf Lager hat sie mit ihrer herzerfrischenden Art stets gute Laune verbreitet. Vor der Disputation hat sie mir damit einiges an Nervosität genommen. Danke auch, daß sie Zweitgutachterin für meine Disputation war.

Ich danke auch allen Mitgliedern der ATLAS Gruppe am DESY und der ATLAS-Tau Gruppe. Es wäre nicht so schön gewesen ohne all die netten und hilfsbereiten Menschen. Vor allem Wolfgang als unser IT-Retter in der Not und Michael als mein langjähriger Büronachbar. Im Laufe der Zeit haben wir viele fruchtbare Diskussionen geführt und nebenbei so machen Umzug bewältigt. Ich möchte auch allen Doktoranden und Diplomanden für die gemeinsame Zeit danken. Und nicht zu vergessen sind Jamie und Krzysztof für ihre großartige Unterstützung während der Analyse. Es hat viel Spaß gemacht!

Fürs Korrekturlesen dieser Arbeit und die hilfreichen Kommentare möchte ich Philip, Stan, Almut, Michael und Jörgen danken. Und natürlich auch allen Besuchern des Probevortrages ein herzlichen Dank. Es ist nicht selbstverständlich mehr 2 Stunden einen Vortrag Seite für Seite durchzugehen, den man eine Woche später noch einmal hören wird. Ohne euch hätte es nicht so gut geklappt!

Natürlich gibt es auch ein Leben abseits der Physik und ab und zu muß man auch mal abschalten können. Dabei kann es durchaus hilfreich sein einen unschuldigen Gummiball gegen eine 4 m entfernte Wand zu schlagen (*unelastischer Stoß*). Vielen Dank an das Squashteam für die gemeinsamen Stunden, allen voran Nina, Jörgen, Martin und Wolfgang. Die Spiele gegen Martin waren immer wieder eine Herausforderung und ich hab sogar 2 oder 3 Spiele gewonnen!

Ich möchte auch Tine und Steffi für unsere Kletterabende danken, aus denen im Laufe der Zeit gemeinsame Kochabende wurden. Ich hoffe ich konnte unter Beweis stellen, daß auch Physiker gut kochen können.

Zum Schluss möchte ich noch meinen Eltern und meinem Bruder danken. Dafür, daß sie immer für mich da sind und immer unterstützen. Ich kann immer auf Euch zählen. Und schließlich Claudia, dafür, daß sie mich ertragen hat, wenn ich eigentlich nicht mehr zu ertragen war und daß sie bis zum Schluß die Nerven behalten hat.